01/11/96

The MODTRAN 2/3 Report and LOWTRAN 7 MODEL

F.X. Kneizys[1]
L.W. Abreu[2]
G.P. Anderson
J.H. Chetwynd
E.P. Shettle[3]
A. Berk[4]
L.S. Bernstein[4]
D.C. Robertson[4]
P. Acharya[4]
L.S. Rothman
J.E.A. Selby[5]
W.O. Gallery[6]
S.A. Clough[6]

Edited By:

L.W. Abreu
G.P. Anderson

[1]. Currently retired
[2] Currently at the Ontar Corporation
[3]. Currently at the Naval Research Laboratory
[4]. Currently at the Spectral Sciences, Inc.
[5]. Currently at the Northrop Corporation
[6]. Currently at the Atmospheric Environmental Research, Inc.

Prepared for:

Phillips Laboratory, Geophysics Directorate
PL/GPOS
29 Randolph Road
Hanscom AFB, MA 01731-3010

Contract F19628-91-C-0132
Ms. Gail Anderson, and Dr. Laurence S. Rothman, Technical Representatives

Prepared by:

Ontar Corporation
9 Village Way
North Andover, MA 01845
Tel: (USA)508-689-9622 Fax: (USA)508-681-4585

MODTRAN Report

Table of Contents

THE MODTRAN 2 / LOWTRAN 7 MODEL

1. INTRODUCTION

This report describes the inter-relationships of the MODTRAN (Ref 1) and LOWTRAN 7 (Ref. 2) models and the coordinated efforts in constructing a fully integrated computer code for predicting atmospheric radiance and transmittance. These models are extensions and upgrades to their predecessors: LOWTRAN 6 (Ref. 3), LOWTRAN 5 (Ref. 4), LOWTRAN 5B (Ref. 5), LOWTRAN 4 (Ref. 6), LOWTRAN 3B (Ref. 7), LOWTRAN 3 (Ref. 8) and LOWTRAN 2 (Ref. 9). All of the options and capabilities of the previous versions have been retained.

The first four sections of the report (Common Elements), contain information relevant to both models. Section 3 is specifically tailored to the MODTRAN 2 model. The remainder of the report is pertinent to both models.

The models calculate atmospheric transmittance, atmospheric background radiance, single-scattered solar and lunar radiance, direct solar and lunar irradiance and multiple-scattered solar and thermal radiance. The spectral resolution of LOWTRAN 7 is 20 cm^{-1} FWHM (Full Width at Half-Maximum) in averaged steps of 5 cm^{-1} in the spectral range of 0 to 50,000 cm^{-1} or 0.2 μm to infinity. The MODTRAN resolution is 2 cm^{-1} FWHM in averaged steps of 1 cm^{-1}. A single parameter band model (Pressure) is used for molecular line absorption in LOWTRAN 7, while MODTRAN utilizes (Pressure, Temperature and a line width). The effects of molecular continuum-type absorption; molecular scattering, aerosol and hydrometeor absorption and scattering are all included. Representative atmospheric aerosol, cloud and rain models are provided within the code with options to replace them with user-modeled or measured values. Spherical refraction and earth curvature (ray bending) are considered in the calculation of the atmospheric slant path and attenuation amounts along the path.

New atmospheric constituent profiles[10] containing separate molecular profiles (0 to 120 km) for thirteen (13) minor and trace gases are provided for use with both models. Six reference atmospheres, each defined by temperature, pressure, density and mixing ratios for H_2O, O_3, CH_4, CO and N_2O, all as a function of altitude (selected from the U.S. Standard Supplements, 1966[11] and the U.S. Standard Atmosphere 1976[12]) allow a wide range of climatological choices.

For LOWTRAN 7, Pierluissi and Maragoudakis[13] have developed separate band models and band model parameters for the absorbing molecules: H_2O, O_3, N_2O, CH_4, CO, O_2, CO_2, NO, NO_2, NH_3 and SO_2 (see section 4.1). Analytic transmittance functions (double-exponential) replace numerical tables stored in previous LOWTRAN models. These band model parameters were developed with and based on degraded line-by-line spectra[14] and validated against laboratory measurements. Modifications to the water vapor continuum absorption at 1 and 10 μm are included in both models. These corrections were based on a series of laboratory and field measurements[15,16,17,18].

For MODTRAN 2, Anderson et al[19] have developed band model parameters from the HITRAN 1992[20] database with pressure and temperature dependence and a defined line width (see section 3). Besides its more recent and accurate derivation, the MODTRAN model also contains geometrical corrections to some long-standing problems with short and long horizontal-like paths[21], errors currently existing in the older versions of LOWTRAN and FASCODE.

New ultraviolet absorption parameters for molecular oxygen (Schumann-Runge bands, Herzberg continuum) have been added to the codes[22,23,24,25,26]. The ozone absorption data in the ultraviolet (Hartley and Huggins bands) has been updated or improved based on more recent measurements[27,28,29,30]. These more recent additions also include temperature-dependent absorption coefficients.

An expanded, more precise extra-terrestrial solar source function is included in the models. The derivation of this solar source function is based on the work of Van Hoosier et al[31,32], Neckel and Labs[33], Werhli[34] and Thekeakara[35]. The spectral range of 0 to 57,470 cm^{-1} is covered and is generally compatible with the resolution of the molecular absorption parameters of both models.

The models use an efficient and accurate multiple scattering parameterization[36,37] based on the two-stream approximation and an adding method for combining atmospheric layers. An interface scheme was developed utilizing a modified 3 term k-distribution method to match the multiple scattering approach to the LOWTRAN band model calculation of molecular gaseous absorption. This interface scheme is not needed in the MODTRAN model due to the more accurate 1 cm^{-1} steps. An estimate of the errors due to the multiple scattering parameterization for solar and thermal radiance calculations is considered to be less than 10 percent.

All of the existing aerosol and rain models in previous versions were extended through the millimeter wavelength region. The Navy Maritime model was modified to improve its wind-speed dependence for the large particle component[38]. Water cloud

models (cumulus, stratus, altostratus, strato-stratocumulus and nimbostratus) residing in RADTRAN[39] and FASCOD2[40] have been added to the models. A sub-visual cirrus cloud model and a thin cirrus cloud model with realistic wavelength dependence and separate absorption, scattering and asymmetry parameters were developed for these radiative transfer models. A new aerosol model for desert-like conditions with wind speed dependence has also been added[41,42]. Both programs currently allow users to modify the aerosol profiles when operating in areas of elevated surfaces.

The stratospheric aerosols provide additional combinations of the wavelength dependent extinction coefficient models (background stratospheric, aged volcanic or fresh volcanic) and the vertical distribution profiles (background and moderate, high or extreme volcanic). The background stratospheric extinction model has been modified to utilize new refractive index data and size distribution measurements[43].

2. COMMON ELEMENTS

2.1 AIRMASS COMPUTATION (SPHERICAL REFRACTIVE GEOMETRY)

The Airmass Computation description in this section is principally from Gallery[44] and the description contained in reference 3.

2.1.1 Introduction

The transmittance and radiance along a path through the atmosphere is principally dependent on the total amount and the distribution of the absorbing or scattering species along the path. The integrated amount along a path is described by various names, including: column density, equivalent absorber amount, and "airmass". While the term "air mass' applies specifically to the total amount of gas along the path, it will be used here to refer loosely to the integrated amounts for all the different species relative to the amount for a vertical path. The calculation of air mass for realistic atmospheric paths requires that the earth's curvature and refraction be taken into account.

The model for calculating air mass has been greatly improved in MODTRAN 2. Previous models assumed that the index of refraction was constant between layer boundaries. The new model assumes a continuous profile for the refractive index, with an exponential profile between layer boundaries. It is more accurate than the previous models and works for all conceivable paths. All the options from the previous LOWTRAN models for specifying slant paths have been retained.

This section describes the model for calculating air mass and presents calculations of air mass for several representative atmospheric paths. For a detailed description of the method described here, see reference 44.

2.1.2 Definition of Equations

The atmosphere is modeled as a set of spherically symmetric shells with boundaries at the altitudes Z_j, j = 1, N. The temperature, pressure, and absorber (gas and aerosol) densities are specified at the layer boundaries. Between boundaries, the temperature profile is assumed to be linear, while the pressure and density profiles are assumed to follow exponential profiles. For example, the density ρ at an altitude z between z_j and z_{j+1} is given by:

$$\rho(z) = \rho_j \exp\left[-\frac{(z - z_j)}{H_\rho}\right]$$

where the density scale height Hρ is

$$H_{\rho} = \frac{(z_{j+1} - z_j)}{\ln(\rho_j / \rho_{j+1})}$$

The scale height varies with each layer and is different for pressure and density.

Consider an optical path through the atmosphere from point a to b as shown in Figure 1. The path is defined by the initial and final altitudes z_a and z_b and by the zenith angle θ_o at a. The other path quantities are: s, the curved path length from a; β, the earth-centered angle; φ, the zenith angle at b; and ψ, the total refractive bending along the path.

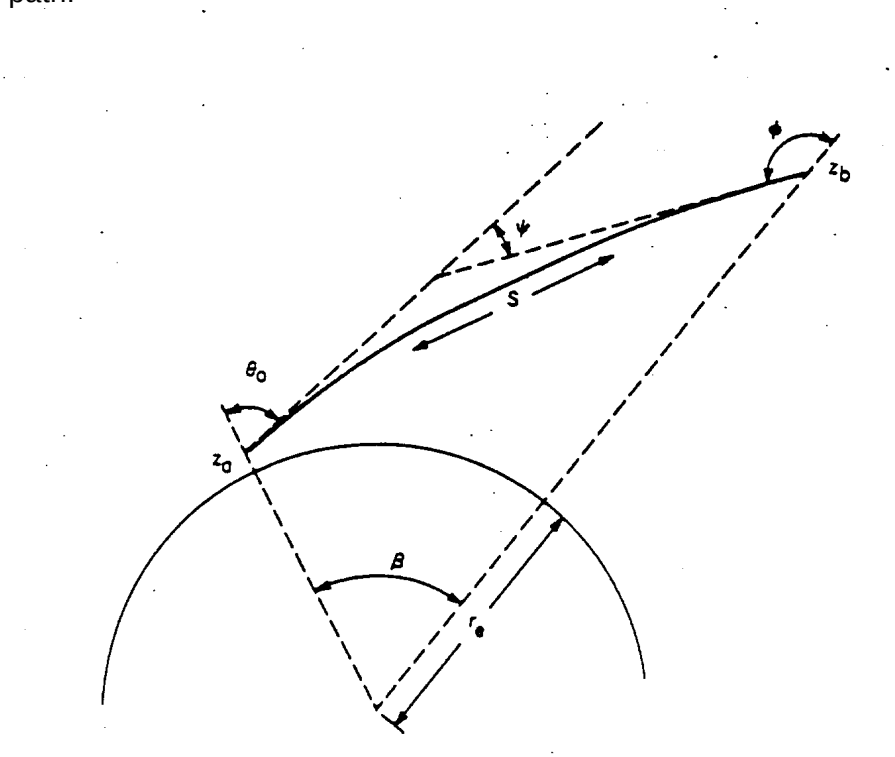

Figure 1. Slant Path Through the Atmosphere From Point a to Point b The integrated amount u of an absorber of density ρ (z) is given by:

$$u = \int_a^b \rho(z)\, ds \qquad (1)$$

$$u = \int_a^b \rho(z)\, (ds/dz) \quad dz \qquad (2)$$

At any point along the path

$$\frac{ds}{dz} = (\cos\theta)^{-1} \tag{3}$$

where θ is the local zenith angle.

Due to the curvature of the earth and to refraction, θ varies along the path. However, if the zenith angle is less than about 80° , the variation of θ along the path is negligible and Eq. (2) can be written as:

$$u = (\cos\theta_0)^{-1} \int_a^b \rho \, dz \tag{4}$$

Eq. (4) is called the secant approximation and is equivalent to assuming a plane-parallel atmosphere. The integral in Eq. (4) has a particularly simple form for an exponential density distribution:

$$\int_a^b \rho \, dz = H_\rho \left[\rho(z_a) - \rho(z_b)\right] \tag{5}$$

where H_ρ is the density scale height. If the path extends over several layers, each with a different scale height, then the integral in Eq. (5) must be broken into separate parts, one for each layer.

For the general case, curvature and refraction must be taken into account in Eq. (2). This is accomplished by a detailed numerical integration of Eq. (2) as follows. The interval from z_a to z_b is divided into a number of sub-intervals defined by z_1,,z_2, . . . $z_{N..\cdot}$.The integral in Eq. (2) is approximated by the sum

$$u = \sum_{i=1}^{N-1} \bar{\rho}_i \, \Delta s_i \tag{6}$$

where

$$\bar{\rho}_i = \frac{1}{\Delta z_i} \int_{z_i}^{z_{i+1}} \rho(z) \, dz \tag{7}$$

$$\Delta s_i = \int_{z_i}^{z_{i+1}} (ds/dz) \, dz \quad . \tag{8}$$

Since the density is assumed to follow an exponential profile, the integral in Eq . (7) can be written analytically as

$$\bar{\rho}_i = \frac{H_\rho}{\Delta z_i} \left[\rho(z_i) - \rho(z_{i+1})\right] \quad , \tag{9}$$

where the scale height H_ρ is constant over the layer from z_a to z_b The integral in Eq. (8) can be obtained numerically as shown in the next section.

The number and spacing of the intervals z_i are chosen so that Eq. (6) is a good approximation to Eq (2) as will also be shown. Again, if the path extends over several layers, with different scale heights in each, then the path integral must be performed separately for each layer. In the discussion that follows, it will be assumed that the path is confined to a single layer in which the scale heights are constant with altitude .

2.1.3 Atmospheric Refraction

The governing equation for a ray passing through the atmosphere is Snell's Law for a spherically symmetric medium, given by

$$n(r)\, r \sin\theta \;=\; C \qquad , \tag{10}$$

where n is the index of refraction, r is the radius to a point along the ray, θ is the zenith angle at that point, and C is a constant of the particular path. If the ray is horizontal at a point r_T, θ is equal to 90^o at that point, and C equals $n(r_T)r_T$; the altitude at that point is called the tangent height.

The index of refraction n is conveniently written as

$$n(r) = 1 + N(r) \; , \tag{11}$$

where N(r) is called the refractivity (see Section 2.1.6 for a discussion of the index of refraction). N is wavenumber dependent and, in the visible and the infrared, N is also very nearly proportional to the total air density. At sea level, in the infrared, N is of the order of 3×10^{-4} . In these calculations, we assume that N follows an exponential profile with a scale height H_N. H_N is determined separately for each atmospheric layer.

The effect of refraction is to bend the path in the direction of increasing N. The radius of curvature K of the refracted ray can be shown to be:

$$K \;=\; -(n'/n)\sin\theta \tag{12}$$

where n' = dn/dr. It is useful to define the quantity R(r) as

$$R(r) = -\frac{r}{n/n'} \quad (13)$$

R is simply the ratio of r to the radius of curvature of a ray tangent at r. R is a property of the atmospheric profile and not the particular path and is a good measure of the importance of refraction at a particular altitude. For example, for the U. S. Standard Atmosphere, R is approximately 0.16 at sea level and decreases exponentially with altitude with a scale height of about 10 km.

To trace a ray through the atmosphere, consider the path shown in Figure 1: θ_o is the zenith angle at Z_a, θ is the zenith angle at Z_b , β is the earth-centered angle, and ψ is the bending along the path. Let s be the length of the path from point a. At any point the differential path quantities are given by

$$ds = \frac{1}{\cos\theta}\, dr \quad (14)$$

$$d\beta = \tan\theta \frac{1}{r}\, dr \quad , \quad (15)$$

where θ is the zenith angle at the point. Substituting for cos θ from Eq. (10) into Eq. (14) gives:

$$ds = \left(1 - \frac{C^2}{n^2 r^2}\right)^{-1/2} dr \quad (16)$$

Eq. (16) is the basic atmospheric ray trace equation. If the function n(r) is known, then Eq. (l6) can be integrated numerically along the path.

However, the difficulty with integrating Eq. (16) is that it has a singularity at $\theta = 90°$, that is, at the tangent height, where $C = n(r_T)\, r_T$. A simple change of variables will remove this singularity and also provide some insight into the importance of refraction. Define a new independent variable x as

$$x = r \cos\theta \quad . \quad (17)$$

(x can be interpreted as the straight-line distance to the geometric tangent point). Differentiating Eq. (17) gives

$$dx = \left[\cos\theta - r \sin\theta \left(d\theta/dr\right)\right] \quad (18)$$

Differentiating Eq. (10) and using Eq. (13) gives

$$d\theta/dr \;=\; -(1-r)\tan\theta/r \qquad (19)$$

Substituting Eq. (19) into Eq. (18) gives

$$dx \;=\; (1-R\sin^2\theta)\,dr/\cos\theta \qquad (20)$$

Comparing Eq. (20) with Eq (14) yields

$$ds \;=\; (1-R\sin^2\theta)^{-1}\,dx \qquad (21)$$

In this form of the equation for ds, the right-hand side is a well-behaved function of r for all paths, including vertical and horizontal paths (except in the unusual case where R is ≥ 1 and the path curves back toward the earth, that is, looming). The intermediate variable x = r cos θ, is also well defined for all paths. In practice, the numerical integration of Eq. (21) is driven in steps of r, from r to r + Δr. The corresponding increment in x is calculated from Eq. (17). The integration of s from Eq. (21) is then straightforward.

2.1.4 Numerical Algorithm

The numerical algorithm used to evaluate Eq. (6) is as follows:

1. Find the minimum and maximum altitude HMIN and HMAX along the path and the zenith angle θ at HMIN. If the path goes through a tangent point, then solve Eq. (10) iteratively for the tangent height.

2. From the given atmospheric profile, construct a new profile at the layer boundaries from HMIN to HMAX, interpolating the pressure, temperature, and densities where necessary.

3. Starting with the lowest layer, trace the path through each layer: a. Divide the layer into sub-layers defined by the altitudes z_j , such that $\Delta z_j \;=\; \tilde{\Delta}s\cos\theta_{\,j-1}$ where $\tilde{\Delta}s$ is a nominal path length (5 km) and θ_{j-1} is the zenith angle at z_{j-1}.

$$\Delta z_j \;=\; \tilde{\Delta}s\cos\theta_{\,j-1}$$

$$z_j = z_{j-1} + \Delta z_j$$

$$r_j = r_e + z_j \quad (r_e \, is \, radius \, of \, the \, earth)$$

$$n_j = 1 + N(z_j)$$

$$\sin\theta_j = \frac{C}{n_j r_j}$$

$$\cos\theta_j = (1 - \sin^2\theta_j)^{1/2}$$

$$x_j = r_j \cos\theta_j$$

$$\Delta x_j = x_j + x_{j-1}$$

$$R_j = \frac{-r_j}{\left[(dN/dr|_j)/n_j\right]}$$

$$ds/dx|_j = (1 - R_j \sin^2\theta_j)^{-1}$$

$$\Delta s_j = 1/2\left(ds/dx|_{j-1} + ds/dx|_j\right)\Delta x_j$$

b. For each species, integrate the density ρ:

$$\rho_j = \rho(z_j)$$

$$\overline{\rho}_j = H_\rho(\rho_j - \rho_{j+1})/\Delta z_j$$

$$u = \sum_{j=1}^{N-1} \overline{\rho}_j \Delta s_j$$

2.1.5 Airmass Calculations

This section will present plots of airmass values for three classes of slant paths. The term "airmass values" refers to the integrated amount of air along a path compared to the amount for a vertical path from ground to space**.** For example, the airmass value for a path from the ground to space with the zenith angle at the ground of 90° is 38.1 for the U. S. Standard Atmosphere (one air mass equals 2.15 X 10^{25} molecules cm^{-2} or 1.034 X 10^{3} gm cm^{-2}). These three paths are described by the initial altitude "H1" and the zenith angle "ANGLE" at H1. The other end of the path is the top of the atmosphere, here taken to be 100 km. The three classes of paths are: 1) H1 = 0 km for ANGLE varying from 0 to 90° ; 2) ANGLE = 90° for H1 varying from 0 to 50 km; 3) H1 = 30 km for ANGLE varying from 85° to 95. 1° at which point the path intersects the earth. The wavenumber for these calculations was 2000 cm^{-1} (5 μm). The dependence of air mass on wavenumber in the infrared is small.

In addition to the airmass value, the amounts of water vapor and of ozone relative to the amounts for a vertical path from ground to space are also shown. The relative amounts of these gases depend upon their vertical distribution; in these cases, the U. S. Standard Atmosphere density profiles are used. Since the distributions of these gases in the atmosphere are so variable, the relative amounts for other profiles could be significantly different. The values for water vapor and ozone shown here should be taken to be illustrative only.

Figure 2 (a and b) shows the airmass value, relative water vapor, and ozone amounts for path 1. Also shown in Figure 2(b) is the secant of the zenith angle. For a large zenith angle, the relative amount of water vapor is greater than the airmass value while the amount of ozone is less. This effect is due to the fact that for large zenith angles, the greater part of the path is near the ground. Water vapor is concentrated in the lower layers, so the relative amount of water vapor is large compared to the vertical path. Ozone, however, is concentrated in the stratosphere, which contains a relatively small part of the path. Note that the secant agrees to better than one percent with the airmass value up to 72° , up to 80° for water vapor, but only up to 60° for ozone. The discrepancy is due mainly to the effect of the earth's curvature and not refraction; by including curvature but neglecting refraction, the relative amounts can be calculated to better than one percent up to 84° for air, 86° for water vapor, and 82° for ozone.

Figure 3 shows the airmass values and relative amounts for path 2. These curves mimic the density profiles of air, water vapor, and ozone respectively, since the bulk of the gas is located within a few kilometers (vertically) of the observer altitude.

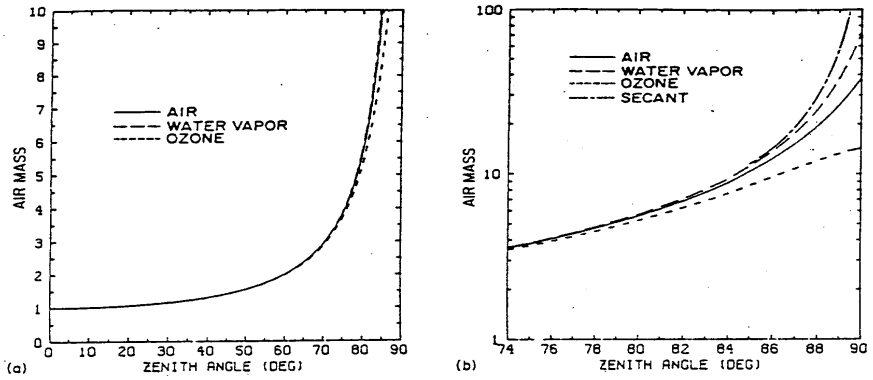

Figure 2. Relative Absorber Amounts vs Zenith Angle for Path 1. (a) 0 to 90° and (b) 74 to 90° (also shown is the secant of the zenith angle)

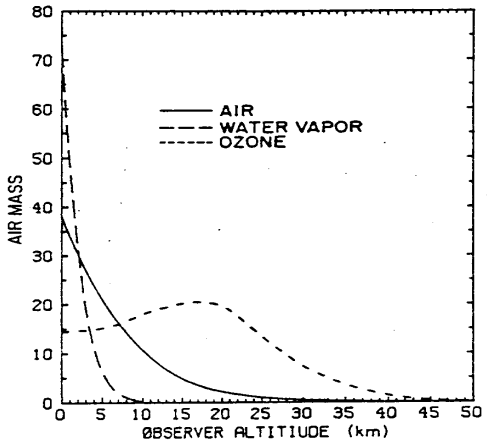

Figure 3 Relative Absorber Amounts vs Observer altitude (H1) for Path 2

The relative amounts shown in Figure 4 correspond to path 3, which is typical of a stratospheric balloon-borne experiment looking at the setting sun. Also shown on the right-hand axis is the tangent height vs zenith angle and the angular diameter of the sun. If the sun is used as the source for a measurement, the airmass value to different points on the face of the sun can vary by a factor of 2 for large zenith angles. The variation in air mass due to this effect can be a major source of uncertainty in the measurement and must be considered carefully.

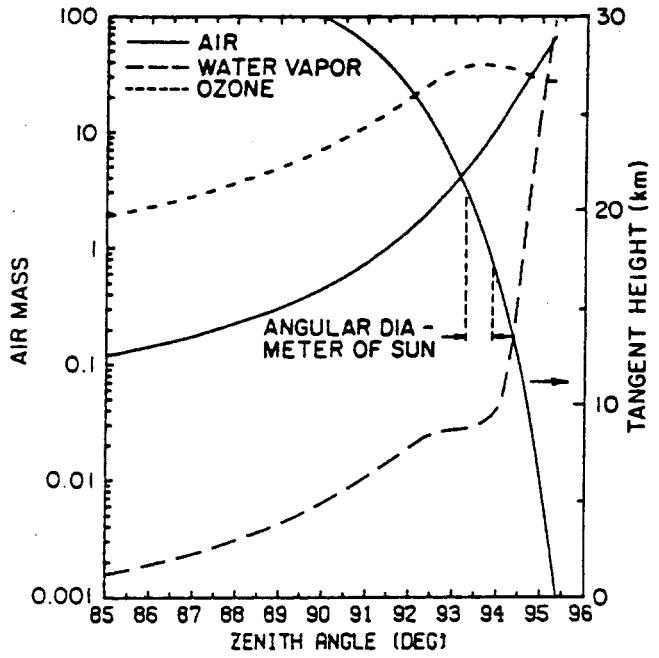

Figure 4. Relative Absorber Amounts vs Zenith Angle for Path 3. Also shown against the right-hand axis is the tangent height vs zenith angle and the angular diameter of the sun

Two other quantities of interest for atmospheric profiles are the tangent height and the refractive bending. The difference in tangent height between an un-refracted and a refracted ray coming in from space is shown as a function of the refracted tangent height in Figure 5 for three atmospheric profiles (the geometry is shown schematically in the inset). The total refractive bending for paths 1 and 2 are shown in Figures 6 and 7 for three atmospheric profiles. Note that the total bending for a path from the ground to space at 90° for the U.S. Standard Atmosphere and the Tropical Atmosphere is about 0.5^{o}, which is the same as the solar diameter.

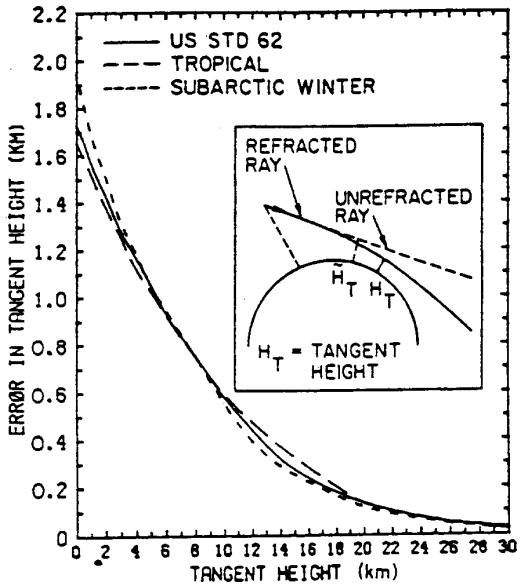

Figure 5. Un-refracted Tangent Height Minus Refracted Tangent Height vs Refracted Tangent Height for a Ray Coming in from Space for Three Atmospheric Profiles. The figure in the inset illustrates the paths

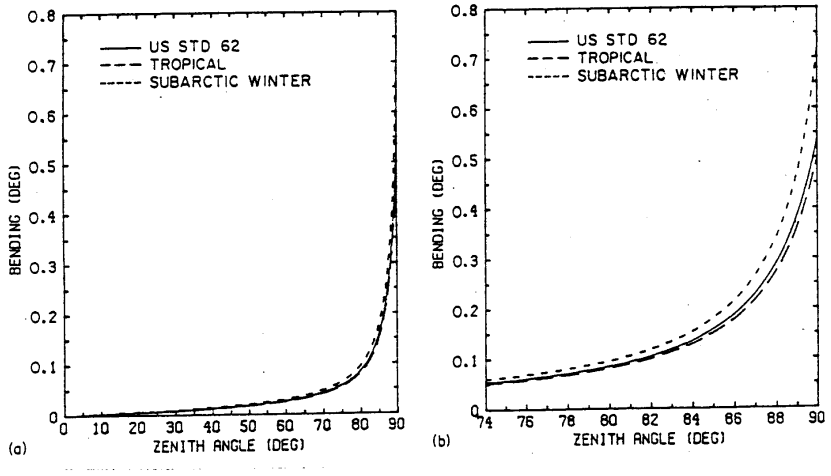

Figure 6. Refractive Bending vs Zenith Angle for Path 1, for Three Atmospheric Profiles. (a) 0 to 90° and (b) 74 to 90°

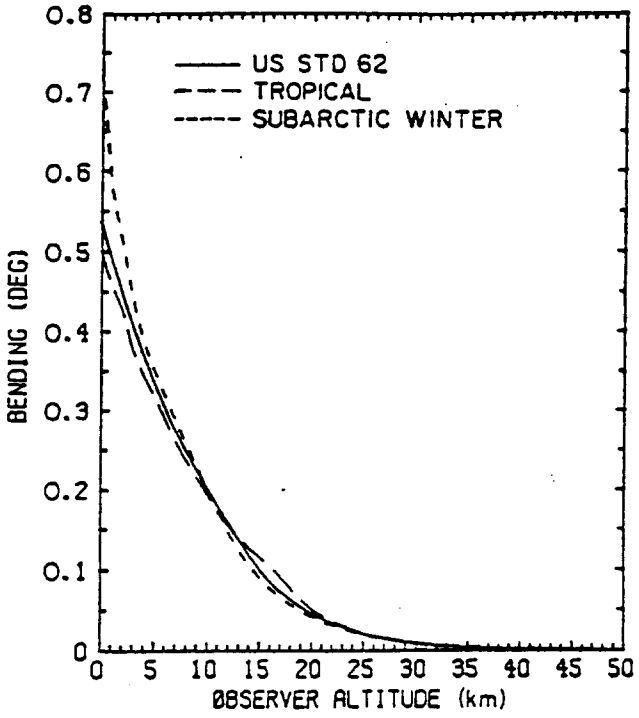

Figure 7. Refractive Bending vs Observer Altitude (H1) for
Three Atmospheric Profiles

2.1.6 Index of Refraction

The equation for the index of refraction n is taken from Edlen[45] and is given by :

$$(n-1)\,x\,10^{6} = \left[a_0 + \frac{a_1}{1-(\nu/b_1)^2} + \frac{a_2}{1-(\nu/b_2)^2}\right] \bullet \frac{(P-P_w)}{P_0} \bullet \frac{296.15}{T}$$

$$+ \left[c_0 - (\nu/c_1)^2\right] \frac{P_w}{P_0} \quad ,$$

where ν is the wavenumber in cm^{-1}, P is the total pressure in mb, P_W is the partial pressure of water vapor, P_0 is 1013.25 mb, T is the temperature in Kelvin, and the constants a, b, and c are:

a_0 = 83.43, a_1 = 185.08, a_2 = 4.11

$b_1 = 1.140 \times 10^5$, $b_2 = 6.24 \times 10^4$

$c_o = 43\ 49$, $c_1 = 1.70 \times 10^4$

The formula used in previous versions of LOWTRAN was a simplified version of this expression.

2.1.7 WATER VAPOR CONTINUUM

An improved water vapor continuum model has been added to the models. This model for the continuum contribution from water vapor absorption was originally developed by Clough et al for use with the line-by-line transmittance and radiance atmospheric code, FASCOD2[40].

For atmospheric applications it is advantageous to express the density dependence of the water vapor continuum absorption in terms of a self and foreign component. The continuum contribution to the absorption coefficient $k_C(\nu)$, is given by the expression:

$$k_C(\nu) = \rho_s \nu \tanh(hc\nu/2kT) \left[\left(\frac{\rho_s}{\rho_0}\right)\tilde{C}_s(\nu,T) + \left(\frac{\rho_f}{\rho_0}\right)\tilde{C}_f(\nu,T)\right]$$

where T is the temperature (^oK), ν the wavenumber (cm^{-1}), hc/k = 1.43879 ° K/cm^{-1}, $(\rho_s/\rho_0)\ and\ (\rho_f/\rho_0)$ are the number-density ratios for the self and foreign continuum; and $\tilde{C}_s\ and\ \tilde{C}_f$ $\left[(cm^{-1}\, mol/cm^2)^{-1}\right]$ are wavenumber-dependent continuum absorption parameters for the self and foreign components. The density ρ_S is the density of the water vapor and ρ_f is the density of all other molecular species; therefore, $\rho_S + \rho_f$ represents the total density. The quantity, ρ_o, is the reference number density defined at 1013 mb and 296K. The present formulation in terms of density has the advantage that the continuum contribution to the absorption coefficient decreases with increasing temperature through the number-density ratio term. The quantities $\tilde{C}_s$ and $\tilde{C}_f$ for water vapor are stored in the program for the spectral range 0 to 20, 000 cm^{-1}.

The values for $\tilde{C}_s$ for water vapor at 296K are shown in Figure 8 together with the experimental values obtained by Burch et al. [46-49]. The strong temperature dependence of the self density-dependent water vapor continuum is treated by storing values of C_S at 260K and 296K and linearly interpolating between the 260K and 296K

values. The 260K result was obtained by extrapolating the fits to the 338K and 296K data of Burch et al.[48]. The results for 260K and 296K are shown in Figure 9.

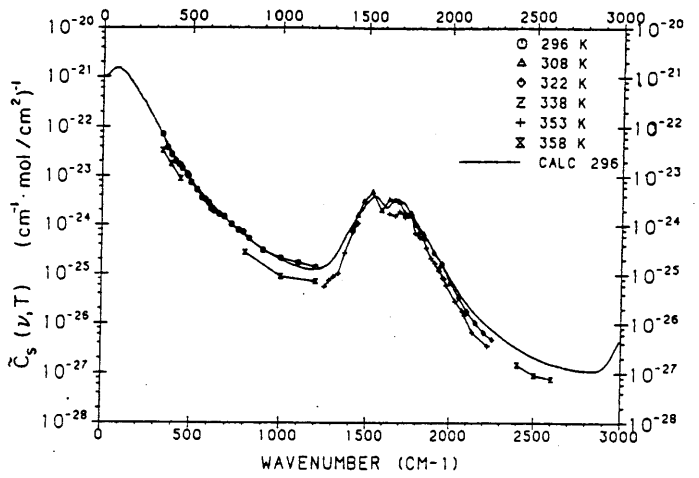

Figure 8. The Self Density-Dependent Continuum Values, $\tilde{C}_s$, for Water Vapor as a Function of Wavenumber. The experimental values are from Burch et al[48]

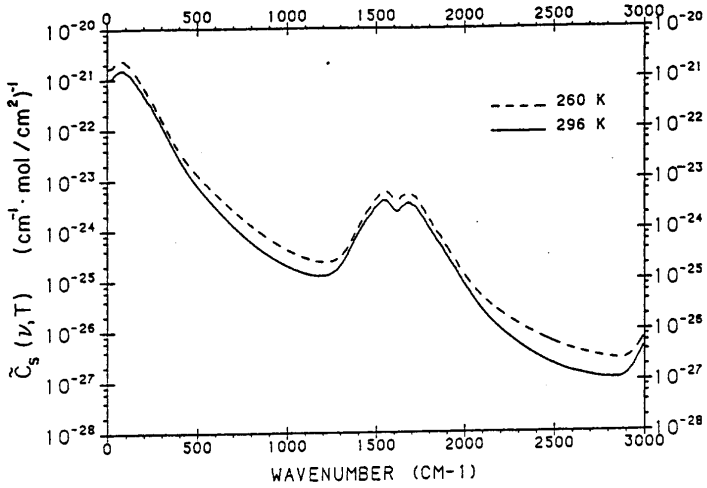

Figure 9. The Self Density Dependent Continuum Values, $\tilde{C}_s$, for Water Vapor as a Fraction of Wavenumber at 260K and 296K. The values from 296K are fits to experimental results[48]; the 260K is extrapolated.

Only values near room temperature are available for the foreign dependence of the water vapor continuum. The continuum values $\tilde{C}_f$ at 296K are shown in Figure 10 and have been obtained by a fit to the data of Burch[46-49]. There is still considerable uncertainty in the foreign values for the spectral window regions at 1000 and 2500 cm^{-1}.

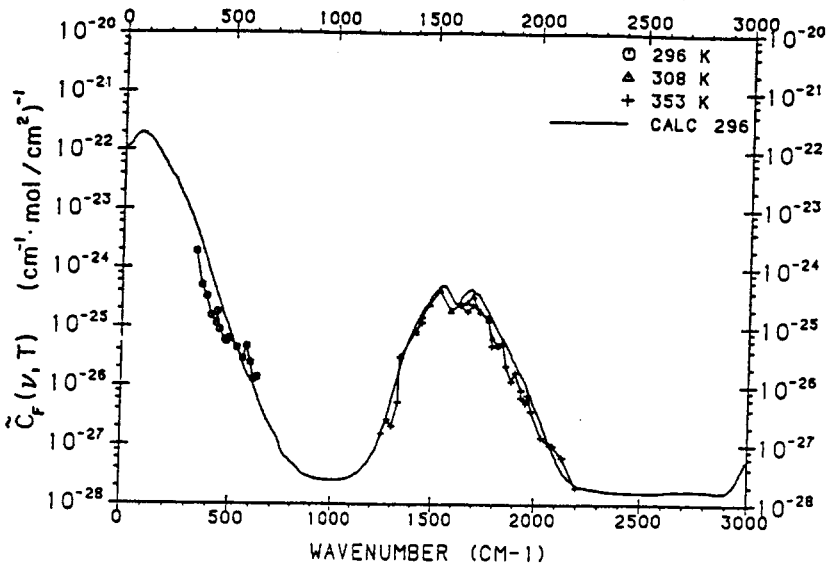

Figure 10. The Foreign Density Dependent Continuum Values, $\tilde{C}_f$, for Water Vapor as a Function of Wavenumber. The experimental values are from Burch, et al[48]

In the MODTRAN code, the total optical depth due to water vapor continuum absorption for an atmospheric slant path of N layers is given by:

$$\sum_{i=1}^{N} \int_i k_c(\nu)\, ds \;=\; C_s(\nu,296) \sum_{i=1}^{N} \int_i \left(\frac{\rho_s}{\rho_0}\right) \rho_s\, ds \;+$$

$$\left[C_s(\nu,260) - C_s(\nu,296)\right] \sum_{i=1}^{N} \left(\frac{296-T_i}{296-260}\right) \int_i \left(\frac{\rho_s}{\rho_0}\right) \rho_s\, ds \;+ \qquad (23)$$

$$C_f(\nu,296) \sum_{i=1}^{N} \int_i \left(\frac{\rho_f}{\rho_0}\right) \rho_s\, ds$$

where ds is the incremental path length, T_i is the temperature of the i'th layer, and:

$$C_s(\nu,296) \;=\; \nu \tanh\left(hc\nu/2k(296)\right) \;\tilde{C}_s(\nu,296)$$

$$C_s(\nu,260) = \nu \tanh\left(hc\nu/2k(260)\right) \tilde{C}_s(\nu,260) \quad (24)$$

$$C_f(\nu,296) = \nu \tanh\left(hc\nu/2k(296)\right) \tilde{C}_f(\nu,296)$$

Calculations of atmospheric slant path transmittance using these modified water vapor continuum absorption coefficients will result in approximately the same attenuation as in the older LOWTRAN models for the atmospheric window regions from 8 to 12 μm and 3.5 to 4.2 μm. However, for other spectral regions, particularly from 4.5 to 5.0 μm, significant improvement in atmospheric transmittance calculations has been made with the inclusion of the contribution of continuum absorption.

2.2 MODEL ATMOSPHERES

The description of the model atmospheres contained in this section is based directly on the AFGL report by Anderson[10] et al.

2.2.1. INTRODUCTION

Atmospheric radiance-transmittance spectral modeling requires an adequate description of the local thermal and constituent environment. A data base consisting of realistic vertical profiles for temperature and gas mixing ratios has been designed expressly for incorporation into such models. Its thermal structure is represented by a subset of the 1966 Atmospheric Supplements[11] (tropical (15N), middle latitude (45N) summer and winter, subarctic (60N) summer and winter) and the U.S. Standard Model Atmosphere, 1976[12] . The accompanying volume mixing ratio profiles rely as much as possible on current measurements and/or theoretical predictions.

More extensive literature reviews of atmospheric structure, variability, dynamics and chemistry are available (for example, Smith[50], WMO[51,52], and Brasseur and Solomon[53]).

This compilation includes only those gases currently part of the HITRAN 1992 database[20]. The range of tabulated atmospheric values for water vapor (H_2O), ozone (O_3), nitrous oxide (N_2O), and methane (CH_4) are primarily inferred from global satellite measurements[54-56]. The carbon monoxide (CO) seasonal profiles, however, rely on the predictions of a photochemical-dymanic model[57]. The remaining individual gas profiles have been derived from a variety of sources. All have been edited to produce the final tabulations; in most cases this consists of smoothing and interpolation to standard altitude levels. Some species, however, require additional extrapolation because of the unavailability of suitable data (particularly above the

stratopause). In general, dayside estimates for diurnally-varying species (O_3, NO, and NO_2, for example) have been adopted.

2.2.2 . ATMOSPHERIC PROFILE DESCRIPTION

The six reference atmospheres, each with associated volume-mixing ratio profiles for H_2O, O_3, N_2O, CO, and CH_4, are presented in Table 1. Along with CO_2, these are the most radiatively active molecules. Sample profiles, appropriate for the U. S. Standard atmospheric conditions (MODEL 6), are shown in Figure 11. Because the mixing ratios of CO_2 and O_2 have been held seasonally invariant, they are listed in Table 2, as part of a set of single profiles numbered according to the HITRAN Database numbering system i.e. H_2O is 1, CO_2 is 2, etc. The first seven molecules in Table 2 are the same as those in Figure 1 for the U.S. Standard Atmosphere. The 25 additional species, as identified on the HITRAN Database are: NO, SO_2, NO_2, NH_3, HNO_3, OH, HF, HCl, HBr, HI, ClO, OCS, H_2CO, HOCl, N_2, HCN, CH_3Cl, H_2O_2, C_2H_2, C_2H_6, PH_3, COF_2, SF_6 and H_2S., See the Anderson[10] report for graphical representations for all the tabular data of these gases. (Note: although N_2 is the dominant atmospheric gas, it appears as only a trace spectral contributor, whereas Argon is a major component of the atmosphere, but does not contribute to the opacity.)

Table 1. Reference Model Atmospheric Profiles

Model = 1 Tropical (15N Annual Average)
Model = 2 Mid-Latitude Summer (45N July)
Model = 3 Mid-Latitude Winter (45N Jan)
Model = 4 Sub-Arctic Summer (60N July)
Model = 5 Sub-Arctic Winter (60N Jan)
Model = 6 U. S. Standard (1976)

This tabular presentation includes: Altitude (km), Pressure (mb), Density (cm^{-3}), and mixing ratios (ppmv) for H_2O, O_3, N_2O, CO, and CH_4. Profiles for CO_2 and O_2 can be found in Table 2.

[(*) indicates subsequent extrapolation adopted for that species]

Table la. Reference Atmospheric Model Profiles, Model 1. Tropical

MODEL = 1 TROPICAL

ALT (KM)	PRES (MB)	TEMP (K)	DENSITY (CM^{-3})	H_20 (PPMV)	O_3 (PPMV)	N_20 (PPMV)	CO (PPMV)	CH_4 (PPMV)
0.00	1.013E+03	299.7	2.450E+19	2.59E+04	2.87E-02	3.20E-01	1.50E-01	1.70E+00
1.00	9.040E+02	293.7	2.231E+19	1.95E+04	3.15E-02	3.20E-01	1.45E-01	1.70E+00
2.00	8.050E+02	287.7	2.028E+19	1.53E+04	3.34E-02	3.20E-01	1.40E-01	1.70E+00

3.00	7.150E+02	283.7	1.827E+19	8.60E+03	3.50E-02	3.20E-01	1.35E-01	1.70E+00
4.00	6.330E+02	277.0	1.656E+19	4.44E+03	3.56E-02	3.20E-01	1.31E-01	1.70E+00
5.00	5.590E+02	270.3	1.499E+19	3.35E+03	3.77E-02	3.20E-01	1.30E-01	1.70E+00
6.00	4.920E+02	263.6	1.353E+19	2.10E+03	3.99E-02	3.20E-01	1.29E-01	1.70E+00
7.00	4.320E+02	257.0	1.218E+19	1.29E+03	4.22E-02	3.20E-01	1.25E-01	1.70E+00
8.00	3.780E+02	250.3	1.095E+19	7.64E+02	4.47E-02	3.20E-01	1.19E-01	1.70E+00
9.00	3.290E+02	243.6	9.789E+18	4.10E+02	5.00E-02	3.20E-01	1.09E-01	1.69E+00
10.00	2.860E+02	237.0	8.747E+18	1.91E+02	5.60E-02	3.18E-01	9.96E-02	1.69E+00
11.00	2.470E+02	230.1	7.780E+18	7.31E+01	6.61E-02	3.14E-01	9.96E-02	1.68E+00
12.00	2.130E+02	223.6	6.904E+18	2.91E+01	7.82E-02	3.10E-01	7.81E-02	1.66E+00
13.00	1.820E+02	217.0	6.079E+18	9.90E+00	9.29E-02	3.05E-01	6.37E-02	1.65E+00
14.00	1.560E+02	210.3	5.377E+18	6.22E+00	1.05E-01	3.00E-01	5.03E-02	1.63E+00
15.00	1.320E+02	203.7	4.697E+18	4.00E+00	1.26E-01	2.94E-01	3.94E-02	1.61E+00
16.00	1.110E+02	197.0	4.084E+18	3.00E+00	1.44E-01	2.88E-01	3.07E-02	1.58E+00
17.00	9.370E+01	194.8	3.486E+18	2.90E+00	2.50E-01	2.78E-01	2.49E-02	1.55E+00
18.00	7.890E+01	198.8	2.877E+18	2.75E+00	5.00E-01	2.67E-01	1.97E-02	1.52E+00
19.00	6.660E 01	202.7	2.381E+18	2.60E+00	9.50E-01	2.53E-01	1.55E-02	1.48E+00
20.00	6.650E+01	206.7	1.981E+18	2.60E+00	1.40E+00	2.37E-01	1.33E-02	1.42E+00
21.00	4.800E+01	210.7	1.651E+18	2.65E+00	1.80E+00	2.19E-01	1.23E-02	1.36E+00
22.00	4.090E+01	214.6	1.381E+18	2.80E+00	2.40E+00	2.05E-01	1.23E-02	1.27E+00
23.00	3.500E+01	217.0	1.169E+18	2.90E+00	3.40E+00	1.97E-01	1.31E-02	1.19E+00
24.00	3.000E+01	219.2	9.920E 17	3.20E+00	4.30E+00	1.88E-01	1.40E-02	1.12E+00
25.00	2.570E+01	221.4	8.413E+17	3.25E+00	5.40E+00	1.76E-01	1.52E-02	1.06E+00
27.50	1.763E+01	227.0	5.629E+17	3.60E+00	7.80E+00	1.59E-01	1.72E-02	9.87E-01
30.00	1.220E+01	232.3	3.807E+17	4.00E+00	9.30E+00	1.42E-01	2.00E-02	9.14E-01
32.50	8.520E+00	237.7	2.598E+17	4.30E+00	9.85E+00	1.17E-01	2.27E-02	8.30E-01
35.00	6.000E+00	243.1	1.789E+17	4 60E+00	9.70E+00	9.28E-02	2.49E-02	7.46E-01
37.50	4.260E+00	248.5	1.243E+17	4.90E+00	8.80E+00	6.69E-02	2.74E-02	6.62E-01
40.00	3.050E+00	254.0	8.703E+16	5.20E+00	7.50E+00	4.51E-02	3.10E-02	5.64E-01
42.50	2.200E+00	259.4	6.147E+16	5.50E+00	5.90E+00	2.75E-02	3.51E-02	4.61E-01
45.00	1.590E+00	264.8	4.352E+16	5.70E+00	4.50E+00	1.59E-02	3.99E-02	3.63E-01
47.50	1.160E+00	269.6	3.119E+16	5.90E+00	3.45E+00	9.38E-03	4.48E-02	2.77E-01
50.00	8.540E-01	270.2	2.291E+16	6.00E+00	2.80E+00	4.75E-03*	5.09E-02	2.10E-01
55.00	4.560E-01	263.4	1.255E+16	6.00E+00	1.80E+00	3.00E-03	5.99E-02	1.65E-01
60.00	2.390E-01	253.1	6.844E+15	6.00E+00	1.10E+00	2.07E-03	6.96E-02	1.50E-01
65.00	1.210E-01	236.0	3.716E+15	5.40E+00	6 50E-01	1.51E-03	9.19E-02	1.50E-01
70.00	5.800E-02	218.9	1.920E+15	4.50E+00	3.00E-01	1.15E-03	1.94E-01	1.50E-01
75.00	2.600E-02	201.8	9.338E+14	3.30E+00	1.80E-01	8.89E-04	5.69E-01	1.50E-01
80.00	1.100E-02	184.8	4.314E+14	2.10E+00	3.30E-01	7.06E-04	1.55E+00	1.50E-01
85.00	4.400E-03	177.1	1.801E+14	1.30E+00	5.00E-01	5.72E-04	3.85E+01	1.50E-01
90.00	1.720E-03	177.0	7.043E+13	8.50E-01	5.20E-01	4.71E-04	6.59E+00	1.40E-01
95.00	6.880E-04	184.3	2.706E+13	5.40E-01	5.00E-01	3.93E-04	1.04E+01	1.30E-01
l00.0	2.890E-04	190.7	1.098E+13	4.00E-01	4.00E-01	3.32E-04	1.71E+01	1.20E-01
105.0	1.300E-04	212.0	4.445E+12	3.40E-01	2.00E-01	2.84E-04	2.47E+01	1.10E-01
110.0	6.470E-05	241.6	1.941E+12	1.80E-01	5.00E-02	2.44E-04	3.36E+01	9.50E-02
115.0	3.600E-05	299.7	8.706E+11	2.40E-01	5.00E-03	2.12E-04	4.15E+01	6.00E-02
120.0	2.250E-05	380.0	4.225E+11	2.00E-01	5.00E-04	1.85E-04	5.00E+01	3.00E-02

Table Ib. Reference Atmospheric Model Profiles, Model 2. Midlatitude Summer

MODEL = 2 MIDLATITUDE SUMMER

ALT (KM)	PRES (MB)	TEMP (K)	DENSITY (CM^{-3})	H_20 (PPMV)	O_3 (PPMV)	N_20 (PPMV)	CO (PPMV)	CH_4 (PPMV)
0.00	1.013E+03	294.2	2.496E+19	1.88E+04	3.02E-02	3.20E-01	1.50E-01	1.70E+00
1.00	9.020E+02	289.7	2.257E+19	1.38E+04	3.34E-02	3.20E-01	1.45E-01	1.70E+00
2.00	8.020E+02	285.2	2.038E+19	9.68E+03	3.69E-02	3.20E-01	1.40E-01	1.70E+00
3.00	7.100E+02	279.2	1.843E+19	5.98E+03	4.22E-02	3.20E-01	1.35E-01	1.70E+00
4 00	6.280E+02	273.2	1.666E+19	3.81E+03	4.82E-02	3.20E-01	1.31E-01	1.70E+00
5 00	5.540E+02	267.2	1.503E+19	2.23E+03	5.51E-02	3.20E-01	1.30E-01	1.69E+00
6.00	4.870E+02	261.2	1.351E+19	1.51E+03	6.41E-02	3.20E-01	1.29E-01	1.67E+00
7.00	4.260E+02	254.7	1.212E+19	1.02E+03	7.76E-02	3.20E-01	1.25E-01	1.65E+00
8.00	3.720E+02	248.2	1.086E+19	6.46E+02	9.13E-02	3.20E-01	1.19E-01	1.63E+00
9.00	3.240E+02	241.7	9.716E+18	4.13E+02	1.11E-01	3.16E-01	1.09E-01	1.62E+00
10.00	2.810E+02	235.3	8.656E+18	2.47E+02	1.30E-01	3.10E-01	9.96E-02	1.58E+00
11.00	2.430E+02	228.8	7.698E+18	9.56E+01	1.79E-01	2.99E-01	8.96E-02	1.54E+00
12.00	2.090E+02	222.3	6.814E+18	2.94E+01	2.23E-01	2.94E-01	7.81E-02	1.51E+00
13.00	1.790E+02	215.8	6.012E+18	8.00E+00	3.00E-01	2.86E-01	6.37E-02	1.48E+00
14.00	1.530E+02	215.7	5.141E+18	5.00E+00	4.40E-0l	2.80E-01	5.03E-02	1.45E+00
15.00	1.300E+02	215.7	4.368E+18	3.40E+00	5.00E-01	2.72E-01	3.94E-02	1.42E+00
16.00	1.110E+02	215.7	3.730E+18	3.30E+00	6.00E-01	2.61E-01	3.07E-02	1.39E+00
17.00	9.500E+01	215.7	3.192E+18	3.20E+00	7.00E-01	2.42E-01	2.49E-02	1.36E+00
18.00	8.120E+01	216.8	2.715E+18	3.15E+00	1.00E+00	2.17E-01	1.97E-02	1.32E+00
19.00	6.950E+01	217.9	2.312E+18	3.20E+00	1.50E+00	1.84E-01	1.55E-02	1.28E+00
20.00	5.950E+01	219.2	1.967E+18	3.30E+00	2.00E+00	1.61E-01	1.33E-02	1.22E+00
21.00	5.100E+01	220.4	1.677E+18	3.45E+00	2.40E+00	1.32E-01	1.23E-02	1.15E+00
22.00	4.370E+01	221.6	1.429E+18	3.60E+00	2.90E+00	1.15E-01	1.23E-02	1.07E+00
23.00	3.760E+01	222.8	1.223E+18	3.85E+00	3.40E+00	1.04E-01	1.31E-02	9.73E-01
24.00	3.220E+01	223.9	1.042E+18	4.00E+00	4.00E+00	9.62E-02	1.40E-02	8.80E-01
25.00	2.770E+01	225.1	8.919E+17	4.20E+00	4.30E+00	8.96E-02	1.52E-02	7.89E-01
27.50	1.907E+01	228.5	6.050E+17	4.45E+00	6.00E+00	8.01E-02	1.72E-02	7.05E-01
30.00	1.320E+01	233.7	4.094E+17	4.70E+00	7.00E+00	6.70E-02	2.00E-02	6.32E-01
32.50	9.300E+00	239.0	2.820E+17	4.85E+00	8.10E+00	4.96E-02	2.27E-02	5.59E-01
35.00	6.520E+00	245.2	1.927E+17	4.95E+00	8.90E+00	3.70E-02	2.49E-02	5.01E-01
37.50	4.640E+00	251.3	1.338E+17	5.00E+00	8.70E+00	2.52E-02	2.72E-02	4.45E-01
40.00	3.330E+00	257.5	9.373E+16	5.10E+00	7.55E+00	1.74E-02	2.96E-02	3.92E-01
42.50	2.410E+00	263.7	6.624E+16	5.30E+00	5.90E+00	1.16E-02	3.14E-02	3.39E-01
45.00	1.760E+00	269.9	4.726E+16	5.45E+00	4.50E+00	7.67E-03	3.31E-02	2.87E-01
47.50	1.290E+00	275.2	3.398E+16	5.50E+00	3.50E+00	5.32E-03	3.49E-02	2.38E-01
50.00	9.510E-01	275.7	2.500E+16	5.50E+00	2.80E+00	3.22E-03*	3.65E-02	1.94E-01
55.00	5.150E-01	269.3	1.386E+16	5.35E+00	1.80E+00	2.03E-03	3.92E-02	1.57E-01
60.00	2.720E-01	257.1	7.668E+15	5.00E+00	1.30E+00	1.40E-03	4.67E-02	1.50E-01
65.00	1.390E-01	240.1	4.196E+15	4.40E+00	8.00E-01	1.02E-03	6.40E-02	1.50E-01
70.00	6.700E-02	218.1	2.227E+15	3.70E+00	4.00E-01	7.77E-04	1.18E-01	1.50E-01
75.00	3.000E-02	196.1	1.109E+15	2.95E+00	1.90E-01	6.26E-04	2.94E-01	1.50E-01
80.00	1.200E-02	174.1	4.996E+14	2.10E+00	2.00E-01	5.17E-04	6.82E-01	1.50E-01
85.00	4.480E-03	165.1	1.967E+14	1.33E+00	5.70E-01	4.35E-04	1.47E+00	1.50E-01
90.00	1.640E-03	165.0	7.204E+13	8.50E-01	7.50E-01	3.73E-04	2.85E+00	1.40E-01
95.00	6.250E-04	178.3	2.541E+13	5.40E-01	7.00E-01	3.24E-04	5.17E+00	1.30E-01
100.0	2.580E-04	190.5	9.816E+12	4.00E-01	4.00E-01	2.84E-04	1.01E+01	1.20E-01
105.0	1.170E-04	222.2	3.816E+12	3.40E-01	2.00E-01	2.52E-04	1.87E+01	1.10E-01
110.0	6.110E-05	262.4	1.688E+12	2.80E-01	5.00E-02	2.26E-04	2.86E+01	9.50E-02
115.0	3.560E-05	316.8	8.145E+11	2.40E-01	5.00E-03	2.04E-04	3.89E+01	6.00E-02
120.0	2.270E-05	380.0	4.330E+11	2.00E-01	5.00E-04	1.85E-04	5.00E+01	3.00E-02

Table 1c. Reference Atmospheric Model Profiles, Model 3. Midlatitude Winter

MODEL = 3 MIDLATITUDE WINTER

ALT (KM)	PRES (MB)	TEMP (K)	DENSITY (CM^{-3})	H_20 (PPMV)	O_3 (PPMV)	N_20 (PPMV)	CO (PPMV)	CH_4 (PPMV)
0.00	1.018E+03	272.2	2.711E+19	4.32E+03	2.78E-02	3.20E-01	1.50E-01	1.70E+00
1.00	8.973E+02	268.7	2.420E+19	3.45E+03	2.80E-02	3.20E-01	1.45E-01	1.70E+00
2.00	7.897E+02	265.2	2.158E+19	2.79E+03	2.85E-02	3.20E-01	1.40E-01	1.70E+00
3.00	6.938E+02	261.7	1.922E+19	2.09E+03	3.20E-02	3.20E-01	1.35E-01	1.70E+00
4.00	6.081E+02	255.7	1.724E+19	1.28E+03	3.57E-02	3.20E-01	1.31E-01	1.70E+00
5.00	5.313E+02	249.7	1.542E+19	8.24E+02	4.72E-02	3.20E-01	1.30E-01	1.69E+00
6.00	4.627E+02	243.7	1.376E+19	5.10E+02	5.84E-02	3.20E-01	1.29E-01	1.67E+00
7.00	4.016E+02	237.7	1.225E+19	2.32E+02	7.89E-02	3.20E-01	1.25E-01	1.65E+00
8.00	3.473E+02	231.7	1.086E+19	1.08E+02	1.04E-01	3.20E-01	1.19E-01	1.63E+00
9.00	2.993E+02	225.7	9.612E+18	5.57E+01	1.57E-01	3.16E-01	1.09E-01	1.62E+00
10.00	2.568E+02	219.7	8.472E+18	2.96E+01	2.37E-01	3.10E-01	9.96E-02	1.58E+00
11.00	2.199E+02	219.2	7.271E+18	1.00E+01	3.62E-01	2 99E-01	8.96E-02	1.54E+00
12.00	1.882E+02	218.7	6.237E+18	6.00E+00	5.23E-01	2.94E-01	7.81E-02	1.51E+00
13.00	1.611E+02	218.2	5.351E+18	5.00E+00	7.04E-01	2 86E-01	6.37E-02	1.48E+00
14.00	1.378E+02	217.7	4.588E+18	4.80E+00	8.00E-01	2.80E-01	5.03E-02	1.45E+00
15.00	1.178E+02	217.2	3.931E+18	4.70E+00	9.00E-01	2.72E-01	3.94E-02	1.42E+00
16.00	1.007E+02	216.7	3.368E+18	4.60E+00	1.10E+00	2.61E-01	3.07E-02	1.39E+00
17.00	8.610E+01	216.2	2.886E+18	4.50E+00	1.40E+00	2.42E-01	2.42E-02	1.36E+00
18.00	7.360E+01	215.7	2.473E+18	4.50E+00	1.80E+00	2.17E-01	1.97E-02	1.32E+00
l9.00	6.280E+01	215.2	2.115E+18	4.50E+00	2.30E+00	1.84E-01	1.55E-02	1.28E+00
20.00	5.370E+01	215.2	1.809E+18	4.50E+00	2.90E+00	1.62E-01	1.33E-02	1.22E+00
21.00	4 580E+01	215.2	1.543E+18	4.50E+00	3.50E+00	1.36E-01	1.23E-02	1.15E+00
22.00	3.910E+01	215.2	1.317E+18	4.53E+00	3.90E+00	1.23E-01	1.23E-02	1.07E+00
23.00	3.340E+01	215.2	1.125E+18	4.55E+00	4.30E+00	1.12E-01	1.31E-02	9.73E-01
24.00	2.860E+01	215.2	9.633E+17	4.60E+00	4.70E+00	1.05E-01	1.40E-02	8.80E-01
25.00	2.440E+01	215.2	8.218E+17	4.65E+00	5.10E+00	9.66E-02	1.50E-02	7.93E-01
27.50	1.646E+01	215.5	5.536E+17	4.70E+00	5.60E+00	8.69E-02	1.60E-02	7.13E-01
30.00	1.110E+01	217.4	3.701E+17	4.75E+00	6.10E+00	7.52E-02	1.71E-02	6.44E-01
32.50	7.560E+00	220.4	2.486E+17	4.80E+00	6.80E+00	6.13E-02	1.85E-02	5.75E-01
35.00	5.180E+00	227.9	1.647E+17	4.85E+00	7.10E+00	5.12E-02	2.00E-02	5.05E-01
37.50	3.600E+00	235.5	1.108E+17	4.90E+00	7.20E+00	3.97E-02	2.15E-02	4.48E-01
40.00	2.530E+00	243.2	7.540E+16	4.95E+00	6.90E+00	3.00E-02	2.33E-02	3.93E-01
42.50	1.800E+00	250.8	5.202E+16	5.00E+00	5.90E+00	2.08E-02	2.62E-02	3.40E-01
45.00	1.290E+00	258.5	3.617E+16	5.00E+00	4.60E+00	1.31E-02	3.06E-02	2.88E-01
47.50	9.400E-01	265.1	2.570E+16	5.00E+00	3.70E+00	8.07E-03	3.80E-02	2.39E-01
50.00	6.830E-01	265.7	1.863E+16	4.95E+00	2.75E+00	4.16E-03*	6.25E-02	1.94E-01
55.00	3.620E-01	260.6	1.007E+16	4.85E+00	1.70E+00	2.63E-03	1.48E-01	1.57E-01
60.00	1.880E-01	250.8	5.433E+15	4.50E+00	1.00E+00	1.81E-03	2.93E-01	1.50E-01
65.00	9.500E-02	240.9	2.858E+15	4.00E+00	5.50E-01	1.32E-03	5.59E-01	1.50E-01
70.00	4.700E-02	230.7	1.477E+15	3.30E+00	3.20E-01	1.01E-03	1.08E+00	1.50E-01
75.00	2.220E-02	220.4	7.301E+14	2.70E+00	2.50E-01	7.88E-04	1.90E+00	1.50E-01
80.00	1.030E-02	210.1	3.553E+14	2.00E+00	2.30E-01	6.33E-04	2.96E+00	1.50E-01
85.00	4.560E-03	199.8	1.654E+14	1.33E+00	5.50E-01	5.19E-04	4.53E+00	1.50E-01
90.00	1.980E-03	199.5	7.194E+13	8.50E-01	8.00E-01	4.33E-04	6.86E+00	1.40E-01
95.00	8.770E-04	208.3	3.052E+13	5.40E-01	8.00E-01	3.67E-04	1.05E+01	1.30E-01
100.0	4.074E-04	218.6	1.351E+13	4.00E-01	4.00E-01	3.14E-04	1.71E+01	1.20E-01
105.0	2.000E-04	237.1	6.114E+12	3.40E-01	2.00E-01	2.72E-04	2.47E+01	1.10E-01
110.0	1.057E-04	259.5	2.952E+12	2.80E-01	5.00E-02	2.37E-04	3.36E+01	9.50E-02
115.0	5.980E-05	293.0	1.479E+12	2.40E-01	5.00E-03	2.09E-04	4.15E+01	6.00E-02
120.0	3.600E-05	333.0	7 836E+11	2.00E-01	5.00E-04	1.85E-04	5.00E+01	3.00E-02

Table 1d. Reference Atmospheric Model Profiles, Model 4. Subarctic Summer

MODEL = 4 SUBARCTIC SUMMER

ALT (KM)	PRES (MB)	TEMP (K)	DENSITY (CM^{-3})	H_20 (PPMV)	O_3 (PPMV)	N_20 (PPMV)	CO (PPMV)	CH_4 (PPMV)
0.00	1.010E+03	287.2	2.549E+19	1.19E+04	2.41E-02	3.10E-01	1.50E-01	1.70E+00
1 00	8.960E+02	281.7	2.305E+19	8.70E+03	2.94E-02	3.10E-01	1.45E-01	1.70E+00
2 00	7.929E+02	276.3	2.080E+19	6.75E+03	3.38E-02	3.10E-01	1.40E-01	1.70E+00
3.00	7.000E+02	270.9	1.873E+19	4.82E+03	3.89E-02	3.10E-01	1.35E-01	1.70E+00
4.00	6.160E+02	265.5	1.682E+19	3.38E+03	4.48E-02	3.08E-01	1.31E-01	1.70E+00
5.00	5.410E+02	260.1	1.508E+19	2.22E+03	5.33E-02	3.02E-01	1.30E-01	1.69E+00
6.00	4.740E+02	253.1	1.357E+19	1.33E+03	6.56E-02	2.91E-01	1.29E-01	1.67E+00
7.00	4.130E+02	246.1	1.216E+19	7.97E+02	7.74E-02	2.82E-01	1.25E-01	1.65E+00
8.00	3.590E+02	239.2	1.088E+19	4.00E+02	9.11E-02	2.76E-01	1.19E-01	1.63E+00
9.00	3.108E+02	232.2	9.701E+18	1.30E+02	1.42E-01	2.70E-01	1.09E-01	1.62E+00
10.00	2.677E+02	225.2	8.616E+18	4.24E+01	1.89E-01	2.65E-01	9.96E-02	1.58E+00
11.00	2.300E+02	225.2	7.402E+18	1.33E+01	3.05E-01	2.60E-01	8.96E-02	1.54E+00
12.00	1.977E+02	225.2	6.363E+18	6.00E+00	4.10E-01	2.55E-01	7.81E-02	1.51E+00
13.00	1.700E+02	225.2	5.471E+18	4.45E+00	5.00E-01	2.49E-01	6.37E-02	1.47E+00
14.00	1.460E+02	225.2	4.699E+18	4.00E+00	6.00E-01	2.43E-01	5.03E-02	1.43E+00
15.00	1.260E+02	225.2	4.055E+18	4.00E+00	7.00E-01	2.36E-01	3.94E-02	1.39E+00
16.00	1.080E+02	225.2	3.476E+18	4.00E+00	8.50E-01	2.28E-01	3.07E-02	1.34E+00
17.00	9.280E+01	225.2	2.987E+18	4.05E+00	1.00E+00	2.18E-01	2.49E-02	1.29E+00
18.00	7.980E+01	225.2	2.568E+18	4.30E+00	1.30E+00	2.04E-01	1.97E-02	1.23E+00
19.00	6.860E+01	225.2	2.208E+18	4.50E+00	1.70E+00	1.82E-01	1.55E-02	1.16E+00
20.00	5.900E+01	225.2	1.899E+18	4.60E+00	2.10E+00	1.57E-01	1.33E-02	1.07E+00
21.00	5.070E+01	225.2	1.632E+18	4.70E+00	2.70E+00	1.35E-01	1.23E-02	9.90E-01
22.00	4.360E+01	225.2	1.403E+18	4.80E+00	3.30E+00	1.22E-01	1.23E-02	9.17E-01
23.00	3.750E+01	225.2	1.207E+18	4.83E+00	3.70E+00	1.10E-01	1.31E-02	8.57E-01
24.00	3.228E+01	226.6	1.033E+18	4.85E+00	4.20E+00	9.89E-02	1.40E-02	8.01E-01
25.00	2.780E+01	228.1	8.834E+17	4.90E+00	4.50E+00	8.78E-02	1.51E-02	7.48E-01
27.50	1.923E+01	231.0	6.034E+17	4.95E+00	5.30E+00	7.33E-02	1.65E-02	6.96E-01
30.00	1.340E+01	235.1	4.131E+17	5.00E+00	5.70E+00	5.94E-02	1.81E-02	6.44E-01
32.50	9.400E+00	240.0	2.839E+17	5.00E+00	6.90E+00	4.15E-02	2.00E-02	5.89E-01
35.00	6.610E+00	247.2	1.938E+17	5.00E+00	7.70E+00	3.03E-02	2.18E-02	5.24E-01
37.50	4.720E+00	254.6	1.344E+17	5.00E+00	7.80E+00	1.95E-02	2.34E-02	4.51E-01
40.00	3.400E+00	262.1	9.402E+16	5.00E+00	7.00E+00	1.27E-02	2.50E-02	3.71E-01
42.50	2.480E+00	269.5	6.670E+16	5.00E+00	5.40E+00	9.00E-03	2.65E-02	2.99E-01
45.00	1.820E+00	273.6	4.821E+16	5.00E+00	4.20E+00	6.29E-03	2.81E-02	2.45E-01
47.50	1.340E+00	276.2	3.516E+16	5.00E+00	3.20E+00	4.56E-03	3.00E-02	2.00E-01
50.00	9.870E-01	277.2	2.581E+16	4.95E+00	2.50E+00	2.80E-03*	3.22E-02	1.66E-01
55.00	5.370E-01	274.0	1.421E+16	4.85E+00	1.70E+00	1.77E-03	3.65E-02	1.50E-01
60 00	2 880E-01	262.7	7.946E+15	4.50E+00	1.20E+00	1.21E-03	4.59E-02	1.50E-01
65 00	1.470E-01	239.7	4.445E+15	4.00E+00	8.00E-01	8.87E-04	6.38E-02	1.50E-01
70.00	7.100E-02	216.6	2.376E+15	3.30E+00	4.00E-01	6.76E-04	1.18E-01	1.50E-01
75.00	3.200E-02	193.6	1.198E+15	2.70E+00	2.00E-01	5.54E-04	3.03E-01	1.50E-01
80.00	1.250E-02	170.6	5.311E+14	2.00E+00	1.80E-01	4.65E-04	7.89E-01	1.50E-01
85.00	4.510E-03	161.7	2.022E+14	1.33E+00	6.50E-01	3.98E-04	1.82E+00	1.50E-01
90.00	1.610E-03	161.6	7.221E+13	8.50E-01	9.00E-01	3.46E-04	3.40E+00	1.40E-01
95.00	6.060E-04	176.8	2.484E+13	5.40E-01	8.00E-01	3.05E-04	5.92E+00	1.30E-01
100.0	2.480E-04	190.4	9.441E+12	4.00E-01	4.00E-01	2.71E-04	1.04E+01	1.20E-01
105.0	1.130E-04	226.0	3.624E+12	3.40E-01	2.00E-01	2.44E-04	1.88E+01	1.10E-01
110.0	6.000E-05	270.1	1.610E+12	2.80E-01	5.00E-02	2.21E-04	2.87E+01	9.50E-02
115.0	3.540E-05	322.7	7.951E+11	2.40E-01	5.00E-03	2.02E-04	3.89E+01	6.00E-02
120.0	2.260E-05	380.0	4.311E+11	2.00E-01	5.00E-04	1.85E-04	5.00E+01	3.00E-02

Table 1e. Reference Atmospheric Model Profiles, Model 5. Subarctic Winter

MODEL = 5 SUBARCTIC WINTER

ALT (KM)	PRES (MB)	TEMP (K)	DENSITY (CM^{-3})	H_20 (PPMV)	O_3 (PPMV)	N_20 (PPMV)	CO (PPMV)	CH_4 (PPMV)
0.00	1.013E+03	257.2	2.855E+19	1.41E+03	1.80E-02	3.20E-01	1.50E-01	1.70E+00
1.00	8.878E+02	259.1	2.484E+19	1.62E+03	2.07E-02	3.20E-01	1.45E-01	1.70E+00
2.00	7.775E+02	255.9	2.202E+19	1.43E+03	2.34E-02	3.20E-01	1.40E-01	1.70E+00
3.00	6.798E+02	252.7	1.950E+19	1.17E+03	2.77E-02	3.20E-01	1.35E-01	1.70E+00
4.00	5.932E+02	247.7	1.736E+19	7.90E+02	3.25E-02	3.20E-01	1.31E-01	1.70E+00
5.00	5.158E+02	240.9	1.552E+19	4.31E+02	3.80E-02	3.20E-01	1.30E-01	1.69E+00
6.00	4.467E+02	234.1	1.383E+19	2.37E+02	4.45E-02	3.20E-01	1.29E-0l	1.67E+00
7.00	3.853E+02	227.3	1.229E+19	1.47E+02	7.25E-02	3.20E-01	1.25E-01	1.65E+00
8.00	3.308E+02	220.6	1.087E+19	3.38E+01	1.04E-01	3.20E-01	1.19E-01	1 63E+00
9.00	2.829E+02	217.2	9.440E+18	2.98E+01	2.10E-01	3.16E-01	1.09E-0l	1.62E+00
10.00	2.418E+02	217.2	8.069E+18	2.00E+01	3.00E-01	3.10E-01	9.96E-02	1.58E+00
11.00	2.067E+02	217.2	6.898E+18	1.00E+01	3.50E-01	2.99E-01	8.96E-02	1.54E+00
12.00	1.766E+02	217.2	5.893E+18	6.00E+00	4.00E-01	2.94E-01	7.81E-02	1.51E+00
13.00	1.510E+02	217.2	5.039E+18	4.45E+00	6.50E-01	2.86E-01	6.37E-02	1.47E+00
14.00	1.291E+02	217.2	4.308E+18	4.50E+00	9.00E-01	2.80E-01	5.03E-02	1.43E+00
15.00	1.103E+02	2l7.2	3.681E+18	4.55E+00	1.20E+00	2.72E-01	3.94E-02	1.39E+00
16.00	9.431E+01	216.6	3.156E+18	4.60E+00	1.50E+00	2.61E-01	3.07E-02	1.34E+00
17.00	8.058E+01	216.0	2.104E+18	4.65E+00	1.90E+00	2.42E-01	2.49E-02	1.29E+00
18.00	6.882E+01	215.4	2.316E+18	4.70E+00	2.45E+00	2.17E-01	1.97E-02	1.23E+00
19.00	5.875E+01	214.8	1.982E+18	4.75E+00	3.10E+00	1.84E-01	1.55E-02	1.16E+00
20.00	5.014E+01	214.2	1.697E+18	4.80E+00	3.70E+00	1.62E-01	1.33E-02	1.08E+00
21.00	4.277E+01	213.6	1.451E+18	4.85E+00	4.00E+00	1.36E-01	1.23E-02	1.01E+00
22.00	3.647E+01	213.0	1.241E+18	4.90E+00	4.20E+00	1.23E-01	1.23E-02	9.56E-01
23.00	3.109E+01	212.4	1.061E+18	4.95E+00	4.50E+00	1.12E-01	1.31E-02	9.01E-01
24.00	2.649E+01	211.8	9.065E+17	5.00E+00	4.60E+00	1.04E-01	1.40E-02	8.48E-01
25.00	2.256E+01	211.2	7.742E+17	5.00E+00	4.70E+00	9.57E-02	1.52E-02	7.96E-01
27.50	1.513E+01	213.6	5.134E+17	5.00E+00	4.90E+00	8.60E-02	1.72E-02	7.45E-01
30.00	1.020E+01	216.0	3.423E+17	5.00E+00	5.40E+00	7.31E-02	2.04E-02	6.94E-01
32.50	6.910E+00	218.5	2.292E+17	5.00E+00	5.90E+00	5.71E-02	2.49E-02	6.43E-01
35.00	4.701E+00	222.3	1.533E+17	5.00E+00	6.20E+00	4.67E-02	3.17E-02	5.88E-01
37.50	3.230E+00	228.5	1.025E+17	5.00E+00	6.25E+00	3.44E-02	4.43E-02	5.24E-01
40.00	2.243E+00	234.7	6.927E+16	5.00E+00	5.90E+00	2.47E-02	6.47E-02	4.51E-01
42.50	1.570E+00	240.8	4.726E+16	5.00E+00	5.10E+00	1.63E-02	1.04E-01	3.71E-01
45.00	1.113E+00	247.0	3.266E+16	5.00E+00	4.10E+00	1.07E-02	1.51E-01	3.00E-01
47.50	7.900E-01	253.2	2.261E+16	5.00E+00	3.00E+00	7.06E-03	2.16E-01	2.45E-01
50.00	5.719E-01	259.3	1.599E+16	4.95E+00	2.60E+00	3.97E-03*	3.14E-01	1.98E-01
55.00	2.990E-01	259.1	8.364E+15	4.85E+00	1.60E+00	2.51E-03	4.84E-01	1.59E-01
60.00	1.550E-01	250.9	4.478E+15	4.50E+00	9.50E-01	1.73E-03	7.15E-01	1.50E-01
65.00	7.900E-02	248.4	2.305E+15	4.00E+00	6.50E-01	1.26E-03	1.07E+00	1.50E-01
70.00	4.000E-02	245.4	1.181E+15	3.30E+00	5.00E-01	9.60E-04	1.52E+00	1.50E-01
75.00	2.000E-02	234.7	6.176E+14	2.70E+00	3.30E-01	7.55E-04	2.17E+00	1.50E-01
80.00	9.660E-03	223.9	3.127E+14	2.00E+00	1.30E-01	6.10E-04	3.06E+00	1.50E-01
85.00	4.500E-03	213.1	1.531E+14	1.33E+00	7.50E-01	5.02E-04	4.56E+00	1.50E-01
90.00	2.022E-03	202.3	7.244E+13	8.50E-01	8.00E-01	4.21E-04	6.88E+00	1.40E-01
95.00	9.070E-04	211.0	3.116E+13	5.40E-01	8.00E-01	3.58E-04	1.06E+01	1.30E-01
100.0	4.230E-04	218.5	1.403E+13	4.00E-01	4 00E-01	3.08E-04	1.71E+01	1.20E-01
105.0	2.070E-04	234.0	6.412E+12	3.40E-01	2.00E-01	2.68E-04	2.47E+01	1.10E-01
110.0	1.080E-04	252.6	3.099E+12	2.80E-01	5.00E-02	2.35E-04	3.36E+01	9.50E-02
115.0	6.000E-05	288.5	1.507E+12	2.40E-01	5.00E-03	2.08E-04	4.15E+01	6.00E-02
120.0	3.590E-05	333.0	7.814E+11	2.00E-01	5.00E-04	1.85E-04	5.00E+01	3.00E-02

Table 1f Reference Atmospheric Model Profiles, Model 6. U. S. Standard

MODEL = 6 U .S . STANDARD, 1976

ALT (KM)	PRES (MB)	TEMP (K)	DENSITY (CM^{-3})	H_20 (PPMV)	O_3 (PPMV)	N_20 (PPMV)	CO (PPMV)	CH_4 (PPMV)
0.00	1.013E+03	288.2	2.548E+19	7.75E+03	2.66E-02	3.20E-01	1.50E-01	1.70E+00
1.00	8.988E+02	281.7	2.313E+19	6.07E+03	2.93E-02	3.20E-01	1.45E-01	1.70E+00
2.00	7.950E+02	275.2	2.094E+19	4.63E+03	3.24E-02	3.20E-01	1.40E-01	1.70E+00
3.00	7.012E+02	268.7	1.891E+19	3.18E+03	3.32E-02	3.20E-01	1.35E-01	1.70E+00
4.00	6.166E+02	262.2	1.704E+19	2.16E+03	3.39E-02	3.20E-01	1.31E-01	1.70E+00
5.00	5.405E+02	255.7	1.532E+19	1.40E+03	3.77E-02	3.20E-01	1.30E-01	1.70E+00
6.00	4.722E+02	249.2	1.373E+19	9.25E+02	4.11E-02	3.20E-01	1.29E-01	1.70E+00
7.00	4.111E+02	242.7	1.228E+19	5.72E+02	5.01E-02	3.20E-01	1.25E-01	1.70E+00
8.00	3.565E+02	236.2	1.094E+19	3.67E+02	5.97E-02	3.20E-01	1.19E-01	1.70E+00
9.00	3.080E+02	229.7	9.719E+18	1.58E+02	9.17E-02	3.20E-01	1.09E-01	1.69E+00
10.00	2.650E+02	223.3	8.602E+18	7.00E+01	1.31E-01	3.18E-01	9.96E-02	1.69E+00
11.00	2.270E+02	216.8	7.589E+18	3.61E+01	2.15E-01	3.14E-01	8.96E-02	1.68E+00
12.00	1.940E+02	216.7	6.489E+18	1.91E+01	3.10E-01	3.10E-01	7.81E-02	1.66E+00
13.00	1.658E+02	216.7	5.546E+18	1.09E+01	3.85E-01	3.05E-01	6.37E-02	1.65E+00
14.00	1.417E+02	216.7	4 739E+18	5.93E+00	5.03E-01	3.00E-01	5.03E-02	1.63E+00
15.00	1.211E+02	216.7	4.050E+18	5.00E+00	6.51E-01	2.94E-01	3.94E-02	1.61E+00
16.00	1.035E+02	216.7	3.462E+18	3.95E+00	8.70E-01	2.88E-01	3.07E-02	1.58E+00
17.00	8.850E+01	216.7	2.960E+18	3.85E+00	1.19E+00	2.78E-01	2.49E-02	1.55E+00
18.00	7.565E+01	216.7	2.530E+18	3.83E+00	1.59E+00	2.67E-01	1.97E-02	1.52E+00
19.00	6.467E+01	216.7	2.163E+18	3.85E+00	2.03E+00	2.53E-01	1.55E-02	1.48E+00
20.00	5.529E+01	216.7	1.849E+18	3.90E+00	2.58E+00	2.37E-01	1.33E-02	1.42E+00
21.00	4.729E+01	217.6	1.575E+18	3.98E+00	3.03E+00	2.19E-01	1.23E-02	1.36E+00
22 00	4.047E+01	218.6	1.342E+18	4.07E+00	3.65E+00	2.05E-01	1.23E-02	1.27E+00
23.00	3.467E+01	219.6	1.144E+18	4.20E+00	4.17E+00	1.97E-01	1.31E-02	1.19E+00
24.00	2.972E+01	220.6	9.765E+17	4.30E+00	4.63E+00	1.88E-01	1.40E-02	1.12E+00
25.00	2.549E+01	221.6	8.337E+17	4.43E+00	5.12E+00	1.76E-01	1.50E-02	1.06E+00
27.50	1.743E+01	224.0	5.640E+17	4.58E+00	5.80E+00	1.59E-01	1.60E-02	9.87E-01
30.00	1.197E+01	226.5	3.830E+17	4.73E+00	6.55E+00	1.42E-01	1.71E-02	9.14E-01
32.50	8.010E+00	230.0	2.524E+17	4.83E+00	7.37E+00	1.17E-01	1.85E-02	8.30E-01
35.00	5.746E+00	236.5	1.761E+17	4.90E+00	7.84E+00	9.28E-02	2.01E-02	7.46E-01
37.50	4.150E+00	242.9	1.238E+17	4.95E+00	7.80E+00	6.69E-02	2.22E-02	6.62E-01
40.00	2.871E+00	250.4	8.310E+16	5.03E+00	7.30E+00	4.51E-02	2.50E-02	5.64E-01
42.50	2.060E+00	257.3	5.803E+16	5.15E+00	6.20E+00	2.75E-02	2.82E-02	4.61E-01
45.00	1.491E+00	264.2	4 090E+16	5.23E+00	5.25E+00	1.59E-02	3.24E-02	3.63E-01
47.50	1.090E+00	270.6	2.920E+16	5.25E+00	4.10E+00	9.38E-03	3.72E-02	2.77E-01
50.00	7.978E-01	270.7	2.136E+16	5.23E+00	3.10E+00	4 75E-03*	4.60E-02	2.10E-01
55.00	4.250E-01	260.8	1.181E+16	5.10E+00	1.80E+00	3.00E-03	6.64E-02	1.65E-01
60.00	2.190E-01	247.0	6.426E+15	4.75E+00	1.10E+00	2.07E-03	1.07E-01	1.50E-01
65.00	1.090E-01	233.3	3.386E+15	4.20E+00	7.00E-01	1.51E-03	1.86E-01	1.50E-01
70.00	5.220E-02	219.6	1.723E+15	3.50E+00	3.00E-01	1.15E-03	3.06E-01	1.50E-01
75.00	2.400E-02	208.4	8.347E+14	2.83E+00	2.50E-01	8.89E-04	6.38E-01	1.50E-01
80.00	1.050E-02	198.6	3.832E+14	2.05E+00	3.00E-01	7.06E-04	1.50E+00	1.50E-01
85.00	4.460E-03	188.9	1.711E+14	1.33E+00	5.00E-01	5.72E-04	3.24E+00	1.50E-01
90.00	1.840E-03	186.9	7.136E+13	8.50E-01	7.00E-01	4.71E-04	5.84E+00	1.40E-01
95.00	7.600E-04	188.4	2.924E+13	5.40E-01	7.00E-01	3.93E-04	1.01E+01	1.30E-01
100.0	3.200E-04	195.1	1.189E+13	4.00E-01	4.00E-01	3.32E-04	1.69E+01	1.20E-01
105.0	1.450E-04	208.8	5.033E+12	3.40E-01	2.00E-01	2.84E-04	2.47E+01	1.10E-01
110.0	7.100E-05	240.0	2.144E+12	2.80E-01	5.00E-02	2.44E-04	3.36E+01	9.50E-02
115.0	4.010E-05	300.0	9.688E+11	2.40E-01	5.00E-03	2.12E-04	4.15E+01	6.00E-02
120.0	2.540E-05	360.0	5.114E+11	2.00E-01	5.00E-04	1.85E-04	5.00E+01	3.00E-02

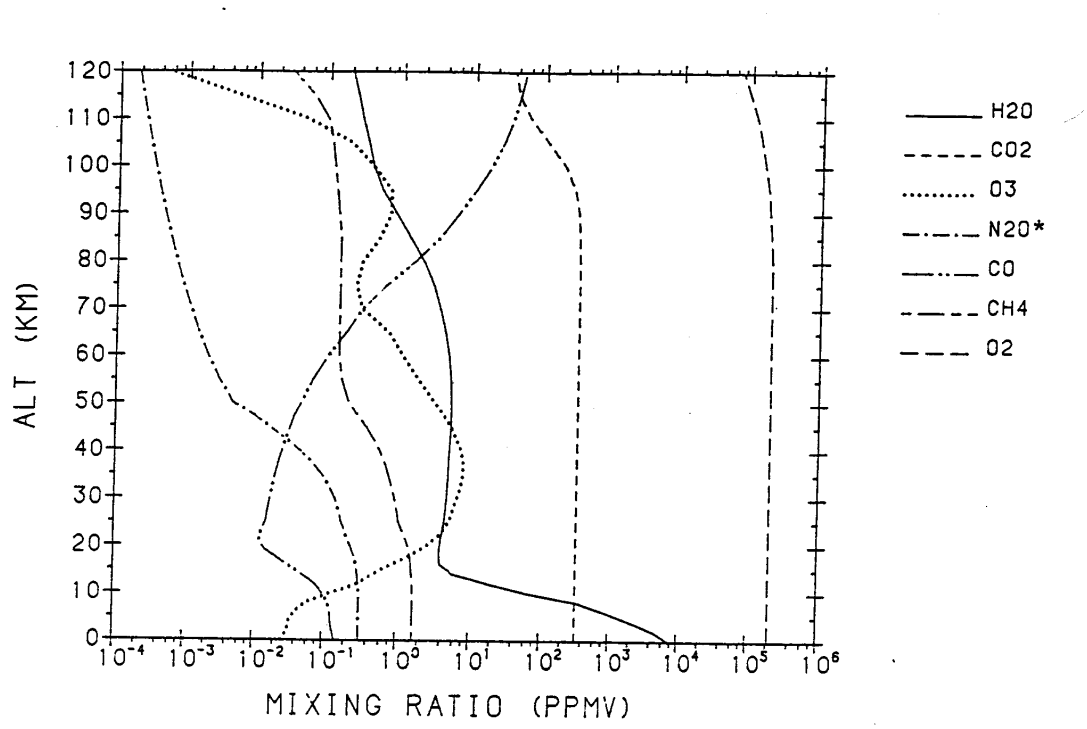

Figure 11. U.S. Standard Model Atmosphere Profiles for the mixing ratios of the major radiating atmospheric gases. This corresponds to Model 6 in Table 1; see text.

[(*) indicates extrapolation adopted for that species; see tabular data]

Table 2. Constituent Profiles (ppmv):

Molecules 1-7 are Model 6 (U.S. Standard) compatible and are repeated here because they duplicate the numbering scheme utilized in the HITRAN 1992 data base. In addition, CO_2 and 0_2 are only defined by a single profile so they have not been included in Table 1.

Molecules 8-28 are provided as single representative profiles. Their natural variability can be very different from the selected profile.

[(*) indicates subsequent extrapolation adopted for that species]

Table 2a. Constituent Profiles (ppmv), H_2O, CO_2, O_3, N_2O, CO, CH_4, O_2

ALT (KM)	1 H_2O (PPMV)	2 CO_2 (PPMV)	3 O_3 (PPMV)	4 N_2O (PPMV)	5 CO (PPMV)	6 CH_4 (PPMV)	7 O_2 (PPMV)
0.0	7.75E+03	3.30E+02	2.66E-02	3.20E-01	1.50E-01	1.70E+00	2.09E+05
1.0	6.07E+03	3.30E+02	2.93E-02	3.20E-01	1.45E-01	1.70E+00	2.09E+05
2.0	4.63E+03	3.30E+02	3.24E-02	3.20E-01	1.40E-01	1.70E+00	2.09E+05
3.0	3.18E+03	3.30E+02	3.32E-02	3.20E-01	1.35E-01	1.70E+00	2.09E+05
4.0	2.16E+03	3.30E+02	3.39E-02	3.20E-01	1.31E-01	1.70E+00	2.09E+05
5.0	1.40E+03	3.30E+02	3.77E-02	3.20E-01	1.30E-01	1.70E+00	2.09E+05
6.0	9.25E+02	3.30E+02	4.11E-02	3.20E-01	1.29E-01	1.70E+00	2.09E+05
7.0	5.72E+02	3.30E+02	5.01E-02	3.20E-01	1.25E-01	1.70E+00	2.09E+05
8.0	3.67E+02	3.30E+02	5.97E-02	3.20E-01	1.19E-01	1.70E+00	2.09E+05
9.0	1.58E+02	3.30E+02	9.17E-02	3.20E-01	1.09E-01	1.69E+00	2.09E+05
10.0	7.00E+01	3.30E+02	1.31E-01	3.18E-01	9.96E-02	1.69E+00	2.09E+05
11.0	3.61E+01	3.30E+02	2.15E-01	3.14E-01	8.96E-02	1.68E+00	2.09E+05
12.0	1.91E+01	3.30E+02	3.10E-01	3.10E-01	7.81E-02	1.66E+00	2.09E+05
13.0	1.09E+01	3.30E+02	3.85E-01	3.05E-01	6.37E-02	1.65E+00	2.09E+05
14.0	5.93E+00	3.30E+02	5.03E-01	3.00E-01	5.03E-02	1.63E+00	2.09E+05
15.0	5.00E+00	3.30E+02	6.51E-01	2.94E-01	3.94E-02	1.61E+00	2.09E+05
16.0	3.95E+00	3.30E+02	8.70E-01	2.88E-01	3.07E-02	1.58E+00	2.09E+05
17.0	3.85E+00	3.30E+02	1.19E+00	2.78E-01	2.49E-02	1.55E+00	2.09E+05
18.0	3.83E+00	3.30E+02	1.59E+00	2.67E-01	1.97E-02	1.52E+00	2.09E+05
19.0	3.85E+00	3.30E+02	2.03E+00	2.53E-01	1.55E-02	1.48E+00	2.09E+05
20.0	3.90E+00	3.30E+02	2.58E+00	2.37E-01	1.33E-02	1.42E+00	2.09E+05
21.0	3.98E+00	3.30E+02	3.03E+00	2.19E-01	1.23E-02	1.36E+00	2.09E+05
22.0	4.07E+00	3.30E+02	3.65E+00	2.05E-01	1.23E-02	1.27E+00	2.09E+05
23.0	4.20E+00	3.30E+02	4.17E+00	1.97E-01	1.31E-02	1.19E+00	2.09E+05
24.0	4.30E+00	3.30E+02	4.63E+00	1.88E-01	1.40E-02	1.12E+00	2.09E+05
25.0	4.43E+00	3.30E+02	5.12E+00	1.76E-01	1.50E-02	1.06E+00	2.09E+05
27.5	4.58E+00	3.30E+02	5.80E+00	1.59E-01	1.60E-02	9.87E-01	2.09E+05
30.0	4.73E+00	3.30E+02	6.55E+00	1.42E-01	1.71E-02	9.14E-01	2.09E+05
32.5	4.83E+00	3.30E+02	7.37E+00	1.17E-01	1.85E-02	8.30E-01	2.09E+05
35.0	4.90E+00	3.30E+02	7.84E+00	9.28E-02	2.01E-02	7.46E-01	2.09E+05
37.5	4.95E+00	3.30E+02	7.80E+00	6.69E-02	2.22E-02	6.62E-01	2.09E+05
40.0	5.03E+00	3.30E+02	7.30E+00	4.51E-02	2.50E-02	5.64E-01	2.09E+05
42.5	5.15E+00	3.30E+02	6.20E+00	2.75E-02	2.82E-02	4.61E-01	2.09E+05
45.0	5.23E+00	3.30E+02	5.25E+00	1.59E-02	3.24E-02	3.63E-01	2.09E+05
47.5	5.25E+00	3.30E+02	4.10E+00	9.38E-03	3.72E-02	2.77E-01	2.09E+05
50.0	5.23E+00	3.30E+02	3.10E+00	4.75E-03*	4.60E-02	2.10E-01	2.09E+05
55.0	5.10E+00	3.30E+02	1.80E+00	3.00E-03	6.64E-02	1.65E-01	2.09E+05
60.0	4.75E+00	3.30E+02	1.10E+00	2.07E-03	1.07E-01	1.50E-01	2.09E+05
65.0	4.20E+00	3.30E+02	7.00E-01	1.51E-03	1.86E-01	1.50E-01	2.09E+05
70.0	3.50E+00	3.30E+02	3.00E-01	1.15E-03	3.06E-01	1.50E-01	2.09E+05
75.0	2.83E+00	3.30E+02	2.50E-01	8.89E-04	6.38E-01	1.50E-01	2.09E+05
80.0	2.05E+00	3.28E+02	3.00E-01	7.06E-04	1.50E+00	1.50E-01	2.09E+05
85.0	1.33E+00	3.20E+02	5.00E-01	5.72E-04	3.24E+00	1.50E-01	2.00E+05
90.0	8.50E-01	3.10E+02	7.00E-01	4.71E-04	5.84E+00	1.40E-01	1.90E+05
95.0	5 40E-01	2.70E+02	7.00E-01	3.93E-04	1.01E+01	1.30E-01	1.80E+05
100.0	4.00E-01	1.95E+02	4.00E-01	3.32E-04	1.69E+01	1.20E-01	1.60E+05
105.0	3.40E-01	1.10E+02	2.00E-01	2.84E-04	2.47E+01	1.10E-01	1.40E+05
110.0	2.80E-01	6.00E+01	5.00E-02	2.44E-04	3.36E+01	9.50E-02	1.20E+05
115.0	2.40E-01	4.00E+01	5.00E-03	2.12E-04	4.15E+01	6.00E-02	9.40E+04
120.0	2.00E-01	3.50E+01	5.00E-04	1.85E-04	5.00E+01	3.00E-02	7.25E+04

Table 2b. Constituent Profiles (ppmv), NO, SO_2, NO_2, NH_3, HNO_3, OH, HF

ALT (KM)	8 NO (PPMV)	9 SO_2 (PPMV)	10 NO_2 (PPMV)	11 NH_3 (PPMV)	12 HNO_3 (PPMV)	13 OH (PPMV)	14 HF (PPMV)
0.0	3.00E-04	3.00E-04	2.30E-05	5.00E-04	5.00E-05	4.40E-08	1.00E-08
1.0	3.00E-04	2.74E-04	2.30E-05	5.00E-04	5.96E-05	4.40E-08	1.00E-08
2.0	3.00E-04	2.36E-04	2.30E-05	4.63E-04	6.93E-05	4.40E-08	1.23E-08
3.0	3.00E-04	1.90E-04	2.30E-05	3.80E-04	7.91E-05	4.40E-08	1.97E-08
4.0	3.00E-04	1.46E-04	2.30E-05	2.88E-04	8.87E-05	4.40E-08	3.18E-08
5.0	3.00E-04	1.18E-04	2.30E-05	2.04E-04	9 75E-05	4.40E-08	5.63E-08
6.0	3.00E-04	9.71E-05	2.30E-05	1.46E-04	1.11E-04	4.40E-08	9.18E-08
7.0	3.00E-04	8.30E-05	2.30E-05	9.88E-05	1.26E-04	4.41E-08	1.53E-07
8.0	3.00E-04	7.21E-05	2.30E-05	6.48E-05	1.39E-04	4.45E-08	2.41E-07
9.0	3.00E-04	6.56E-05	2.32E-05	3.77E-05	1.53E-04	4.56E-08	4.04E-07
10.0	3.00E-04	6.08E-05	2.38E-05	2.03E-05	1.74E-04	4.68E-08	6.57E-07
11.0	3.00E-04	5.79E-05	2.62E-05	1.09E-05	2.02E-04	4.80E-08	1.20E-06
12.0	3.00E-04	5.60E-05	3.15E-05	6.30E-06	2.41E-04	4.94E-08	1.96E-06
13.0	2.99E-04	5.59E-05	4.45E-05	3.12E-06	2.76E-04	5.19E-08	3.12E-06
14.0	2.95E-04	5.64E-05	7.48E-05	1.11E-06	3.33E-04	5.65E-08	4.62E-06
15.0	2.83E-04	5.75E-05	1.71E-04	4.47E-07	4.52E-04	6.75E-08	7.09E-06
16.0	2.68E-04	5.75E-05	3.19E-04	2.11E-07	7.37E-04	8.25E-08	1.05E-05
17.0	2.52E-04	5.37E-05	5.19E-04	1.10E-07	1.31E-03	1.04E-07	1.69E-05
18.0	2.40E-04	4.78E-05	7.71E-04	6.70E-08	2.11E-03	1.30E-07	2.57E-05
19.0	2.44E-04	3.97E-05	1.06E-03	3.97E-08	3.17E-03	1.64E-07	4.02E-05
20.0	2.55E-04	3.19E-05	1.39E-03	2.41E-08	4.20E-03	2.16E-07	5.77E-05
21.0	2.77E-04	2.67E-05	1.76E-03	1.92E-08	4.94E-03	3.40E-07	7.77E-05
22.0	3.07E-04	2.28E-05	2.16E-03	1.72E-08	5.46E-03	5.09E-07	9.90E-05
23.0	3.60E-04	2.07E-05	2.58E-03	1.59E-08	5.74E-03	7.59E-07	1.23E-04
24.0	4.51E-04	1.90E-05	3.06E-03	1.44E-08	5.84E-03	1.16E-06	1.50E-04
25.0	6.85E-04	1.75E-05	3.74E-03	1.23E-08	5.61E-03	2.18E-06	1.82E-04
27.5	1.28E-03	1.54E-05	4.81E-03	9.37E-09	4.82E-03	5.00E-06	2.30E-04
30.0	2.45E-03	1.34E-05	6.16E-03	6.35E-09	3.74E-03	1.17E-05	2.83E-04
32.5	4.53E-03	1.21E-05	7.21E-03	3.68E-09	2.59E-03	3.40E-05	3.20E-04
35.0	7.14E-03	1.16E-05	7.28E-03	1.82E-09	1.64E-03	8.35E-05	3.48E-04
37.5	9.34E-03	1.21E-05	6.26E-03	9.26E-10	9.68E-04	1.70E-04	3.72E-04
40.0	1.12E-02	1.36E-05	4.03E-03	2.94E-10*	5.33E-04	2.85E-04	3.95E-04
42.5	1.19E-02	1.65E-05	2.17E-03	8.72E-11	2.52E-04	4.06E-04	4.10E-04
45.0	1.17E-02	2.10E-05	1.15E-03	2.98E-11	1.21E-04	5.11E-04	4.21E-04
47.5	1.10E-02	2.77E-05	6.66E-04	1.30E-11	7.70E-05	5.79E-04	4.24E-04
50.0	1.03E-02	3.56E-05	4.43E-04*	7.13E-12	5.55E-05*	6.75E-04	4.25E-04*
55.0	1.01E-02	4.59E-05	3.39E-04	4.80E-12	4.45E-05	9.53E-04	4.25E-04
60.0	1.01E-02	5.15E-05	2.85E-04	3.66E-12	3.84E-05	1.76E-03	4.25E-04
65.0	1.03E-02	5.11E-05	2.53E-04	3.00E-12	3.49E-05	3.74E-03	4.25E-04
70.0	1.15E-02	4.32E-05	2.31E-04	2.57E-12	3.27E-05	7.19E-03	4.25E-04
75.0	1.61E-02	2.83E-05	2.15E-04	2.27E-12	3.12E-05	1.12E-02	4.25E-04
80.0	2.68E-02	1.33E-05	2.02E-04	2.04E-12	3.01E-05	1.13E-02	4.25E-04
85.0	7 01E-02	5.56E-06	1.92E-04	1.85E-12	2.92E-05	6.10E-03	4.25E-04
90.0	2.13E-01	2.24E-06	1.83E-04	1.71E-12	2.84E-05	1.51E-03	4.25E-04
95.0	7.12E-01	8.96E-07	1.76E-04	1.59E-12	2.78E-05	2.42E-04	4.25E-04
100.0	2.08E+00	3.58E-07	1.70E-04	1.48E-12	2.73E-05	4.47E-05	4.25E-04
105.0	4.50E+00	1.43E-07	1.64E-04	1.40E-12	2.68E-05	1.77E-05	4.25E-04
110.0	7.98E+00	5.73E-08	1.59E-04	1.32E-12	2.64E-05	1.19E-05	4.25E-04
115.0	1.00E+01	2.29E-08	1.55E-04	1.25E-12	2.60E-05	1.35E-05	4.25E-04
120.0	1.00E+01	9.17E-09	1.51E-04	1.19E-12	2.57E-05	2.20E-05	4.25E-04

Table 2c. Constituent Profiles (ppmv), HCl, HBr, HI, ClO, OCS, H_2CO, HOCl

ALT (KM)	15 HCL (PPMV)	16 HBR (PPMV)	17 HI (PPMV)	18 CLO (PPMV)	19 OCS (PPMV)	20 H_2CO (PPMV)	21 HOCL (PPMV)
0.0	1.00E-03	1.70E-06	3.00E-06*	1.00E-08	6.00E-04	2.40E-03	7.70E-06
1.0	7.49E-04	1.70E-06	3.00E-06	1.00E-08	5.90E-04	1.07E-03	1.06E-05
2.0	5.61E-04	1.70E-06	3.00E-06	1.00E-08	5.80E-04	4.04E-04	1.22E-05
3.0	4.22E-04	1.70E-06	3.00E-06	1.00E-08	5.70E-04	2.27E-04	1.14E-05
4.0	3.19E-04	1.70E-06	3.00E-06	1.00E-08	5.62E-04	1.40E-04	9.80E-06
5.0	2.39E-04	1.70E-06	3.00E-06	1.00E-08	5.55E-04	1.00E-04	8.01E-06
6.0	1.79E-04	1.70E-06	3.00E-06	1.00E-08	5.48E-04	7.44E-05	6.42E-06
7.0	1.32E-04	1.70E-06	3.00E-06	1.00E-08	5.40E-04	6.04E-05	5.42E-06
8.0	9.96E-05	1.70E-06	3.00E-06	1.01E-08	5.32E-04	5.01E-05	4.70E-06
9.0	7.48E-05	1.70E-06	3.00E-06	1.05E-08	5.25E-04	4.22E-05	4.41E-06
10.0	5.68E-05	1.70E-06	3.00E-06	1.21E-08	5.18E-04	3.63E-05	4.34E-06
11.0	4.59E-05	1.70E-06	3.00E-06	1.87E-08	5.09E-04	3.43E-05	4.65E-06
12.0	4.36E-05	1.70E-06	3 00E-06	3 18E-08	4.98E-04	3.39E-05	5.01E-06
13 0	6.51E-05	1.70E-06	3.00E-06	5.61E-08	4.82E-04	3.50E-05	5.22E-06
14.0	1.01E-04	1.70E-06	3.00E-06	9.99E-08	4.60E-04	3.62E-05	5.60E-06
15.0	1.63E-04	1.70E-06	3.00E-06	1.78E-07	4.26E-04	3.62E-05	6.86E-06
16.0	2.37E-04	1.70E-06	3.00E-06	3.16E-07	3.88E-04	3.58E-05	8.77E-06
17.0	3 13E-04	1.70E-06	3.00E-06	5.65E-07	3.48E-04	3.50E-05	1.20E-05
18.0	3.85E-04	1.70E-06	3.00E-06	1.04E-06	3.09E-04	3.42E-05	1.63E-05
19.0	4.42E-04	1.70E-06	3.00E-06	2.04E-06	2.74E-04	3.39E-05	2.26E-05
20.0	4.89E-04	1.70E-06	3.00E-06	4.64E-06	2.41E-04	3.43E-05	3.07E-05
21.0	5.22E-04	1.70E-06	3.00E-06	8.15E-06	2.14E-04	3.68E-05	4.29E-05
22.0	5.49E-04	1.70E-06	3.00E-06	1.07E-05	1.88E-04	4.03E-05	5.76E-05
23.0	5.75E-04	1.70E-06	3.00E-06	1.52E-05	1.64E-04	4.50E-05	7.65E-05
24.0	6.04E-04	1.70E-06	3.00E-06	2.24E-05	1 37E-04	5.06E-05	9.92E-05
25.0	6.51E-04	1 71E-06	3.00E-06	3.97E-05	1.08E-04	5.82E-05	1.31E-04
27.5	7.51E-04	1.76E-06	3.00E-06	8.48E-05	6.70E-05	7.21E-05	1.84E-04
30.0	9.88E-04	1.90E-06	3.00E-06	1.85E-04	2.96E-05	8.73E-05	2.45E-04
32.5	1.28E-03	2.26E-06	3.00E-06	3.57E-04	1 21E-05	1.01E-04	2.96E-04
35.0	1.57E-03	2.82E-06	3.00E-06	5.08E-04	4.31E-06	1.11E-04	3.21E-04
37.5	1.69E-03	3.69E-06	3.00E-06	6.07E-04	1.60E-06	1.13E-04	3.04E-04
40.0	1.74E-03	4 91E-06	3.00E-06	5.95E-04	6.71E-07	1.03E-04	2.48E-04
42.5	1.76E-03	6.13E-06	3.00E-06	4.33E-04	4.35E-07	7.95E-05	1.64E-04
45.0	1.79E-03	6.85E-06	3.00E-06	2.51E-04	3.34E-07	4.82E-05	9.74E-05
47.5	1.80E-03	7.08E-06	3.00E-06	1.56E-04	2.80E-07	1.63E-05	4.92E-05
50.0	1.80E-03*	7.14E-06*	3.00E-06	1.04E-04*	2.47E-07*	5.10E-06*	2.53E-05*
55.0	1.80E-03	7.15E-06	3.00E-06	7.69E-05	2.28E-07	2.00E-06	1.50E-05
60.0	1.80E-03	7.15E-06	3.00E-06	6.30E-05	2.16E-07	1.05E-06	1.05E-05
65.0	1.80E-03	7.15E-06	3.00E-06	5.52E-05	2.08E-07	6.86E-07	8.34E-06
70.0	1.80E-03	7.15E-06	3.00E-06	5.04E-05	2.03E-07	5.14E-07	7.11E-06
75.0	1.80E-03	7.15E-06	3.00E-06	4.72E-05	1.98E-07	4.16E-07	6.33E-06
80.0	1.80E-03	7.15E-06	3.00E-06	4.49E-05	1.95E-07	3.53E-07	5.78E-06
85.0	1.80E-03	7.15E-06	3.00E-06	4.30E-05	1.92E-07	3 09E-07	5.37E-06
90.0	1.80E-03	7.15E-06	3.00E-06	4.16E-05	1.89E-07	2.76E-07	5.05E-06
95.0	1.80E-03	7.15E-06	3.00E-06	4.03E-05	1.87E-07	2.50E-07	4.78E-06
100.0	1.80E-03	7.15E-06	3.00E-06	3.93E-05	1.85E-07	2.30E-07	4.56E-06
105.0	1.80E-03	7.15E-06	3.00E-06	3.83E-05	1.83E-07	2.13E-07	4.37E-06
110.0	1.80E-03	7.15E-06	3.00E-06	3.75E-05	1.81E-07	1.98E-07	4.21E-06
115.0	1.80E-03	7.15E-06	3.00E-06	3.68E-05	1.80E-07	1.86E-07	4.06E-06
120.0	1.80E-03	7 15E-06	3.00E-06	3.61E-05	1.78E-07	1.75E-07	3.93E-06

Table 2d. Constituent Profiles (ppmv), N_2, HCN, CH_3Cl, H_20_2, C_2H_2, C_2H_6, PH_3

ALT (KM)	22 N_2 (PPMV)	23 HCN (PPMV)	24 CH_3CL (PPMV)	25 H_2O_2 (PPMV)	26 C_2H_2 (PPMV)	27 C_2H_6 (PPMV)	28 PH_3 (PPMV)
0.0	7.81E+05	1.70E-04	7 00E-04	2.00E-04	3 00E-04	2.00E-03	1.00E-14*
1.0	7.81E+05	1.65E-04	6.70E-04	1.95E-04	1.72E-04	2.00E-03	1.00E-14
2.0	7.81E+05	1.63E-04	6.43E-04	1.92E-04	9.57E-05	2.00E-03	1.00E-14
3.0	7.81E+05	1.61E-04	6.22E-04	1.89E-04	6.74E-05	2.00E-03	1.00E-14
4.0	7.81E+05	1.60E-04	6.07E-04	1.84E-04	5.07E-05	1.98E-03	1.00E-14
5.0	7.81E+05	1.60E-04	6.02E-04	1.77E-04	3.99E-05	1.95E-03	1.00E-14
6.0	7.81E+05	1.60E-04	6.00E-04	1.66E-04	3.19E-05	1.90E-03	1.00E-14
7.0	7.81E+05	1.60E-04	6.00E-04	1.49E-04	2.80E-05	1.85E-03	1.00E-14
8.0	7.81E+05	1.60E-04	5.98E-04	1.23E-04	2.55E-05	1.79E-03	1.00E-14
9.0	7.81E+05	1.60E-04	5.94E-04	9.09E-05	2.40E-05	1.72E-03	1.00E-14
10.0	7.81E+05	1.60E-04	5.88E-04	5.79E-05	2.27E-05	1.58E-03	1.00E-14
11.0	7.81E+05	1.60E-04	5.79E-04	3.43E-05	2.08E-05	1.30E-03	1.00E-14
12.0	7.81E+05	1.60E-04	5.66E-04	1.95E-05	1.76E-05	9.86E-04	1.00E-14
13.0	7.81E+05	1.59E-04	5.48E-04	1.08E-05	1.23E-05	7.22E-04	1.00E-14
14.0	7.81E+05	1.57E-04	5.28E-04	6.59E-06	7.32E-06	4.96E-04	1.00E-14
15.0	7.81E+05	1.55E-04	5.03E-04	4.20E-06	4.52E-06	3.35E-04	1.00E-14
16.0	7.81E+05	1.52E-04	4 77E-04	2.94E-06	2.59E-06	2.14E-04	1.00E-14
17.0	7.81E+05	1.49E-04	4.49E-04	2.30E-06	1.55E-06	1.49E-04	1.00E-14
18.0	7.81E+05	1.45E-04	4.21E-04	2.24E-06	8.63E-07	1.05E-04	1.00E-14
19.0	7.81E+05	1.41E-04	3.95E-04	2.68E-06	5.30E-07	7.96E-05	1.00E-14
20.0	7.81E+05	1.37E-04	3.69E-04	3.68E-06	3.10E-07	6.01E-05	1.00E-14
21.0	7.81E+05	1.34E-04	3.43E-04	5.62E-06	1.89E-07	4.57E-05	1.00E-14
22.0	7.81E+05	1.30E-04	3.17E-04	1.03E-05	1.04E-07	3.40E-05	1.00E-14
23.0	7.81E+05	1.25E-04	2.86E-04	1.97E-05	5.75E-08	2.60E-05	1.00E-14
24.0	7.81E+05	1.19E-04	2.48E-04	3.70E-05	2.23E-08	1.89E-05	1.00E-14
25.0	7.81E+05	1.13E-04	1.91E-04	6.20E-05	8.51E-09	1.22E-05	1.00E-14
27.5	7.81E+05	1.05E-04	1.10E-04	1.03E-04	4.09E-09	5.74E-06	1.00E-14
30.0	7.81E+05	9 73E-05	4.72E-05	1.36E-04	2.52E-09	2.14E-06	1.00E-14
32.5	7.81E+05	9.04E-05	1.79E-05	1.36E-04	1.86E-09	8.49E-07	1.00E-14
35.0	7.81E+05	8.46E-05	7.35E-06	1.13E-04	1.52E-09	3.42E-07	1.00E-14
37.5	7.81E+05	8.02E-05	3.03E-06	8.51E-05	1.32E-09	1.34E-07	1.00E-14
40.0	7.81E+05	7.63E-05	1.32E-06	6.37E-05	1.18E-09	5.39E-08*	1.00E-14
42.5	7.81E+05	7.30E-05	8.69E-07	5.17E-05	1.08E-09	2.25E-08	1.00E-14
45.0	7.81E+05	7.00E-05	6.68E-07	4.44E-05	9.97E-10	1.04E-08	1.00E-14
47.5	7.81E+05	6.70E-05	5.60E-07	3.80E-05	9.34E-10	6.57E-09	1.00E-14
50.0	7.81E+05	6.43E-05*	4.94E-07*	3.48E-05	8.83E-10*	4.74E-09	1.00E-14
55.0	7.81E+05	6.21E-05	4.56E-07	3.62E-05	8.43E-10	3.79E-09	1.00E-14
60.0	7.81E+05	6.02E-05	4.32E-07	5.25E-05	8.10E-10	3.28E-09	1.00E-14
65.0	7.81E+05	5.88E-05	4.17E-07	1.26E-04	7.83E-10	2.98E-09	1.00E-14
70.0	7.81E+05	5.75E-05	4.05E-07	3.77E-04	7.60E-10	2.79E-09	1.00E-14
75.0	7.81E+05	5.62E-05	3.96E-07	1.12E-03	7.40E-10	2.66E-09	1.00E-14
80.0	7.81E+05	5.50E-05	3.89E-07	2.00E-03	7.23E-10	2.56E-09	1.00E-14
85.0	7.81E+05	5.37E-05	3.83E-07	1.68E-03	7.07E-10	2.49E-09	1.00E-14
90.0	7.80E+05	5.25E-05	3.78E-07	4 31E-04	6.94E-10	2.43E-09	1.00E-14
95.0	7.79E+05	5.12E-05	3.73E-07	4.98E-05	6.81E-10	2.37E-09	1.00E-14
100.0	7.77E+05	5.00E-05	3.69E-07	6.76E-06	6.70E-10	2.33E-09	1.00E-14
105.0	7.74E+05	4.87E-05	3.66E-07	8.38E-07	6.59E-10	2.29E-09	1.00E-14
110.0	7.70E+05	4.75E-05	3.62E-07	9.56E-08	6.49E-10	2.25E-09	1.00E-14
115.0	7.65E+05	4.62E-05	3.59E-07	1.00E-08	6.40E-10	2.22E-09	1.00E-14
120.0	7.60E+05	4.50E-05	3.56E-07	1.00E-09	6.32E-10	2.19E-09	1.00E-14

The altitude increments for both Table 1 and Table 2 are 1 km between 0 and 25 km, 2.5 km between 25 and 50 km, and 5 km between 50 and 120 km. These increments (and the subset of reference atmospheres themselves) have been chosen for their compatibility with existing profiles in other radiation models (particularly LOWTRAN 7), facilitating validation and inter-comparison tests. The units are: altitude in (km), temperature in (K), pressure in (mb), and mixing ratios in (ppmv). This profile set is available from PL/GPOS in computer-accessible formats, either as tables or FORTRAN data statements appropriate for direct incorporation into computer simulations (e.g. FASCOD3P).

A comprehensive bibliography on reference atmospheric constituent profiles appears in Appendix B of the Anderson report[10].

2.2.3. ERROR ESTIMATES and VARIABILITY

The exactness of these tabulated values vary with species and altitude. At their best, they offer approximately 10-30% relative consistency for U.S. Standard Atmosphere conditions throughout the troposphere and stratosphere; exceptions include PH_3 which is unmeasured in the earth's atmosphere. The mesospheric and thermospheric profiles are much less certain and, in fact, are only defined for temperature, pressure, and the following constituents: H_2O, CO_2, O_3, CO, CH_4, O_2, NO, SO_2, OH, and H_2O_2 . Mixing ratios for the remaining species have been extrapolated from measurements (usually near the stratopause) using a logarithmically decreasing mixing ratio scale height; the onset of such profile extrapolations is marked by asterisks (*) in the tables and figures. This, of course, leads to unsupported estimates of abundance in the upper atmosphere. [The adopted logarithmic extrapolation scheme is a compromise between using either: (a) constant or, (b) constantly decreasing mixing ratios. The former introduces erroneous relative changes between extrapolated species. The latter, while obviously connoting the lack of data, introduces an abrupt discontinuity into the profiles.] The mixing ratios of all extrapolated species are, in any case, very small.

2.2.4. LIMITATIONS

Representative profiles do not necessarily resemble in situ environments, leading to constraints on their general applicability. WMO and COSPAR[58] have released new sets of standard temperature-density profiles in 1986 which provide significant enhancements to the NASA, 1966 Supplements and CIRA, 1972 Reference Atmospheres[59] . (A subset of the CIRA, 1972 profiles is available in this format.)

However, a more detailed climatology does not ensure adequate simulation of observed variability. Particularly in disturbed winter conditions, dynamic wave activity can bring about rapid changes in temperature and pressure, which can then propagate from the troposphere into and through the stratosphere.

In addition to any tropospheric meteorologically-driven changes in temperature, the water vapor and anthropogenic pollutants (CO, CO_2, O_3, nitrogen-oxygen compounds, etc.) exhibit factors of 100 or more local variability. Dynamic perturbations are less extreme in the stratosphere; however, horizontal gradients on local, latitudinal or seasonal scales often exceed factors of 2- 10. In the mesosphere and lower thermosphere, in addition to the extrapolated data, natural excursions brought on by responses to dynamic and solar influences can be substantial. Calculated radiances or transmittances which rely upon default choices represent only a reasonable set of possibilities; they do not replicate actual measurement conditions. When detailed comparisons between theoretical radiance/transmittance calculations and actual data are required, supporting sources (radiosondes, thermosondes, in situ measurements) are recommended.

2.3 AEROSOL MODELS

2.3.1 Introduction

The aerosol models built into MODTRAN 2 have been completely revised from the earlier versions of the LOWTRAN code. Earlier versions of LOWTRAN (before LOWTRAN 5) used the same model for aerosol composition and size distribution at all altitudes, simply changing the concentrations of the aerosols with height which means that the wavelength dependence of the aerosol extinction was independent of altitude.

The variation of the aerosol optical properties with altitude is now modeled by dividing the atmosphere into four height regions each having a different type of aerosol. These regions are the boundary or mixing layer (0 to 2 km), the upper troposphere (2 to 10 km), the lower stratosphere (10 to 30 km), and the upper atmosphere (30 to 100 km).

The earlier versions of LOWTRAN neglected changes in aerosol properties caused by variations in relative humidity. These aerosol models were representative of moderate relative humidities (around 80 percent). The models for the troposphere (rural, urban, maritime and tropospheric) which were previously used in earlier LOWTRAN models have been updated according to more recent measurements and also are now given as a function of the relative humidity. In addition, a wind-

dependent desert aerosol model, a new background stratospheric aerosol model and two new cirrus cloud models have been introduced into the program.

Only a brief description of the aerosol models and their experimental and theoretical bases will be presented in this report since they are described more fully elsewhere (see Shettle and Fenn[60]).

2.3.2 Vertical Distribution in the Lower Atmosphere

The range of conditions in the boundary layer (up to 2 km) is represented by four different aerosol models (rural, urban, maritime or desert) for each of several meteorological ranges* between 2 and 50 km, and as a function of humidity. In the boundary layer the shape of the aerosol size distribution and the composition of the three surface models are assumed to be invariant with altitude. Therefore, only the total particle number is being varied. Although the total number density of air molecules decreases approximately exponentially with altitude, there is considerable experimental data which show that the aerosol concentration very often has a rather different vertical profile. One finds that, especially under moderate to low visibility conditions, the aerosols are concentrated in a uniformly mixed layer from the surface up to about 1 to 2 km altitude and that this haze layer has a rather sharp top, which appears to be associated with the height of the minimum temperature lapse rate[63].

The vertical distribution for clear to very clear conditions, or meteorological ranges from 23 and 50 km, is taken to be exponential, similar to the profiles used in previous

* The terms "meteorological range" and "visibility' are not always used correctly in the literature. Correctly [61,62] visibility is the greatest distance at which it is just possible to see and identify with the unaided eye: (a) in the daytime, a dark object against the horizon sky; and (b) at night, a known moderately intense light source. Meteorological range is defined quantitatively, eliminating the subjective nature of the observer and the distinction between day and night. Meteorological range V is defined by the Koschmieder formula

$$V = 1/\beta \ \ln 1/\varepsilon = 3.9l2/\beta$$

where β is the extinction coefficient, and ε is the threshold contrast, set equal to 0. 02. As used in the MODTRAN computer code, the inputs are in terms of meteorological range, with β, the extinction coefficient, evaluated at 0. 55 μm. If only an observer visibility V_{obs} is available, the meteorological range can be estimated as $V \approx (1.3 \pm 0.3) * V_{obs}$.

versions of LOWTRAN. However, for the hazy conditions (10-, 5-, and 2-km meteorological ranges) the aerosol extinction is taken to be independent of height up to 1 km with a pronounced decrease above that height.

Above the boundary layer in the troposphere the distribution and nature of the atmospheric aerosols becomes less sensitive to geography and weather variations. Instead, the seasonal variations are considered to be the dominating factor. The aerosol concentration measurements of Blifford and Ringer[64] and Hoffman et al[65] indicate that there is an increase in the particulate concentration the upper troposphere during the spring and summer months. This is also supported by an analysis of searchlight data by Elterman et al.[66]

The vertical distribution of the aerosol concentrations for the different models is shown in Figure 12. Between 2 and 30 km, where a distinction on a seasonal basis is made, the spring-summer conditions are indicated with a solid line and fall-winter conditions are indicated by a dashed line.

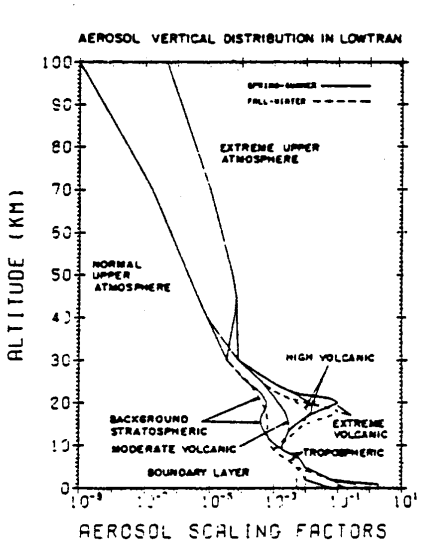

Figure 12a. Vertical Profiles of Aerosol Scaling Factors vs Altitude

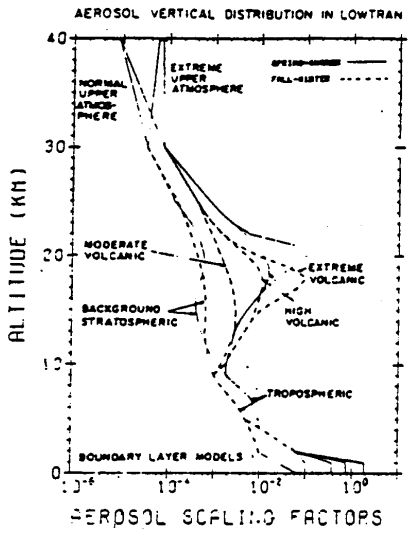

Figure 12b. Vertical Profiles of Aerosol Scaling Factors vs Altitude with the Region from 0 to 40 km Expanded

2.3.2.1 Use of Aerosol Vertical Profiles in MODTRAN

Introduction: The aerosol attenuation coefficients, $\beta_{atn}(z,\lambda)$, as a function of altitude, z, and wavelength, λ, in the MODTRAN/LOWTRAN/FASCODE propagation models are

generated as a product of an altitude dependent aerosol concentration, s(z), and a wavelength dependent aerosol attenuation, $k_{atn}(\lambda)$:

$$\beta_{atn}(z,\lambda) \quad = \quad s(z) \bullet k_{atn}(\lambda) \qquad (25)$$

Where 'atn' represents 'ext' or 'abs' for the extinction or absorption respectively. [The codes calculate the scattering coefficients as the difference *of* the extinction and absorption coefficients, $\beta_{scat}(z,\lambda) = \beta_{ext}(z,\lambda) - \beta_{abs}(z,\lambda)$]. The altitude-dependent scaling factor, s(z), and the normalized attenuation coefficients, $k_{atn}(\lambda)$, in principle can be defined in any self-consistent way such that their product gives the attenuation coefficients, β_{atn}, with the correct units, [km^{-1}]. The way these are currently implemented in the propagation codes is discussed in the following sections.

Altitude Dependent Scaling Factor: As currently implemented in the codes, the scaling factor, s(z), is the extinction coefficient at a wavelength of 0.55 μm, [km^{-1}]. It is calculated by Subroutine AERPRF using the data in Block Data PRFDTA. The data in PRFDTA is plotted as a function of altitude in Fig. 7 of the LOWTRAN 5 report[4] (pg 24) and Fig. 18-13 of the Handbook of Geophysics[67] (pg l8-14). The values are also tabulated in the Handbook in Table 18-10a (pg l8-l8). The choice of values used depends on the Surface Meteorological Range, VIS (for z = 0 to 5 km), the Season, ISEASN (for z = 2 to 30 km), and the Volcanic Conditions, IVULCN (for z = 9 to 40 km).

The value of s(z) at the surface, z = 0, is related to the meteorological range, VIS, by the Koschmieder formula (see the footnote on pg 26 of LOWTRAN 7):

$$VIS \quad = \quad 3.912 / \left[s(z=0) + \beta_{Ray} \right] \qquad (26)$$

where β_{Ray} is the Rayleigh scattering (≈ 0.0l2 krn^{-1}) at the surface for a wavelength of 0.55 μm. This leads to the following expression for s(0):

$$s(0) \quad = \quad (3.912/VIS) - \beta_{Ray} \quad \equiv \quad \beta_{ext}(0,0.55) \qquad (27)$$

Wavelength-Dependent Normalized Attenuation Coefficients: The normalized extinction or absorption coefficients, $k_{ext}(\lambda)$ or $k_{abs}(\lambda)$, are currently stored as the [unitless] ratios of the aerosol model dependent attenuation coefficients to the extinction coefficient at a wavelength of 0.55 μm for that model:

$$k_{ext}(\lambda) = Ext(\lambda)/Ext(\lambda = 0.55\mu m) \; and \; k_{abs}(\lambda) = Abs(\lambda)/Ext(\lambda = 0.55\mu m) \quad (28)$$

[Note with this definition, $k_{ext}(\lambda=0.55\mu m)=1.0$]. The appropriate values of $k_{ext}(\lambda)$ and $k_{abs}(\lambda)$ are chosen by Subroutine EXABIN, using the data in Block Data EXTDTA.

A different aerosol model, (with differing wavelength dependencies), is used for each of 4 altitude regions; the Boundary Layer, (0 to 2 km); the Free Troposphere, (2 to 9 km); the Lower Stratosphere, (9 to 30 krn); and the Upper Atmosphere, (30 to 100 km {120 km in FASCODE}).

The choice, of which aerosol models are used within each of the 4 altitude regions, is controlled by IHAZE(within the 'Boundary Layer') and by IVULCN (within the 'Lower Stratosphere'). The Tropospheric Aerosol Model is always used within the 'Free Troposphere', (unless overridden by the user when specifying their own model atmosphere, by their choice for IHA 1, on Card 2C3). Similarly the Meteoric Dust Aerosol Model is always used within the 'Upper Atmosphere', (unless overridden by a user specified aerosol profile).

Asymmetry Parameter and Phase Function: The values used for the asymmetry parameter, g, and the phase function, $P(\theta)$, are determined by the choice of aerosol model for given altitude region and by the wavelength. They are independent of altitude within that altitude region.

User Defined Aerosol Profiles And Attenuation Coefficients: If the user specifies their own vertical distributions of aerosol concentration or their own aerosol attenuation coefficient models, they must do so consistently with the way these quantities are utilized by the propagation codes as discussed above. Thus the user specified values of AHAZE on 80-byte formatted record 2C3 (when MODEL = 7), should be the aerosol (or cloud) extinction at a wavelength of 0.55 μm, with units of krn^{-1}. If the user instead provides the equivalent liquid water content, EQLWCZ (in gm/m^3), the codes internally compute the proper values for AHAZE. If the user provides their own aerosol attenuation model with 80-byte formatted records 2D, 2D1, and 2D2, the values of the normalized extinction and absorption coefficients, EXTC and ABSC, must follow the specification of Eq. (26), for $k_{ext}(\lambda)$ and $k_{abs}(\lambda)$.

The one exception to this is if the user provides their own values for *both* the aerosol scaling factor, s(z), with AHAZE, and the normalized attenuation coefficients, $k_{atn}(\lambda)$, with EXTC and ABSC. In this case, as long as AHAZE and both EXTC & ABSC are specified in a self-consistent manner so that their product, the aerosol attenuation coefficients, $\beta_{atn}(z,\lambda)$, as a function of altitude, z, and wavelength, λ, (as given by Eq. 25) has units of km^{-1}. So

for example, the 'scaling factor', s(z), *could be* given as the aerosol number density per volume or the aerosol mass per volume, with the 'normalized attenuation coefficient', $k_{atn}(\lambda)$, being the attenuation cross-section per aerosol particle or the attenuation cross-section per unit mass respectively.

2.3.3 Effects of Humidity Variations on Aerosol Properties

The basic effect of changes in the relative humidity on the aerosols, is that as the relative humidity increases, the water vapor condenses out of the atmosphere onto the existing atmospheric particulates. This condensed water increases the size of the aerosols, and changes their composition and their effective refractive index. The resulting effect of the aerosols on the absorption and scattering of light will correspondingly be modified. There have been a number of studies of the change of aerosol properties as a function of relative humidity[60,68]. The most comprehensive of these, especially in terms of the resulting effects on the aerosol properties is the work of Hanel[68,69] .

The growth of the particulates as a function of relative humidity, is based on the results tabulated by Hanel[68] for different types of aerosols. Once the wet aerosol particle size is determined, the complex refractive index is calculated as the volume-weighted average of the refractive indices of the dry aerosol substance and water[70].

2.3.3.1 Rural Aerosols

The "rural model" is intended to represent the aerosol conditions one finds in continental areas which are not directly influenced by urban and/or industrial aerosol sources. This continental, rural aerosol background is partly the product of reactions between various gases in the atmosphere and partly due to dust particles picked up from the surface. The particle concentration is largely dependent on the history of the air mass carrying the aerosol particles. In stagnating air masses, for example, under winter-type temperature inversions, the concentration may increase to values causing the surface layer visibilities to drop to a few kilometers .

The rural aerosols are assumed to be composed of a mixture of 70 percent of water-soluble substance (ammonium and calcium sulfate and also organic compounds) and 30 percent dust-like aerosols. The refractive index for these components is based on the measurements of Volz.[71,72].

The rural aerosol size distribution is parameterized as the sum of two log-normal size distributions, to represent the multi-modal nature of the atmospheric aerosols that have been discussed in various studies. These parameters for rural model size

distribution fall within what Whitby and Cantrell[73] give as a typical range of values for the accumulation (small) and coarse (large) particle modes.

To allow for the dependence of the humidity effects on the size of the dry aerosol, the growth of the aerosol was computed separately for the accumulation and coarse particle components. In computing the aerosol growth, changes in the width of the size distribution was assumed negligible so only the mode radius was modified by humidity changes. The effective refractive indices for the two size components are then computed as function of relative humidity.

Using Mie theory for scattering by spherical particles, the extinction and absorption coefficients for each of several different relative humidities were calculated. Figure 13

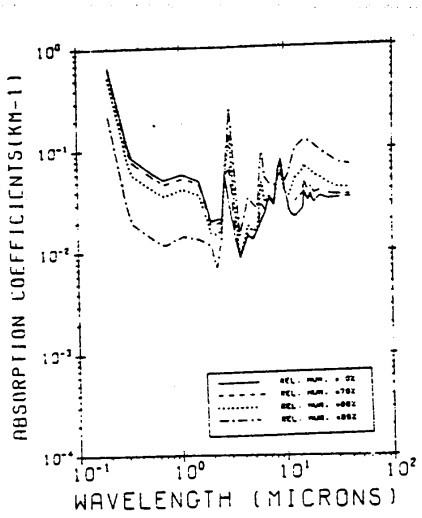

Figure 13a. Extinction Coefficients for the Rural Aerosol Model (Normalized to 1. 0 at 0. 55μm)

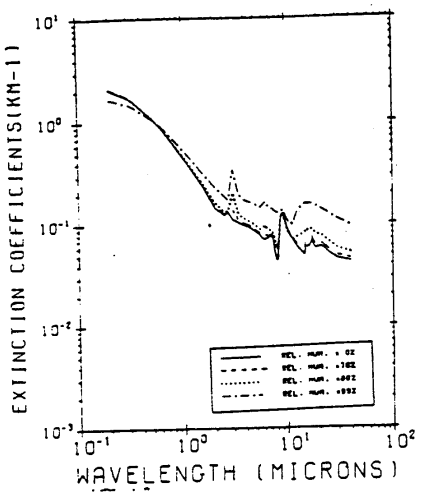

Figure 13b. Absorption Coefficients for the Rural Aerosol Model Corresponding to Figure 13a.

shows the resulting values for the different relative humidities which are stored in the MODTRAN code. The values have been normalized to an extinction coefficient of 1.0 at a wavelength of 0. 55 μm, which is the method used within the program.

2.3.3.2 Urban Aerosol Model

In urban areas the rural aerosol background gets modified by the addition of aerosols from combustion products and industrial sources. The urban aerosol model therefore was taken to be a mixture of the rural aerosol with carbonaceous aerosols. The soot like aerosols are assumed to have the same size distribution as both components of the rural model. The proportions of the soot like aerosols and the rural type of aerosol mixture are assumed to be 20 percent and 80

percent respectively. The refractive index of the soot like aerosols was based on the soot data in Twitty and Weinman's[74] survey of the refractive index of carbonaceous materials .

Figure 14 shows the extinction and absorption coefficients for the urban models vs wavelength. As with the rural model the values are normalized so the extinction coefficient is 1. 0, at a wavelength of 0. 55μm.

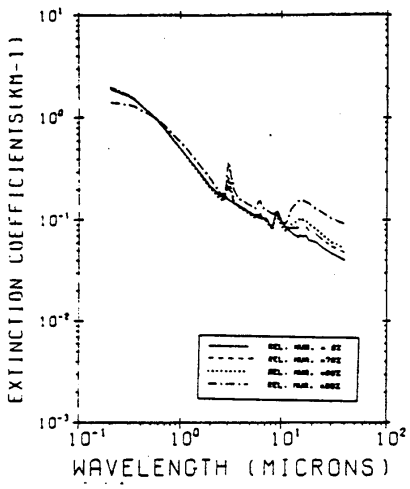

Figure 14a. Extinction Coefficients for the Urban Aerosol Model (Normalized to 1. 0 at 0. 55μm)

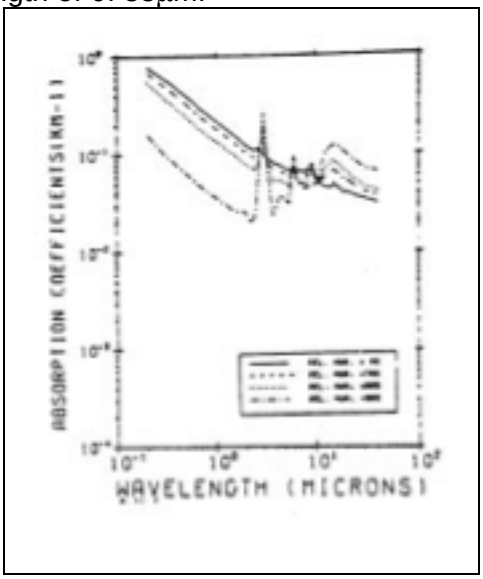

Figure 14b. Absorption Coefficients for the Urban Aerosol Model Corresponding to Figure 14a

2.3.3.3 Maritime Aerosol Model

The composition and distribution of aerosols of oceanic origin is significantly different from continental aerosol types. These aerosols are largely sea-salt particles which are produced by the evaporation of sea-spray droplets and then have continued growing due to accretion of water under high relative humidity conditions. Together with a background aerosol of more or less pronounced continental character, they form a fairly uniform maritime aerosol which is representative of the boundary layer in the lower 2 to 3 km of the atmosphere over the oceans, but which also will occur over the continents in a maritime air mass. This maritime model should be distinguished from the direct sea-spray aerosol which exists in the lower 10 to 20 meters above the ocean surface and which is strongly dependent on wind speed .

Therefore, the maritime aerosol model has been composed of two components: one which developed from sea-spray; and a continental component

which is assumed identical to the rural aerosol with the exception that the very large particles were eliminated, since they will eventually be lost due to fallout as the air masses move across the oceans. This model is similar to the one suggested by Junge[75,76] and is supported by a large body of experimental data.[60]

The refractive index is the same as that for a solution of sea salt in water, using a volume-weighted average of the refractive indices of water and sea salt. The

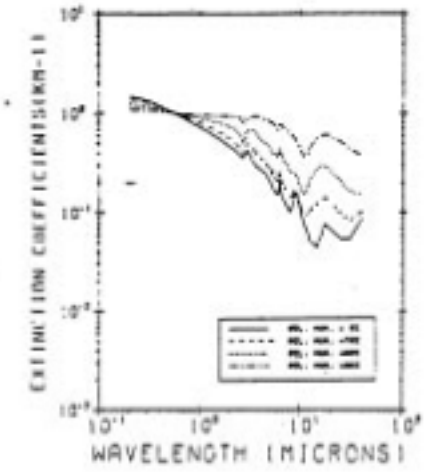

Figure 15a. Extinction Coefficients for the Maritime Aerosol Model (Normalized to 1.0 at 0.55μm)

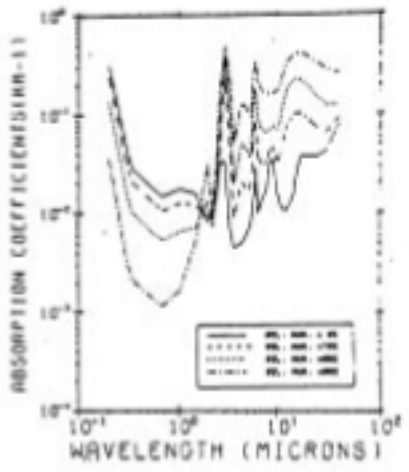

Figure 15b. Absorption Coefficients for the Maritime Aerosol Model Corresponding to Figure 15a.

refractive index of the sea salt is primarily taken from the measurements of Volz.[77] The normalized extinction and absorption coefficients vs wavelength for the maritime aerosols are shown in Figure 15 for several relative humidities.

2.3.3.4 Tropospheric Aerosol Model

Above the boundary layer in the troposphere, the aerosol properties become more uniform and can be described by a general tropospheric aerosol model. The tropospheric model represents an extremely clear condition and can be represented by the rural model without the large particle component. Larger aerosol particles will be depleted due to settling with time. This is consistent with the changes in aerosol size distribution with altitude suggested by Whitby and Cantrell.[73]

There is some indication from experimental data, that the tropospheric aerosol concentrations are somewhat higher during the spring-summer season than during the fall-winter period.[64,65] Different vertical distributions are given to represent these seasonal changes (see Section 2.3.2).

The dependence of the particle size on relative humidity is the same as for the small particle component of the rural model. The resulting normalized extinction and absorption coefficients are shown in Figure 16 for the different relative humidities.

2.3.3.5 Fog Models

When the air becomes nearly saturated with water vapor (relative humidity close to 100 percent), fog can form (assuming sufficient condensation nuclei are present). Saturation of the air can occur as the result of two different processes; the mixing of air masses with different temperatures and/or humidities (advection fogs), or by cooling of the air to the point where the temperature approaches the dew-point temperature (radiation fogs).[78]

To represent the range of the different types of fog, we chose two of the fog models presented by Silverman and Sprague,[79] following the work of Dyachenko.[80] These were chosen to represent the range of measured size distributions, and correspond to what Silverman and Sprague[79] identified as typical of radiation fogs and advection fogs. They also describe developing

and mature fogs, respectively. The normalized extinction and absorption coefficients for the two fog models are shown in Figure 17 as a function of wavelength.

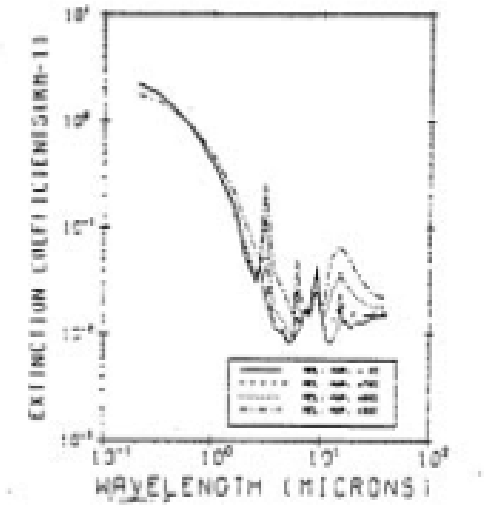

Figure 16a. Extinction Coefficients for the Tropospheric Aerosol Model (Normalized to 1.0 at 0.55μm)

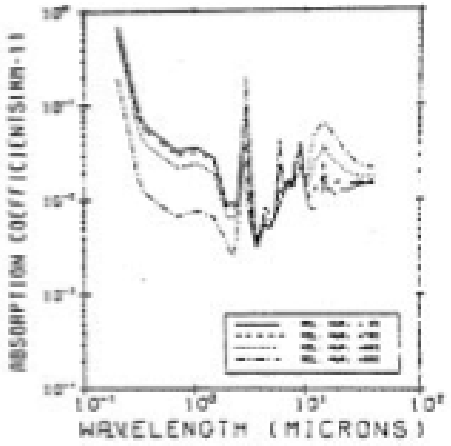

Figure 16b. Absorption Coefficients for the Tropospheric Aerosol Model Corresponding to Figure 16a

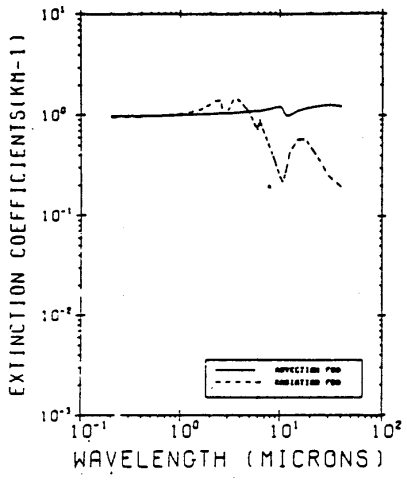

Figure 17a. Extinction Coefficients for the Fog Models (Normalized to 1. 0 at 0. 55μm)

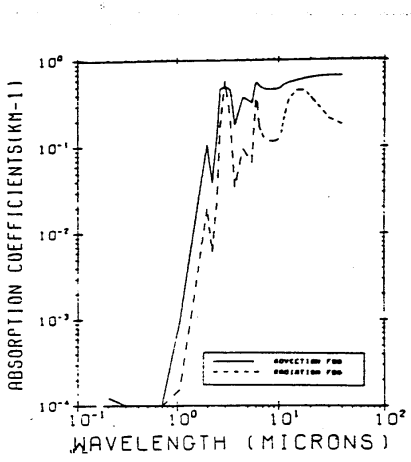

Figure 17b. Absorption Coefficients for the Fog Models Corresponding to Figure 17a

2.3.3.6 Wind Dependent Desert Aerosol Model

This synopsis of the wind dependent desert aerosol model is based on the Longtin, et al,[81] report. For a comprehensive description of the desert aerosol model please refer to that report.

Aerosols can be found throughout the atmosphere. They can have a role in cloud formation and precipitation processes and plus they can have an impact on the radiation balance of the earth-atmosphere system. The radiative impact will depend on the size, shape and composition of the aerosols, as well as their spatial distribution in the atmosphere and the nature of the underlying surface.

Aerosols can be separated into a set of generic categories based primarily on their (spatial) location in the atmosphere. Each aerosol "type" has its own characteristic optical properties that distinguish it from other aerosols. For most aerosol types, a set of parameters exist for calculating aerosol radiative properties with reasonable accuracy.

An important aerosol type is the desert aerosol which is representative of arid and semi-arid regions. The desert aerosol model is included because about one-third of the earth's land surface area consists of arid and semi-arid terrain and because the radiative effects of desert aerosols are important during dust storm conditions. In addition, the source regions of desert aerosols have high solar insolation and strong convective processes that enable the particles to be lifted to altitudes where synoptic-scale air motions can transport the particles well beyond their source regions.

A tentative desert aerosol model was developed[82] for use in the Phillips Laboratory's Geophysics Directorate's atmospheric propagation models. This model was based primarily on recommendations from a meeting of experts conducted by the World Climate Research Programme[83]. The current desert aerosol model contains many improvements over the original Shettle model.

PHYSICAL PROPERTIES OF DESERT AEROSOLS

The desert aerosol model that has been recommended by the World Climate Research Programme and utilized by Shettle is based on a limited data set. The formulation uses data that were obtained primarily in the Middle East, although measurements from other arid and desert locations have been included. Table 3 provides a partial listing of measurements[84-94] that relate to the physical properties of aerosols in arid or desert environments.

Table 3. Summary of Aerosol Measurements for Arid or Semi-Arid Environments

LOCATION	Period of Measurements	Measurement Type	Reference
Central Sahara	Feb 1979-Feb 1982	SD	d'Almeida and schutz[84]
Haswell, Colorado	Unknown	SD	Patterson and Gillette[85]
Plains, Texas	Unknown	SD	Patterson and Gillette[85]
Camp Derj and Sebha, Libya	Unknown	SD	Schutz and Jaenicke[86]
Mitzpe Ramon Negev, Israel	Winter and Early Spring 1976	SD, RAD Comp	Levin and Lindberg[87]
Beer-Sheva, Israel	June 1977 - May 1978	Comp, TML	Kushelevsky et al.[88]
Arizona and Utah	June - July 1979	Comp, TML	Cahill et al.[89]
Namib Desert	Nov 1976 - April 1977	Comp	Annegarn et al.[90]
Tularosa Basin, NM	Aug 1984 - Aug 1985	Comp, SD	Pinnick et al.[91]
Mitzpe Ramon Negev, Israel	Dust Storm on 6 June 1977	SD, RAD	Levin et al.[92]
Grand Canyon, AZ	Dec 1979 - Nov 1981	TML, RAD	Malm and Johnson[93]

Iran and Pakistan	Unknown	RAD	Otterman et al.[94]

* KEY: SD - Size Distributions, Comp - Composition, RAD - Radiative Measurements
TML - Total Mass Loadings

Source Regions and Transport Characteristics

Desert aerosols have been measured at great distances from their source regions. Saharan aerosols have been measured well into the tropical North Atlantic[95,96] and in Mediterranean countries[97-99].

Desert aerosols originating from Asian deserts have been measured in the Hawaiian Islands[100]. The bulk aerosols in the lower few kilometers of the troposphere over the tropical North Atlantic consist primarily of sea-salt aerosols and mineral aerosols originating from the arid and semi-arid regions of West Africa[95] .
These measurements indicate that the aerosols at a given location are not necessarily representative of the underlying soils. d'Almeida and Schutz[84] have shown from their data of soil samples and aerosol samples from across the Sahara desert that the aerosols are largely made up of crustal material that are representative of loose and finely grained soils. They state that flood plains near mountains offer probable production source areas for desert aerosols rather than dune-like deposits. These results are consistent with those of Chester et al.[99] who performed an elemental analysis of aerosols from over the Tyrrhenian Sea. Their data indicated that the aerosols are characteristic of crystal material rather than from dune areas.

Size Distributions

Aerosol size distributions are often modeled by the sum of two or three log normal distributions,

$$\frac{dN(r)}{d\log r} = \sum_{i=1}^{2,3} \frac{N_i}{(2\pi)^{1/2}\log\sigma_i} \exp\left(-\frac{\left[\log(r/R_i)\right]^2}{2(\log\sigma_i)^2}\right) \qquad (29)$$

where N(r) is the particle concentration for particles greater than a given radius r, N_i is the total number of particles for the distribution i, σ_i is the geometric standard

deviation and R_i is the geometric mean radius. The individual distributions are often meant to represent different size classifications that are representative of different production processes. Three size ranges; ($10^{-7} < r < 10^{-5}$ cm; $10^{-5} < r < 10^{-4}$ cm; and $r > 10^{-4}$ cm) are typically used to describe aerosols in the atmosphere (see reference 83). The size ranges are referred to, respectively, as the Aitken or nucleation mode, the large or accumulation mode and the giant or coarse mode.

Based on an analysis of tropospheric aerosol measurements, Patterson and Gillette[85] characterized the distributions with three modes that they referred to respectively as, modes C, A, and B. Mode C represents particles centered at about 0.02 - 0.5 μm and is representative of background aerosols. Mode A particles cover the radius range of 1 - 10 μm and consist of particles produced from the parent soil by a sandblasting process. This component of the size distribution is determined by the lifting force of the local winds. Mode B particles peak at about 30 μm radius and are primarily found when the wind speed is high and the dust loading is significant. Under heavy dust loading conditions, Patterson and Gillette found that only modes A and B were present as a result of soil erosion and sandblasting along with the subsequent injection of this material into the atmosphere. These results suggest that different size distribution formulations are needed to describe background desert and dust storm conditions.

The size distributions used in the tentative AFGL desert aerosol model, which were based on recommendations from the World Climate Research Programme, are shown in Table 4.

Table 4. Parameters Used in the Background Desert and Desert Dust Storm Aerosol Models

MODEL	i	Ni (cm^{-3})	log (σ_i)	R_i (μm)
	1	997	0.328	0.0010
Background	2	842 4	0.505	0.0218
	3	$7.10 * 10^{-4}$	0.277	6.24
	1	726	0.247	0.0010
Dust Storm	2	1,140	0.770	0.0188

3	$1.78 * 10^{-1}$	0.438	10.8

These values are based primarily on measurements[95,101,102] from the Sahara desert. For calm (or background) conditions, the parameters are similar to those for "remote continental aerosols." The parameters for the dust storm conditions are based on the work of Schutz and Jaenicke[86], Jaenicke and Schutz[101] and d'*A*lmeida and Jaenicke[102]. The major difference between the model for background and dust storm conditions is in the number of large particles in mode 3, the component associated with large particles that are injected by high winds. Therefore, the values for the dust storm model represent extreme values and should be linked to wind velocity.

Composition

Compositional measurements indicate that desert aerosols are a mixture of different kinds of materials. Desert aerosols consist of a background component and a component representative of local soil sources. Depending upon location, desert aerosols can also have an anthropogenic component .

Simple visual examination of desert dust reveals many of the particles to have a light brown to tan appearance[87] ,unlike urban aerosols that are generally gray or black. Elements commonly found in desert aerosols[87-91] include sodium, calcium, silicon, aluminum and sulfur. Silicon, presumably in the form of quartz and calcium, appear to be the most common elements in the desert aerosol[87,88]. The five most common elements found by Kushelevsky et al.[88] were calcium, silicon, sulfur, iron and chlorine. Calcium, silicon and iron are primarily crustal in nature while sulfur and chlorine can have both crustal and industrial sources. Chlorine can also be derived from sea spray[90].

Particles with radii less than about 0.4 μm appear to have a large ammonium sulfate and ammonium bisulfate component while larger particles have quartz, clay components and other elements associated with soil or crustal sources[89,90,91,99].

Generally speaking, desert aerosols are not hygroscopic. The only exception to this is a "well aged" desert aerosol in which the background component has acted as a condensation nuclei as a result of numerous trips up and down through the desert atmosphere.

Abundance' s of the elements can vary from sample to sample as a function of wind speed (i.e., increased mass loading) and wind direction (i.e., source region). Cahill et al.[89] observed a seasonal variation in the amount of silicon particulate in samples collected in Arizona and Utah. Their results, which consisted of one year of data, indicated that for particles in the range 3.5 to 15 μm, the silicon abundance increased

to a maximum in the spring and then decreased to a minimum in the winter. Table 5, from Kushelevsky et al.[88] summarizes how the abundance' s of these elements can vary on a day-to-day basis and when averaged over different meteorological conditions.

Carbon is generally found in very small abundance' s in desert aerosols. However, due to its strong absorption, a small increase in the carbon amount, as little as 1%, can lead to a large increase in the total absorption properties of desert aerosols.

Table 5. Variation of Elemental Concentrations in Middle Eastern Desert Aerosols as (a) A Function of Source Region and (b) Averaged Over Meteorological Conditions. Measurements were made by Kushelevsky et al. at Beer-Sheva, Israel using Instrumental Neutron Activation Analysis and X-ray Fluorescence

(a)

WIND DIRECTION ~	MEAN WIND SPEED ~(m s^{-1})	TOTAL SUSPENDED PARTICULATE ~ (g m^{-3})·	NOTES	ELEMENTAL CONCENTRATIONS (%) Ca	Si	S	Fe	Cl
W-E	2.04	291		10	9	2	2	2
N-W	2.01	243		18	13	2	2	1
N-W	1.85	160		14	13	4	2	2
W-E	1.67	36	Rain	1	5	4	1	4
NW-E	2.29	104	Rain	9	11	3	2	2
W-SE	1.83	50	Rain	19	20	5	4	7
N-E	4.59	581	Dust Storm	18	21	1	3	0.4
W-SW	2.00	610	Dust Storm	17	18	1	2	1
W	2.73	1600	Dust Storm	22	17	0.3	2	0.1
N-E	2.25	613	Sharav	15	19	1	2	1
E-SE-E	2.87	412	Sharav	17	23	1	3	1
W Variable	3.16	5080	Sharav	16	18	0.2	3	0.2

(b)

METEOROLOGICAL CONDITIONS	ELEMENTAL CONCENTRATIONS (%) Ca	Si	S	Fe	Cl
Normal	12.2	11.5	3.1	1.9	2.5
Rain	12.6	14.6	4.5	2.4	3.6
Dust Storm	16.8	18.0	0.6	2.4	0.5

Note: Sharav, or Khamsin, is a Dust Storm Characterized by Hot Winds from the North African Desert.

It Typically Occurs During the Period Between Easter and Pentecost

Effects of Wind

Enormous amounts of clay and sand can be loaded into the desert atmosphere during windy conditions. During calm conditions the desert aerosol resembles aerosols other than that which would be produced from the underlying soil. In particular, Patterson and Gillette[85] have studied the composition of the desert aerosol in light, medium and heavy mass loading conditions and have found that particles having radii between 0.02 and 0.5 μm were generally grey or black and represented the global background aerosol. Furthermore, these particles were always present in the same amount regardless of the amount of mass loading. Similar findings reported in the World Climate Programme study confirmed that under very calm conditions the composition of the desert aerosol resembles that of a remote continental aerosol.

Local wind conditions provide the mechanism to inject and transport aerosols. Wind also provides a mechanism for the generation of additional aerosols via a sandblasting process. The amount of aerosol injection and generation depends upon factors such as wind speed[103,104], soil moisture, and the extent of vegetation[105], soil texture and the amount of soil crusting[106].

Soil movement as a result of aerodynamic forces occurs for wind speeds above a given threshold value. This wind speed threshold will vary as a function of soil condition and on the amounts of non-erodible elements, such as rocks and pebbles, on top of the soil. Utilizing a portable wind tunnel, Gillette[104] examined the threshold velocities for three different kinds of soils, two types of desert soil and one farmland soil. A relatively smooth desert soil had a threshold velocity of 34.2 cm s^{-1} while one with a pebble covering had a threshold velocity of 121.9 cm s^{-1}.

The size distribution of the aerosols that are injected into the air as a result of wind erosion has been found to be similar to that of the underlying soil[105].

Indices of Refraction

The index of refraction characterizes the optical properties of a particular material. It can be expressed as the complex number:

$$m = n + ik , \qquad (30)$$

where n and k are related to the phase velocity and attenuation, respectively, of an electromagnetic wave as it passes through the material. In general, the index of refraction of a material will not be the same for all wavelengths of radiation.

2.3.4 Vertical Distribution in the Stratosphere and Mesosphere

Measurement programs carried out over many years show that in the 10- to 30-km region there exists a background aerosol in the stratosphere which has a rather uniform global distribution. This background aerosol is considered to be mostly composed of sulfate particles formed by photochemical reactions.

These background levels are occasionally increased by factors of 100 or more due to the injection of dust from massive volcanic eruptions. Once such particles have been injected into the stratosphere they are spread out over large portions of the globe by the stratospheric circulation and diffusion processes, and it requires months or even years for them to become slowly removed from the stratosphere.[107-109]

There occurs also a seasonal and geographic variation of the stratospheric aerosol layer which is related to the height of the tropopause; a peak in the aerosol mixing ratio (that is, ratio of aerosol to air molecules) occurs several kilometers above the tropopause. [65,110]

The range of possible vertical distributions is represented by four different profiles (background stratospheric, moderate, high and extreme volcanic). Each of these distributions is then modified according to the season. The different scaling factors for these vertical profiles are shown in Figure 11.

The vertical distribution in the upper atmosphere above 30 to 40 km is very uncertain because of the difficulty of obtaining reliable data. In situ measurements are limited to those obtained by rocket flights, and these altitudes are beyond the normal operational range of most lidar and searchlight systems which provide most of the remotely sensed data up to 30 or 40 km.

The most likely profile for this region is the one labeled as "Normal Upper Atmosphere" in Figure 11; it corresponds to a constant turbidity ratio of ≈ 0.2 above 40 km. This agrees with the aerosol extinction profile obtained by Cunnold et al[111] by inverting measurements of the horizon radiance from an X- 15 aircraft. Measurements of the solar extinction through the atmospheric limb from the Apollo-Soyuz mission[112] tend to support this model.

Ivlev's[113,114] model for the upper atmosphere is shown as the curve labeled "Extreme Upper Atmosphere" in Figure 11. It is largely based on twilight

observations[115] which neglected multiple-scattering effects. As a consequence, the model has to assume very high particulate concentrations in the upper atmosphere in order to be consistent with observations.

Nevertheless, extinction coefficients for the extreme upper-atmospheric model are consistent with the extreme values that have been observed in layers of a few kilometers thickness by lidar, [116,117] inferred from rocket observations of skylight,[118,119] and studies of noctilucent clouds.[120]

2.3.4.1 Improved Background Stratospheric Aerosol Model

INTRODUCTION

This is a synopsis of the Background Stratospheric Aerosol Model developed by Hummel et. al. [43]. This is an improved background stratospheric aerosol model in which temperature dependent indices of refraction for H_2SO_4 have been used with a log normal size distribution. For a complete understanding of this modified model please refer to that document.

Aerosols commonly found at stratospheric altitudes, 10 - 30 km, are a result of photochemical formation involving sulfur compounds. These background aerosols are generally uniform over the globe. The concentrations of these stratospheric aerosols can be increased dramatically following massive volcanic eruptions. Additional sulfur based aerosols can be photochemically created from the sulfur gases in an eruption cloud. Volcanic ash and debris can also be injected into these altitudes.

Three stratospheric aerosol models[601] have been developed for use in the transmittance/radiance models MODTRAN 2 and FASCODE. The three models are for background stratospheric conditions, fresh volcanic aerosols, and aged volcanic aerosols. These models have also been adapted for use in the Standard Radiation Atmosphere (SRA)[121] models.

The background stratospheric aerosol consists of a 75 % solution of sulfuric acid in water. The wavelength dependent index of refraction for the solution is based on laboratory measurements at 300 K[122,123,124]. The indices of refraction for the volcanic ash are based on the measurements of Volz[125]. The size distributions for all three stratospheric aerosols are given by modified gamma distributions. Stratospheric temperatures are well below 300 K. Values of the index of refraction for H_2SO_4 are now available at 250 K[126] and can be used to calculate temperature dependent indices of refraction for H_2SO_4 for temperatures appropriate for stratospheric conditions. Also, recent measurements of the size distribution of stratospheric

aerosols indicate that a log normal distribution may be more appropriate for stratospheric aerosols than a modified gamma distribution (see p. 30 of Ref [83]).

Measurements of Stratospheric Aerosols

Two recent major volcanic eruptions have provided researchers with the opportunity to study stratospheric and volcanic aerosols in depth. The eruptions were Mt. St. Helens in 1980 and El Chichon in 1982. In both cases, the eruptions were intensely studied by ground and aircraft based lidars, balloons, aircraft and satellites.

Lidar Studies

Lidar provides a tool to study particulate matter in the stratosphere. Lidars at various locations around the world have permitted researchers to study the distribution of volcanic materials injected into the stratosphere since the 1970' s. The altitude resolution that can potentially be obtained from lidars allows researchers to study both the temporal and spatial details of volcanic eruption clouds. The worldwide network of lidars (e.g. References 127-132) provided extensive coverage of the eruption clouds from the Mount St. Helens and El Chichon eruptions. These lidars have also detected the presence of so-called "mystery clouds", clouds that cannot be traced to the eruption of known volcanoes.

The lidars used for probing the upper troposphere and stratosphere use the lidar backscattering ratio to identify layers of non-molecular scattering. The lidar back-scattering ratio as a function of altitude, B(z), is given as:

$$B(z) = 1 + f_A(z) / f_M(z) \qquad (31)$$

where $f_A(z)$ is the aerosol backscattering function and $f_M(z)$ is the molecular backscattering function. A requirement for the use of (31) is the assumption that at some altitude the returned lidar signal is only from molecular scatters. This altitude, often called the matching altitude, is used to determine the atmospheric density profile required to give $f_M(z)$. Once this is known, any return greater than that produced by a pure molecular atmosphere is assumed to be from particulates. The matching altitude is generally taken to fall in the 30 km range, although Clemesha and Simonich[129] feel that the matching altitude should be taken at higher altitudes.

Table 6 summarizes results of several lidar studies[128-131&133-137] made under background and volcanic conditions. The studies indicate that a backscatter ratio of between 1.1 and 1.4 is representative of background stratospheric conditions. The backscatter ratio following an eruption is highly variable and depends on the force of the eruption, as measured by the amount of material injected and the height of the eruption cloud, as well as the sulfur content of the eruption cloud.

The lidar studies have detailed the layering of material following volcanic eruptions. The layers are highly dynamic and can change fairly quickly as a result of variations in the stratospheric circulation and as particles settle out.

Table 6. Summary of Lidar Studies of Background and Volcanic Aerosol Conditions in the Stratosphere

LOCATION	TIME PERIOD	WAVELENGTH (μm)	ALTITUDE REGION (km)	AVERAGE BACKSCATTER RATIO
	July-August 1970	0.589	20	1.4
Brazil[131,135]	1973	0.589	20	1.06 - 1.12
(23° S, 46° W)	August 1975	0.589	20	1.28
	April 1976	0.589	20	1.15
	1982	0.589	15 - 20	> 5.0 (Peak)
	May 1978-Apr 1979	0.694	16	1.052 ± 0.02
	May-June 1979	0.694	16	1.12 - 1.42
Japan	May 1978-Apr 1979	0.694	20	1.116 ± 0.05
(33°N, 130° E)	Nov 1979	0.532	21	1.05
(Ref 132,133,	Nov 1979	1.064	21	1.46 ± 0.19
136,137,138)	Dec 1979	0.532	21	1.2 (Peak)
	Dec 1979	1.064	21	2.0 (Peak)
	Apr 1982	0.532	24.5	400 (Peak)
Japan[138]	Apr-July 1982	0.694	24 - 26	44 (peak)
(35° N, 137°E)				
Italy[130]	Sept-Dec 1979	0.589	14 - 20	< 1.2
(42° N, 23° E)	June-July 1980	0.589	14- 20	2.0
Italy[139]	Mar Apr 1982	0.589	15 - 25	1.5 (Peak)
(42° N, 13° E)				

Balloon Measurements

Hofmann and Rosen have made extensive measurements of background stratospheric[138] and volcanic aerosols[139,140,141] using balloon-borne instruments that can reach altitudes up to about 35 km. Their typical balloon package carries optical particle counters to measure condensation nuclei for particles with radii $r \geq 0.01$ μm and a dustsonde for particles with $r \geq 0.15$ and $r \geq 0.25$ μm. A more recent version[140] also carries a large particle counter for $r > 0.25$, 0.95, 1.2 and 1.8 μm.

The particle size measurements provide integral values of the particle concentrations with sizes greater than or equal to the respective cut-off radii. By taking ratios of these concentrations, a set of size ratios can be obtained that can be related to size distribution.

The balloon packages have also been equipped with an intake heater that heats the air samples to around 150° C. This allows one to distinguish from volatile and nonvolatile aerosols. This technique has identified the volatile aerosols as having an average mixture of 75 % H_2SO_4 and 25 % H_2O.

The balloon measurements of background conditions yielded average peak aerosol concentrations that would correspond to back scattering ratios of about 1.09 - 1.17 at 0.6943 μm[142]. These results agree well with the lidar results summarized in Table 6.

Hofmann and Rosen conducted thirty six balloon flights from Laramie, Wyoming (41° N) to study the Mt. St. Helens eruption cloud during the year following the eruption[139] The Mt. St. Helens eruption cloud was observed as four different layers at different altitudes over the 12 - 24 km region. The cloud was first observed at about 12 - 15 km in the vicinity of the jet stream. After about a week, a layer appeared in the 15 - 18 km range over Laramie. This layer became the main layer from the eruption. Material was also injected into the 18 - 24 km range where the summer stratospheric winds shift from westerlies to easterlies. The third layer was at 18 - 20 km where the winds were shifting and the fourth at 20 - 24 km where the winds were blowing from the east.

Hofmann and Rosen also studied the El Chichon cloud for eighteen months following its eruption[140,141] . Those flights were from Laramie and from locations in southern Texas (27° N - 29°N).

The flights discovered two major layers of aerosols separated by a very clean region. The first was around the tropopause and extended to about 21 km. The second layer was centered around 25 km and was generally about 5 km thick. The two layers may have resulted from two separate eruptions. The lower layer may have

resulted from the initial 28 March 1982 eruption while the higher one may have come from the more violent 4 April 1982 eruption.

The upper layer was dominated by larger particles consisting of a mixture of about 80 % H_2SO_4 and 20 % H_2O while the lower layer consisted of an aerosol with a concentration of 60 - 65 % sulfuric acid. The difference in acid concentration was due to the warmer temperatures and lower water vapor abundance' s in the upper layer.

Table 7 shows the peak aerosol concentrations measured above 20 km from the two locations as a function of time following the eruption. The data displayed only cover three of the size ranges measured. Data from a flight on February 5, 1982 are given as representative of pre-eruption values. The differences between the two locations result from the Texas flights penetrating denser regions of the eruption cloud.

The size distribution determined from balloon measurements taken 45 days after the eruption was bi-modal with mode radii of 0.02 and 0.7 μm. After about June 1982, the production of condensation nuclei (e.g., the curve of $r \geq 0.01$ μm) had essentially ceased and fallen back to pre-eruption values.

Table 7. Peak Aerosol Concentrations Above 20 km for Three Size Ranges As a Function of Time After the Eruption of El Chichon as Measured from Laramie, Wyoming and Southern Texas[142] . The data from 2/5/82 are given as representative of pre-eruption values

	PEAK AEROSOL CONCENTRATIONS					
DAYS AFTER ERUPTION	**$r \geq 0.01$ μm (# cm^{-3})**		**$r \geq 0.15$ μm (# cm^{-3})**		**$r \geq 0.25$ μm (# cm^{-3})**	
	Wyo	**Texas**	**Wyo**	**Texas**	**Wyo**	**Texas**
(2/5/82)	8		0.5		0.1	
2	25		0.8		0.1	
10	50		0.8		0.1	
20	48		0.7		0.1	
40	45		0.65		0.13	
45	700		22		16	
60	38	400	0.6	20	0.16	15
73	400		4.0		1.1	
80	200	160	4.2	16	2.0	13
95	45		8.0		6.0	
100	38	65	5.0	15	3.0	11
110	23		2.0		1.2	
120	24	30	4.0	12	2.8	10
125	24		5.2		4.0	

140	15	12	4.0	11	2.8	0.9
152	10		3.5		2.0	
160	13	13	5.0	11.5	4.0	0.85
178	10		1.8		0.8	
180	11	13.5	2.3	11	1.0	0.8
190	13		10.0		2.0	
200	12	14	7.0	10	2.5	0.7
215	11		4.0		3.0	
220	10		5.0		3.2	
240	10		7.1		5.2	

Aircraft Measurements

Extensive aircraft measurements of stratospheric aerosols were made of the Mt. St. Helens and El Chichon eruptions. Flight paths were often chosen to overlap other measurements such as the balloon measurements of Hofmann and Rosen.

Size Distribution Measurements

Oberbeck et al [143] collected particles from the Mt. St. Helens eruption cloud for a year using wire impactors flown upon the NASA U-2. The aircraft sampled the stratospheric aerosols at an altitude of 18.3 km, the height where the main aerosol layer eventually formed.

Table 8 shows the sampled aerosol particle concentrations for two size ranges, $r < 0.15$ μm and $r > 0.15$ μm, for the year following the eruption. In the six months after the eruption, the total volume of aerosols with radii greater than 0.03 μm increased. The concentration of particles with radii less than 0.15 μm decreased while the concentration of particles with radii greater than 0.15 μm increased. This is consistent with the dispersal of an initially high concentration of small particles and the growth of aerosols by condensation. The aerosol levels returned to normal in about a year.

The El Chichon eruption was studied extensively by aircraft. One series of measurements involved measuring stratospheric size distributions with "Knollenberg" counters[144]. The measurements made prior to the eruption revealed relatively featureless size distributions. The data over the range 0.1 to 1.0 μm revealed particles that were largely H_2SO_4. Their number density varied with altitude from about 20 cm^{-3} at 17 km to about 1 cm^{-3} at 20 km.

Flights following the eruption suggested two dominant size modes. The first mode consisted of small particles (0.1 - 0.8 μm) that were primarily H_2SO_4 and large particles (0.8 - 30 μm) that were primarily volcanic ash. Later flights indicated that particles up to 2.0 μm were largely H_2SO_4 although some of the particles may have been coated with sulfuric acid.

Table 8. Aerosol Concentrations From the Mt. St. Helens Eruption Cloud at 18.3 km in two Size Ranges as Measured by Wire Impactor[143]

DATE	MONTHS AFTER ERUPTION	r > 0.15 μm (cm^{-3})	r < 0.15 μm (cm^{-3})
5/20/80	0	2.0	11.0
6/25/80	1	1.8	22.5
7/16/80	2	2.5	18.0
10/29/80	5	3.5	14.0
12/02/80	6.5	4.0	15.0
12/17/80	7	2.5	6.0
4/10/81	12	1.5	3.0

Oberbeck et al[145] also studied the El Chichon eruption cloud with the Ames Wire Impactor. Table 9 summarizes the total aerosol concentrations as measured at different altitudes. The size distribution measured prior to the eruption could be fitted with a log normal distribution with a total concentration of between 3.4 and 4.3 cm^{-3}, a mode radius of 0.08 μm and a standard deviation of about 1.68. After the eruption, the distribution was best represented with two log normal size distributions, an enhanced background of sulfuric acid particles with a larger mode radius and a sedimentation mode consisting of large silicates.

Table 9. Total Aerosol Concentrations From the El Chichon Eruption Cloud at Various Altitudes as Measured by the Ames Wire Impactor[145]

DATE	MONTHS AFTER ERUPTION	ALTITUDE (km)	N (cm^{-3})
10/16/81	—	18.3	6.3
5/5/82	1	20.7	3.9
7/23/82	3.5	20.7	7.8
9/23/82	5.5	19.8	13.68
11/4/82	7	20.7	6.2
11/5/82	7	20.7	5.4

12/13/82	8	20.7	7.9

Wilson et al[146] summarized many of the NASA U-2 measurements made at 20 km of aerosol particles less than 2.5 μm in diameter, following the El Chichon eruption. Their results indicated that the background aerosols were dominated by particles with radii smaller than 0.05 or 0.03 μm. Measurements in April and May 1982 indicated significant increases in the sub 0.1 μm aerosol concentration that can only be explained by gas-phase reactions leading to the formation of secondary (non-eruption) aerosols. Measurements in the same size range made in late 1982 showed considerable depletion, suggesting coagulation of small particles to form larger ones.

Transmission Measurements

Witteborn et al[147] obtained infrared transmission spectra for the atmosphere above 11 km for latitudes between 2° S and 50° N. The measurements were made in December 1982 when the stratospheric aerosols were still considerably enhanced by the El Chichon eruption. The absorption was obtained by ratioing the transmission at 8.5 μm, where the H_2SO_4 absorption is strongest, to the transmission at 12 μm, where the atmospheric transmission is nearly unity. The average absorption per unit air

mass was evaluated at 0.019, of which 0.010 was attributable to the presence of H_2SO_4 aerosols. They also reported that the ratio of optical depth at 8.5 μm to that at 0.5 μm, obtained by Dutton and DeLuisi[148] was about 0.14 at 20° N.

Composition Measurements

Woods and Chuan[149] sampled the El Chichon volcanic cloud using a quartz crystal micro balance (QCM) cascade impactor flown on the NASA U - 2. The QCM collected and classified particles into 10 size intervals from less than 0.05 μm to greater than 25 μm diameter. The collected aerosols were then analyzed for composition.

The compositional analysis indicated that the sub-micron particles were largely sulfuric acid droplets. This is contrasted with Mt. Agung in which the primary component was volcanic ash. Their measurements of the sulfuric acid aerosols indicated that they occurred in a relatively narrow size range with diameters from about 0.08 to 0.45 μm. Particles above this range were primarily lithic and magnetic materials from the volcano. Halite particles were also found and were believed to be from a salt dome that was located beneath El Chichon.

Patterson and co-workers have measured the optical properties of volcanic ash in visible wavelengths for ash from Mt. St. Helens[150] and El Chichon[151] . Their studies indicate that the imaginary component of the refractive index of the ash varies from volcano to volcano. The Mt. St. Helens ash had an imaginary component that decreased from about 0.01 at 0.3 μm to about 0.0015 at 0.7 μm. The corresponding values for the El Chichon ash were nearly constant at 0.001 over the same wavelength range.

Parameters of the Background Stratospheric Aerosol Model

Figure 18 shows the extinction, scattering and absorption coefficients of the improved background stratospheric aerosol model. Table 10 lists the radiative parameters for the model at 215 K. Figures 19 (a) to (d) compare the respective parameters against those developed by Shettle and Fenn[60] and used in earlier versions of LOWTRAN and FASCODE.

The extinction coefficients for the model are smaller than those used by Shettle and Fenn. The differences are greatest for wavelengths longer than 10 μm. The differences are almost entirely due to changes in the absorption coefficient, as shown in Figure 19 (c). The differences in the scattering coefficients and asymmetry parameters are slight.

The changes seen in the new formulation are due almost entirely to the new indices of refraction. Figure 20 compares the extinction coefficients as a function of wavelength of the new model, against those calculated using the proposed indices of refraction and the old modified gamma size distribution, and versus those calculated using the indices of refraction at 300 K and the proposed log normal size distribution. As shown, the change in indices of refraction is responsible for the majority of the differences.

Table 10. Radiative Parameters for the Improved Background Stratospheric Aerosol Model at 215 K. The numbers in parentheses are powers of ten

LAMBDA (μm)	INDEX OF REFRACTION n_r	n_i	EXTINCTION (km^{-1})	SCATTERING (km^{-1})	ABSORPTION (km^{-1})	SINGLE SCATTERING ALBEDO	ASYMMETRY PARAMETER
0.2000	1.526	0.0000	8.5042(-4)	8.5042(-4)	9.9774(-11)	1.000	0.6749
0.2500	1.512	0.0000	8.2526(-4)	8.2526(-4)	7.7618(-11)	1.000	0.6850
0.3000	1.496	0.0000	7.6454(-4)	7.6454(-4)	6.1260(-11)	1.000	0.6943
0.3371	1.484	0.0000	7.0676(-4)	7.0676(-4)	5.3356(-11)	1.000	0.6991
0.4000	1.464	0.0000	5.9964(-4)	5.9964(-4)	4.2364(-11)	1.000	0.7038
0.4880	1.456	0.0000	4.7910(-4)	4.7910(-4)	3.2920(-11)	1.000	0.6944

0.5145	1.454	0.0000	4.4694(-4)	4.4694(-4)	3.0642(-11)	1.000	0.6910
0.5500	1.454	0.0000	4.0980(-4)	4.0980(-4)	2.8160(-11)	1.000	0.6846
0.6328	1.452	0.0000	3.3318(-4)	3.3318(-4)	3.4244(-11)	1.000	0.6694
0.6943	1.452	0.0000	2.8750(-4)	2.8750(-4)	4.1196(-11)	1.000	0.6572
0.8600	1.448	0.0000	1.9352(-4)	1.9352(-4)	2.7574(-10)	1.000	0.6251
1.0600	1.443	0.0000	1.2364(-4)	1.2363(-4)	1.7375(-9)	1.000	0.5861
1.3000	1.432	0.0000	7.3706(-5)	7.3696(-5)	8.6378(-9)	1.000	0.5405
1.5360	1.425	-0.0001	4.6880(-5)	4.6786(-5)	9.4560(-8)	0.998	0.4965
1.8000	1.411	-0.0006	2.8732(-5)	2.8426(-5)	3.0578(-7)	0.989	0.4499
2.0000	1.405	-0.0013	2.0992(-5)	2.0382(-5)	6.1016(-7)	0.971	0.4164
2.2500	1.390	-0.0019	1.4050(-5)	1.3297(-5)	7.5308(-7)	0.946	0.3772
2.5000	1.362	-0.0040	9.6202(-6)	8.2414(-6)	1.3788(-6)	0.857	0.3385
2.7000	1.319	-0.0060	6.9164(-6)	4.9962(-6)	1.9202(-6)	0.722	0.3069
3.0000	1.288	-0.0875	2.7254(-5)	2.9016(-6)	2.4352(-5)	0.106	0.2599
3.2000	1.292	-0.1440	3.9576(-5)	2.6414(-6)	3.6936(-5)	0.067	0.2352

Table 10. (Continued)

LAMBDA	INDEX OF REFRACTION		EXTINCTION	SCATTERING	ABSORPTION	SINGLE SCATTERING	ASYMMETRY
(μm)	n_r	n_i	(km^{-1})	(km^{-1})	(km^{-1})	ALBEDO	PARAMETER
3.3923	1.366	-0.1780	4.4846(-5)	3.3360(-6)	4.1510(-5)	0.074	0.2234
3.5000	1.383	-0.1790	4.3322(-5)	3.2514(-6)	4.0072(-5)	0.075	0.2165
3.7500	1.420	-0.1650	3.6740(-5)	2.9738(-6)	3.3766(-5)	0.081	0.2028
4.0000	1.435	-0.1510	3.1134(-5)	2.5120(-6)	2.8622(-5)	0.081	0.1878
4.5000	1.427	-0.1560	2.7706(-5)	1.6342(-6)	2.6072(-5)	0.059	0.1554
5.0000	1.411	-0.1370	2.1660(-5)	1.0347(-6)	2.0624(-5)	0.048	0.1291
5.5000	1.376	-0.1950	2.7660(-5)	6.9628(-7)	2.6964(-5)	0.025	0.1057
6.0000	1.485	-0.1950	2.3758(-5)	7.4808(-7)	2.3010(-5)	0.031	0.0962
6.2000	1.485	-0.1470	1.7405(-5)	6.2782(-7)	1.6777(-5)	0.036	0.0909
6.5000	1.421	-0.0841	9.9074(-6)	3.8906(-7)	9.5182(-6)	0.039	0.0802
7.2000	1.235	-0.1660	1.8893(-5)	1.2362(-7)	1.8769(-5)	0.007	0.0595
7.9000	1.148	-0.4610	5.0566(-5)	2.5844(-7)	5.0306(-5)	0.005	0.0458
8.2000	1.220	-0.7090	7.2532(-5)	5.4006(-7)	7.1992(-5)	0.007	0.0413
8.5000	1.457	-0.8400	6.8040(-5)	6.9298(-7)	6.7348(-5)	0.010	0.0418
8.7000	1.753	-0.8170	5.0772(-5)	7.0854(-7)	5.0062(-5)	0.014	0.0479
9.0000	1.767	-0.6040	3.6972(-5)	4.7534(-7)	3.6496(-5)	0.013	0.0483
9.2000	1.704	-0.5570	3.5158(-5)	3.8212(-7)	3.4776(-5)	0.011	0.0451
9.5000	1.791	-0.7360	4.0840(-5)	4.6384(-7)	4.0378(-5)	0.011	0.0425
9.8000	2.128	-0.4650	1.9955(-5)	4.3004(-7)	1.9525(-5)	0.022	0.0525
10.0000	2.094	-0.3060	1.3457(-5)	3.5238(-7)	1.3105(-5)	0.026	0.0504
10.5910	1.805	-0.2100	1.0871(-5)	1.7696(-7)	1.0694(-6)	0.016	0.0379
11.0000	1.823	-0.4330	2.0778(-5)	1.8759(-7)	2.0590(-5)	0.009	0.0346
11.5000	2.024	-0.1990	7.9792(-6)	1.7553(-7)	7.8036(-6)	0.022	0.0365
12.5000	1.808	-0.1100	4.7986(-6)	8.6996(-8)	4.7116(-6)	0.018	0.0273
13.0000	1.790	-0.1120	4.7434(-6)	7.1830(-8)	4.6716(-6)	0.015	0.0250
14.0000	1.739	-0.1340	5.4362(-6)	4.8632(-8)	5.3876(-6)	0.009	0.0209
14.8000	1.663	-0.1630	6.6002(-6)	3.3622(-8)	6.5666(-6)	0.005	0.0180
15.0000	1.656	-0.1810	7.2602(-6)	3.1790(-8)	7.2284(-6)	0.004	0.0174
16.4000	1.692	-0.4630	1.6200(-5)	3.2838(-8)	1.6168(-5)	0.002	0.0144
17.2000	2.003	-0.6160	1.5554(-5)	4.4028(-8)	1.5510(-5)	0.003	0.0151
18.0000	2.207	-0.1660	3.5504(-6)	3.4570(-8)	3.5158(-6)	0.010	0.0163
18.5000	2.041	-0.0940	2.2486(-6)	2.5334(-8)	2.2232(-6)	0.011	0.0141
20.0000	1.895	-0.0558	1.3897(-6)	1.4947(-8)	1.3747(-6)	0.011	0.0111
21.3000	1.809	-0.1460	3.6235(-6)	1.0301(-8)	3.6128(-6)	0.003	0.0094
22.5000	1.942	-0.1870	3.9294(-6)	1.0351(-8)	3.9190(-6)	0.003	0.0090
25.0000	1.993	–0.0274	5.0360(-7)	7.0124(-9)	4.9658(-7)	0.014	0.0075
27.9000	1.916	-0.0221	3.8602(-7)	4.0356(-9)	3.8198(-7)	0.010	0.0058
30.0000	1.866	-0.0259	4.3630(-7)	2.7856(-9)	4.3352(-7)	0.006	0.0049
35.0000	1.856	-0.0315	4.5664(-7)	1.4768(-9)	4.5516(-7)	0.003	0.0036
40.0000	2.093	-0.1310	1.3585(-6)	1.2212(-9)	1.3573(-6)	0.001	0.0031
50.0000	2.163	-0.2380	1.8508(-6)	5.5384(-10)	1.8503(-6)	0.000	0.0020
60.0000	2.163	-0.2630	1.7005(-6)	2.6910(-10)	1.7002(-6)	0.000	0.0014
80.0000	2.156	-0.2760	1.3442(-6)	8.4884(-11)	1.3441(-6)	0.000	0.0008
100.0000	2.173	-0.2610	1.0032(-6)	3.5132(-11)	1.0032(--6)	0.000	0.0005
150.0000	2.183	-0.1720	4.3904(-7)	6.8248(-12)	4.3902(-7)	0.000	0.0002
200.0000	2.176	-0.1070	2.0646(-7)	2.1174(-12)	2.0646(-7)	0.000	0.0001
300.0000	2.179	–0.0386	4.9588(-8)	4.1658(-13)	4.9588(-8)	0.000	0.0001

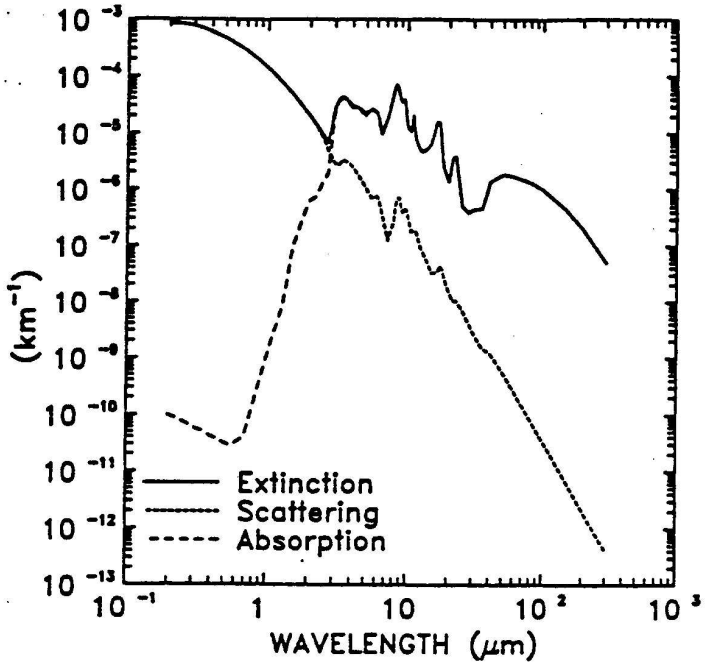

Figure 18. Extinction, Scattering and Absorption Coefficients as a Function of Wavelength for the Improved Background Stratospheric Aerosol Model

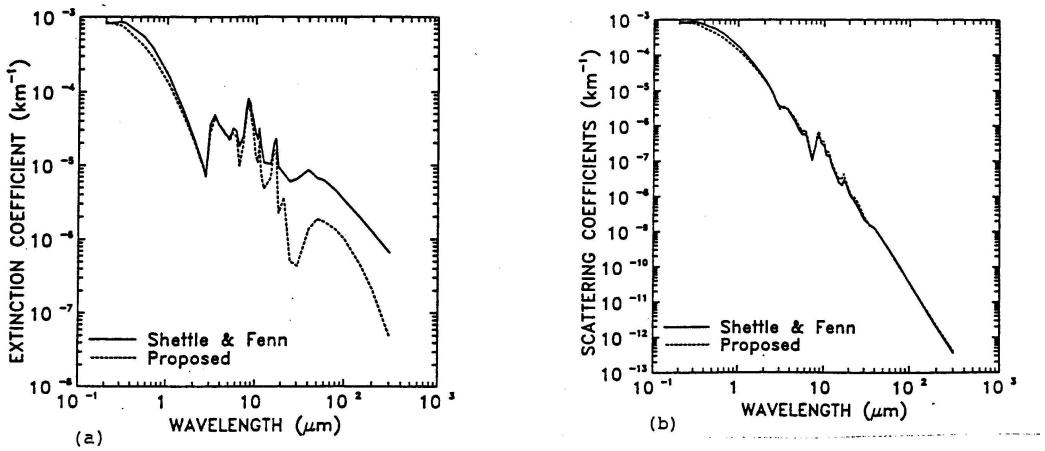

Figure 19. Comparison of the Improved Background Stratospheric Aerosol Model and that in Shettle and Fenn (a) Extinction Coefficients, (b) Scattering Coefficients, (c) Absorption Coefficients, and (d) Asymmetry Parameter

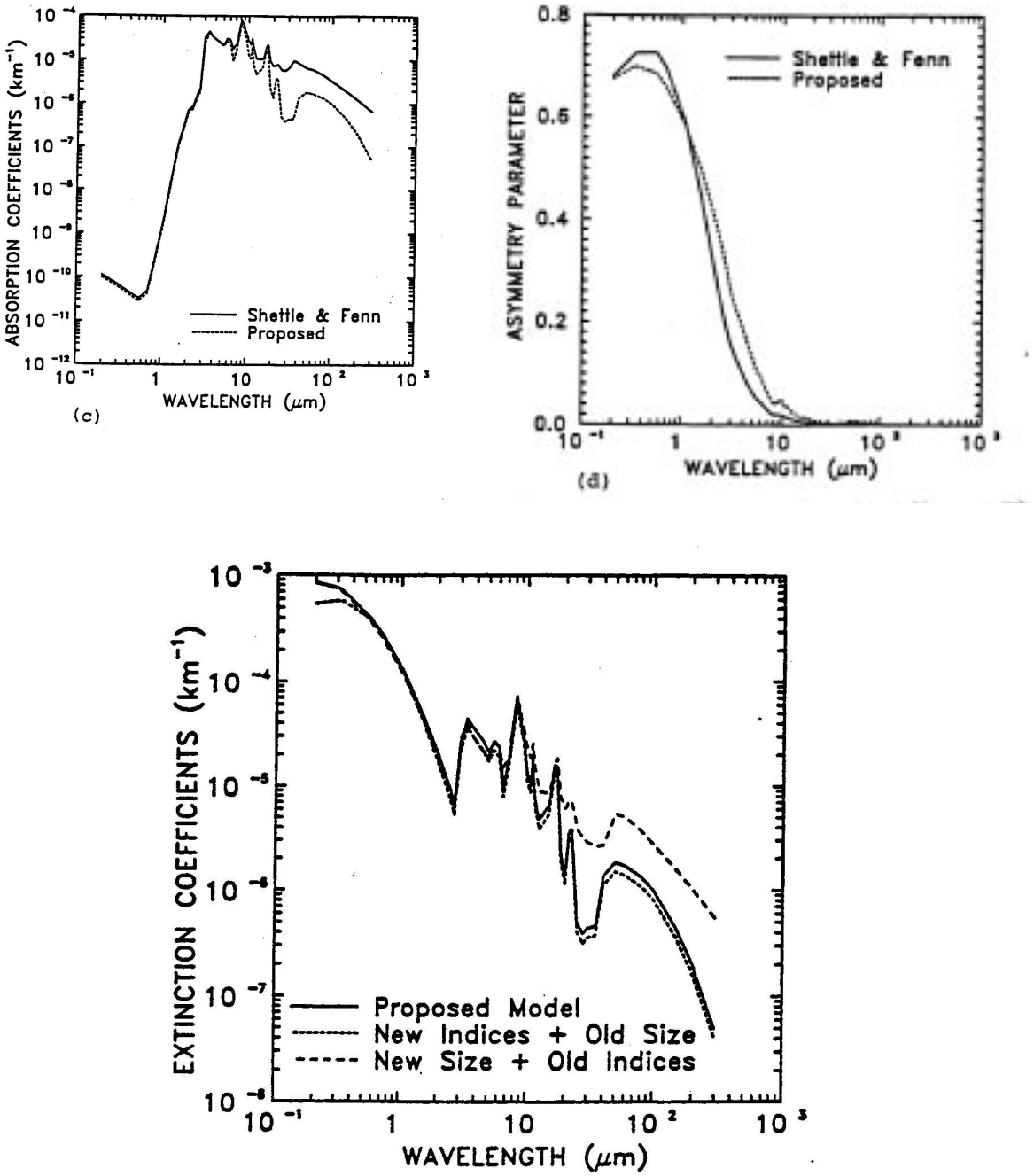

Figure 20. Extinction Coefficients as a Function of Wavelength for the Model (Solid Line), Calculated Using the New Indices of Refraction and the Modified Gamma Size Distribution (Dotted Line) and Calculated Using the Indices of Refraction at 300 K and the Proposed Log Normal Size Distribution

2.3.4.2 Volcanic Aerosol Models

There are two volcanic size distribution models: a "fresh volcanic model" which represents the size distribution of aerosols shortly after a volcanic eruption; and an "aged volcanic model" representing the aerosols about a year after an eruption. Both size distributions were chosen mainly on the basis of Mossop's[152] measurements following the eruption of Mt. Agung.

The refractive index for these models is based on the measurements of Volz[72]. The resulting normalized extinction and absorption coefficients for these two models are shown in Figure 21.

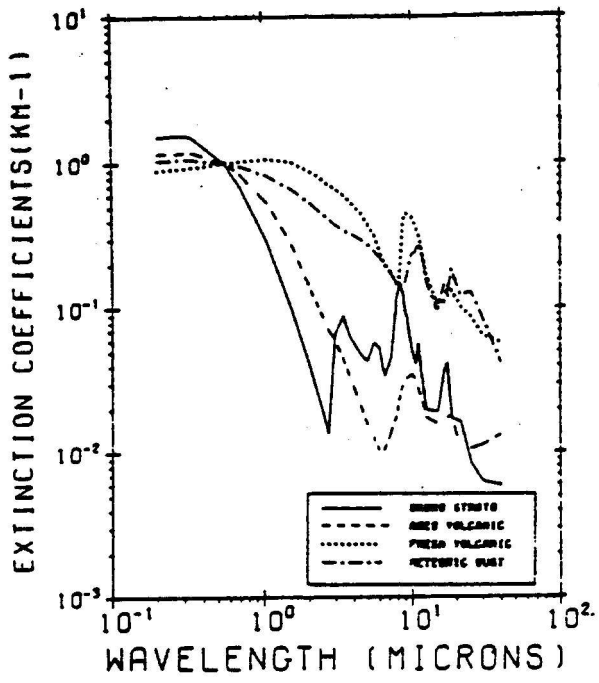

Figure 21a. Extinction Coefficients for the Upper Atmospheric Aerosol Models (Normalized to 1. 0 at 0.55 μm)

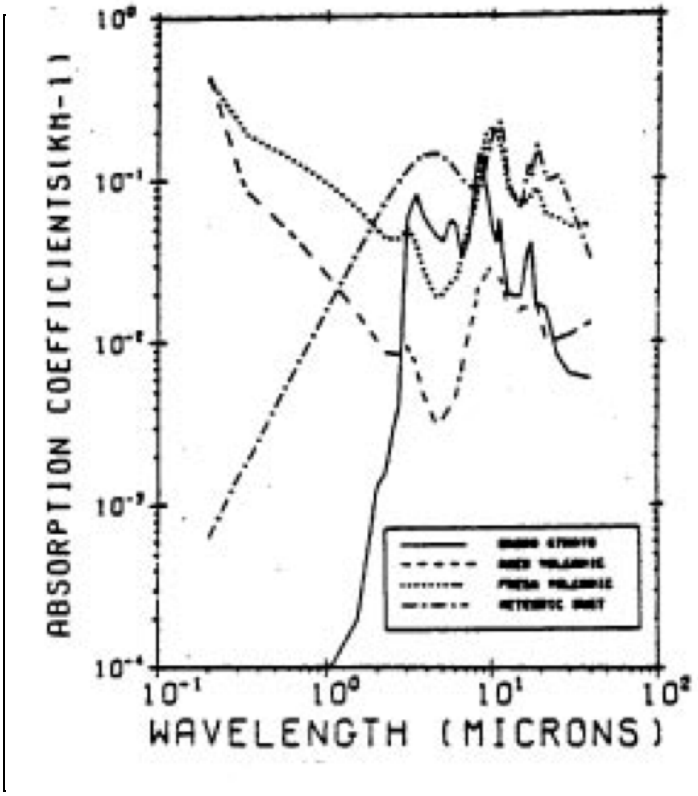

Figure 21b. Absorption Coefficients for the Upper Atmospheric Aerosol Models Corresponding to Figure 21a.

2.3.4.3 Upper Atmosphere Aerosol Model

The major component of the normal upper-atmospheric aerosols is considered to be meteoric dust, which is consistent with the conclusions reached by Newkirk and Eddy[153] and later Rosen[154] in his review article. meteoric or cometary dust also form some of the layers occasionally observed in the upper atmosphere. Poultney[117,155] has related the lidar observations of layers in the upper atmosphere either to cometary sources of micro-meteoroid showers or noctilucent cloud observations. Divari et al[156] have related observations of increased brightness of the twilight sky to the Orinid meteor shower.

The refractive index of meteoric dust is based on the work of Shettle and Volz[157] who determined the complex refractive index for a mixture of chondrite dust which represents the major type of meteorite falling on the earth. [158]

The size distribution is similar in shape to the one developed by Farlow and Ferry[159] by applying Kornblum's[160,161] theoretical analysis (of the micro-meteoroid interaction with the atmosphere and their resulting concentration In the mesosphere) to the NASA[162] model of the meteoroid influx on the atmosphere. There are two important differences between the present size distribution model and Farlow and

Ferry' s.[159] First, the present model has proportionately more smaller particles, and second, the number densities for all size ranges are several orders of magnitude larger than in Farlow and Ferry' s[159] model. These differences are consistent with rocket observations in the upper atmosphere.[159,163,164]

The normalized extinction and absorption coefficients for this meteoric dust model for the aerosols of the upper atmosphere are shown in Figure 21 as a function of wavelength.

2.3.5 Use of the Aerosol Models

The aerosol models defined in this report are representative of various general types of environments. Yet, the simple question: "Which model should be used for what location and weather situation?" is difficult to answer precisely. Some discussion on this point is necessary to give the user some guidance in choosing the appropriate model for a given condition.

2.3.5.1 Boundary Layer Models

For the boundary layer of the atmosphere up to 1 to 2 km above the surface, the composition of the aerosol particles is primarily controlled by sources (natural and man-made) at the earth' s surface. The aerosol content of the atmosphere at a given location, will therefore depend on the trajectory of the local airmass during the preceding several days, and the meteorological history of the airmass. The amount of mixing in the atmosphere is controlled by the temperature profile and the winds. Precipitation will tend to wash the aerosols out of the atmosphere, although it should be noted that "frontal showers" often mark the boundary between two different air masses with generally different histories and correspondingly different aerosol contents.

The "rural" and the "urban" model are intended to distinguish between aerosol types of natural and man-made origin over a land area. Clearly, the man-made aerosol will be predominantly found in urban-industrial areas. However, it is quite likely that after the passage of a cold front, clear polar air also covers an urban area and that therefore the rural aerosol model, which is free of the component of industrial-carbonaceous aerosols, is more applicable. After a few days, as the clean airmass begins to accumulate local pollution , the urban model will once again become more representative.

Conversely, very often the pollution plume from major urban-industrial areas may, under stagnant weather conditions, diffuse over portions of a continent (for example, Central Europe, Northeastern United States), including its rural sections.

There is also a distinct difference between the composition of aerosols over the ocean and those over land areas due to the different surface-based sources. Aerosols in maritime environments have a very pronounced component of sea-salt particles from the sea water. Sea-salt particles are formed from sea spray from breaking waves. The larger particles fall out, but the smaller particles are transported up with the atmospheric mixing in the boundary layer. In coastal regions the relative proportions of particles of continental and oceanic origins will vary, depending on the strength and direction of the prevailing winds at time of observation.

While changes in visibility are often associated with changes in the relative humidity, (as the relative humidity approaches 100 percent the visibility tends to decrease), it is not possible to define a unique functional relationship between the visibility and relative humidity in the natural atmosphere. The reason for this is that any change in atmospheric moisture content is generally also associated with a change in the aerosol population itself due to change of the airmass. Only if the aerosol is contained in a closed system, where only the humidity changes, can such a unique relationship be developed. The measurements presented by Filippov and Mirumyants[165] clearly illustrate the difficulties in defining a simple unique expression relating visibility and relative humidity.

2.3.5.2 Desert Aerosol Model

The desert aerosol model has a sand component consisting of quartz particles and quartz particles contaminated with a 10% concentration of hematite. The 0 ms^{-1} wind speed is representative of background desert conditions, while a wind speed of 30 ms^{-1} would represent dust storm conditions. Wind speeds greater than 0 and less than 30 ms^{-1} are representative of conditions between these two extremes.

A number of important features of this model are worth commenting on. First there is selective absorption at visible wavelengths which becomes more pronounced as the wind speed increases. The selective absorption is due to the hematite in the sand component and will make the desert aerosol appear slightly reddish in color during dust storm conditions. The carbonaceous particles contribute very little to the total absorption of visible radiation primarily because their abundance is too small.

Another important consideration is the structure of the IR absorption. The peaks in the absorption near 3, 7 and 9 μm for 0 ms^{-1} wind speed conditions are primarily due to the strong absorption bands of ammonium sulfate. For dust storm conditions however, the absorption in the IR is dominated by the sand component. Interestingly, there are minima in the absorption and maxima in the scattering near 8 and 20 μm,

which correspond to the centers of the strong crystal lattice absorption bands of quartz. It is believed that this phenomenon is a result of the quartz in the sand component acting as a reflector. To show this, consider an electromagnetic wave propagating in air as it encounters a plane boundary having a complex index of refraction, m = n + ik. For normal incidence, the reflectance is given by:

$$\text{Reflectance} = \frac{(n-1)^2 + k^2}{(n+1)^2 + k^2} \quad . \tag{31}$$

When n « 1, n » 1 or k » 1 (as is the case for the absorption bands of quartz), the reflectance approaches 1.0. Thus the incident radiation is reflected and the absorption drops because the incident wave cannot penetrate the material to be absorbed.

Another point to consider is that the extinction is wavelength dependent for winds of 0 ms^{-1} but nearly constant at 20 and 30 ms^{-1}. These differences are driven by the relative contributions of the aerosol components. For winds of 0 ms^{-1} , only the smaller water soluble particles with respect to the wavelength dominate the extinction at visible and near IR wavelengths and, therefore, a wavelength dependence exists. On the other hand, in high wind speed conditions, the extinction is dominated by the much larger sand particles that approach the geometric optics regime.

The single scattering albedo at the UV and shorter visible wavelengths decrease significantly as the wind speed increases. This effect becomes less pronounced for the longer visible and near IR wavelengths. In the middle IR region, single scattering albedos for 0 and 30 ms^{-1} winds exhibit a high degree of structure. Specifically, sharp minima occur near 3, 7 and 9 μm, which can be attributed to absorption by ammonium sulfate. For winds exceeding 30 ms^{-1} , large peaks occur near 9 and 20 μm which is caused by excess scattering by the quartz in the sand component. Beyond 40 μm, single scattering albedos for 0 ms^{-1} winds are much lower than those for winds of 30 ms^{-1} . This should not be interpreted as significant absorption, since the magnitude of the absorption is small beyond 40 μm for lighter winds.

Generally speaking, the asymmetry parameter values as a function of wavelength are greater for dust storm conditions than those for background conditions throughout the 0.2 to 300 μm region. This is not surprising because the scattering for dust storm conditions is dominated by the large sand particles (with respect to the wavelength of radiation) which have their scattering peaked in the forward direction.

2.3.5.3 Tropospheric Aerosol Model

The tropospheric aerosol model has been developed primarily for application in the troposphere, above the boundary layer, where the aerosols are not as sensitive to local surface sources. However, the tropospheric model should be used near ground level for particularly clear and calm conditions (in pollution free areas with visibilities greater than 30 to 40 km), where there has been little turbulent mixing for a period of 1 to 2 days, permitting the larger particles to have settled out of the atmosphere without being replaced by dust, blown into the air from the surface. (The sedimentation rate of a 10-μm radius aerosol particle in the lower troposphere is approximately 1 km per day.)[166]

2.3.5.4 Fog Models

The fog models described in Section 2.3.3.5 were presented in terms of the atmospheric conditions leading to the development of the fog, so this provides a good basis for deciding which fog model to use. In more general terms, the visibilities will be less than 200 meters for thick fogs and the extinction will be virtually independent of wavelength. For these conditions the advection fog model should be used. For light to moderate fogs, the visibility will be 200 to 1000 meters and there will be a noticeable difference between the extinction for visible wavelengths and in the 8- to 12-μm window. For these cases the radiatlon fog model should be used. For thin fog conditions where the visibility may be 1 to 2 km, the 99 percent relative humidity aerosol models may represent the wavelength dependence of the atmospheric extinction as well as any of the fog models.

2.3.5.5 Stratospheric and Upper Atmospheric Models

At irregular intervals (on the order of years) there are volcanic eruptions which inject significant amounts of aerosols into the stratosphere. For the first few months following such an eruption the fresh volcanic size distribution model would generally be the best one to use, and for the next year or so after that the aged volcanic size distribution model should be used. Under generally inactive volcanic periods, the background stratospheric model would be appropriate.

The choice of which vertical distribution profile to use would depend on the severity of the volcanic eruption and how long ago it was. The moderate volcanic profile is representative of the stratospheric conditions throughout the Northern Hemisphere during the mid and late 1960' s following the eruption of Mt. Agung. It is also typical of conditions during late 1974 and 1975 after the Volcan de Fuego eruption. This profile

is also representative of conditions following the eruption of Mt. Pinatubo in June 1991 and continuing into mid 1993.

The high and extreme volcanic models are somewhat speculative as there have been no direct measurements of the vertical distribution of aerosol for such conditions. They are however consistent with the total optical thickness for aerosols inferred shortly after several major volcanic eruptions,[108,109,167] such as Katmai and Krakatoa, as well as the effects of Mt. Agung in the Southern Hemisphere.

Enhanced Aerosols After a Volcanic Eruption

A volcanic eruption will increase the numbers and size distribution of sulfuric acid particles as a result of SO_2 injections into the stratosphere. The specific impact on aerosol loading in terms of size distribution and mixture of H_2SO_4 and water will vary from eruption to eruption.

Figure 22 shows the extinction coefficients for stratospheric aerosols that have been "enhanced" by the chemical production and sedimentation of sulfuric acid particles. The calculations were based on the sum of two log normal size distributions based upon the work of Oberbeck et al.[145] following the eruption of El Chichon. The first distribution represents an enhanced background and has a particle density of 6 cm^{-3}, mode radius of 0.14 μm and a standard deviation of 1.72. The second distribution results from the sedimentation of smaller particles and is represented by a particle density of 1.5 cm^{-3}, a mode radius of 0.54 μm and a standard deviation of 1.22. The calculations were done with the proposed indices of refraction at 215 K and those at 300 K.

Both curves show a nearly flat response as a function of wavelength up to about 1.0 μm. Significant differences between the curves do not begin to appear until beyond 20 μm as a result of the differences in the imaginary component of the indices of refraction.

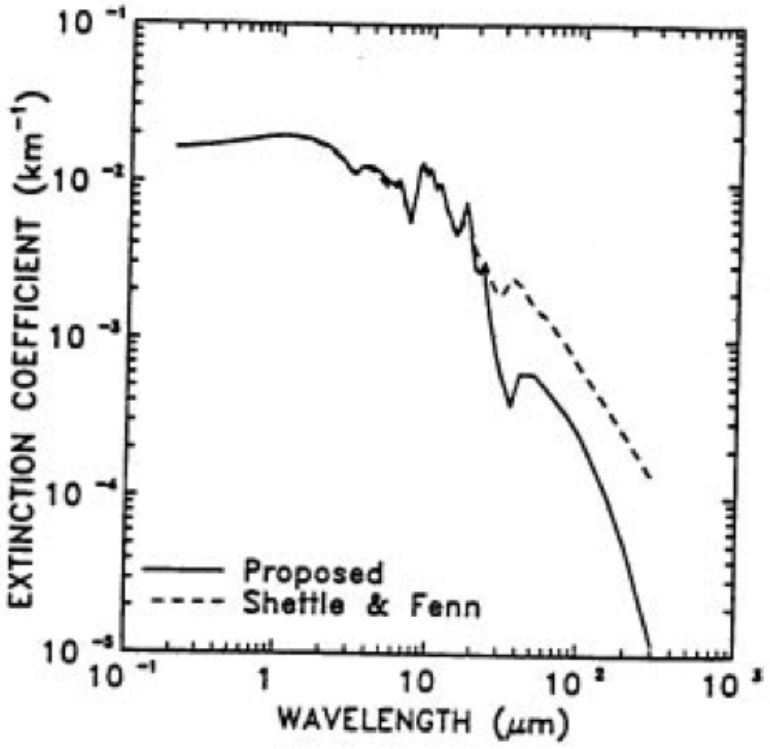

Figure 22. Extinction Coefficients as a Function of Wavelength for a Postulated Enhanced Stratospheric Aerosol Layer

2.3.5.6 Seasonal and Latitude Dependence of Aerosol Vertical Distribution

In the mid-latitudes as the names suggest, the spring-summer aerosol vertical profiles are intended to be used during the spring and summer seasons and the fall-winter profiles used during the fall and winter seasons. However, the seasonal changes in aerosol distribution are partially a reflection of the changes in the tropopause height (especially for stratospheric aerosols). So in the tropical regions where the tropopause is generally higher, it is recommended that the spring-summer aerosol profile be used. Analogously, in the subarctic regions where the tropopause is lower, it is recommended that the fall-winter profile be used.

2.3.5.7 Remarks on Applicability of the Aerosol Models

Typical conditions for which the different aerosol models apply as discussed in detail above are summarized in Table 11. However, it must be emphasized that these models only represent a simplified version of typical conditions. It is not practical to include all the details of natural aerosol distributions nor are existing experimental data sufficient to describe the frequency of occurrence of the different conditions. While these aerosol models were developed to be as representative as possible of different

atmospheric conditions, it should be kept in mind that the "rural" aerosol model does not necessarily exactly reproduce the optical properties in a given rural location at a specific time and date, any more than the mid-latitude summer model atmosphere would exactly reproduce the actual temperature and water vapor profiles for that same specific time and location.

Table 11. Typical Conditions for Aerosol Model Applications

1. Lower Atmospheric Models

1.1 Rural Model
- 1) Natural environment, midlatitude, overland.
- 2) Clean air in urban regions, following passage of a cold front.

1.2 Urban Model
- 1) Urban industrial aerosol.
- 2) Stagnant polluted air extending into rural regions.

1.3 Maritime Model
- 1) Mid-ocean (at least 300 km offshore) with moderate winds (above the first 10 to 20 meters).
- 2) Continental areas under strong prevailing wind from the ocean.

1.4 Tropospheric Model
- 1) Atmospheric region between top of boundary layer (approximately 2 km) and tropopause (8-18 km, depending on latitude and season).
- 2) Clean, calm air (meteorological range--40 km) in surface layer over land.

1. 5 Fog Models

1. 5.1 Advective Fog
- 1) Mixing of air masses of different moisture content and temperature, leading to saturation.
- 2) Lacking specific knowledge on the formation process, for mature fogs with meteorological range: $V \leq 200$ meters.

1. 5.2 Radiation Fog
- 1) Radiational cooling knowledge of the air to the dew point at night.
- 2) Lacking specific knowledge on the formation process, for developing fogs or meteorological ranges: $200 \leq V \leq 1000$ *meters*

1. 5.3 99 Percent Relative Humidity Aerosol Models
- 1) Light fogs ($1 \leq V \leq 2$ km).

2. Stratospheric and Mesospheric Aerosol Models

2. 1 Background Stratospheric Model

For time periods without any direct influence of volcanic dust contamination, for example, 1977 to 1980.

2.2 Moderate Volcanic Profile with Fresh Particle Size Distribution

For optical thickness approximately 0.03, up to a few years after eruption, for example, Northern Hemisphere, 1964 to 1968.

2.3 High Volcanic Profile and Fresh or Aged Particle Size Distribution
For optical thickness approximately 0. 1, up to a few months after eruption, for example, Southern Hemisphere. 1964-1965.

2.4 Extreme Volcanic Profile with Fresh Particle Size Distribution
For optical thickness approximately 0.3 or higher, up to a few weeks after a major eruption, for example, 1883 (Krakatoa) or 1912 (Katmai).

2.3.6. NAVY Maritime Aerosol Model

This chapter provides a brief description of the Navy maritime aerosol model and its implementation in MODTRAN. A complete discussion of the model is given by Gathman[38]. Since this model includes an explicit dependence on wind speed it is recommended that it be used instead of the maritime model, (developed for earlier versions of LOWTRAN) which assumed moderate wind speeds (see Shettle & Fenn)[60]. The latter model is retained in MODTRAN for comparison purposes.

2.3.6.1 Description of the Model

The aerosol population found over the world' s ocean is significantly different in composition and distribution from that of a continental origin. These aerosol are largely derived from the sea. They are produced by the evaporation of sea spray and from jet and film droplets. Jet droplets are ejected into the air by the bursting of small air bubbles at the sea surface. The bursting of the bubble film leaves behind many smaller film droplets that may also be diffused into the air. These mechanisms are wind dependent and require white water phenomenon in order to produce aerosol.

Once the aerosol droplets are airborne, they undergo additional sorting and mixing processes. The marine boundary layer is usually capped by a temperature inversion and, within this boundary layer, the smaller marine aerosol together with any background aerosol form a fairly uniform aerosol spatial distribution. Once introduced into the atmosphere, the lifetime of an aerosol particle is dependent on the size of the particular aerosol particle. Those with very small sizes have a very long residence time in the boundary layer if there are no washout processes taking place. On the other hand, those with very large sizes have a short residence time and do not contribute to the stationary long-term aerosol population.

The Navy maritime aerosol model differentiates between these various types of aerosol by postulating that the marine atmosphere is composed of three distinct populations, each of which is described by a log normal size distribution. The parameters that describe the analytical form of the size distribution are then related to both recent meteorological history and current meteorological observations .

The smallest component of the model is a continental component. This is the background aerosol and although it apparently has little to do with current wind parameters, it is dependent on the elapsed time required for the air mass to traverse the sea from the continent to the point of observation. Quantification of this component in terms of routine meteorological measurements is difficult, but for convenience an integer from 1 to 10 is used to specify the ICSTL parameter, which gives a qualitative indication of the continental contribution: a value of 1 representing relatively pure maritime aerosol, and a value of ICSTL = 10 meaning a significant continental component.

The second component, the stationary component of the maritime aerosol, is the part of the maritime aerosol that depends on the current and past history of the wind and represents that portion of the spectra that are produced by the high wind and white water phenomenon but do not fall out rapidly. The amplitude of this component is related to the average wind speed over the past 24 hours, and is specified by the WHH parameter.

The third or "fresh" component of the Navy aerosol model is a log normal population of aerosol that is related to the current wind speed (specified in the program by the WSS parameter). The amplitude of this component is a function of the current wind speed and reflects the current action of the production of drops produced by white water as a result of wind wave actions.

The amplitudes of both the second and third components of the aerosol population reflect the necessity of wind speed being above a certain minimum value before white water phenomena are observed and thus, marine aerosol produced. This minimum value is 2.2 m/s.

The model is also responsive to the current relative humidity. It is well known that particles composed of sea salt are hygroscopic and change their composition and size as a function of the relative humidity. The model uses the "swelling factor ' proposed by Fitzgerald[168], which adjusts the mode radii of the three components of the model, but does not alter the total number of particles that are airborne. The model also adjusts the complex index of refraction of the aerosol based on the volume weighted method of Hãnel[169], using the refractive index of soluble aerosol (Volz)[77] for the dry component and that of pure water from Hale and Querry.[70]

2.3.6.2 Use of the Navy Maritime Model

As discussed in the preceding section, this model requires three parameters to be specified in addition to those used by the other aerosol models (that is visibility and

relative humidity). These additional parameters are: (1) ICSTL, which indicates the degree of continental influence, (2) WHH, the average wind speed over the past day, and (3) WSS, the current wind speed. The MODTRAN program will use default values for any unspecified parameter.

Three methods can be used to estimate ICSTL. The first is by plotting the airmass trajectory and determining the elapsed time, t, since the air parcel left land. This time is related to ICSTL by the following empirical equation:

$$ICSTL \quad = \quad INT\left(9\exp\left[-t\,(days)/4\right]+1\right) \quad , \tag{32}$$

where INT(x) truncates to the nearest integer less than x.

Secondly, if measurements of the current radon 222 concentrations in the atmosphere are available (Larson and Bressan)[171], then the air mass parameter can be estimated by the formula:

$$ICSTL \quad = \quad INT\left(Rn/4\right)+1 \quad , \tag{33}$$

where Rn is the concentration of radon 222 in pCi/m^3 . This relationship can be used because radon 222 is introduced into the atmosphere only by processes occurring over land. Therefore, since this radioactive substance has a half-life of 3. 86 days, the concentration of radon 222 is then related to the time since the air parcel left the land.

A third method for determining ICSTL consists of subjectively choosing an integer between 1 and 10 to determine the "quality" of the air mass, with a value of "1" being for pure oceanic air and a value of "10" if the air has recently been ashore over a polluted industrial area. Values in between can be used to specify the various grey areas between these two extremes. If the user does not input a value for the parameter ICSTL, the LOWTRAN code will use a default value of ICSTL = 3.

The current wind speed, WSS, and the average wind speed over the past 24 hours, WHH, should be input in units of m/s. If the average wind speed is input as 0 or is given a negative value, a default value will be chosen that depends on the model atmosphere being used, (specified by the parameter MODEL). These default wind speeds are shown in Table 12. The default wind speeds are based on average values for observations made in the indicated region, except for the user-defined cases (MODEL = 0 or 7), which use a global mean value. If the current wind speed, WSS, is not specified, it is set equal to the average wind speed, WHH.

Table 12. Default Wind Speeds for Different Model Atmospheres

MODEL	Model Atmosphere	Default Wind Speed (m/s)
0	User-defined (Horizontal Path)	6. 9
1	Tropical	4. 1
2	Midlatitude summer	4. 1
3	Midlatitude winter	10.29
4	Subarctic summer	6.69
5	Subarctic winter	12.35
6	U S. Standard	7.2
	User-defined	6.9

Visibility observations at sea are usually only estimates because of the lack of targets at fixed distances from the observer. Therefore, it is suggested in the use of this model that, unless visibility is measured accurately, the default visibility condition be used. This is important because user-specified visibility inputs adjust all of the extinction and absorption coefficients in the calculations in order to force the calculated extinction at 0. 55 μm to agree with the visibility and, if inaccurate, may introduce excessive error into the calculations.

The Navy model is designed to operate accurately within certain limits of input parameters. While parameter values outside of these limits are permitted by the overall MODTRAN 2 program, the accuracy of the predictions outside of these limits is reduced. The design limits of the model parameters are:

50 percent ≤ Relative Humidity ≤ 98 percent

0 m/s ≤ WSS ≤ 20 m/s

0 m/s ≤ WHH ≤ 20 m/s, and

0. 8 km ≤ VIS ≤ 80 km .

For relative humidities or wind speeds outside these design limits the program will internally reset the value to the nearest limit, rather than try to extrapolate the aerosol properties.

2.3.6.3 Sample Calculations with the Navy Model

This section briefly presents some sample results of transmittance calculations using the Navy maritime aerosol model. Figure 23 shows the transmittance for a 10-km horizontal path at the surface, for each of the standard model atmospheres in MODTRAN. These calculations were all done using the default values for all the parameters. Thus, ICSTL was set to 3, the wind speed depended on the model atmosphere (see Table 12), and the maritime aerosol model calculated the visibility

based on the aerosol properties with these parameter values and the relative humidity for the model atmosphere. The values of the parameters for these different cases are summarized in Table 13.

The differences in the transmittances shown in Figure 23 are due both to variations in the aerosol properties for different atmospheric conditions and to the different amounts of water vapor in the various model atmospheres. The transmittance in the 3 through 5 μm (2000 through 3300 cm^{-1}) window is more sensitive to changes in the aerosol properties and in the 8 through 13 μm (750 through 1250 cm^{-1}) window, the transmittance is more sensitive to the variations in the water vapor.

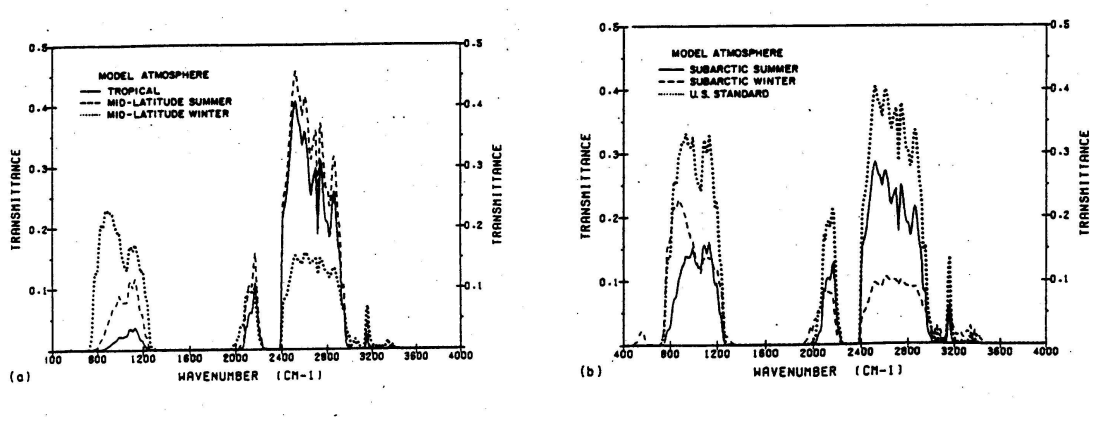

Figure 23. Atmospheric Transmittance for a 10-km Horizontal Path at the surface with the Navy Maritime Aerosol Model. (a) for the tropical, midlatitude summer, and midlatitude winter model atmospheres and (b) for the subarctic summer. subarctic winter, and U. S. Standard atmospheres.

Table 13. Conditions for Sample Runs of the Navy Maritime Aerosol Model

MODEL	Atmosphere	Wind (m/s)	Rel Hum (percent)	Vis (km)	ρH_2O (gm/m^3)
1	Tropical	4.10	73	49.4	19.0
2	Midlatitude summer	4.10	70	52.2	14.0
3	Midlatitude w inter	10.29	71	17.8	3.5
4	Subarctic summer	6.69	72	28.3	9.1
5	Subarctic winter	12.35	73	14.2	1.2
6	U. S. Standard	7.20	49	39.5	5.9

2.3.7 ARMY Veritcal Structure Algorithm

2.3.7.1 Introduction

An algorithm for modeling the vertical structure of aerosols has been added to the MODTRAN 2 code. It was developed initially to describe the vertical distribution of the atmospheric aerosols for conditions of limited visibility and beneath low-lying stratus cloud decks[171]. The formalism has been extended so it can also represent cases with no cloud ceiling and moderate to high visibility[172]. The algorithm will generate the vertical aerosol profile within the boundary layer from input parameters, such as surface visibility and the cloud ceiling height. This model is designed for use within the lowest 2 km of the atmosphere.

2.3.7.2 The Vertical Profile Model

In low visibility situations, due either to haze or fog, increasing numbers of observations show that the measured visibility at the surface is not representative of conditions a few hundreds of meters, or even tens of meters, above the surface. Thus, the "slant path visibility" can be significantly different from the "horizontal visibility". In a significant fraction of the cases the visibility decreases as the height above the surface increases. These cases are of special concern here.

Detailed data on the vertical structure of fogs and hazes have been gathered in the Federal Republic of Germany on several different occasions.[173,174] Droplet size **distributions** in the 0.5- to 47-μm range have been measured from a balloon-borne instrument, thus yielding vertical profiles.[175] Extinction coefficients at desired wavelengths or the liquid water content can be calculated from these measured droplet size distributions.

The vertical structure of these profiles has been examined previously by Duncan et al,[176] who characterized the vertical structure in the form

$$y = a' x + b' \quad , \tag{34}$$

where $x = \log_{10} k(z)$, $y = \log_{10} k(z + 20)$, a' and b' are coefficients that were chosen to fit the data, and $k(z)$ is the value of the extinction coefficient at the altitude z; $k(z + 20)$ is then the value of this variable at an altitude of $z + 20$ m. Thus, one can work stepwise from the surface up through the cloud boundary layer. Figure 24 shows the fit of Eq. (34) to the data. It should be noticed that there is a sharp change in slope at

a value of about 7.1 km^{-1} for the extinction. The physical significance of this inflection point is discussed below.

The point of intersection of the two line segments physically represents the changes in extinction due to changes in the state of particle growth as one moves from a sub-saturated environment (lower line segment), where relative humidities are less than 100 percent, to a super-saturated environment, (upper line segment). Thus, this point of intersection will be taken to represent the cloud base or lower cloud boundary.

Since $x = \log_{10}\ k(z)$ in Eq. (34) and y is really just $x + \Delta x$ over an altitude interval Δz, the relation for the extinction as a function of altitude can be expressed as[171]

$$k_e(0.55\,\mu m) \quad = \quad A \exp\left[B \exp(Cz)\right] \quad , \tag{35}$$

where A, B, and C are functions of preselected boundary values, the initial or starting value of extinction, and the cloud ceiling height. Note that since there are two straight line segments, the coefficients A, B, and C have different values, depending on which part of the data curve (in Figure 24) is being followed.

The rate at which the extinction changes with altitude below the cloud base actually depends on the cloud ceiling height Zc The lower line segment in Figure 24 represents an average of several sets of data and therefore gives a single, average value for the

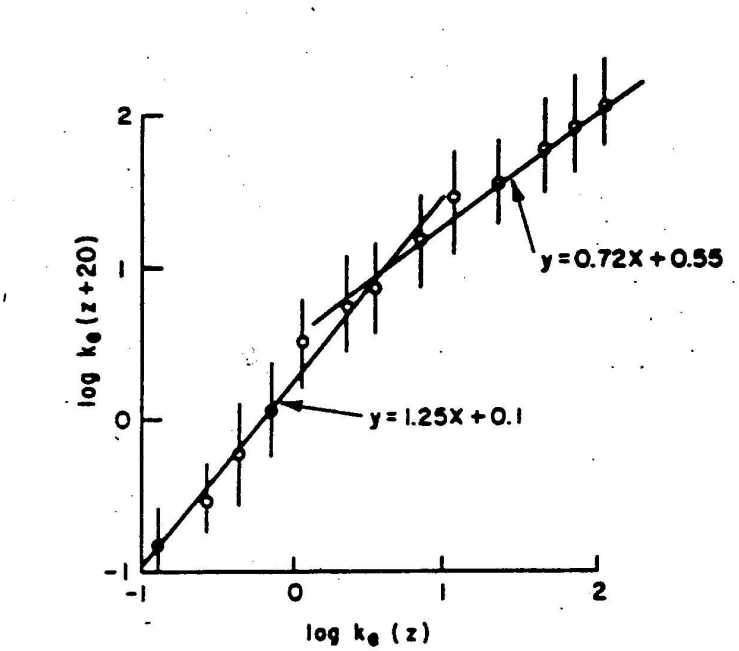

Figure 24. Relationship Between the Extinction Coefficient (at 0.55 μm) at Altitudes z and z + 20 m. The vertical lines are the error bars for the data (after Duncan et al)[176]

coefficient C in Eq. (35). The explicit dependence of C on the cloud ceiling height can be incorporated by defining the coefficient C as

$$C = \frac{1}{z_c} \ln\left[\frac{\ln(E/A)}{\ln(D/A)}\right] , \qquad (36)$$

where E is the value of the extinction at the cloud base, D is the observed value of extinction at the surface, and A is the same coefficient used in Eq. (35). In this case A is the lower limit to the extinction in the hazy/foggy region below the cloud. Figure 25 shows the visible extinction coefficient plotted as a function of altitude for the same initial surface value, but several different cloud ceiling heights. The solid line represents the (average) values from the line segments in Figure 24. The dashed vertical line represents the value of the extinction for the cloud base given by the intersection of the line segments in Figure 24. The solid line to the right of the dashed vertical line represents the extinction profile inside the cloud and can be appended to any one of the vertical profiles to the left.

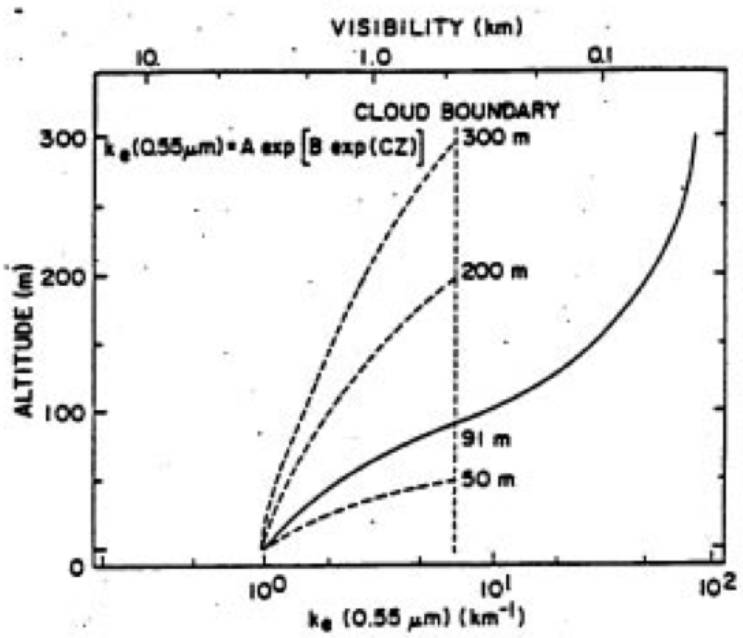

Figure 25. The Vertical Profile of the 0.55-μm Extinction Coefficient for Various Cloud Ceiling Heights. The solid line shows the average profiles from Figure 24, the dashed vertical line represents the value at the cloud boundary

Initially the algorithm for the vertical structure of hazes, fogs, and clouds represented by Eq. (35) was developed for low visibility/low stratus conditions and is based on inputs of the surface meteorological range (extinction coefficient) and the cloud ceiling height. This algorithm has now been extended to cases where there may be no cloud ceiling and where the extinction coefficient decreases with increasing altitude.[172]

2.3.7.3 Applicability of the Vertical Structure Algorithm

Three initial visibility conditions are considered. The first condition is for stratus clouds and thick fogs (which in this instance may be treated as a cloud at the ground); the second condition is for hazes and fog; and the third condition is for the clear to hazy atmosphere. The vertical structure of visibility can be represented by four different types of curves as illustrated in Figure 26. Curves 1 and 2 represent the cases where the extinction coefficient increases (that is, visibility degrades) with increasing altitude; these cases are representative of the vertical structure of extinction for thick fogs or for low visibility/low stratus conditions. Curves 3 and 4 represent cases where the extinction coefficient decreases (that is, visibility improves) with increasing altitude. Each of these cases will now be briefly outlined.

Case 1: This curve is to be used for dense fogs at ground level or when one is at the cloud base or in the cloud. Physically this curve represents the increase in liquid

water content (LWC), and consequently the increase in extinction coefficient and decrease in visibility, of a saturated parcel of air rising at the wet adiabatic lapse rate. This curve should be used only when the initial extinction coefficient (or meteorological range) is in the thick fog/cloud region, shown between the two dashed lines representing boundary values on the right-hand side of Figure 26.

Case 2: This curve is to be used for low visibility conditions beneath the clouds due to haze or fog when there is a low cloud ceiling present.

Case 3: This curve is to be used when there is a shallow radiation fog present or when a haze layer is capped by a distinct (low-lying) temperature inversion. A cloud ceiling is not present.

Case 4: This profile is to be used for cases where there is reasonable vertical homogeneity for visibility in a clear to slightly hazy atmosphere that may have a shallow haze layer near the surface. A cloud ceiling is not present.

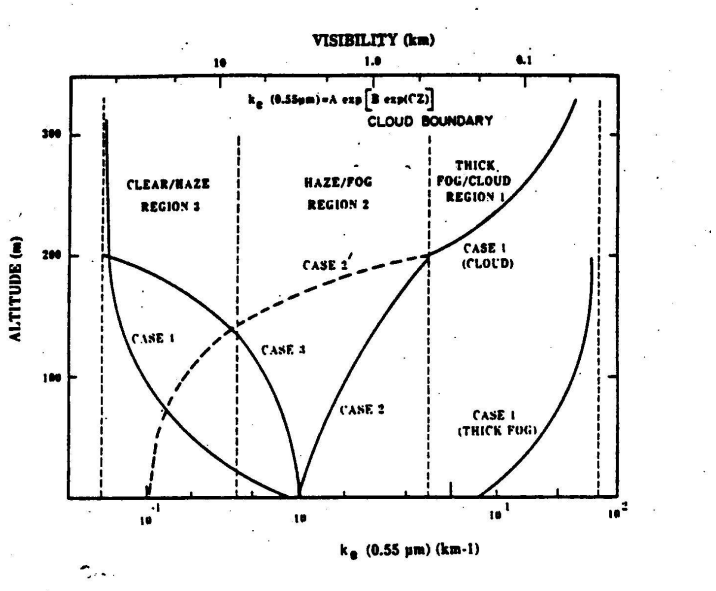

Figure 26. Four Different Cases Represented by the Vertical Structure Algorithm

Profiles of the 0. 55-μm extinction coefficient are shown in Figure 26 for these different cases. Two examples of representative profiles are shown for case 1. The first example is for a thick fog at the surface, which is represented by an extinction coefficient profile that increases with height. When the depth of the fog is not known (which is usually the case because the sky is obscured), a default depth of 200 m is recommended. The second example is for a low-lying stratus cloud; for illustration the cloud ceiling height is taken to be 200 m. This profile should only be used from the

cloud base to the cloud top. Again, cloud thickness is usually not a measured quantity, and a default value of 200 m is recommended. The two examples shown here are actually the same profile, one starting at the surface for the thick fog and the other starting at the cloud base of a low-lying stratus cloud. Within region 1, thick fog/cloud, only profiles of the case 1 type should be used. For a dense, shallow radiation fog, use a profile for case 3 as described below.

A representative profile for the structure beneath a stratus cloud is shown for case 2. In this instance the visibility conditions at the surface are representative of region 2, haze/fog, and the cloud ceiling height is 200 m. The slope and shape of the vertical structure profile beneath the cloud deck are a function of the initial value of the (surface) visibility and the cloud ceiling height. For haze/fog conditions, when a cloud ceiling height less than 2 km is present, a profile of the case 2 type should always be used.

Often a low-lying cloud cover is present when the surface visibility is clear to only slightly hazy. In this instance a vertical structure profile similar to case ' 2 is appropriate. This profile is denoted as case 2 ' and is shown in Figure 26 as an alternate profile for the instance of a 200-m cloud ceiling height. The only difference between case 2 and case 2 ' is the manner of choosing the value of the coefficient A, which in turn influences the shape of the vertical profile.

A shallow radiation fog or a haze layer bounded by a temperature inversion can be represented by a vertical structure profile as shown in Figure 26 for case 3. The boundary layer heights for such occurrences are often difficult to estimate. Temperature inversion heights can be obtained from acoustic sounders or radiosonde observations; often, visual sightings can be used to estimate depths of shallow fogs or haze layers. A nominal boundary layer height of 200 m has been selected for illustrative purposes. For radiation fogs where the depth is not known, a default value of 200 m is selected (a more realistic value for radiation fogs is about 50 m). To override the default value, read in the depth of the radiation fog as 50 m by setting ZINVSA to 0.05 km. For inversion layers where the height of the inversion or boundary layer is not known, a default value of 2 km is selected.

Case 4 is represented by a profile for the condition where the vertical structure is essentially constant with altitude, with the exception of the lowest hundred meters of the boundary layer. An appropriate default value is the nominal background value for the 0.55-μm extinction coefficient for the fair weather case. Numerous observations have shown that the extinction coefficient is essentially constant within the planetary layer for well mixed conditions. Setting the coefficient C equal to zero in Eq. (35) will

cause the algorithm to default to the observed surface value while providing a constant vertical profile.

Table 14 gives the tabular values of the 0.55-μm extinction coefficients that are to be used as boundary values for the different cases in their respective regions of applicability.

Table 14. Summary of the Conditions and Parameter Values for Different VSA Cases k_e (0.55 μm) = A exp [B exp (Cz)]

	Case 1 (B < 0, C < 0)	Case 2 (B > 0, C > 0)	Case 2' (B > 0, C > 0)	Case 3 (B < 0, C > 0)	Case 4 (B > 0, C < 0)
Range of k	7.1 - 92 km^{-1}	0.40 - 7.1 km^{-1}	0.05 - 0.40 km^{-1}	0.05 - 7.1 km^{-1}	0.05 - 7.1 km^{-1}
Region of applicability	thick fog/clouds (ceiling obscured)	haze/fog ceiling < 2000 m	clear/haze ceiling < 2000 m	no ceiling, or ceiling > 2000 m, distinct low-lying inversion or boundary layer	no ceiling, or ceiling > 2000 m, no inversion or boundary layer
Surface visibility (that is, meteorological range)	Visibility ≤ 0.5 km	Visibility ≈ 0.5-10 km	Visibility > 10 km	Visibility > 0.5 km	Visibility > 0.5 km
A	92 km^{-1}	0.40 km^{-1}	0.9 × D	1.1 × D	0.05 km^{-1}*
B	ln (D/A)	ln (D/A)	ln (D/A)	ln (D/A)	ln (D/A)
C	-0.014 m^{-1}	$\frac{1}{Z_c} \ln\left[\frac{\ln(E/A)}{\ln(D/A)}\right]$	$\frac{1}{Z_c} \ln\left[\frac{\ln(E/A)}{\ln(D/A)}\right]$	$\frac{1}{Z_b} \ln\left[\frac{\ln(E/A)}{\ln(D/A)}\right]$	-0.015 m^{-1} (default value)
D	initial value at surface or at cloud boundary (note D < A)	initial value at surface (note D > A)	initial value at surface (note D < 0.4 km^{-1})	initial value at surface (note D < A)	initial value at surface (note D > A)
E	(not used)	7.1 km^{-1}	7.1 km^{-1}	0.05 km^{-1}*	(not used)
Z_c	(not used)**	ceiling height (m)	ceiling height (m)	inversion or boundary layer height (m)	(not used)

*A nominal background value for the lower troposphere.
**When the fog or cloud depth is not known (usually the case), the algorithm should be used only up to 200 m above the surface or cloud boundary (a default value for the stratus cloud thickness).

2.3.7.4 Activation of the Vertical Structure Algorithm

The operation of the Vertical Structure Algorithm (VSA) is controlled by three parameters, in addition to the Meteorological Range at the surface (VIS) and type of aerosol (IHAZE) for the boundary layer. These three additional parameters are: the cloud ceiling height (altitude of the cloud base), the thickness of the cloud or fog, and the height of the inversion or boundary layer, ZCVSA, ZTVSA, and ZINVSA respectively. The type of aerosol vertical profile generated depends on the values input for these parameters. The different cases or profile types selected are summarized in Table 15. Note that the value of ZINVSA will be ignored unless ZCVSA < 0.

The VSA defines the aerosol extinction at nine heights, from the ground to the top of the cloud (ZCVSA + ZTVSA) or the top of the boundary layer (ZINVSA). Ten meters above this cloud-top or boundary-layer level, the aerosol profile reverts to the standard MODTRAN aerosol vertical distribution (or the user-supplied profile for a MODEL = 7 case). For these nine heights the air pressure, temperature, and the ozone concentration are found by interpolation from the model atmosphere indicated by the parameter MODEL (see the Users Guide to LOWTRAN 7[2] Section 10).

If the user is not utilizing MODTRAN' s built-in cloud models (ICLD=1-10), the relative humidity for the MODTRAN model atmospheres does not consider the presence of clouds (that is, all the model atmospheres have RH ≤ 80 percent at all altitudes). The VSA model estimates the relative humidity as a function of the visible (λ = 0.55 μm) extinction for the nine levels:

$$RH\,(z) \;=\; \begin{cases} 86.407 + 6.953 \bullet \ln\left[k_e(z)\right], & k_e < 7.064\ km^{-1} \\ 100\% & , k_e \geq 7.064\ km^{-1} \end{cases} \qquad (37)$$

If the user inputs their own relative humidity profile (MODEL = 7), that will be used instead of Eq. (37).

Table 15. Data Inputs and Default Values for the Different VSA Cases

Case	Selected by	Defaults (Used if the indicated parameter = 0)
1. Fog	VIS ≤ 0.5 km, ZCVSA ≥ 0	ZCVSA = 0, ZTVSA = 0.2 km
2. Haze / light Fog Below Cloud	0.5 < 0=VIS ≤ 10 km, ZCVSA ≥ 0	ZCVSA depends on VIS ZTVSA = 0.2 km
2' .Moderate / high Visibility Below Cloud	VIS > 10 km, ZCVSA ≥ 0	ZCVSA = 1.8 km ZTVSA = 0.2 km

3. Radiation Fog / Haze Layer, No Low Cloud	VIS > 0.5 km, ZCVSA < 0, ZINVSA ≥ 0	ZINVSA = 0.2 RAD FOG
		If (VIS<2.0 km or IHAZE = 9)
		2.0 HAZE
		If(VIS>2.0 km and IHAZE ≠ 9)

4. No Boundary Layer	VIS > 0.5 km, ZCVSA < 0,	

or Low Cloud ZINVSA ≥ 0

2.4 Particulate Extinction

2.4.1. The Rain Model

2.4.1.1 Introduction

The rain model described in this section was chosen because it is able to relate the transmission over a given path to the most directly obtainable meteorological parameter. This parameter is the rain rate in mm/h, reported by worldwide weather stations on a six hourly basis.

The Marshall-Palmer (M-P)[177] raindrop size distribution was chosen because the two main components are rain rate and drop diameter, and the M-P raindrop size distribution is widely accepted in the research community. The M-P distribution is the same one being used in the millimeter region (Falcone et al)[39] by the FASCOD3P (Anderson et al)[178] high-resolution atmospheric transmittance/radiance modeling code.

2.4.1.2 Formulation of the Model

The M-P drop size distribution is given in Eq. (38)

$$\frac{dN}{dD} = n(D) = N_o \exp(-\Lambda D) \quad , \tag{38}$$

where

$$N_o = 8{,}000.\ mm^{-1}\ m^{-3} \tag{39a}$$

$$\Lambda = 4.1\, R^{-0.21} \tag{39b}$$

R = rain rate (mm hr $^{-1}$)

D = drop diameter (mm)

From Mie theory we can write the extinction coefficient, k_{ext}:

$$k_{ext} = \int_0^{\infty} \frac{\pi}{4} D^2 \; Q_{ext} \left[\pi D/\lambda, m(\lambda)\right] \frac{dN}{dD} \; dD \quad , \tag{40}$$

where Q_{ext} is the Mie Extinction Efficiency, λ is the wavelength, and $m(\lambda)$ is the complex refractive index of water. Since for rain 0. 1 < D < 5 mm, in the visible and infrared we have (D >> λ). Therefore, $Q_{ext} \approx 2$, independent of the wavelength. Using this assumption and Eq. (38) in Eq. (40) we have:

$$k_{ext} \approx \frac{\pi}{2} \; N_o \int_0^{\infty} D^2 \exp\left(-\Lambda D\right) dD \quad . \tag{41}$$

Carrying out the integration, this simplifies to:

$$k_{ext} \approx \pi \; N_o \; \Lambda^{-3} \quad . \tag{42}$$

Substituting Eq. (39) in Eq. (42) yields:

$$k_{ext} \approx 0.365 \; R^{0.63}\left(km^{-1}\right) \quad . \tag{43}$$

We should note here that this derivation shows that the extinction due to rain is independent of wavelength, assuming

$$\lambda << D \approx 0.1 \, to \, 10 \, mm \, .$$

In practice this assumption applies throughout the visible and the IR windows. The transmittance over path length, s, in km, can be written as

$$\tau = \exp\left(-ks\right) \quad , \tag{44}$$

or using Eq. (43)

$$\tau = \exp\left(-0.365 \, R^{0.63} \, s\right) \quad . \tag{45}$$

It should be recognized that the extinction [Eq. (43)] or transmittance [Eq. (45)] measured by a transmissometer will, in general, have to be corrected for forward scattering effects. However, since this correction is a function of the receiver and

source geometries it is beyond the scope of the current MODTRAN model. A discussion of this correction is given by Shettle et al[179].

2.4.1.3 Other Raindrop-Size Distributions

Several researchers have attempted to relate the parameters in the exponential raindrop size distribution to the type of rainfall (for example, Joss and Waldvogel,[180] and Sekhon and Srivastava [181]). These different parameterizations lead to an expression similar to Eq. (43) for the extinction:

$$k_{ext} = A \bullet R^{B} \quad . \qquad (46)$$

For the convenience of the MODTRAN users who may wish to modify SUBROUTINE TNRAIN, to implement one of these other models, the parameters for size distributions and extinction coefficients are summarized in Table 16.

Table 16. Parameters Relating Size Distribution [Eq. (38)] Extinction

Coefficient [Eq. (46)] to Rain Rate for Different Types of Rain

Tvpe of Rain	N_o (mm^{-1} m^{-3})	Λ (mm^{-1})	A	B
Marshall-Palmer[177]	8, 000	4.1 $R^{-0.21}$	0.365	0.63
Drizzle (Joss and Waldvogel)[180]	30, 000	5.7 $R^{-0.21}$	0 509	0.63
Widespread (Joss and Waldvogel)[180]	7,000	4.1 $R^{-0.21}$	0.319	0.63
Thunderstorm (Joss and Waldvogel)[180]	1,400	3.0 $R^{-0.21}$	0.163	0.63
Thunderstorm (Sekhon and Srivastava)[181]	7,000 $R^{0.37}$	3.8 $R^{-0.14}$	0.401	0.79

The divergence between the two different thunderstorm models indicates the difficulty in making such parameterizations and the uncertainty in the parameter values given.

2.4.1.4 Sample Output of Typical Rain Cases

The atmospheric transmittance, using the M-P model with the MODTRAN code for rain rates varying from 1 to 100 mm/hr is shown in Figure 27 for 400 through 4000 cm 1 and in Figure 28 for 4000 through 40000 cm 1,

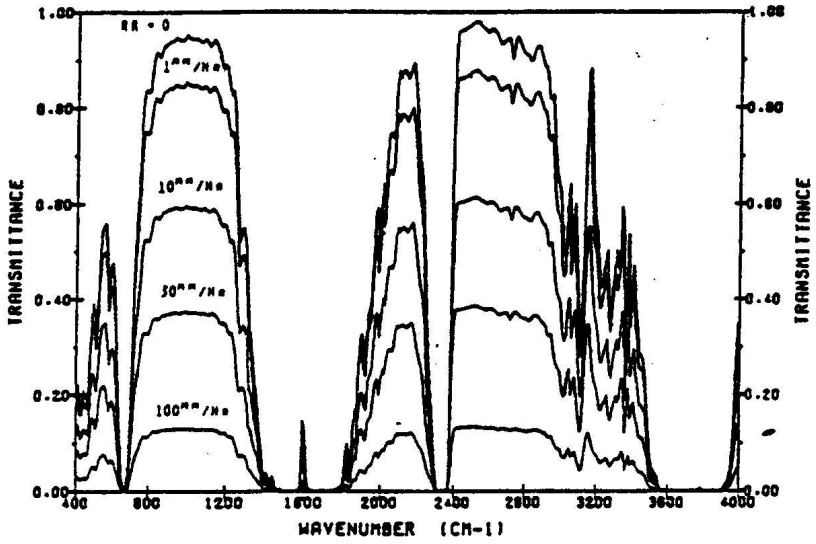

Figure 27. Atmospheric Transmittance for Different Rainrates (RR) and for Frequencies From 400 to 4000 cm^{-1}. The measurement path is 300 m at the surface with T = T_{dew} = 10° C, with a meteorological range of 23 km in the absence of rain.

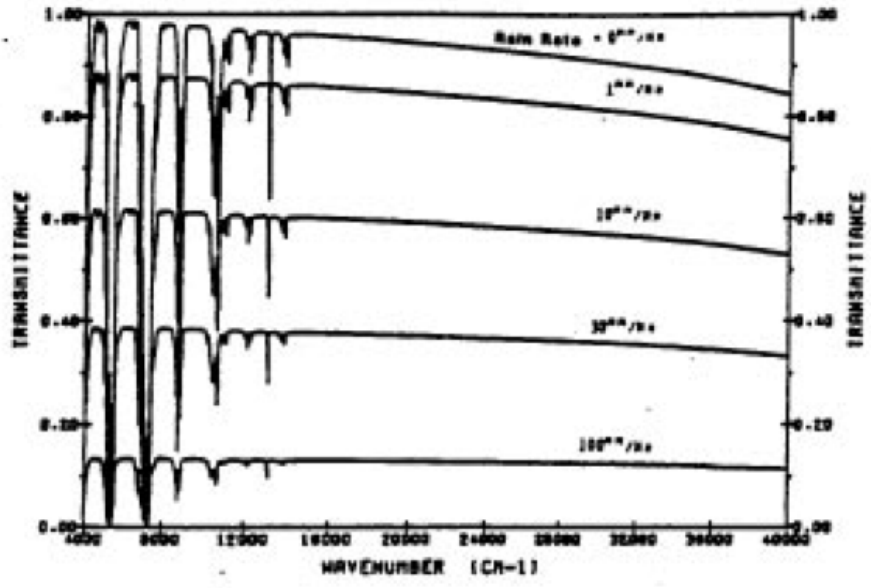

Figure 28. Atmospheric Transmittance for Different Rain rates (RR) and for Frequencies From 4000 to 40000 cm 1. The measurement path is 300 m at the surface with T = T_{dew} = 10° C, with a meteorological range of 23 km in the absence of rain

2.4.2 Water Clouds

2.4.2.1 Introduction

Meteorologists classify clouds as low, middle or high according to the following rough estimates by Berry et al.[182]

low clouds	0-2000 meters
middle clouds	2000-6500 meters
high clouds	> 6500 meters

In addition, the vertical development of clouds should also be included. Table 17 relates the general classification of clouds to specific cloud type nomenclature.

Table 17. Cloud Heights and Vertical Development

Cloud Type	Cloud Symbol	Cloud Heights
Low clouds		
Stratus	St	0-2000 meters
Stratocumulus	Sc	
Nimbostratus	Ns	
Middle Clouds		2000-6500 meters
Altostratus	As	
Altocumulus	Ac	
Vertically Developed Clouds		
Cumulus	Cu	700-8000 meters
Cumulonimbus	Cb	700-20000 meters

The water clouds covered in this section belong to the families of low and middle cloud classification. Specific references for various cloud types are Mason,[183] Borovikov,[184] Berry et al.,[182] Carrier,[185] Luke,[186] Diem,[187] Weickman and Aufra Kampe,[188] Durbin,[189] Gates and Shaw,[190] and Squires and Twomey.[191]

2.4.2.2 Choice of Cloud Models

The five water cloud models included in MODTRAN are; Stratus, Stratocumulus, Nimbostratus, Altostratus, and Cumulus. These models are based on a subset of the cloud models developed by Silverman and Sprague(1970),[192] and described in considerable detail by Falcone et al.[39](1979). They were selected in part to encompass as wide a range as possible of the IR optical properties of the cloud models developed by Silverman and Sprague and to include typically recognizable

cloud types. The droplet size distributions for the models are represented by a modified gamma distribution, with $\gamma = 1$:

$$\frac{dN}{dr} = n(r) = a\, r^{\alpha} \exp\left(-b\, r^{\gamma}\right) \quad . \qquad (47)$$

where a, α, b, and γ are parameters defining the size distribution. The values of the parameters characterizing the fog and cloud droplet size distributions are summarized in Table 18.

2.4.2.3 Structure of Cloud Models

Cloud water content is related to cloud droplet spectra. The values as originally proposed by Silverman and Sprague are for "typical" clouds. These "typical" clouds are not average values. For example, Silverman' s Cloud Model 5 (our Cumulus, ICLD = 1) has a liquid water content of 1g/m^3 (Table 18). This type of cloud may have typical values of liquid water from 0.5 to 1 g/m^3 with values as high as 4 g/m^3 depending on geographical location (for example, New England vs. Florida). Liquid water content of clouds is very important because the cloud droplets are Rayleigh scatterers (see Figures 6-8 and Figure 13 in the Falcone et al.[39] report). Research has shown (Blau et al.[193]) that the liquid water content of non-precipitating clouds have values from 0.1 g/m^3 to 0.5 g/m^3 whereas precipitating clouds often have LWC greater than 1.0 g/m^3

Table 18. Parameters for Fog and Cloud Size Distribution Models Used

Cloud Type	α	b	a	N_o* (cm^{-3})	W* (g-m^{-3})	R_N(μm)	R_M(μm)	Ext*(km^{-1}) λ=0.55 μm
Heavy Advection Fog	3	0.3	0.027	20	0.37	10.0	20.0	28.74
Moderate Radiation Fog	6	3.0	607.5	200	0.02	2.0	3.0	8.672
Cumulus	3	0.5	2.604	250	1.00	6.0	12.0	130.8
Stratus	2	0.6	27.0	250	0.29	3.33	8.33	55.18
Stratus/Strato-Cumulus	2	0.75	52.734	250	0.15	2.67	6.67	35.65
Alto-Stratus	5	1.111	6.268	400	0.41	4.5	7.2	91.04

Nimbostratus	2	0.425	7.676	200	0.65	4.7	11.76	87.08
Clrrus	6	0.09375	2.21 (10^{-12})	0.025	0.06405	64.0	96.0	1.011
Thin Clrrus	6	1.5	0.011865	0.5	3.128 (10^{-4})	4.0	6.0	0.0831

* Nominal values are shown for the number density, (N_o), the liquid water (or ice) content (W), and the visible extinction (Ext); they can be specified by the user in running the code. R_N, and R_M denote the mode radii for the number and mass distribution respectively.

The structure of a typical modeled cloud with 3-8 mm/hr of rain is shown in Figure 29.

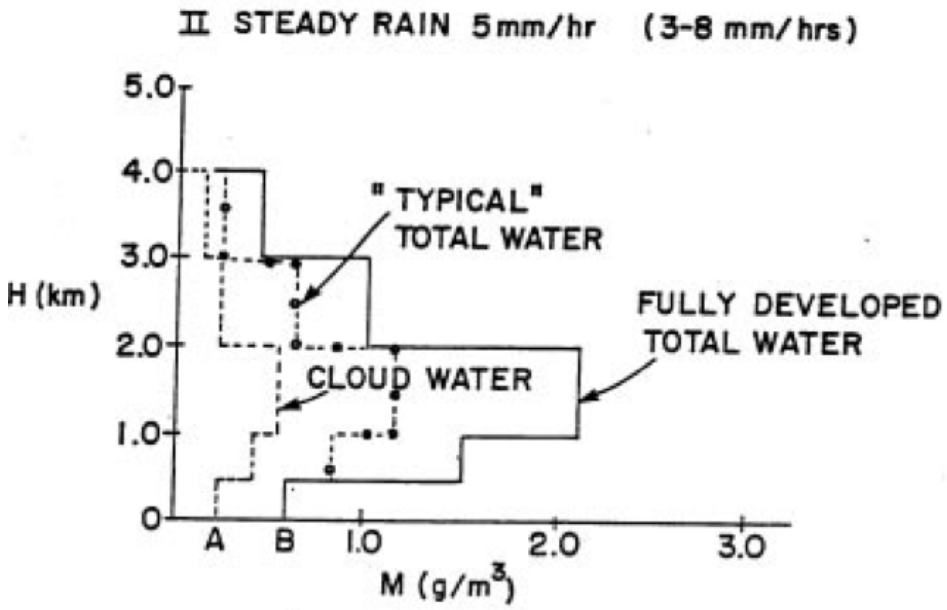

Figure 29. Model of a "typical" cloud with 5mm/hr steady rain

2.4.2.4 Radiative Properties of Clouds

The radiative properties of the clouds were derived from complete Mie[194] scattering calculations using the refractive index of water from Hale and Querry (1973)[70] for wavelengths through 200 μm, and for the longer wavelengths (in the mm region) the formulations of Ray (1972)[195] were utilized. The resulting extinction coefficients for the cloud models are displayed in Figure 30 as a function of wavelength.

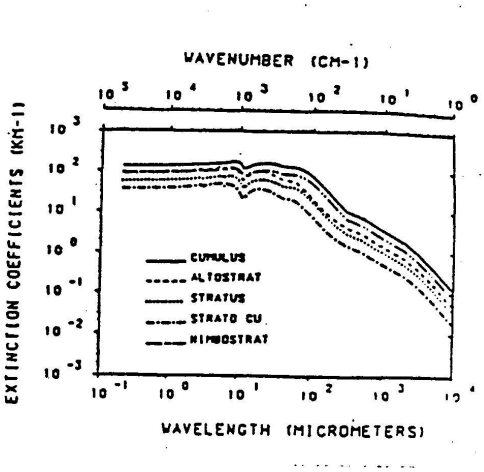

Figure 30. Spectral Dependence of the extinction coefficients for each water cloud model.

2.4.3 Ice Clouds

Three cirrus cloud models are retained in MODTRAN. The NOAA cirrus cloud model (next section) is aptly described by Hall et al. in chapter 7 of the LOWTRAN 6 report[3]. The NOAA model is retained for comparison with earlier LOWTRAN and FASCODE models. The regular cirrus model and the sub-visual cirrus model, described after the NOAA model, can be utilized in radiance calculations.

According to the International Cloud Atlas,[196] cirrus clouds are "composed almost exclusively of ice crystals". Since there is a scarcity of freezing nuclei active above -20°C in the atmosphere, cirrus clouds are not often found at higher temperatures. In polar regions and in wintertime temperate zones near the Arctic or Antarctic, these low temperatures generally occur in the middle or upper troposphere.

2.4.3.1 NOAA CIRRUS CLOUD MODEL

The NOAA empirically based cirrus cloud model developed for the calculation of transmittance through cirrus clouds should be considered valid from the ultraviolet 0.317 μm to the 10 μm window. The derivation of the model is based on numerous worldwide cirrus measurement programs and cirrus climatologies. This model does not separate the scattering and absorption and therefore cannot be used for radiance calculations.

2.4.3.2 Sub-Visual Cirrus Cloud Model

MATERIAL NOT YET COMPLETED

3. THE MODTRAN MODEL

3.1 Introduction

MODTRAN is a moderate resolution version of LOWTRAN 7 (Ref. 2). MODTRAN's spectral resolution is 2 cm^{-1}(FWHM). Molecular absorption is calculated in 1 cm^{-1} spectral bins, while the other parts of the calculation remain unchanged. The molecular species affected are :

water vapor, carbon dioxide, ozone, nitrous oxide, carbon monoxide, methane, oxygen, nitric oxide, sulfur dioxide, nitrogen dioxide, ammonia and nitric acid.

Their absorption properties (the band model parameters) are calculated from the HITRAN 1992 line atlas[20], which contains all lines in the 0 - 22,600 cm^{-1} spectral region that have significant absorption for atmospheric paths. The increased resolution of MODTRAN spans the same spectral region as LOWTRAN. Calculations at larger wavenumbers, the visible and ultraviolet spectral regions (> 22600 cm^{-1}), are performed at the lower spectral resolution of LOWTRAN, 20 cm^{-1} .

A new set of band models for calculating transmittance has been developed for the MODTRAN code. The increased spectral resolution is achieved using an approach developed earlier for a 5 cm^{-1} option to LOWTRAN 5 (Ref. 5). In that earlier approach, band model parameters were calculated from the existing (1980) HITRAN database and used to determine the equivalent width of the absorbing molecular gases in 5 cm^{-1} spectral intervals. The MODTRAN 2 band model parameters are calculated in 1 cm^{-1} intervals.

The molecular transmittance calculation for each bin has three elements. First, the Voigt lineshape of an "Average" line is integrated over the 1 cm^{-1} interval; when a bin contains more than one line of a given species, the lines are assumed to be randomly distributed with statistical overlap; finally, the contribution from lines whose centers are in nearby bins is calculated as a molecular "continuum" component. The other LOWTRAN components, which have insignificant spectral structure at 1 cm^{-1}, are calculated at their 5 cm^{-1} increments and interpolated to arrive at the total transmittance for each interval. The calculational grid consists of non-overlapping 1 cm^{-1} bins, which are degraded to the desired spectral resolution with an internal triangular slit function. Since these bins are square and non-overlapping, the nominal spectral resolution of MODTRAN is reported as 2 cm^{-1} (FWHM).

The comparison of MODTRAN and LOWTRAN 7 calculations shown in Figure 35 illustrates the increased spectral resolution. The figure shows the transmittance calculated at 2 and 20 cm^{-1} resolution for a low altitude slant path through the US Standard Atmosphere. The 2 cm^{-1} curve results from the internal triangular slit function (*IFWHM*=2), and the 20 cm^{-1} curve is the regular LOWTRAN 7 result interpolated to 5 cm^{-1} intervals. The MODTRAN calculation resolves line structure below 2180 cm^{-1} (primarily water), the band center of the N_2O fundamental at 2220 cm^{-1}, and the CO_2 band center at 2284 cm^{-1} .

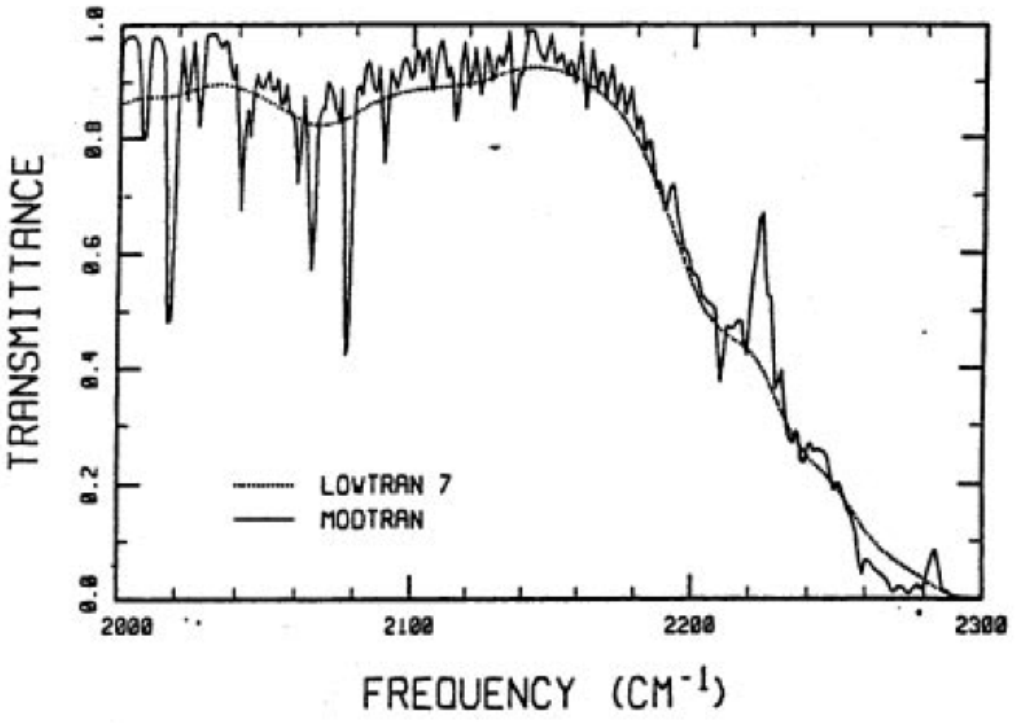

Figure 35. Atmospheric Transmittance for a Slant Path from 5 to 10 km at 15° from Zenith and Through the US Standard Atmosphere with no Haze. The Solid Curve was Calculated with MODTRAN at 2 cm^{-1} Spectral Resolution, and the Dotted Curve with LOWTRAN 7 at 20 cm^{-1} Resolution.

The input data sequence for MODTRAN is identical to that of LOWTRAN 7 except for two additional parameters on Cards 1 and 4. A logical parameter, MODTRN, has been added to the front end of CARD 1,

```
READ(IRD,'  (L1,I4,12I5,F8.3,F7.2)'  )MODTRN,MODEL,ITYPE,IEMSCT,
1  IMULT,M1,M2,M3,M4,M5,M6,MDEF,IM,NOPRT,TB0UND,SALB
```

and the input to CARD 4 has been changed to integer format with a resolution parameter, *IFWHM*, added

```
READ(IRD,'  (4I10)'  )IV1,IV2,IDV,IFWHM.
```

MODTRN is simply a switch which when set to F (false) permits the running of LOWTRAN 7 and when set to T (true) activates MODTRAN. The parameter *IFWHM*, which is only read if *MODTRN* is true, specifies the full width at half maximum, FWHM, of an internal triangular slit function.

MODTRAN and LOWTRAN 7 differ in their approaches to calculating molecular transmittance. For several different spectral intervals LOWTRAN 7 uses a one-parameter band model (absorption coefficient) plus molecular density scaling functions. The MODTRAN band model uses three temperature-dependent parameters, an absorption coefficient, a line-density parameter and an average linewidth. The spectral region is partitioned into 1 cm^{-1} bins for each molecule. Within each bin, contributions from transitions whose line centers fall within the bin are modeled separately from nearby lines centered outside of that bin (see Figure 36). The absorption due to lines within the bin is calculated by integrating over a Voigt line shape.[200] The Curtis-Godson[201] approximation, which is accurate for the moderate temperature variations found in the earth' s atmosphere, is used to replace multi-layered paths by an equivalent homogeneous one.

The k-distribution method, which is used in the multiple scattering treatment of LOWTRAN 7 to correct for averaging over large spectral intervals, is not necessary in the MODTRAN model. This is true because three (monochromatic) k values are used for the 5 cm^{-1} steps of LOWTRAN 7, while the 1 cm^{-1} MODTRAN steps provide an equivalent accuracy for the multiple scattering option.

MODTRAN is better suited than LOWTRAN for atmospheric paths which lie completely above 30 km. This is due to the integration over the Voigt lineshape combined with the explicit temperature and pressure dependencies of the band model parameters. The Voigt lineshape is necessary at these altitudes because the Doppler

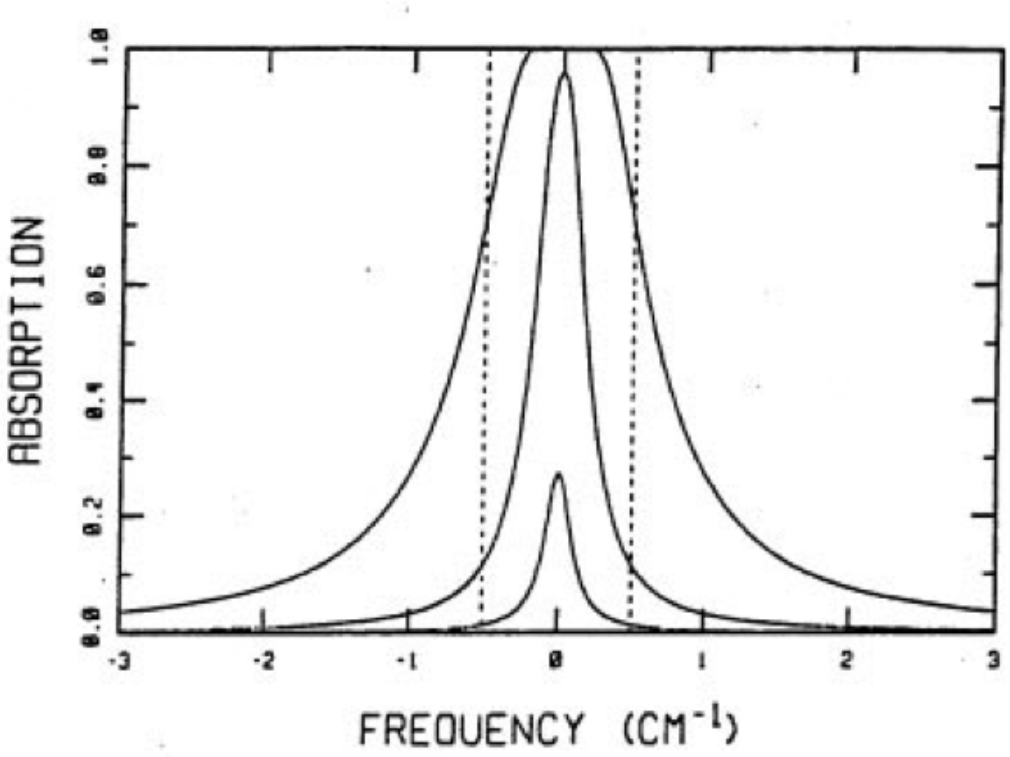

Figure 36. Absorption from Lorentzian Lines with Optical Depths of 0.1, 1, and 10. Halfwidth was Set to 0.1 cm^{-1}. In the Band Model Transmittance Formulation, Absorption from Line Centers (Segment of Curves Falling Within the Spectral Bin Denoted by the Dashed Lines) is Modeled Separately from Absorption due to Line Tails (Outside the Dashed Lines).

linewidth is greater than the Lorentz. The 20 cm^{-1} versions of LOWTRAN suffer because they use a single set of band model parameters (nominally sea level at 296 K) coupled with spectrally independent scaling functions for the molecular densities. It is also worth mentioning that, for paths which lie completely above 60 km, another problem arises: many of the molecules are no longer in local thermodynamic equilibrium (LTE). This means that the strengths of some molecular bands can no longer be determined from the ambient temperature. MODTRAN gives reasonable results for those bands which are in LTE; the problem is identifying those spectral regions which are not in LTE.

3.2 MOLECULAR BAND MODEL PARAMETERS

The basic idea behind band model techniques[5,202,203] is to determine a set of parameters from which transmittance over finite frequency intervals can be calculated. In MODTRAN, three band model parameters are used, an absorption coefficient, a line

density and a line width. The absorption coefficient measures the total strength of lines in an interval. The line density is a line-strength weighted average for the number of lines in the interval, and the line-width parameter is a line-strength weighted average line width.

MODTRAN uses a bin width of one wavenumber, $\Delta\nu$ = 1 cm^{-1}. Line data from the HITRAN 1992 database[20] is used to calculate the band model parameters. The compilation contains data on molecular lines in the frequency range 0 to 22600 cm^{-1}. For each molecule with lines whose centers fall within a given spectral bin, the temperature-dependent absorption coefficients and line densities along with the line-width parameter are stored for subsequent use in calculating molecular absorption; a single temperature-dependent absorption coefficient parameter is used to determine the tail contributions to each spectral bin from lines centered in nearby bins.

3.2.1 Line-Center Parameters

Each frequency bin corresponds to a 1 cm^{-1} interval and contains parameters for molecules with lines in that interval. The molecules for which band model parameters have been determined are:

H_2O, CO_2, O_3, N_2O, CO, CH_4, O_2, NO, SO_2, NO_2, NH_3 & HNO_3

The molecular absorption coefficients (S/d) (cm^{-1} amagats^{-1}) are calculated at 5 reference temperatures:

$$T = 200, 225, 250, 275 \,\&\, 300\ K \quad . \tag{48}$$

Linear interpolation is used to calculate absorption coefficients at temperatures between 200 and 300 K. For temperatures below 200 and above 300 K, the extreme values, (S/d) (T=200K) and (S/d) (T=300K), respectively, are used. The absorption band model parameters are calculated from the individual line strengths,

$$(S/d) = \frac{1}{\Delta\nu} \sum_j S_j\,(T) \quad , \tag{49}$$

Here $S_j(T)$ is the integrated line strength at temperature T of the j' th line of molecule m in bin i. The line strength at an arbitrary temperature is scaled from the HITRAN line strength at its standard temperature, T_S = 296 K, by:

$$S_j(T) = \frac{Q_r(T_s)Q_v(T_s)}{Q_r(T)Q_v(T)}$$

$$\frac{1-\exp(-hc\nu_j/kT)}{1-\exp(-hc\nu_j/kT_s)} \exp\left(\frac{E_j}{k}\frac{T-T_s}{T\,T_s}\right) S_j(T_s) \qquad (50)$$

where Q_r and Q_v are the rotational and vibrational partition functions, E_j is the energy of the lower transition state, and ν_j is the transition frequency. The constants are the speed of light (c), the Boltzman constant (k), and the Planck constant (h).

A collision-broadened or Lorentz line-width parameter γ_{c° is defined at STP (T_o = 273.15 K, P_o = 1013.25 mb). A single value can be stored because the pressure and temperature dependence of the Lorentz line width is easily modeled,

$$\gamma_c(T,P) = \gamma_c^o \frac{P}{P_o}(T_o/T)^x \qquad (51)$$

where the exponent x has been set to 1/2 for all molecules except CO_2, for which x has been taken as 3/4. The γ°_c band model parameter is calculated as a line-strength weighted average over the tabulated Lorentz line widths $\gamma_{c,j}(T_S)$:

$$\gamma_c^0 = (T_s/T_0)^x \left[\sum_j \gamma_{c,j}(T_s) S_j(T_s)\right] / \left[\sum_j S_j(T_s)\right] \qquad (52)$$

Like the absorption coefficients, the line-density band-model parameters (1/d) (cm) are calculated at the five reference temperatures and interpolated when used by the band model subroutines. The line density is defined by:

$$(1/d) = \frac{1}{\Delta\nu}\left(\sum_{j=1}^{N} S_j\right)^2 / \sum_{j=1}^{N} S_j^{\,2} \quad . \qquad (53)$$

This definition for the line spacing, which is derived in the appendix of the Berk report,[1] produces a smaller value than the usual definition involving a sum over the square root of the line strengths.[223,224] The new form results when account is taken of finite bin

widths. The absorption of a line within a finite bin is less than its total line strength: this is consistent with a decreased value for (1/d).

3.2.2 Line-Tail Parameters

The line-tail parameters consist of line contributions from lines located outside of a given bin but within ± 25 cm^{-1}. The line-tail absorption coefficient band-model parameters C (cm^{-1} $amagat^{-1}$) are determined by integrating the Lorentz line shape over this interval:

$$C = \frac{1}{\pi \Delta\nu} \sum_{k=i-25}^{i+25} (1-\delta_{ki}) \left\{ \frac{[(S/d)\,\gamma_c]_k}{(k-i)^2+1/4} f[(k-i)\Delta\nu] + \frac{[(S/d)\,\gamma_c]_k}{(k+i)^2+1/4} f[(k+i)\Delta\nu] \right\} , \quad (54)$$

where the delta function serves to exclude the k=i term from the sum (i.e., the line center contribution), and f[Δν] is a lineshape form factor. The form factor is 1.0 within 25 cm^{-1} of the line centers. Except for H_2O and CO_2, tail contributions beyond 25 cm^{-1} are assumed negligible and are not included. The usual LOWTRAN 7 water continuum consists of tail contributions from lines located beyond 25 cm^{-1} plus extrapolated (flat) values of this contribution within 25 cm^{-1} (for smoothness). For CO_2, the continuum from FASCOD2[40] has been added to the parameter C to account for the tail contributions from lines beyond 25 cm^{-1} :

$$C \rightarrow C + \nu_i \tanh\left(\frac{hc\nu_i}{2kT}\right) \frac{T_s}{T} \tilde{C}(\nu_i) \quad (55)$$

Here, $\tilde{C}(\nu_i)$ is the frequency interpolated value from the FASCOD2 block data /*FCO2*/. For both H_2O and CO_2, the value of C has also been reduced by an amount equal to its value at 25 cm^{-1} from the line center since this contribution is already included in the continuum data. The constant C is proportional to pressure (which arises from the Lorentz line width, Equation (51)):

$$C(P) = \frac{P}{P_0} C(P_0) \quad (56)$$

3.2.3 Parameter Data File

Because of the large amount of data, the band-model parameters are stored in an external file that is written in binary format; this allows for quicker access during the calculation. Each entry corresponds to a 1 cm^{-1} interval and contains a molecular parameter set. Since no data for molecules without lines in a given interval are stored, a parameter identifying the active species is included.

The first entry of a parameter set is the bin number, i. From the bin number, the midpoint of the interval is calculated

$$\nu_i = i\,\Delta\nu \quad , \tag{57}$$

and all lines whose centers fall in the half-opened interval $[\nu_i - \Delta\nu/2, \nu_i + \Delta\nu/2]$ contribute to bin i.

The molecular parameter set is identified by the parameter m. The HITRAN database[20] convention is used for this labeling

m	1	2	3	4	5	6	7	8	9	10	11	12
molecule	H_2O	CO_2	O_3	N_2O	CO	CH_4	O_2	NO	SO_2	NO_2	NH_3	HNO_3

The next entries in the parameter set are the molecular absorption coefficients (S/d) (cm^{-1} amagats^{-1}) calculated at the five reference temperatures. These entries are followed by the STP Lorentz half width, $\gamma°_C$, multiplied by 10^4 and stored as an integer. Line-spacing parameters (1/d) for the five reference temperatures complete the line-center parameter sets.

For line tails, each line contains data on one or two molecules. These line-tail parameter sets use the same format as the line-center parameter sets. Again, the first entry is the bin number i and the second entry is the molecule designation m. To recognize that these parameter sets denote line-tail contributions, their molecule labels are offset by 12.

m	13	14	15	16	17	18	19	20	21	22	23	24
molecule	H_2O	CO_2	O_3	N_2O	CO	CH_4	O_2	NO	SO_2	NO_2	NH_3	HNO_3

The continuum parameters, C, are stored in place of the (S/d). Unless all tail contributions have been defined for frequency bin i, the molecular designation and

continuum parameters for a second molecule follow the first on the same parameter set.

A sample of the formatted data for frequency bins 2294 and 2295 is shown below:

```
2294  1    2.561E-07   9.816E-07   3.157E-06   8.694E-06   2.083E-05        592   1.814E+00   2.645E+00   3.273E+00   3.359E+00   3.182E+00
2294  2    1.384E+00   1.436E+00   1.598E+00   1.904E+00   2.377E+00        730   1.138E+00   1.375E+00   1.837E+00   2.486E+00   3.021E+00
2294  4    1.961E-03   2.842E-03   3.769E-03   4.683E-03   5.540E-03        757   2.227E+00   2.385E+00   2.517E+00   2.627E+00   2.720E+00
2294  13   1.681E-08   6.871E-08   2.090E-07   5.126E-07   1.071E-06        14    8.325E-02   7.507E-02   7.245E-02   7.535E-02   8.356E-02
2294  15   5.052E-09   5.037E-09   4.896E-09   4.678E-09   4.116E-09        16    3.339E-04   4.363E-04   5.346E-04   6.230E-04   6.978E-04
2294  18   3.393E-06   3.291E-06   3.529E-06   4.055E-06   1.816E-06        0     0.000E+00   0.000E+00   0.000E+00   0.000E+00   0.000E+00
2295  2    3.195E-02   7.865E-02   1.678E-01   3.166E-01   5.403E-01        688   2.986E+00   2.537E+00   2.305E+00   2.217E+00   2.211E+00
2295  4    2.653E-03   3.804E-03   5.003E-03   6.174E-03   7.261E-03        766   2.729E+00   2.966E+00   3.161E+00   3.320E+00   3.449E+00
2295  6    1.511E-06   1.603E-06   1.659E-06   1.687E-06   1.691E-06        725   1.824E+00   1.898E+00   1.946E+00   1.975E+00   1.991E+00
2295  13   2.796E-08   1.118E-07   3.432E-07   8.628E-07   1.860E-06        14    1.309E-01   1.257E-01   1.302E-01   1.444E-01   1.675E-01
2295  16   3.903E-04   4.882E-04   5.769E-04   6.524E-04   7.129E-04        18    2.271E-06   3.894E-06   6.420E-06   9.811E-06   1.393E-05
```

In bin 2294, there are H_2O, CO_2 and N_2O line center parameter sets and tail data for H_2O, CO_2, O_3, N_2O and CH_4. In bin 2295, there is no line center data for H_2O, but lines do exist for CH_4. Also, bin 2295 does not contain any O_3 continuum data.

3.3 BAND-MODEL TRANSMITTANCE FORMULATION

3.3.1 Line-Center Transmittance

The band-model transmittance formulation[5] developed for the 5 cm^{-1} option to LOWTRAN 5 (Ref. 4) was used to create a moderate resolution option for LOWTRAN 7. The expression used to calculate molecular transmittance is based on a statistical model for a finite number of lines within a spectral interval, and is given by:

$$\tau = \left(1 - \langle W_{sl} \rangle / \Delta\nu\right)^{\langle n \rangle} \quad , \tag{58}$$

where τ is the transmittance, $\langle W_{sl} \rangle$ is the Voigt single-line equivalent width for the line-strength distribution in a spectral interval, and <n> is the path-averaged effective number of lines in the bin:

$$\langle n \rangle = \Delta\nu \langle 1/d \rangle \quad . \tag{59}$$

<1/d> is the path-averaged line spacing.

For large <n> [(S/d) and $\Delta\nu$ fixed], the transmittance simplifies to the more recognizable exponential form, Beer' s Law, given by:

$$\tau \rightarrow \exp\left(-\langle W_{sl} \rangle \langle 1/d \rangle\right) \quad (60)$$

for the relatively low temperatures encountered in the earth' s atmosphere,the number of lines in a bin from a single molecular species is usually small so that the power law transmittance formulation is preferred.

There are many approximations available for calculating the equivalent width of a Voigt line shape; different ones are valid for different regimes, Doppler or collision broadening, weak line or strong line, etc. However, no single approximation is adequate for the range of pressures and optical path lengths encountered in atmospheric transmission calculations. Rather than incorporating different approximations, a direct evaluation of the exact expression for the equivalent width of a single line in a finite spectral interval; $\langle W_{sl} \rangle$is given by:

$$\langle W_{sl} \rangle = \frac{\Delta\nu}{X_m} \int_0^{X_m} 1 - \exp\left\{-\left[Su/d\right] \sqrt{\ln 2/\pi}\, F(X,Y) / \langle \gamma_d/d \rangle\right\} dx \quad (61)$$

$$F(X,Y) = \frac{Y}{\pi} \int_{-\infty}^{\infty} \frac{\exp(-T^2)\, dT}{Y^2 + (X-T)^2} \quad , \quad (62)$$

$$X_m = \frac{1}{2} \sqrt{\ln 2} \langle n \rangle / \langle \gamma_d/d \rangle \quad , \quad (63)$$

$$Y = \sqrt{\ln 2} \langle \gamma_c/d \rangle / \langle \gamma_d/d \rangle \quad , \quad (64)$$

where F(X,Y) is the Voigt line shape function, [Su/d] is the total optical depth, and $\langle \gamma_d/d \rangle$ and $\langle \gamma_c/d \rangle$ are the path averaged Doppler and collision broadened line shape band model parameters, respectively. To accurately calculate $\langle W_{sl} \rangle$, we separate its contributions as shown:

$$\langle W_{sl} \rangle = \langle W_{sl}{}^0 \rangle - \langle W_{sl}{}^1 \rangle \quad (65)$$

$$\langle W_{sl}{}^0 \rangle = \frac{\Delta\nu}{X_m} \int_0^{\infty} 1 - \exp\left\{-\left[Su/d\right] \sqrt{\ln 2/\pi}\, F(X,Y) / \langle \gamma_d/d \rangle\right\} dx \quad 66)$$

$$\langle W_{sl}{}^1 \rangle = \frac{\Delta\nu}{X_m} \int_{X_m}^{\infty} 1 - \exp\left\{-\left[Su/d\right] \sqrt{\ln 2/\pi}\, F(X,Y) / \langle \gamma_d/d \rangle\right\} dx \quad (67)$$

The tail contribution, $\langle W_{sl}{}^{1} \rangle$ can easily be evaluated in terms of the error function since X_m >> Y for cases calculated with MODTRAN:

$$\langle W_{sl}{}^{1} \rangle \approx \exp(-z^2) + \sqrt{\pi}\, z\, erf(z) - 1 \quad , \qquad (68)$$

$$z \equiv \frac{2}{\langle n \rangle} \sqrt{[Su/d] \langle \gamma_c / d \rangle / \pi} \quad . \qquad (69)$$

To determine $\langle W_{sl}{}^{0} \rangle$, an interpolation between the Lorentz and Doppler limits is used. Based on an interpolation formula developed by Ludwig et. al. [Equations (5-25) and (5-26)],[220] the Lorentz and Doppler equivalent widths are given by:

$$L \equiv \frac{4}{4 + [Su/d] / \langle \gamma_c / d \rangle} \quad , \qquad (70)$$

$$D \equiv \frac{2}{\ln 2} \frac{\langle \gamma_d / d \rangle^2}{[Su/d]^2} \ln\left(1 + \frac{\ln 2}{2} \frac{[Su/d]^2}{\langle \gamma_d / d \rangle^2}\right) \quad , \qquad (71)$$

$\langle W_{sl}{}^{0} \rangle$ is determined from the following interpolation formula which is more numerically stable:

$$\langle W_{sl}{}^{0} \rangle^2 = \frac{[Su/d]^2}{\langle 1/d \rangle^2} \left\{ 1 - (1-L)(1-D) \Big/ \sqrt{1 - LD(2-L)(2-D)} \right\} \qquad 72)$$

Figure 37 shows a comparison of Equation (72) to exact calculations for the equivalent width of a single, isolated spectral line with a Voigt lineshape. The lowest curve is the pure Doppler limit and the highest curve is the Lorentz limit. The exact values are taken from Penner.[225] The predictions of Equation (72) are shown as solid lines for the same values of the parameter Y in Equation (64). The overall agreement between the two families of curves illustrates the quality of the interpolation formula.

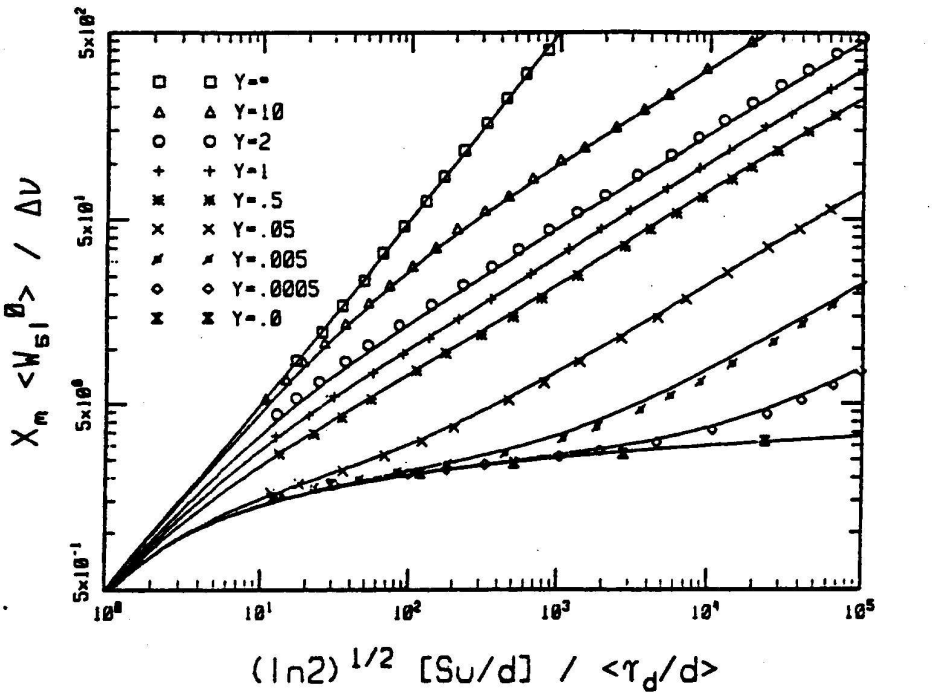

Figure 37. Curves of Growth for Spectral Lines with Combined Doppler and Lorentz Line Broadening. The Exact Calculations[225] are Presented as Individual Values. The NASA Formula,[220] Equation (72), is Shown as Solid Lines. The Values of Y From Bottom to Top are: 0, 0.0005, 0.005, 0.05, 0.5, 1.0, 2, 10, and ∞.

3.3.1.1 Curtis-Godson Approximation

Path averages are calculated with the Curtis-Godson approximation.[220-222] This approximation replaces an inhomogeneous path with a homogeneous one by using average values for the various band-model parameters. The Curtis-Godson approximation is very accurate for paths where the temperature and concentration gradients are not particularly steep. This is the case for atmospheric paths where the temperature variations for arbitrary paths fall within the range of 200 to 300 K. The total optical depth is a sum over contributions from the individual layers and is given by:

$$\left[Su/d\right] = \sum_{\ell} (S/d)_{\ell} \quad (\Delta u)_{\ell} \quad , \qquad (73)$$

where $(\Delta u)_{\ell}$ is the incremental absorber amount from layer l and $(S/d)_{\ell}$ is the absorption coefficient band-model parameter at the temperature of the layer l. Note,

frequency and species indices are implicitly assumed for this and subsequent equations.

The optical depth is used as the weighting function in calculating the path averages:

$$\langle 1/d \rangle = \frac{1}{[Su/d]} \sum_{\ell} (1/d)_{\ell} \quad (S/d)_{\ell} \quad (\Delta u)_{\ell} \tag{74}$$

$$\langle \gamma_c/d \rangle = \frac{1}{[Su/d]} \sum_{\ell} (\gamma_c)_{\ell} \quad (1/d)_{\ell} \quad (S/d)_{\ell} \quad (\Delta u)_{\ell} \tag{75}$$

$$\langle \gamma_d/d \rangle = \frac{1}{[Su/d]} \sum_{\ell} (\gamma_d)_{\ell} \quad (1/d)_{\ell} \quad (S/d)_{\ell} \quad (\Delta u)_{\ell} \tag{76}$$

The band model parameters were defined in the previous section, and $(\gamma_d)_{\ell}$ is the usual Doppler width in (cm^{-1}):

$$(\gamma_d)_{\ell} = \frac{\nu_i}{c} \sqrt{2(\ln 2) NkT/M} \quad . \tag{77}$$

where M is equal to the molecular mass (g/mole) of the molecule and N is Avogadro' s number.

3.3.2 Line-Wing Absorption

The power-law transmittance, Equation (58), considers only lines which originate within a given spectral interval, and for these lines, only that fraction of the line profile which falls within the interval is included in the computation of the equivalent width. This approximation is reasonable in the strongly absorbing region of a band; however, because the absorptivity is expressed in terms of the local line strength distribution, it becomes a poor approximation in regions where the tail contributions from nearby lines dominate the contributions from weak or non-existent lines within a given interval (bin). This typically occurs in the center and far wings of a band (i.e., past the band head), and also in spectral intervals containing no lines which are in the vicinity of strong lines. For these situations, the local absorption is dominated by the accumulated tails of the stronger lines located outside the interval. The effect of line wing absorption is included in the transmittance by adjoining an exponential term:

$$\tau = \left(1-\langle W_{sl}\rangle/\Delta\nu\right)^{\langle n\rangle} \; e^{-[Cu]} \quad , \tag{78}$$

where $[Cu]$ is the total continuum optical depth:

$$[Cu] = \sum_{\ell}(C)_{\ell} \; (\Delta u)_{\ell} \quad . \tag{79}$$

The layer subscript $\ell \quad on \quad C$, labels both the pressure Equation (56) and temperature (interpolated) dependencies.

3.4 Integration With LOWTRAN 7

Integration of the MODTRAN subroutines into LOWTRAN 7 was accomplished with minimal changes to the original code. In subroutine TRANS, a single call to subroutine BMDATA reads the first necessary wavenumber block of band model parameters and calculates wavenumber independent quantities. For each wavenumber, calls to subroutine BMOD are made once for initialization and then additionally in the loop over atmospheric layers that calculates the molecular transmittance. In MSRAD, the call to FLXADD is replaced by a call to BMFLUX for the moderate-resolution option.

3.4.1 New Subroutines

The new MODTRAN subroutines are listed in this section. For a detailed description of the functions of each subroutine refer to References 1 and 21.

The principal subroutines added for the basic MODTRAN band model are; BMDATA, BMOD, BMLOAD, BMTRAN, BMERFU, BMFLUX, and DRIVER. Many additional routines have been added for the Upgraded Line-of-Sight Geometry[21] (section 3.5).

3.4.2 Necessary Modifications to LOWTRAN 7

Modifications to LOWTRAN 7 have been kept to a minimum. As mentioned earlier, the switch MODTRN has been added to /CARD 1 /. Only if MODTRN is .TRUE. are any of these changes activated.

Most of the routines from LOWTRAN 7 remain unchanged. A number of routines have been modified only in that the blank common along with the labeled commons /CARD1/, /CARD4/, /SOLS/ and /TRAN/ have been changed. These routines are ABCDTA, AEREXT, AERNSM, CIRR18, CIRRUS, CLDPRF, DESATT, EQULWC, EXABIN, FLXADD, LAYVSA, PHASEF, RDLXA, RDNSM, RFPATH, SSRAD and VSANSM.

A number of routines have undergone minor modifications. Routines GEO and SSGEO were altered in order to make the following changes/additions:

(1) The matrices WPATH (WPATHS) and WPMS (WPMSS) have been combined into the single matrix WPATH (WPATHS),

(2) Layer pressures and temperatures are stored for use by the band model routines, and

(3) Curtis-Godson averaged pressures and temperatures are determined for solar paths.

STDMDL calculates actual rather than scaled molecular column densities when MODTRN is .TRUE.. Finally, routine MSRAD computes molecular optical thicknesses and calls routine BMFLUX.

Significant changes were made to the MAIN program routine. It has been split into two routines. The new MAIN consists of almost 1000 lines of introductory comments and a single call to the new subroutine DRIVER. DRIVER is the driving routine for MODTRAN and it contains all the executable statements from the MAIN program of LOWTRAN 7. In addition, it defines a pointer array called KPOINT that maps the HITRAN molecular labels (1-12) into the LOWTRAN 7 labels. Also, DRIVER checks the spectral inputs. For moderate resolution, the variables *IVl, IV2* and *IDV* need not be multiples of 5, and the additional variable *IFWHM* must be read.

Considerable modifications were required for the subroutine TRANS. This routine is currently divided into three separate subroutines: TRANS, LOOP and BMDATA. When MODTRN is .TRUE., TRANS:

(1) sets the internal frequency step size to 1 cm^{-1} ,

(2) calls the MODTRAN subroutines to calculate molecular transmittance,

(3) interpolates transmittances calculated at 5 cm^{-1} intervals for the aerosols and molecular continua, and employs a discretized triangular slit function with FWHM set to *IFWHM* to automatically degrade the 1 cm^{-1} bin results to

the requested spectral resolution.

Note that the discretized triangular slit function when *IFWHM* is set to 1 cm^{-1} is a 1 cm^{-1} rectangular slit function, as shown in Figure 38. The figure also demonstrates that, when the printing step-size parameter *IDV* (=2 here) is larger than *IFWHM*, the frequency range is under-sampled.

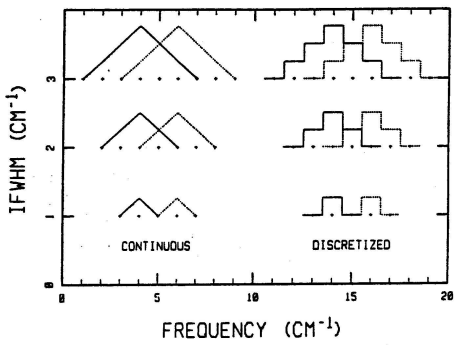

Figure 38. Comparison of Continuous and Discretized Triangular Slit Functions. FASCODE Uses the Weighting from the Continuous Function, but MODTRAN Uses the Discretized Approximation. For this Example, *IDV* = 2 and the Curves are Shown for *IFWHM* = 1, 2, and 3.

LOWTRAN 7 and MODTRAN also differ in their approaches to handling molecular transmittance. Since the LOWTRAN model has been optimized for 296 K, low level paths, LOWTRAN should not be used for atmospheric paths completely above 30 km. MODTRAN, on the other hand, uses a Voigt lineshape, which is applicable at higher altitudes. Figures 39-41 demonstrate MODTRAN' s high altitude capabilities. First, Figure 39 shows that LOWTRAN 7 and MODTRAN do indeed predict vastly different radiances at higher altitudes. Radiation levels from H_2O rotations along a 60 km limb path are shown. The LOWTRAN spectral radiances are much too low at these altitudes. To demonstrate that MODTRAN calculations are correct, validations have been performed against SHARC 2,[226] the Strategic High Altitude Radiation Code. SHARC performs NLTE (non-local thermodynamic equilibrium calculations from 60 to 300 km altitude. However, at 60 km, vibration state populations are essentially LTE and H_2O rotations are always treated as LTE in SHARC, so comparisons between MODTRAN and SHARC should produce similar results. With a 60 km limb path, the two codes predict similar spectral radiances for H_2O rotations (Figure 40) and for the 15 μm CO_2 band (Figure 41), which is mostly LTE. The SHARC calculations were done at a spectral resolution of 0.5 cm^{-1} and degraded to 1 cm^{-1} (FWHM).

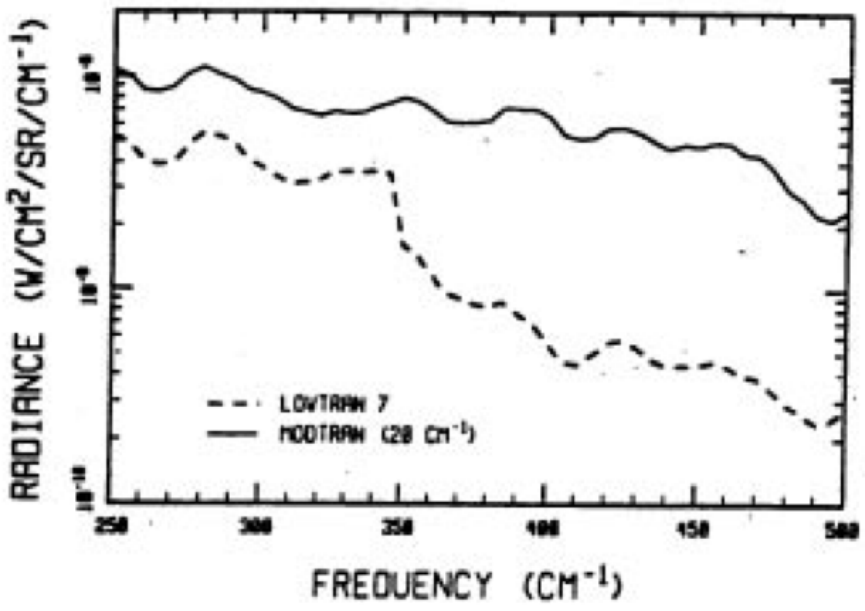

Figure 39. LOWTRAN 7 and MODTRAN Predictions for Radiation from the H_2O Rotational Band for a 60 km Limb Path. At These Altitudes, LOWTRAN Under Predicts the Radiance.

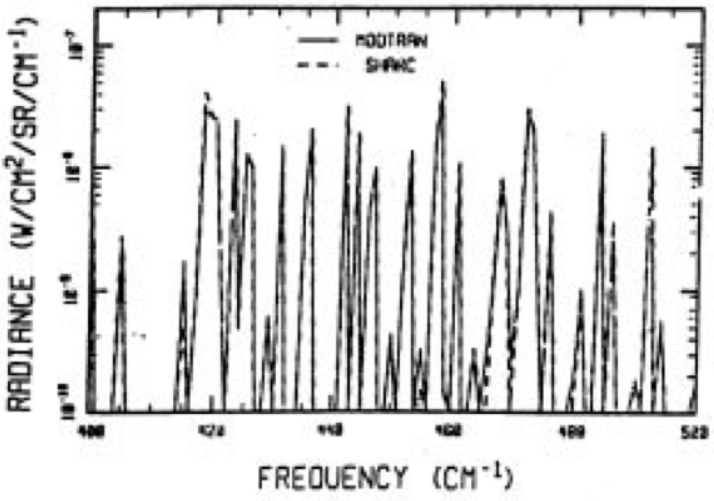

Figure 40. MODTRAN and SHARC Predictions of H_2O Rotations for 60 km Limb.

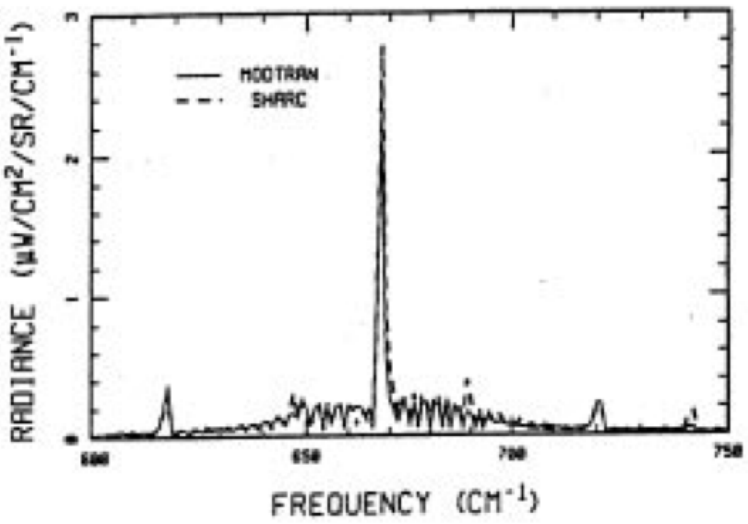

Figure 41. MODTRAN and SHARC Predictions of the 15 μm CO_2 Band for 60 km Limb.

3.5 Upgraded Line-of-Sight Geometry

The geometry package in MODTRAN allows the user several different options for unambiguously specifying the line-of-sight (LOS). For a detailed description of the possible choices refer to the Users Guide To LOWTRAN 7 (Ref. 2). The routines are capable of calculating some unspecified parameters and creating a "complete set" of LOS parameters. However, for some particular paths, the output parameters are often different from the chosen inputs. This is particularly noticeable for slant paths specified by range and zenith angle, especially those paths which are near-horizontal, and for many input sets where the LOS is only a few kilometers or less. These problems have been corrected by upgrading the geometry package.

3.5.1 LOS Specification

The input parameters for characterizing a general LOS path are listed in Table 20. It should be noted that HMIN is also the tangent altitude for long limb viewing paths, which reach a minimum altitude (tangent point) and then increase in altitude. The three generic path types recognized by MODTRAN are listed in Table 21. The type is selected by assigning the appropriate value to the input variable ITYPE. The ITYPE = 3 path is a special case of ITYPE = 2 where H2 is space, that is, the outer boundary of the highest atmospheric layer (100 km).

Table 20. The LOS Parameters

H1	sensor or observer altitude
H2	final altitude
ANGLE	zenith angle at H1
BETA	earth-center angle
RANGE	distance along the LOS between H1 and H2
HMIN	minimum altitude of the LOS

Table 21. Path Types in MODTRAN

ITYPE	PATH DESCRIPTION
1	horizontal homogeneous path with constant temperature, pressure and concentrations
2	vertical or slant path between H1 and H2
3	vertical or slant path to space from H1

For slant paths, one of four parameter sets are used to specify a path. They are H1 and two additional parameters. Table 22 lists the four possibilities, each identified by a case label: 2A, 2B, 2C or 2D. These case designations are internal to the MODTRAN code. Some of these input schemes are converted into other equivalent schemes for subsequent calculations. The most convenient parameter set for tracing a ray through the atmosphere is CASE 2A, so all paths are eventually converted to this case. CASE 2B is converted to 2A by determining H2. CASE 2C is converted to 2D by determining BETA, and finally both 2C and 2D are converted to 2A by determining ANGLE. Potential accuracy problems generated in any one case can then carry over into other cases.

Table 22. Parameter Sets for ITYPE = 2 Paths.

CASE LABEL	SPECIFIED PARAMETERS
2A	H1, H2, ANGLE
2B	H1, ANGLE, RANGE
2C	H1, H2, RANGE
2D	H1, H2, BETA

3.5.2 Geometry Problems

The mismatch between the input and output LOS parameters are confined to some slant paths specified by ITYPE = 2 and 3. The following is a listing of the specific problems in these mismatches:

(1) Simple numerical precision problems;
(2) Calculation of H2 without refraction effects for CASE 2B;
(3) Failure to converge when determining ANGLE for CASES 2C and 2D; and
(4) Short slant paths.

Since ITYPE = 3 is a special case of ITYPE = 2 and utilizes the same routines, the ITYPE = 2 LOS upgrades automatically carry over to the ITYPE = 3 cases. The following approach was taken:

(1) Improved numerical accuracy of some specific algorithms;
(2) For slant paths exceeding 2 km, solve refraction and convergence problems; and
(3) Ignore refraction for short slant paths.

3.5.3 Improved Numerical Accuracy

Some FORTRAN statements were replaced by identical equivalent statements that are numerically stable. As an example, the expression:

$$R_1^2 + R_2^2 - 2R_1R_2\cos\beta \qquad (80)$$

where $R_i = R_e + H_i$, i = 1, 2 and R_e = earth radius, is replaced by:

$$(H_1 - H_2)^2 \quad + \quad 4R_1R_2 \quad \sin^2(\beta/2) \qquad (81)$$

In the first expression, the third term nearly equals the sum of the first two terms for small values of β. The inclusion of R_e^2 in all terms means that, for small β, a large number is subtracted from another number of comparable magnitude. This leads to a significant loss in accuracy. The second expression is more accurate because some R_e' s have been eliminated.

A Taylor series expansion is also used for improving the numerical accuracy of small beta cases:

$$(H_1 - H_2)^2 \quad - R_1R_2 \quad \left\{-(\beta^6/135) \quad + \quad (\beta^4/12) - \beta^2\right\} \qquad . \qquad (82)$$

The sextic term is first in this expansion, because in summing up a series of terms in a computer, it is more accurate to start with the smaller terms. A number of FORTRAN variables were changed from single to double precision.

The resulting improved numerical accuracy was sufficient to obtain agreement among input and output parameters for CASE 2A and for many input sets of CASE 2C. However, these improvements did not solve all of the CASE 2C problems.

Table 23 compares the MODTRAN and MODTRAN2 output ranges for various input schemes of CASE 2C. For some small input ranges, MODTRAN output ranges differ greatly from the input values. For input ranges of 2.0, 6.0 and 20.0 km, MODTRAN' s calculation of ANGLE failed to converge, thereby yielding no output ranges.

3.5.4 Slant Paths

Consistency for the CASE 2B input cases is obtained by determining H2 by a refractive calculation when converting to 2A. A modified iterative procedure for determining BETA produces accurate convergence for the 2D cases.

CASE 2B (H1, ANGLE, RANGE)

Table 23. Examples for CASE 2C with H1=5 and H2=5 km.

	RANGE (km)	
INPUT	MODTRAN	MODTRAN2
2.01	-----	2.00
4.70	5.31	4.72
6.00	-----	6.01
8.0	7.51	8.01
9.0	7.51	9.01
10.0	9.20	10.02
20.0	-----	20.01
50.0	50.51	50.02
100.0	100.52	100.01
200.0	199.96	200.01
300.0	300.13	300.01

The LOS path for this case is converted to CASE 2A by computing H2, but without refraction. Once H2 is calculated, CASE 2A proceeds by including atmospheric refraction effects. A new set of routines includes refraction in the initial H2 calculation. As a result, the input and output parameters are now in general agreement as shown in Table 24. Since refraction tends to bend the rays towards the earth, the H2 values

calculated with refraction (MODTRAN2) are consistently less than those calculated via straight line geometry (MODTRAN).

Table 24. Examples for CASE 2B with H1 = 5 km and ANGLE = 92°.

	RANGE (km)		H2 (km)	
INPUT	MODTRAN	MODTRAN2	MODTRAN	MODTRAN2
10	10	10	4.66	4.66
50	49	50	3.45	3.43
100	96	100	2.29	2.20
150	136	150	1.53	1.30
200	162	200	1.16	0.74
250	358	250	1.18	0.52
300	385	300	1.59	0.64
350	427	350	2.39	1.11

The value of H2 with refraction is calculated by summing the differential elements of range, ds, along the LOS from H1 to H2. The most convenient variable of integration is the radial distance, r, of a point on the ray from the center of the earth. Thus H2 is the altitude at which the integrated path length equals the input RANGE. This method of determining H2 is non-iterative and rapid.

CASE 2D (H1, H2, BETA)

For this case MODTRAN computes ANGLE iteratively. Initially, an educated guess of ANGLE based on straight line geometry is made, and the corresponding BETA is computed by including refraction. If this calculated BETA does not agree with the input, a new guess of ANGLE is made, and the process is repeated until convergence occurs. If the iteration does not converge, the calculations are skipped. A new iterative algorithm based on a Newton-Raphson scheme was adopted to consistently produce acceptable convergence. In this scheme, ANGLE is incremented by an amount based on its derivative with respect to BETA. The examples shown in Table 23 for which MODTRAN did not yield any output ranges were caused by convergence problems with CASE 2D (to which all CASE 2C inputs were converted to). As can be seen, MODTRAN2 yields very accurate output ranges for these input scenarios.

3.5.4.1 Short Slant Paths

Short slant paths are defined as paths whose lengths are less than 2 kilometers. These are treated differently than the general slant paths, because even in double precision the refractive calculations were numerically unstable.

Since refraction is insignificant at these short ranges, it is ignored. All short slant paths are converted into CASE 2A. A DATA statement in the DRIVER subroutine governs the value of the switch (currently 2 km) for short slant paths. The MODTRAN2 results for ranges slightly less than 2 km and slightly greater than 2 km have a smooth convergence. However, the user should be aware of this controlling switch when performing detailed studies centered on this range.

4. ATMOSPHERIC TRANSMITTANCE

4.1 LOWTRAN 7 Molecular Transmittance Band Models

The molecular transmittance band models described here is summarized from the Pierluissi and Maragoudakis report.[13]

4.1.1 Introduction

The calculation of the molecular transmittance band models for LOWTRAN 7 is best summarized by referring to Tables 25 and 26. Table 25 shows that the older versions of LOWTRAN had modeled water vapor from 350 to 14520 cm^{-1}, with two gaps in between for which calculations were not advisable. Ozone·had extended continuously from 575 to 3270 cm^{-1} in the infrared region. Likewise, the single model for all the uniformly mixed gases had extended from 500 to 13245 cm^{-1}, with a wide spectral gap in between. Table 26 shows that the water vapor model had been·extended continuously from 0 to 17860 cm^{-1}, while ozone has been corrected by eliminating some spectral regions for which calculations were unnecessary. The five individual models for the uniformly-mixed gases allow for the use of different combinations of absorber concentrations, and extended the spectral coverage from 0 to 15955 cm^{-1}. Finally, Table 26 shows the addition of the four trace gases which were added to LOWTRAN 7.

Table 25. Summary of the Molecular Absorption Band Models In LOWTRAN 6.

ABSORBER	SPECTRAL RANGE (cm^{-1})
Water Vapor (H_2O)	350-9195, 9878-12795, 13400-14520
Ozone (O_3)	575-3270, 13000-24200, 27500-50000
Uniformly-Mixed Gases (CH_4, N_2O, O_2, CO, CO_2)	500-8070, 12950-13245

Table 26. Summary of the Molecular Absorption Band Models in LOWTRAN 7

ABSORBER	SPECTRAL RANGE (cm^{-1})
WATER Vapor (H_2O)	0-17860
Ozone (O_3)	0-200, 515-1275, 1630-2295, 2670-3260, 13000-24200, 27500-50000
Uniformly-Mixed Gases:	
Methane (CH_4)	1065-1775, 2345-3230, 4110-4690, 5865-6135
Nitrous Oxide (N_2O)	0-120, 490-775, 865-995, 1065-1385, 1545-2040, 2090-2655, 2705-2865, 3245-3925, 4260-4470, 4540-4785, 4910-5165
Oxygen (O_2)	0-265, 7650-8080, 9235-9490, 12850-13220, 14300-14600, 15695-15955
Carbon Monoxide (CO)	0-175, 1940-2285, 4040-4370
Carbon Dioxide (CO_2)	425-1440, 1805-2855, 3070-4065, 4530-5380, 5905-7025, 7395-7785, 8030-8335, 9340-9670
Trace Gases:	
Nitric Oxide (NO)	1700-2005
Nitrogen Dioxide (NO_2)	580-925, 1515-1695, 2800-2970
Ammonia (NH_3)	0-2150
Sulfur Dioxide (SO_2)	0-185, 400-650, 950-1460, 2415-2580

4.1.2 The Transmittance Function

The molecular transmittance τ averaged over a spectral interval $\Delta\nu$ with a triangular instrument response function of 20 cm^{-1} full-width at half intensity, was approximated by the exponential function[227]

$$\tau = \exp\left\{-(CW)^a\right\} \quad (83)$$

where

$$W = (P/P_o)^n \ (T_o/T)^m \ U \tag{84}$$

$$C = 10C' \quad , \tag{85}$$

$$U = 0.7732 \bullet 10^{-4} \ M\rho_a Z \qquad \textbf{for all absorbers except } \mathbf{H_2O}. \tag{86}$$

$$U = 0.1\rho_w z \qquad \textbf{for } \mathbf{H_2O} \tag{87}$$

In these equations P(atm), T(K), M(ppmv), ρ_W (g/m^3), and ρ_a (g/m^3) are vertical profiles of pressure, temperature, volume-mixing ratio, water vapor density, and air density, respectively. In Eq. (86), U (atm cm) is the absorber amount, while U (g/cm^2) is the absorber amount in Eq. (87). The path length is Z(km), and the subscript "o" denotes conditions at a standard temperature and pressure (viz. one atm and 273.15 K, respectively). The band model is further defined by the absorber parameters set (a, n, and m), and by a set of C' values at 5 cm^{-1} spectral intervals. In Eq. (85), C is redefined in terms of C' for computational convenience. The complete parameter set a, n, m, and C' , i = 1,2,...I, for I spectral intervals, was obtained from the equation

$$\varepsilon = \sum_i \sum_j \left\{\tau(i,j) - \tau_m(i,j)\right\}^2 \tag{88}$$

where ε is the least-squares error, minimized using the conjugate gradient descent, j = 1,2,...,J is an index for the data values, τ is a transmittance datum, and τ_m is the band model in Eq. (83).

Equation (83) is useful as a transmittance function because it is analytically simple and asymptotic to one and zero, respectively, as the argument ranges from zero to infinity. It was used with an earlier version of LOWTRAN[228] for curve-fitting to the empirical transmission tables in LOWTRAN 3B for water vapor, the uniformly-mixed gases, and ozone. Although not much physical significance may be attributed to this function, Pierluissi and Gomez[229] have shown that in some cases empirical approximations have out-performed theoretically-based band models such as the Elsasser[230] model and the Goody[231] random model. It does not approach the functional form of any such classical models in either the limiting weak-line or strong-line conditions (i.e., U/P very small or very large, respectively). Pierluissi, et al.[227] reported that it leads to a transmittance polynomial proposed by Smith[232] for use with water

vapor and carbon dioxide, which in turn, originated as an approximation to the strong-line limit to the random model. These earlier classical models were derived mostly for homogeneous paths, specific absorption-line configurations, and Lorentzian-broadening conditions. Equation (83) is used here along in-homogenous paths, for non-specific absorption-line configurations and for combinations of Lorentzian and Doppler broadening conditions.

The transmittance data used in connection with Eq. (88) in the determination of the complete set of the model parameters, consisted primarily of a combination of laboratory measurements and averaged line-by-line spectra. The line-by-line spectra were generated through calculations with FASCOD1C[14] which in turn used standard atmospheric profiles[233] and with the AFGL line parameter compilation[234,235]. The modeling of H_2O involved laboratory measurements[236,237] which were not considered in earlier versions of LOWTRAN. Table 27 summarizes the range of all of the transmittance-data parameters adopted for the LOWTRAN 7 band model.

The absorber vertical concentrations for each one of the gases modeled consisted of the profiles proposed by Smith[50], extrapolated so as to match the 33 altitude increments historically used in the LOWTRAN models. These vertical absorption concentrations were than updated with the Anderson[10] atmospheric constituent profiles.

4.1.3 Model Development

The numerical procedures discussed briefly in a previous section, were used with the available data to determine the parameters a, n, m, and C' for the 11 absorbers. In Eqs. (83) through (85) the parameters a, n and m are normally expected to be spectrally independent for a given absorber. The parameter C' is, then, expected to assume all the spectral variability of the band absorption. Although this was the case in general for all the gases having a small number of bands, a few required the use of different sets of parameters throughout the absorption spectrum. Table 28 summarizes the results derived from the modeling efforts. The criterion used for deciding on the number of bands to be modeled with a single-parameter set was that the RMS transmittance deviation between the model and the modeling data remained below 2 percent.

TABLE 27. Range of Calculated and Measured Transmittance Data Used in the Validation of the Band Models for Molecular Absorption

RANGE OF MODEL DATA

ABSORBER	SPECTRAL RANGE (cm^{-1})	PRESSURE (ATM) MEAS.	PRESSURE (ATM) CALC.	TEMP-PERATURE (K) MEAS.	TEMP-PERATURE (K) CALC.	ABSORBER Amount (ATM CM) MEAS.	ABSORBER Amount (ATM CM) CALC.	REFERENCES
Ammonia	0-2150	0.163E+0	0.102E+0		217	0.935E-2	0.962E-2	
(NH_3)		to	to	300	to	to	to	238
		0.824E+0	1.000E+0		300	0.308E+0	0.316E-1	
Carbon Dioxide	425-1440							
(CO_2)	1805-2855							
	3070-4065	0.100E-1	0.117E-1	216	217	0.804E-1	0.856E-2	
	4530-5380	to	to	to	to	to	to	236,241,242,243
	5905-7025	1.000E+0	1.000E+0	300	288	0.235E+5	0.300E+5	
	7395-7785							
	8030-8335							
	9340-9670							
Carbon Monoxide	0-175	0.304E+0	0.102E+0		230	0.730E-1	0.350E-1	
(CO)	1940-2285	to	to	300	to	to	to	236
	4040-4370	1.000E+0	1.000E+0		300	0.143E+3	0.275E+3	
Methane	1065-1775	0.100E+0	0.102E+0	302	217	0.922E-1	0.997E-1	
(CH_4)	2345-3230	to	to	to	to	to	to	236
	4110-4690	1.000E+0	1.000E+0	310	300	1.375E-1	1.359E+2	
	5865-6135							
Nitric Oxide	1700-2005	0.136E-1	0.546E-1		217	0.722E-1	0.619E-3	
(NO)		to	to	300	to	to	to	239
		0.966E+0	1.000E+0		288	0.310E+0	0.310E+0	

TABLE 27. (Continued) Range of Calculated and Measured Transmittance Data Used in the Validation of the Band Models for Molecular Absorption

RANGE OF MODEL DATA

ABSORBER	SPECTRAL RANGE (cm^{-1})	PRESSURE (ATM) MEAS.	PRESSURE (ATM) CALC.	TEMP-PERATURE (K) MEAS.	TEMP-PERATURE (K) CALC.	ABSORBER Amount (ATM CM) MEAS.	ABSORBER Amount (ATM CM) CALC.	REFERENCES
Nitrogen Dioxide	580-925	0.663E-1	0.551E-1	298	217	0.823E-2	0.948E-3	
(NO_2)	1515-1695	to	to	to	to	to	to	237
	2800-2970	1.000E+0	1.000E+0	328	288	0.919E+0	0.119E+0	
Nitrous Oxide	0-120							
(N_2O)	490-775							
	865-995							
	1065-1385	0.515E-4	0.102E+0	296	217	0.686E-3	0.962E-3	
	1545-2040	to	to	to	to	to	to	236
	2090-2655	0.484E+0	1.000E+0	301	300	0.387E+3	0.829E+2	
	2705-2865							
	3245-3925							
	4260-4470							
	4540-4785							
	4910-5165							
Oxygen	0-265	0.940E+0	0.102E+0		217	0.237E+4	0.489E+3	
(O_2)	7650-8080		to	300	to	to	to	240
	9235-9490		1.000E+0		300	0.219E+6	0.256E+9	
	12850-13220							
	14300-14600							
	15695-15955							
Ozone	0-200		0.102E+0		217		0.992E-3	
(O_3)	515-1275		to	300	to		to	
	1630-2295		1.000E+0		288		0.992E+1	
	2670-3560							

TABLE 27. (CONTINUED) Range of Calculated and Measured Transmittance Data Used in the Validation of the Band Models for Molecular Absorption

RANGE OF MODEL DATA

ABSORBER	SPECTRAL RANGE (cm^{-1})	PRESSURE (ATM) MEAS.	PRESSURE (ATM) CALC.	TEMP-PERATURE (K) MEAS.	TEMP-PERATURE (K) CALC.	ABSORBER Amount (ATM CM) MEAS.	ABSORBER Amount (ATM CM) CALC.	REFERENCES
Sulfur Dioxide	0-185	0.500E-1	0.102E+0	296	217	0.186E-1	0.987E-2	
(SO_2)	400-650	to	to	to	to	to	to	244
	950-1460	1.000E+0	1.000E+0	298	300	0.584E+1	0.290E+2	
	2415-2580							
Water Vapor			0.102E+0		217		0.964E-3	
(H_2O)	0-1000		to		to		to	
			1.000E+0		288		0.483E+4	
	1005-16045		0.102E+0		217		0.254E+3	
	16340-17860		to		to		to	237
			1.000E+0		288		0.255E+6	

The resulting spectral parameters C' at 5 cm^{-1} intervals are tabulated in Appendix A of the Pierluissi report,[13]

It is worth noting at this point that in the process of determining the band-model parameters in the region from zero to 20 cm^{-1}, it was necessary to mimic the lines in this region from zero to 20 cm^{-1}. This allowed for the calculation of mean transmittances at 5 cm^{-1} intervals using a triangular scanning function of 20 cm^{-1} full-width at half intensity on the monochromatic transmittance spectra.

Plots of the transmission functions (i.e. τ versus CW) for each absorber are also of interest when comparing the relative behavior of the different absorbers. Figures (42) through (45) depict the composite transmission functions for the uniformly-mixed gases, the trace gases, water vapor, and ozone. Plots of the spectral parameter C' for each absorber are included in Appendix B and individual transmission curves for each model are included in Appendix C of the Pierluissi report.[13]

Table 28. Summary of the Absorber Parameters for the Band Models Developed.

Absorber	Spectral Range (cm^{-1})	Absorber A	Model N	Parameters M	RMS Error (%)
Ammonia	0-385	0.4704	0.8023	-0.9111	1.41
(NH_3)	390-2150	0.6035	0.6968	0.3377	0.76
Carbon	425-835	0.6176	0.6705	-2.2560	1.84
Dioxide	840-1440	0.6810	0.7038	-5.0768	2.18
(CO_2)	1805-2855	0.6033	0.7258	-1.6740	2.27
	3070-3755	0.6146	0.6982	-1.8107	1.95
	3760-4065	0.6513	0.8867	-0.5327	2.49
	4530-5380	0.6050	0.7883	-1.3244	3.33
	5905-7025	0.6160	0.6899	-0.8152	1.28
	7395-7785	0.7070	0.6035	0.6026	0.30
	8030-8335	0.7070	0.6035	0.6026	0.30
	9340-9670	0.7070	0.6035	0.6026	0.30
Carbon	0-175	0.6397	0.7589	0.6911	0.28
Monoxide	1940-2285	0.6133	0.9267	0.1716	0.71
(CO)	4040-4370	0.6133	0.9267	0.1716	0.71
Methane	1065-1775	0.5844	0.7139	-0.4185	1.56
(CH_4)	2345-3230	0.5844	0.7139	-0.4185	1.56
	4110-4690	0.5844	0.7139	-0.4185	1.56
	5865-6135	0.5844	0.7139	-0.4185	1.56
Nitric Oxide	1700-2005	0.6613	0.5265	-0.4702	0.31
(NO)					
Nitrogen	580-925	0.7249	0.3956	-0.0545	1.49
Dioxide	1515-1695	0.7249	0.3956	-0.0545	1.49
(NO_2)	2800-2970	0.7249	0.3956	-0.0545	1.49
Nitrous	0-120	0.8997	0.3783	0.9399	0.24
Oxide	490-775	0.7201	0.7203	0.1836	1.49
(N_2O)	865-995	0.7201	0.7203	0.1836	1.49
	1065-1385	0.7201	0.7203	0.1836	1.49
	1545-2040	0.7201	0.7203	0.1836	1.49
	2090-2655	0.7201	0.7203	0.1836	1.49
	2705-2865	0.6933	0.7764	1.1931	1.23
	3245-3925	0.6933	0.7764	1.1931	1.23
	4260-4470	0.6933	0.7764	1.1931	1.23
	4540-4785	0.6933	0.7764	1.1931	1.23
	4910-5165	0.6933	0.7764	1.1931	1.23

Table 28. (Continued) Summary of the Absorber Parameters for the Band Models Developed.

Absorber	Spectral Range (cm^{-1})	Absorber A	Model N	Parameters M	RMS Error (%)
Oxygen	0-265	0.6011	1.1879	2.97381	1.42
(O_2)	7650-8080	0.5641	0.9353	0.1936	0.96
	9235-9490	0.5641	0.9353	0.1936	0.96
	12850-13220	0.5641	0.9353	0.1936	0.96
	14300-14600	0.5641	0.9353	0.1936	0.96
	15695-15955	0.5641	0.9353	0.1936	0.96
Ozone	0-200	0.8559	0.4200	1.3909	1.34
(O_3)	515-1275	0.7593	0.4221	0.7678	2.25
	1630-2295	0.7819	0.3739	0.1225	1.13
	2670-2845	0.9175	0.1770	0.9827	0.30
	2850-3260	0.7703	0.3921	0.1942	0.25
Sulfur	0-185	0.8907	0.2943	1.2316	1.24
Dioxide	400-650	0.8466	0.2135	0.0733	2.38
(SO_2)	950-1460	0.8466	0.2135	0.0733	2.38
	2415-2580	0.8466	0.2135	0.0733	2.38
Water	0-345	0.5274	0.9810	0.3324	1.99
Vapor	350-1000	0.5299	1.1406	-2.6343	1.26
(H_2O)	1005-1640	0.5416	0.9834	-2.5294	0.85
	1645-2530	0.5479	1.0043	-2.4359	1.08
	2535-3420	0.5495	0.9681	-1.9537	2.74
	3425-4310	0.5464	0.9555	-1.5378	1.54
	4315-6150	0.5454	0.9362	-1.6338	2.37
	6155-8000	0.5474	0.9233	-0.9398	1.97
	8005-9615	0.5579	0.8658	-0.1034	1.29
	9620-11540	0.5621	0.8874	-0.2576	1.52
	11545-13070	0.5847	0.7982	0.0588	0.93
	13075-14860	0.6076	0.8088	0.2816	1.23
	14865-16045	0.6508	0.6642	0.2764	0.59
	16340-17860	0.6570	0.6656	0.5061	0.77

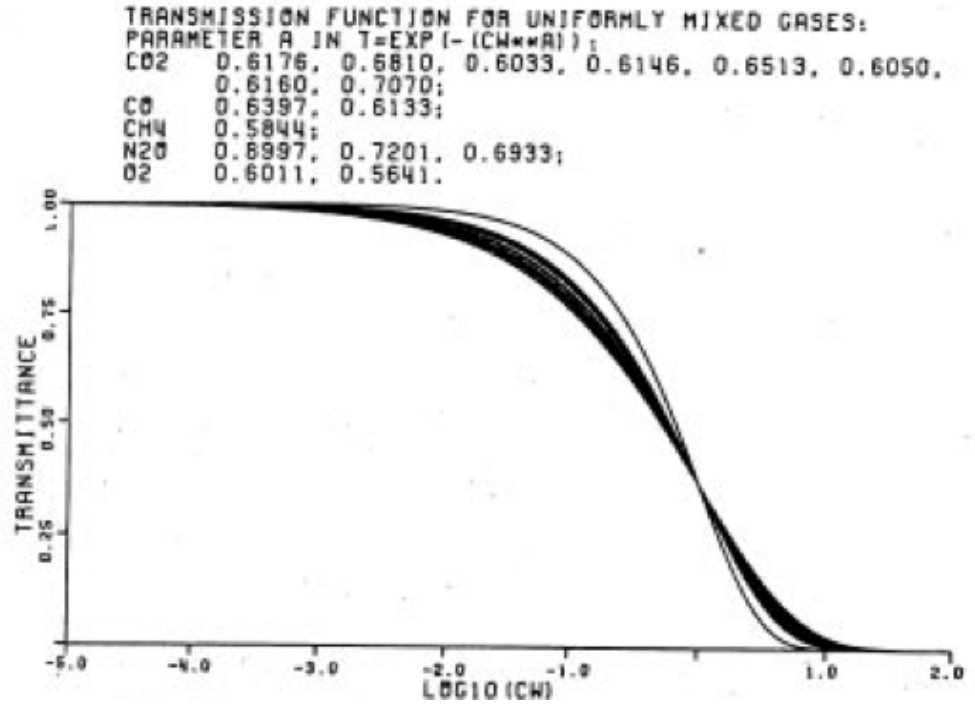

Figure 42. Composite Plot of the Transmission Functions (Eq. 83) for the Uniformly-Mixed Gases.

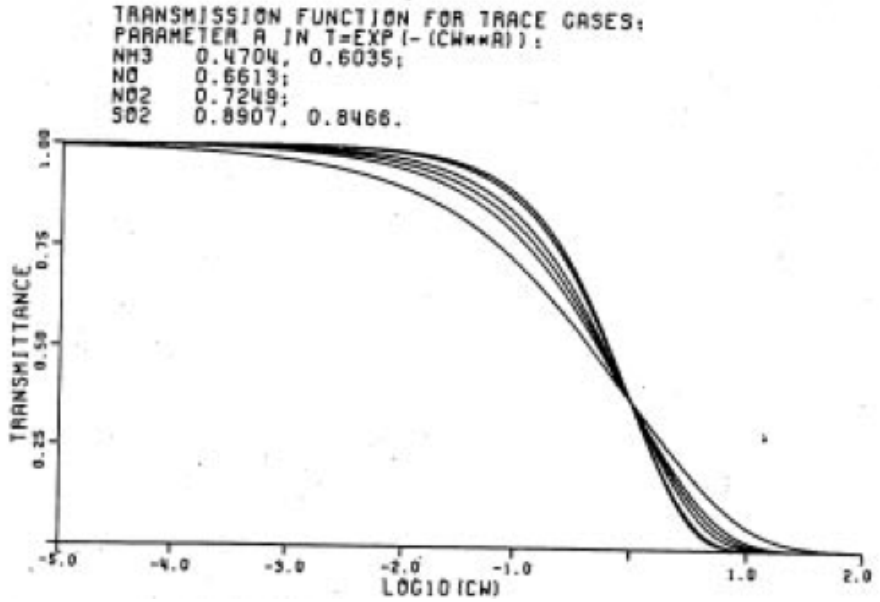

Figure 43. Composite Plot of the Transmission Functions (Eq. 83) for the Trace Gases.

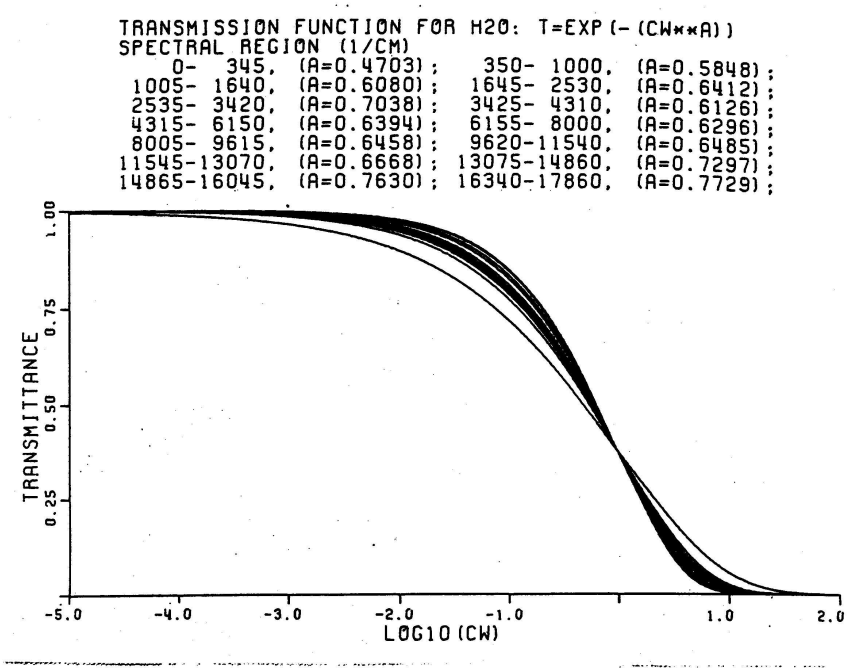

Figure 44. Composite Plot of the Transmission Functions (Eq. 83) for Water Vapor.

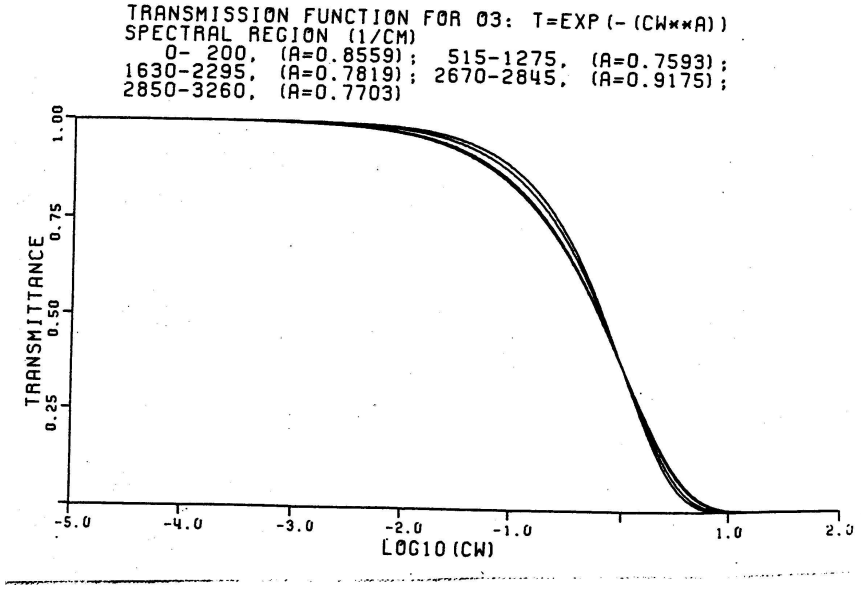

Figure 45. Composite Plot of the Transmission Functions (Eq. 83) for Ozone.

4.1.4 Comparisons with Measurements

Prior to the determination of the model parameters, the line-by-line data were compared with available measurements. Magnetic tapes containing measured spectra for CO_2, CH_4, NO_2, N_2O, SO_2, and H_2O were used. Only graphical data were available for NH_3, CO, NO, O_2, and O_3,. Graphical comparisons of ozone spectra were made only over a narrow spectral region and, hence, are not worthy of further discussion. However, H_2O comparisons were made over nearly the entire infrared region and were included in two separate reports. Appendix D of the Pierluissi report [13] shows some representative plots of both the nearly monochromatic spectra and of the corresponding degraded values.

Once the spectral comparisons were completed and the band-model parameters determined, comparisons were then made between the degraded line-by-line and model-calculated transmittances. Appendix E (Ref. 13) shows typical comparisons for H_2O and O_3, while similar comparisons for the remaining gases may be found in an earlier report by Pierluissi.[245] Special calculations were made for several bands for the remaining gases. Such cases included bands in the spectral region from 0 to 350 cm^{-1} of NH_3, CO, N_2O, O_2, O_3, SO_2, and H_2O, as well as several others, primarily in the infrared region. Sample comparisons between the degraded line-by-line and band-model calculations for the gases absorbing in the region from 0 to 350 cm^{-1} are shown separately in Appendix F of the Pierluissi report. [13]

Upon completion of the modeling of all the absorbing species, the resulting band models were incorporated into LOWTRAN 7. Figures (46) through (48) show the spectral differences between the transmittances from LOWTRAN 6 and those calculated with the LOWTRAN 7 band models for the combined uniformly-mixed gases, water vapor and ozone, respectively. They are for a path tangent to the earth' s surface, extending from one end of the U.S. Standard Atmosphere to the other. They indicate that, in general, transmittance was over-estimated in LOWTRAN 6. This difference may be attributed to inaccuracies in the band models, as well as to absorption bands not modeled in the original LOWTRAN development. More examples of these types of comparisons are shown in Appendix G (Ref. 13). Additional transmittance plots for those paths using the proposed band models are included in Appendix H (Ref. 13).

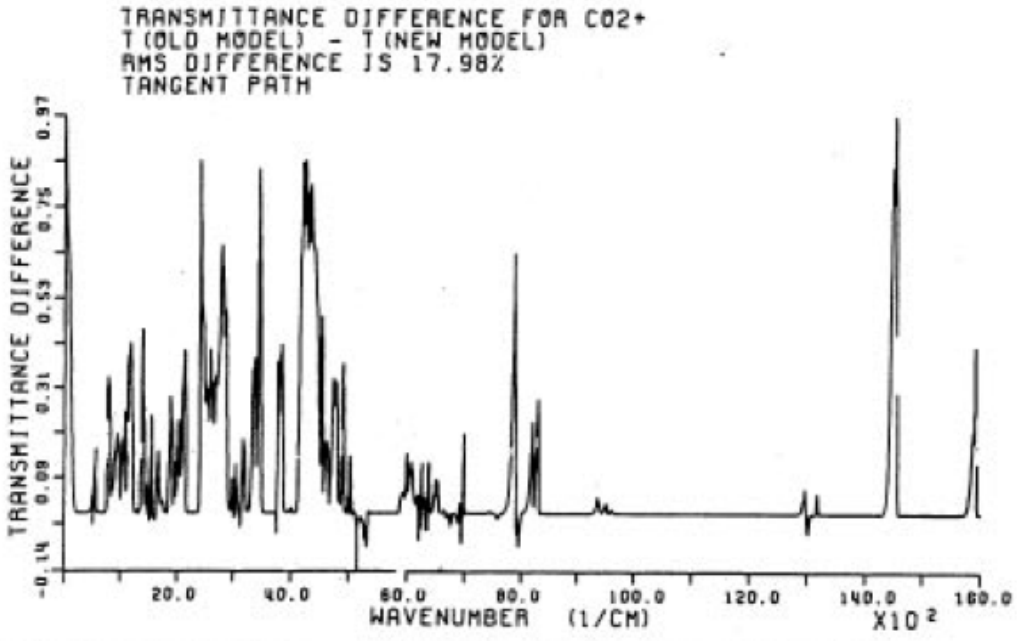

Figure 46. Transmittance Difference Between LOWTRAN 6 Calculations and the LOWTRAN 7 Model for the Uniformly-Mixed Gases Along a Path Tangent to the Earth' s Surface in the U.S. Standard Atmosphere.

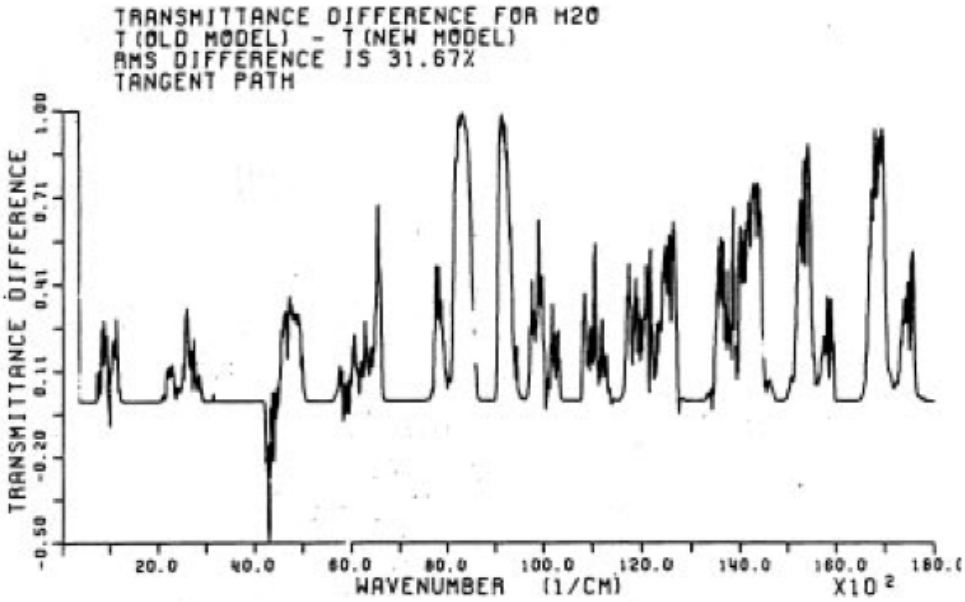

Figure 47. Transmittance Difference Between LOWTRAN 6 Calculations and the LOWTRAN 7 Model for Water Vapor Along a Path Tangent to the Earth' s Surface in the U.S. Standard Atmosphere.

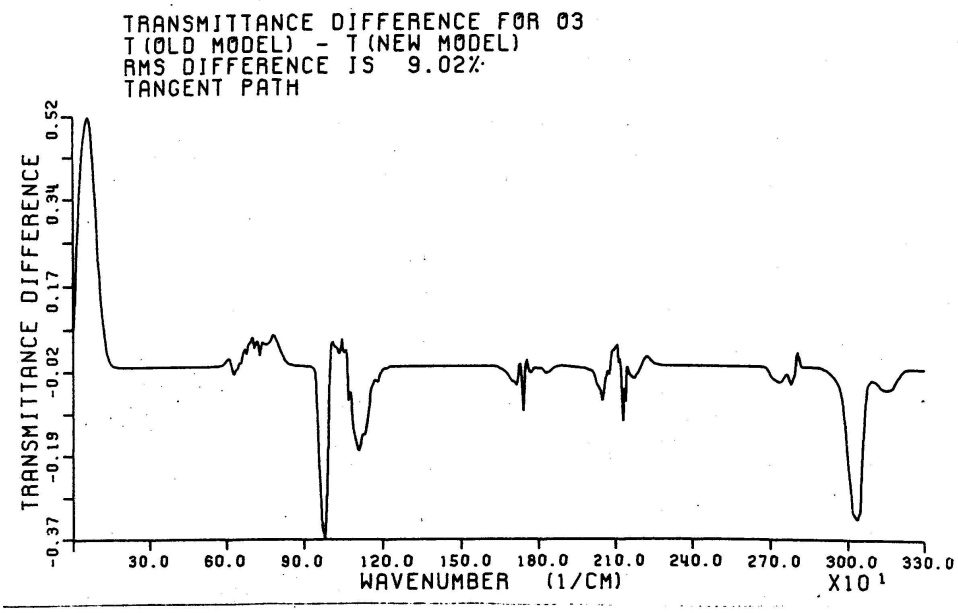

Figure 48. Transmittance Difference Between LOWTRAN 6 Calculations and the LOWTRAN 7 Model for Ozone Along a Path Tangent to the Earth' s Surface in the U.S. Standard Atmosphere.

The band models were designed for 20 cm^{-1} intervals and the spectral parameters repeated at 5 cm^{-1} steps for easy incorporation into upgraded versions of LOWTRAN. The transmission function consisted of an exponential, defined by one spectral and three absorber parameters, representing a simple power relation between the pressure, temperature, and absorber amount along a slant atmospheric path. The determination of the parameters was accomplished through the use of non-linear numerical techniques.

Initially, the available measured data for CO_2, CH_4, NO_2, N_2O, SO_2, and H_2O were compared for accuracy with line-by-line calculations using FASCOD1C. Graphical data in the form of spectral curves were available for comparison for NH_3, CO, NO, O_2, and O_3. Following this form of validation, the line-by-line data, and in some cases the transmittance measurements, were used in the determination of all the band-model parameters for all the gases of interest. Comparisons were then made between the degraded measurements, the degraded transmittance calculations, and the recalculated transmittances using the resulting band models.

As a result of all the transmittance comparisons made in the process of the development and validation of the band models for molecular absorption, the following conclusions may be made:

1. The high-resolution transmittance measurements available in magnetic tape form for CO_2, CH_4, NO_2, N_2O, SO, and H_2O, and in graphical form for NH_3, CO, NO, O_2, and O_3, agreed reasonably well with line-by-line calculations using FASCOD1C.

2. Calculations using the band-model parameters, agreed within a mean (over all wavenumbers and gases) RMS transmittance difference of 2.0% with the degraded line-by-line data used in their determination.

3. Calculations using these LOWTRAN 7 band models with the corresponding transmittances computed with LOWTRAN 6 agreed within 2.85% for the uniformly-mixed gases, 16.36% for H_2O and 1.84% for O_3, along a vertical path from sea level to the top of the U.S. Standard Atmosphere.

4.2 Nitric Acid

The transmittance due to HNO_3 has been assumed to lie in the weak-line or linear region. Absorption coefficients digitized at 5 cm^{-1} intervals for the 5.9-μm, 7.5-μm, and 11.3-μm bands of HNO_3 are in the LOWTRAN model. These coefficients were obtained by Goldman, Kyle and Bonomo[246] by fitting their experimental results with the statistical band-model approximation, and these results are displayed in Figure 49.

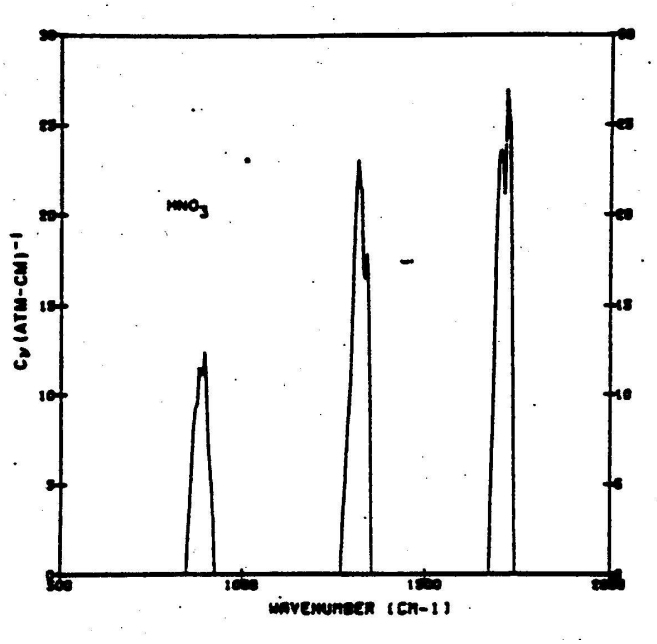

Figure 49. Absorption Coefficient C_ν for Nitric Acid, from 500 to 2000 cm^{-1}.

4.3 Nitrogen Continuum Absorption

The continuum due to collision-induced absorption by nitrogen in the 4-μm region, is included in the LOWTRAN model based on the measurements of Reddy and Cho[247] and Shapiro and Gush[248] (see also McClatchey et al[249]). The nitrogen continuum absorption is displayed in Figure 50. The transmittance due to continuum absorption is assumed to follow a simple exponential law.

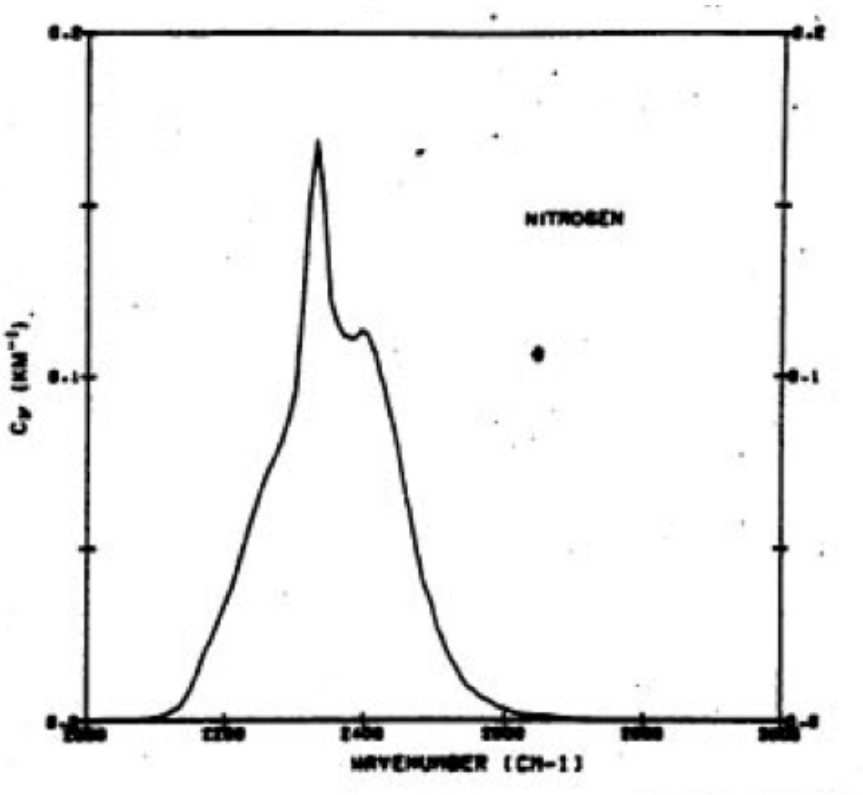

Figure 50. Absorption Coefficient C_ν for the Nitrogen Continuum, from 2000 to 3000 cm^{-1}.

4.4 Molecular Scattering

The attenuation coefficient (km^{-1}) due to molecular scattering, (stored in the variable ABS(6)), is introduced into MODTRAN via the following expression:

$$ABS(6) = \nu^4 / (9.26799 \bullet 10^{18} - 1.07123 \bullet 10^{9} \bullet \nu^2) \qquad (89)$$

where ν is in wavenumbers (cm^{-1}). The above expression was obtained from a least square fit to molecular scattering coefficients reported by Penndorf[250]. This function improves the fit in the ultraviolet region.

4.5 Ultra Violet Absorption

Spectroscopic data describing the ultraviolet absorption properties of molecular oxygen and ozone have been collected for incorporation into the FASCODE and MODTRAN models. This data includes the O_2 Herzberg continuum and Schumann-Runge bands as well as the O_3 Hartley and Huggins bands. These systems result in the dissociation of the parent molecule and the creation of atomic oxygen.

4.5.1 UV Oxygen Absorption

The dissociation of oxygen allotropes is of paramount importance to the chemical makeup of the earth' s atmosphere. The strongly absorbing O_2 Schumann-Runge and weaker Herzberg systems influence differing altitude regimes in the atmosphere because of the relative strengths of their respective transition probabilities. Figure 51 (after Watanabe[255]) shows the approximate depth of penetration of solar irradiance throughout the UV spectral range. In general, solar radiation in the 0.175 to 2.0 μm spectral region is completely absorbed by the Schumann-Runge system at altitudes above 40 km. At longer wavelengths (greater than 0.2 μm) absorption by ozone begins to compete with the residual Schumann-Runge and Herzberg absorption; the combination does not allow solar energy at wavelengths less than 0.3 μm to penetrate to the surface. In addition to this shielding of high energy solar radiation, the UV absorption properties of ozone provide the dominant source of stratospheric heating.

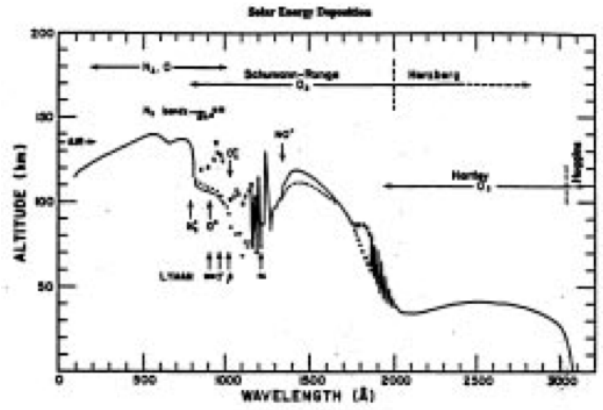

Figure 51. The Approximate Altitude at Which 1/eth of the Solar Irradiance is Deposited; after Watanabe.[255] In the UV Wavelength Spectral Range, MODTRAN Includes the Effects of the Ozone Hartley and Huggins Bands Plus Portions of the Molecular Oxygen Schumann-Runge and Herzberg Systems.

HERZBERG CONTINUUM

While the Herzberg continuum absorption is small relative to both the Schumann-Runge and ozone contributions, it is extremely important to the maintenance of the stratospheric photochemical balance. Until recently the Herzberg continuum was believed to be almost 40% stronger than the currently accepted estimate. Since it lacks any detailed spectral structure, the absorption properties are readily described by an analytic function proposed by Johnson et. al.[23] After fitting the combined measurements of U.S. and French laboratories[22] to a function of this form, the cross section can be expressed as:

$$\sigma(0,\mu m) \;=\; 6.88E-24\; R \exp\left[-69.7374\left\{\ln(R)\right\}^2\right] \qquad (96)$$

where: R = 0.20487/(μ)
and μ = wavelength in μm.

The longevity of the erroneously large Herzberg values can be traced to their pressure dependence, related to dimer formation. The cross sections are so small that laboratory determinations have to rely on high pressure techniques to create the necessary opacities. Historically, extrapolation to zero pressure was attempted, but with little success. In fact, long-path, low pressure stratospheric measurements of attenuation of solar irradiance provided the first verification that the laboratory estimates were seriously in error.[256,257]

Accurate determination of the pressure dependence of O_2 within an O_2 environment is an important part of any laboratory measurement of the cross section. Yoshino et.al.[22] provide an equation of the form:

$$\sigma(p,\mu m) \;=\; \sigma(o,\mu m)\left(1.+\left(\Gamma(\mu m)/\sigma(o,\mu m)\right)\bullet P_{O2}(Torr)\right) \qquad (97)$$

where Γ(μm) represents the pressure dependent term. However, because of coding considerations the MODTRAN formulations replace the spectrally dependent Γ with a proportionality constant,

$$\Gamma(\mu m)/\sigma(o,\mu m) \;\approx\; 1.81E-3 \quad , \qquad (98)$$

that is consistent to within 10% for most of the Herzberg spectral range (between 0.20 and 0.23 μm); see Fig. 52. The errors gradually increase to 30% at 0.24 μm. The magnitude of this wavelength-dependent error is generally tolerable because the pressure contribution is often a fractionally small portion of the diminishing O_2 cross

section which is overwhelmed by the ozone cross section. However, near the surface (high pressures and low ozone mixing ratios) the errors can become significant.

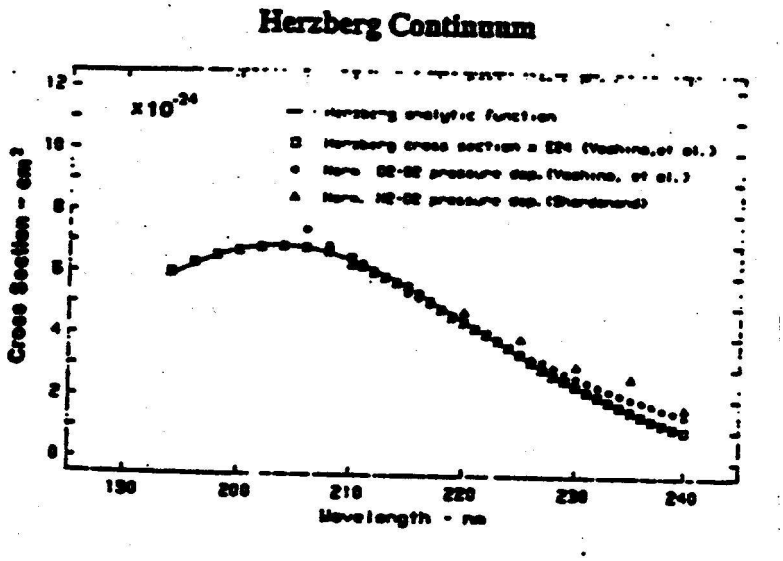

Figure 52. The Form of the Analytic Function Used to Express the Herzberg Continuum

Within MODTRAN 2, Plus the Supporting Measurements for that Continuum and its Normalized Pressure-Dependent Terms.

Atmospheric pressure dependence is also governed by interaction with Nitrogen (O_2 - N_2 dimer formation). Shardanand[24] has provided an estimate of this effect, N_2 being approximately 45% as efficient as pure O_2. Figure 52 shows the degree of spectral similarity between the N_2 dimer effect and the pure Herzberg absorption, $\sigma(o,\mu m)$, hence it has similarly been scaled to $\sigma(o,\mu m)$. The pressure dependence of the Herzberg continuum for a combination of 21% oxygen and 78% nitrogen, including the 45% efficiency factor is then:

$$\sigma(p,\mu m) = \sigma(o,\mu m)\left(1. + 0.83(P/P_o)(T_o/T)\right) \quad . \qquad (99)$$

The total pressure has been replaced by a normalized density function with P_o and T_o at STP.

As mentioned above, the Herzberg bands are not included explicitly in MODTRAN. While they would not contribute to the photochemical production of odd oxygen, there is some contribution in the calculation of total transmittance.[259] This has been approximated in MODTRAN by extending the Herzberg analytic equation to longer wavelengths (0.277 μm or 36000 cm^{-1}) with a linearly smooth damping to zero

absorption at that arbitrary cutoff. The errors introduced by this approximation are potentially serious for transmittance calculations for ozone-poor lines of sight (such as solar-blind calculations at the surface[260]). However, for most general cases the effect of the omission is not discernible. A more correct band model approximation is planned for an upgraded version of MODTRAN.

SCHUMANN-RUNGE BANDS

The O_2 Schumann-Runge band analysis has been addressed in two ways: (1) a line-by-line spectroscopic atlas, similar in format to the HITRAN database[20], has been calculated from published energy levels; and (2) a one parameter 20 cm^{-1} resolution band model has been generated for incorporation into LOWTRAN and MODTRAN. Using the new atlas, line-by-line syntheses of the Schumann-Runge cross sections, including temperature-dependence of the vibronic population levels, have been created using FASCOD3P. It is important to note, that while the Schumann-Runge system exhibits very rich spectral structure, including rotational splitting at fractions of a wavenumber separation, the half widths of the lines are sufficiently broadened by pre-dissociation to be independent of pressure and temperature. Figure 53 shows a portion of the new database, with line positions and relative strengths at line center; the triplet structure is not depicted. Individual band groupings are easily identified.

The 20 cm^{-1} band model for the Schumann-Runge system (as currently available in MODTRAN) was developed from a similar line-by-line formulation [25] with additional laboratory measurements.[261] The band model is inadequate for detailed spectroscopic calculations because it does not correctly simulate the strong temperature-dependence of the O_2 cross sections due to the change in population of the first excited state
(v" = 1). This effect is strongest in the spectral regions away from the v" = 0 band heads (i.e. in the window regions). Solar energy penetrates deepest into the atmosphere in just these window regions, so an improved formulation is mandatory if it is needed for photochemical calculations.

Given these stated inaccuracies, the band model does show reasonable agreement with in situ measurements of the depleted solar irradiance. In Figure 54 data from the 1983 balloon flight of a single dispersion half-meter Ebert-Fastie spectrometer [262] is compared to simulated data using the new Schumann-Runge band model. These calculations also include other major portions of the LOWTRAN 7 algorithm, specifically the Herzberg continuum and ozone cross sections. The only exception to LOWTRAN 7

compatibility is the solar irradiance; the lack of solar spectral signature can be seen near 0.199 μm (199 nm) in the simulated data. This band model algorithm is patterned on

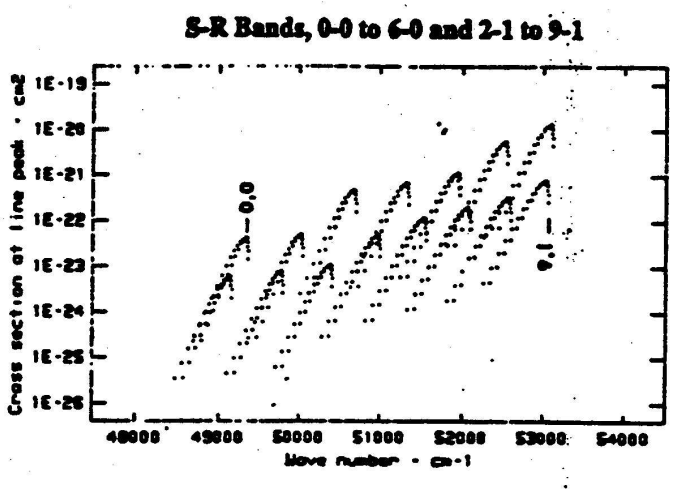

Figure 53. Calculated Line Positions and Strengths for a Portion of the Schumann-Runge Band system. MODTRAN Directly Accesses Only those Bands with Frequencies Less than 50,000 cm^{-1}, Although Coding for the Entire Depicted Range is Included.

the one principally developed for the IR by Pierluissi and Maragoudakis,[13] including the use of the Pierluissi fitting parameters for O_2. A single spectral function [C(μm)] has been calculated for the wavelength range from 0.1875 to 0.203 μm. With a more sensitive band model, the wavelength range of MODTRAN can be extended to include the entire Schumann-Runge system. The expectation is that this new band model will separate the v" = 0 from the v" = 1 bands, with the treatment of the ground state transitions remaining as described above. [**NOTE**: while the preliminary band model parameters are available within the MODTRAN 2 coding, they are not directly accessible for wavelengths smaller than 0.2 μm. This limitation is currently imposed by an "IF TEST" related only to the non-availability of the aerosol functions for these wavelengths. The solar irradiance, Rayleigh scattering coefficients and an estimated Herzberg continuum are all provided.]

4.5.2 UV Ozone Absorption

Absorption by ozone, the remaining UV-active oxygen allotrope, is described in both MODTRAN and FASCODE by a temperature-dependent (quadratic) continuum. This continuum includes two major bands, the spectrally overlapping Huggins and Hartley systems. [NOTE: Steinfeld, et.al.[263] present an excellent review.] The Hartley band is

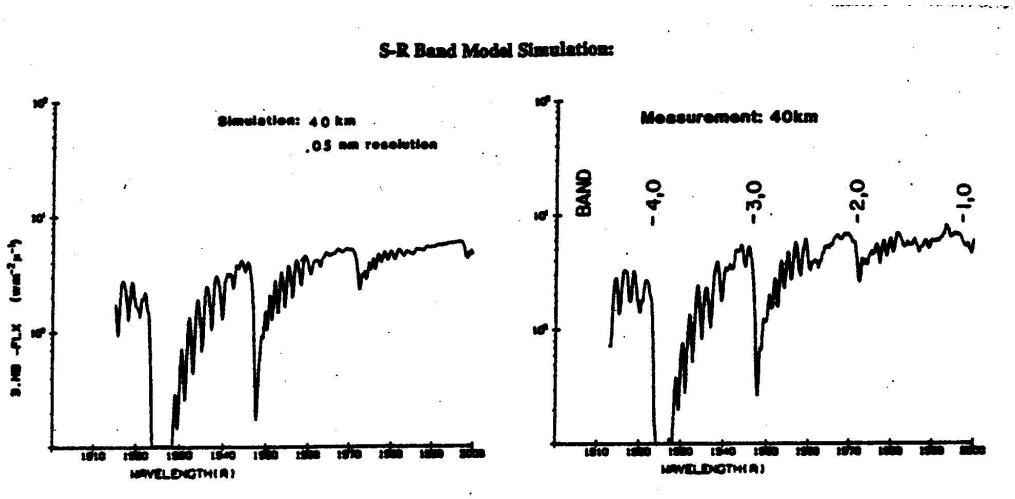

Figure 54. A Comparison of the LOWTRAN 7 Schumann-Runge Band Model Algorithm and an Actual Balloon-Borne Measurement of in situ Solar Irradiance. The Balloon Altitude was Approximately 40 km with the Sun at 24° Zenith Angle. The Model Easily Reproduces the 4-0, 3-0, 2-0 and 1-0 Band Heads.

by far the more efficient at production of the first excited state of atomic oxygen, $O(^1D)$, with approximately 88% efficiency, while the Huggins band fragmentation generally leads to the ground state product for atomic oxygen, $O(^3P)$:

$O_3 + h\nu \rightarrow O_2(^3\Sigma) + O(^3P)$: Huggins

$0.36\ \mu m > \text{wavelengths} > 0.31\ \mu m$

and:

$O_3 + h\nu \rightarrow O_2(^1\Delta) + O(^1D)$: Hartley

$\text{wavelengths} < 0.31\ \mu m$

The atomic oxygen excitation state is critical to subsequent photochemical reactions because $O(^1D)$ is the energetically preferred partner. The Hartley band absorption is very strong, exhibiting only marginal structure and generally no temperature-dependence. The Huggins system has a much more pronounced band structure and moderate to strong temperature-dependence, although the features are still broad enough not to be amenable to detailed line-by-line representation (Figure 55). Katayama [264] has established definitive vibrational assignments and inferred a band origin.

Research studies of the ozone absorption cross section have been available since the early 1900' s. The relatively recent measurements of Bass and Paur[27] form the basis of MODTRAN 2 and FASCOD3 formulation. Their values, including quadratic temperature-dependence, are provided at 5 cm^{-1} intervals from 41000 to 30000 cm^{-1} (0.24 to 0.33 μm). Subsequent measurements of Molina and Molina[28] have been used in combination with those of Yoshino et.al.[29] to expand the temperature-dependent range to 0.34 μm, with a final extension to 0.36 μm using the values of Cacciani, et.al.[30,265] . At wavelengths less than 0.24 μm, the temperature-independent values of Molina and Molina were again adopted (between 0.18 and 0.24 μm). These various data sources agree very well (usually better than 3%) in the regions of overlap. All feature replication is real and suitable; that is, the small spectral features are represented at their natural resolution whereby a line-by-line calculation would not provide significantly greater detail.

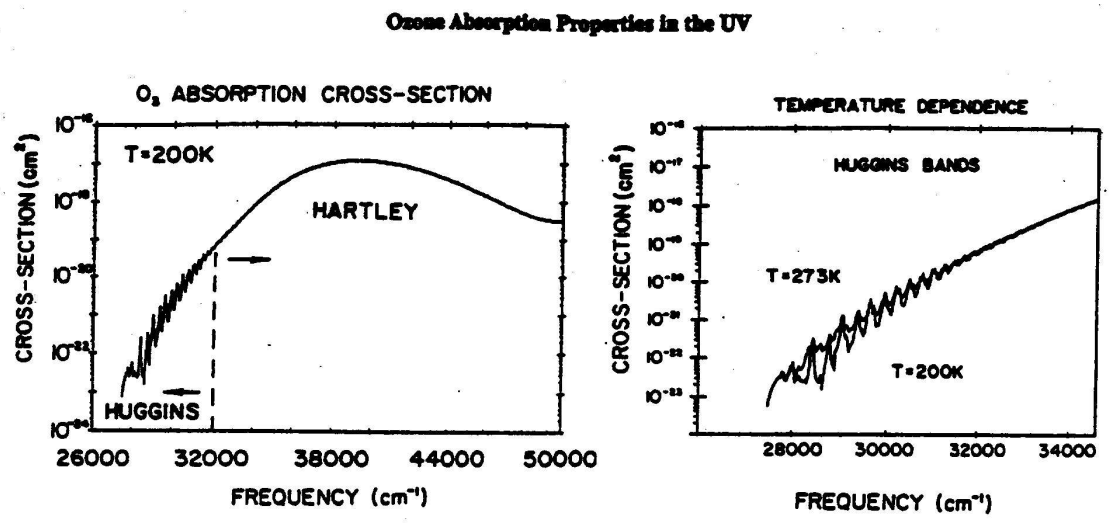

Figure 55. The Ozone Absorption Cross Sections as Available in MODTRAN. Structure at the Center of the Hartley System does not Appear in this Logarithmic Representation but is Provided in the Code.

4.6 Aerosol Transmittance

Within a given atmospheric layer of path length DS, in km, the transmittance, $\tau(\nu)$, due to aerosol extinction is given by

$$\bar{\tau}(\nu) \;=\; EXP\left[-EXTV\,(\nu)\bullet HAZE\;\bullet DS\right] \qquad (100)$$

where EXTV(ν) is the normalized extinction coefficient for the wavenumber ν of the appropriate aerosol model and altitude. HAZE is the aerosol scaling factor (see section 2.3).

EXTV(ν) is found by interpolation of the values stored in the code for the required wavenumber and relative humidity. HAZE is determined by interpolation of the appropriate aerosol scaling-factor profiles according to the meteorological range and season.

5. ATMOSPHERIC RADIANCE

5.1 Radiative Transfer Equations

The radiance algorithm for MODTRAN 2 has been modified to specifically handle optically thick layers. Cornette[266] had reported on a possible correction for LOWTRAN 7.

Considering a single isolated layer, a direct application of the simple radiance equation leads to:

$$R \;=\; B\,d\tau \quad or \quad R \;=\; (1-\tau) \tag{101}$$

where R = Radiance, B = Planck Function, and $d\tau = (1-\tau)$, the change in transmittance, τ across the layer. The Planck Function is defined for a Curtis- Godson density-weighted temperature for the layer. For an optically thin case, the observed radiance in this scenario is independent of viewing direction. [Note that for typical lines-of-sight across a multi-layered atmospheric path, radiance is dependent on viewing direction while total transmittance remains independent of the observer' s position.] However, if this single layer is optically thick and includes a directional temperature gradient, the observed radiance will be either larger (emanating from a warmer thermal region closer to the observer) or smaller (emanating from the closer cooler region). One approach in accommodating the opacity-imposed directionality consists of subdividing the layers into less optically thick entities. This approach is very awkward so various pragmatic solutions have been considered. Wiscombe[267] and Ridgway et.al.[268] recently suggested a method whereby the Planck Function and optical depth is assumed to vary linearly between the boundaries of the layer. Following this approach, Clough et al[269] produced an expression (his Eq. 13), dependent on the Planck (B) functions for the Curtis-Godson temperature and the nearest boundary temperature, coupled with both the layer transmittance and optical depth:

$$R \;=\; (1-\tau)\;\left\{B_n + 2(B-B_n)\left[\frac{1}{\tau} - \frac{\tau}{(1-\tau)}\right]\right\} \tag{102}$$

where the subscript n implies the nearest boundary, t = layer optical depth between boundaries, and τ = layer transmittance, for a single layer. For a multi-layer scenario, this local layer radiance becomes the input for its neighbor, and the full path solution is

reached through recursive calculations; (see Eq. 31 of Clough, et al[14]). The layer transmittance then becomes: $\tau = \tau(b+1)/\tau(b)$ where $\tau(b)$ and $\tau(b+1)$ are the full path transmittances from observer to boundary b and (b+1), respectively. The required optical depth term is an "effective" optical depth, due to the degraded 2 cm^{-1} resolution, and is derived from the ratios of adjacent full path transmittances at MODTRAN resolution:

$$T = -\ln\left\{\tau(b+1)/\tau(b)\right\} \quad (103)$$

The radiance equation for a single layer (Eq. 102), including the "linear in tau" approximation, appears the same as the simple radiance equation (Eq. 101) if the bracketed quantity { } is thought to contain an "equivalent" Planck function, defined by the optical depth weighting. This technique is fully implemented in MODTRAN 2 and provides excellent agreement with FASCOD3P results for optically thick calculations. Figure 56 depicts a comparison between FASCOD3P and MODTRAN 2 calculations in the optically thick 15 micron CO_2 band.

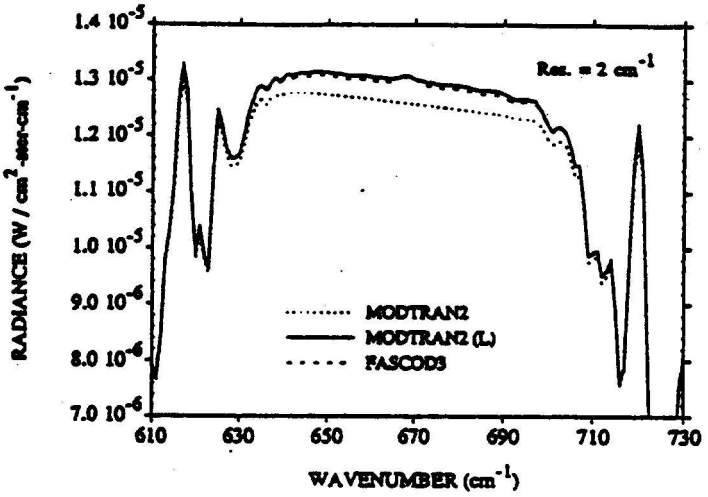

Figure 56. Radiance Calculations in the Optically Thick 15 μm Band for a Single 1 km Path with Boundary Temperatures of 288.15k and 281.15k, as Observed from the Warmer Boundary. The FASCOD3P Calculation Employs a Slightly Different Approximation to the "linear in tau" Algorithm used in MODTRAN 2. The Dotted Curve Represents the Old MODTRAN Calculation Which is Deficient Within the Band Center.

5.2 Improved Solar Source Function

An earlier version of LOWTRAN (Kneizys et al[3]) had included the solar spectrum (based on Thekeakara[35]) for calculating the single-scattered and/or directly transmitted

solar radiances. The data used for this spectrum was not at a resolution consistent with the treatment of molecular absorption in either LOWTRAN or MODTRAN. (Note - in LOWTRAN 6 the visible and UV ozone absorption were provided at 200 and 500 cm^{-1} intervals respectively. Concerns have been raised in the literature on the accuracy of the Thekeakara[35] data (see Frhlich[270], and the references therein).

These particular concerns led to the development of a new solar spectrum for LOWTRAN 7 and MODTRAN. The primary data sources used for the different spectral regions are summarized in Table 30.

Table 30. Data Sources Used for the Solar Spectrum

Wavelength Range (μm)	Frequency Range (cm^{-1})	Source
0.17400 to 0.35088	28500 to 57470	VanHoosier et al. (1987)[31] (SUSIM)
0.35094 to 0.86806	11520 to 28495	Neckel & Labs (1984)[33]
0.86843 to 3.2258	3100 to 11515	Wehrli (1985)[34]
3.2258 to 3.4483	2900 to 3100	Smooth Transition between Wehrli and Thekeakara
3.4483 to ∞	0 to 2900	Thekeakara (1974)[35]

The smooth transition between the Thekeakara and Wehrli data was accomplished as follows:

$$S(x) = \begin{cases} Thekeakara, & x < 2900 cm^{-1} \\ w(x) \bullet Thekeakara + \left[1 - w(x)\right] \bullet Wehrli, & 2900 < x < 3100 cm^{-1} \\ Wehrli, & 3100 cm^{-1} < x \end{cases}$$

where: S(x) is the solar spectrum at a frequency, x,

and w(x) is given by the expression:

$$w(x) = (x-b)^2 \quad \frac{(2x - 3a + b)}{(b-a)^3} \qquad (104)$$

This polynomial has the following properties:

w(a) = 1
w(b) = 0
w' (a) = w' (b) = 0

where: a = 2900 cm^{-1} and b = 3100 cm^{-1} .

In other words, over the interval from ' a' to ' b' , w(x) goes from a value of one to zero, with the derivative equal to zero at the end points.

The individual data sets, from the different sources, were determined at a resolution compatible with the models by passing a 20 cm^{-1} triangular scanning function over the data values. This data is then tabulated at 5 cm^{-1} intervals for the frequency range of 0 to 57495 cm^{-1}, to ensure adequate sampling, and to maintain consistency within the models. Except for the SUSIM data (VanHoosier et al.)[32], which was measured with a 0.15 nm resolution, the remaining data sets were all measured at a coarser resolution than 20 cm^{-1}. The low frequency data (x < 500 cm^{-1}) was tabulated directly as interpolated from the Thekeakara[35] values, since the strong decrease with frequency, causes a systematic increase of the values when smoothed with the 20 cm^{-1} scanning function.

Within the context of LOWTRAN and MODTRAN, the solar flux values have been stored in a look-up table. In an effort to reduce memory requirements, the effect on the accuracy of eliminating portions of the data and re-generating them by interpolation was examined. For the SUSIM data (x > 28500 cm^{-1}) the values were retained at a 10 cm^{-1} spacing. For the remainder of the data (x < 28500 cm^{-1}) the values were used with a 20 cm^{-1} spacing. A four-point Lagrange interpolation scheme was used. For the low frequencies (x < 100 cm^{-1}), the look-up table and interpolation were replaced with a simple power-law fit to the solar flux values. The scenario described here is implemented in the FORTRAN Function *FSUN*.

5.3 SOLAR/LUNAR SINGLE SCATTERING MODEL

5.3.1 Introduction

The radiation propagating through the atmosphere originates from the following sources: gaseous emission along the line-of-sight, transmitted extraterrestrial

(solar/lunar) sources or background emission (earth or target), and radiation scattered into the line-of-sight by aerosols or molecules.

Previous versions of LOWTRAN have calculated atmospheric radiance due only to gaseous and background emissions. While in many cases these two sources dominate the atmospheric radiance, there are other cases of interest where the scattered radiance is of equal or greater importance. Until now LOWTRAN has treated scattering only as a loss mechanism.

A number of techniques exist that include the full effects of scattering on atmospheric radiance: these include for example, Monte Carlo and "adding/doubling" techniques. These techniques take into account multiple scattering and can include both external and internal sources. These techniques however, tend to be computationally expensive and some of them are incompatible with the spectrally-averaged band model used in MODTRAN.

In many situations, a complete multiple scattering calculation is not necessary and the scattered radiation is dominated by solar radiation that has been scattered only once. Calculations of the single solar (or lunar) scattered radiation is relatively simple and fits well within the context and structure of MODTRAN.

Calculation of single scattering has been incorporated as an option in MODTRAN. The next two sections of this chapter develop the algorithm for single scattering and show the verification of the MODTRAN calculations against other methods. Then the phase functions for scattering by atmospheric aerosols and molecules will be explained. Next, sample calculations of solar scattering are shown that illustrate the conditions where the singly scattered radiation becomes significant compared to the emitted radiation. Finally, recommendations are given concerning the range of applicability of the single scattering model. For a more detailed discussion of the single scattering model, see Reference 271.

5.3.2 Radiative Transfer

Before proceeding further, it will be helpful to introduce the following nomenclature:

SUPERSCRIPTS;

A	aerosol
M	molecular

SUBSCRIPTS:

e	extinction
a	absorption
s	scattering

ps	primary solar path (sun to scattering point)
op	line-of-sight optical path (scattering point to observer)

OTHER QUANTITIES:

k	monochromatic volumetric extinction, absorption, or scattering coefficient
$\tau = e^{-ks}$	monochromatic transmittance over a homogeneous path length is due to extinction absorption, or scattering
$P(\gamma)$	scattering phase function for a scattering angle γ
I^{SUN}	solar extraterrestrial intensity
I^{MOON}	lunar extraterrestrial intensity

Note that the dependence of most quantities on the spectral frequency ν will be shown by a subscript ν, although it will sometimes be suppressed for simplicity of notation when the concept is clear from context.

The monochromatic intensity (radiance) seen by an observer looking along a particular directional path is the sum of contributions from all sources lying along the line-of-sight. The sources are either primary sources (infrared emission) or scattering sources. The scattering source function J for scattering points along the observer' s line-of-sight can be expressed in terms of the local incoming intensity at each point by $I_\nu(\hat{n}')$ by

$$J_\nu(\hat{n}) = \int I_\nu(\hat{n}')\left(P_\nu^A\ k_s^A + P_\nu^M\ k_s^M\right) d\Omega' \quad , \tag{105}$$

where $\hat{n}$ is the unit vector directed toward the observer and $\hat{n}'(\Omega')$ is to be integrated over the solid angle denoted by Ω' . With only single solar/lunar scattering included, the incident intensity $I_\nu(\hat{n}')$ is given by:

$$I_\nu(\hat{n}') = I_\nu^{SUN}\ \tau_{e,ps}^{A+M} \quad \delta(\hat{n}', \hat{n}_s') \tag{106}$$

where $\hat{n}_s'$ is the direction of the incident solar/lunar radiation at the scattering point. A schematic of the scattering geometry for a particular sun/observer orientation is displayed in Figure 57. The path that the sunlight/moonlight takes in passing through the atmosphere prior to being scattered at any scattering point P will be called the ' primary solar' path. Other sources besides direct extraterrestrial illumination could of course contribute to the pre-scattered intensity $I_\nu(\hat{n}')$. One might include other direct sources such as gaseous emission and boundary surface radiation plus previously scattered radiation, but only un-scattered sunlight/moonlight is included in the present

scattering source function. The resulting source function is found by using EQ. (106) in EQ. (105) to obtain

$$J_\nu = F_\nu^{SUN} \tau_{e,ps}^{A+M} \left(P_\nu^A(\gamma) k_s^A + P_\nu^M(\gamma) k_s^M \right) \quad (107)$$

Note that P^A, P^M, k_s^A , *and* k_s^M vary with altitude (atmospheric density and composition) and are generally slowly varying functions of frequency. Note also that the scattering angle $\gamma = \arccos\left(\hat{n} \cdot \hat{n}_s'\right)$ would be constant (independent of the particular scattering point) along a line-of-sight in the absence of refractive bending. Both the primary solar path and the line-of-sight optical path actually bend somewhat, so that γ can be expected to vary by as much as a few degrees along the line-of-sight.

The primary solar transmittance $\tau_{e,ps}^{A+M}$ depends strongly on the optical path length of the primary solar path (prior to scattering), so that this factor can be expected to vary considerably from one scattering point to the next.

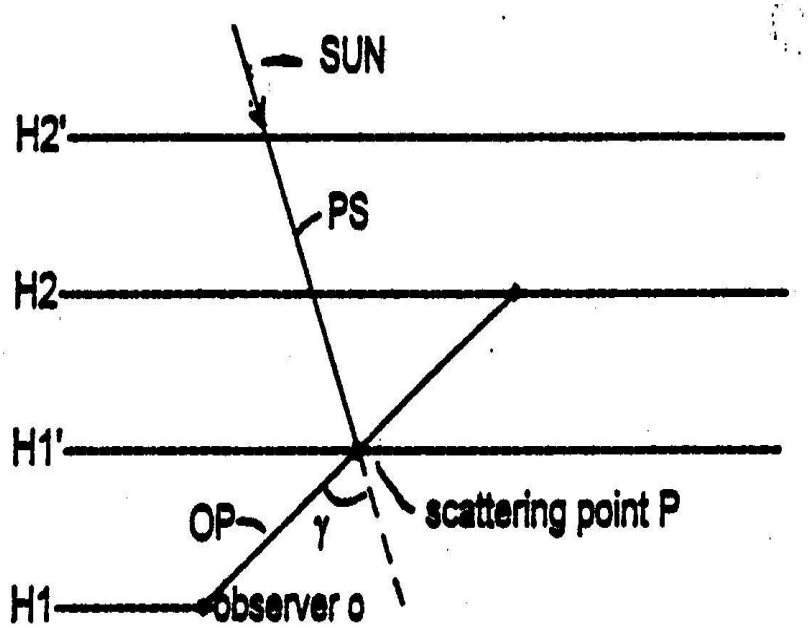

Figure 57. Schematic Representation of the Single Scattering Geometry. The Scattering Point at H1' is Shown for an Observer Looking up from an Altitude H1

The monochromatic intensity at the observer due to all of the single scattering sources within the line-of-sight is obtained by summing over the optical path, the product of the source function and the transmission function that gives

$$I_{\nu}^{SCAT} = \int J_{\nu} \; \tau_{e,op}^{A+M} \; ds_{op}$$

$$= I_{\nu}^{SUN} \int \tau_{e,ps}^{A+M} \; \tau_{e,op}^{A+M} \; \left(P_{\nu}^{A} \; k_{s}^{A} + P_{\nu}^{M} \; k_{s}^{M} \right) ds_{op} \qquad (108)$$

The scattering optical depth increment $k_S \; ds_{op}$ can be expressed in terms of the incremental transmittance for both aerosol and molecular scattering as

$$K_{s}^{X} \; ds_{op} = \frac{d\tau_{s,op}^{X}}{\tau_{s,op}^{X}} \quad , \qquad (109)$$

with X being either A or M. The intensity can therefore be written as:

$$I_{\nu}^{SCAT} = I_{\nu}^{SUN} \int \tau_{e,ps+op}^{A+M} \left[P_{\nu}^{A} \; \frac{d\tau_{s,op}^{A}}{\tau_{s,op}^{A}} + P_{\nu}^{M} \; \frac{d\tau_{s,op}^{M}}{\tau_{s,op}^{M}} \right] \quad , \qquad (110)$$

which includes two separate integrals covering aerosol and molecular scattering effects. The above equation, which provides for a monochromatic calculation at any frequency
ν, is now adapted for use with the molecular band transmission model used in LOWTRAN. The spectrally averaged intensity $\bar{I}$ is formally defined in terms of a convolution of the spectral intensity with a triangular instrument shape function $g(\nu)$ taken over a spectral width (half width at half maximum) of approximately $\delta\nu = 10$ cm^{-1}, that is,

$$\bar{I}_{\nu} = \frac{1}{\delta_{\nu}} \int I_{\nu} \, g(\nu - \nu') \; d\nu' \quad . \qquad (111)$$

The spectrally averaged, scattered intensity can be expressed in terms of known LOWTRAN quantities provided that only the molecular absorption transmittance is a rapidly varying function of frequency. All other quantities are assumed to be constant over the spectral interval $\delta\nu$. The result is

$$\bar{I}_{\nu}^{SCAT} = \bar{I}_{\nu}^{SUN} \int \tau_{e,ps+op}^{-A+M} \left[P_{\nu}^{A} \; \frac{d\tau_{s,op}^{A}}{\tau_{s,op}^{A}} + P_{\nu}^{M} \; \frac{d\tau_{s,op}^{M}}{\tau_{s,op}^{M}} \right] \qquad (112)$$

The quantity $\tau^{-A+M}_{e,ps+op}$ represents the spectrally averaged transmittance that is calculated in LOWTRAN. Therefore, the molecular band models and aerosol models of LOWTRAN provide a direct means of calculating the path transmittance required for each of the scattering points. In order to maintain compatibility with the spherical shell atmosphere of LOWTRAN, the integral over the path of scattering sources is replaced by a layer-by-layer sum along the line-of-sight.

For an optical path traversing N layers in an upward or downward direction this process gives

$$\bar{I}_\nu^{SCAT} = \bar{I}_\nu^{SUN} \sum_{j=1}^{N} \left[< \frac{\bar{\tau}^{A+M}_{e,ps+op} \; P^A_j}{\tau^A_{s,op}} > j \, \Delta\tau^A_{s,op,j} \right.$$

$$\left. + < \frac{\bar{\tau}^{A+M}_{e,ps+op} \; P^M_j}{\tau^M_{s,op}} > j \, \Delta\tau^M_{s,op,j} \right] \quad . \qquad (113)$$

The quantity $\Delta\tau_j$ is the change in molecular or aerosol scattering transmittance in passing through layer j, while $< >_j$ denotes an average value for that layer. Evaluating EQ. (113) requires the equivalent absorber amounts for both the line-of-sight and the primary solar paths associated with each scattering point, plus the scattering angle at each scattering point. The calculation of these amounts and angles is described in Appendix C of Ref. 3. The layer-by-layer sum of the singly scattered intensity is computed simultaneously with the existing direct thermal radiance using the following expression

$$\bar{I}_\nu^{SCAT} = \bar{I}_\nu^{SUN} \sum_{i=1}^{n-1} \sum_{X=(A,M)} \left[\tau^X_{s,op,i} - \tau^X_{s,op,i+1} \right] \cdot$$

$$\frac{1}{2} \left[\frac{\bar{\tau}^{A+M}_{e,ps+op,i} \; P^X_i}{\tau^M_{s,op,i}} + \frac{\bar{\tau}^{A+M}_{e,ps+op,i+1} \; P^X_{i+1}}{\tau^X_{s,op,i+1}} \right] \quad , \qquad (114)$$

where n is the number of scattering points (layer boundaries). The layer average $< >_j$ in EQ. (113) has been evaluated in EQ. (114) using the properties of only the two scattering points that bound each layer path segment. In this scheme, the observer position coincides with i = 1 and the end of the line-of-sight with i = n.

If the optical path intersects the earth, then EQ. (114) has an additional term representing the sunlight reflected from the ground. The ground is assumed to be a diffuse Lambertian reflector. The irradiance at the ground is proportional to cos (θ), where θ is the solar zenith angle at the ground. The ground reflected sunlight is given by the term

$$I_{\nu}^{SUN}\ \tau_{e,\,ps+op,\,n}\,A\cos(\theta)/2\pi \qquad , \qquad (115)$$

where A is the ground albedo.

The ground albedo is assumed to be independent of frequency and is read in as an input to MODTRAN with a default of 0 (no reflection).

The extraterrestrial solar intensity $\bar{I}_{\nu}^{SUN}$ is obtained from the data compiled by Thekaekara [35] The intensity is corrected for variation in the earth-to-sun distance due to the earth' s elliptical orbit. The lunar extra-terrestrial intensity is obtained by reflecting the solar intensity off of the moon' s surface as in Reference 272.

$$\bar{I}_{\nu}^{MOON} = 2.04472 * 10^{-7}\ \bar{I}_{\nu}^{SUN}\ \partial_{\nu}\ P_{\gamma'}^{MOON}$$

Here α_{ν} is the wavenumber dependent geometric albedo of the moon[273,274] while $P_{\gamma'}^{MOON}$ is the moon' s phase function giving the relative intensity as a function of the phase angle γ' of the moon.[275] Note that P(γ' = 0) = 1 for a full moon.

To ensure that the single scattering algorithm was correctly implemented, LOWTRAN calculations were compared to calculations of single scattered radiance by an independent, well-developed model. This model is a modification of the plane-parallel, monochromatic multiple scattering code described in Reference 276. This model, based on the adding/doubling technique, was modified to compute only single scattered radiance. Since LOWTRAN gaseous transmission functions do not obey Beer' s Law, gaseous absorption was deleted in the calculations by setting the gaseous transmittances in LOWTRAN equal to 1.0. Statements were added to LOWTRAN to calculate and write total optical depths and albedos based on the remaining attenuation mechanisms. This data was then used in the modified adding/doubling programs. Comparisons were limited to cases where both the solar and line-of-sight zenith angles were within the range where the plane parallel approximation is valid.

An example of the comparisons is shown in Table 31. The optical path in this case is from ground to space with a zenith angle of 12.95°, the solar zenith angle is also 12.95°. A Henyey-Greenstein phase function was used [see Eqs. (117 and (118]. The total optical depth for the optical path from ground to space is 0.183. The table presents the ratio of the LOWTRAN scattered radiance to the single scattered plane-parallel calculation for asymmetry factors g of 0 and 0.8 and for relative azimuthal angles of 0°, 90°, and 180°. The radiances shown are the upward radiances at 100 km, both the upward and downward radiance at 2 km, and the downward radiance at the ground. In all cases, the LOWTRAN scattered radiance is within one percent of the radiance calculated by the adding/doubling program.

5.3.3 Phase Functions for Scattering by Atmospheric Aerosols and Molecules

The angular scattering of light by the atmosphere is specified by the phase function that gives the differential probability of the scattered radiation going in a given direction. The scattering by the aerosols and air molecules are treated separately using the appropriate phase function for each. The angular distribution from the two types of scattering are combined, weighted by the corresponding scattering coefficients so the integral over all possible scattering directions (that is, a sphere) is unity:

The phase functions as used in the program are normalized so the integral over all possible scattering directions (that is, a sphere) is unity:

$$\int_{4\pi} \int P(\gamma) \quad d\,\Omega \quad = \quad 1 \qquad (116)$$

with this normalization, $P(\gamma)\ \Delta\Omega$ is the fraction of the scattered radiation that is scattered into a solid angle $\Delta\Omega$ about an angle γ relative to the direction of the incident light

Table 31 Ratio of Single Scattered Radiance, LOWTRAN, to an Adding/Doubling Technique (See Text for Description). The Geometry is illustrated in the lower part of the Figure.

TOP ↑	g	0.0	0.8	ψ
(100 km)		1.0022	1.0023	0°
			1.0024	90°
			1.0020	180°
			(a)	

2 km	g	0.0	0.8	ψ
		1.0015 ↑	1.0014	
		1.0000 ↓	1.0000	0°
			↑ 1.0014	
			↓ 0.9962	90°
			↑ 1.0015	
			↓ 0.9907	180°
			(b)	
Bottom ↓	g	0.0	0.8	ψ
		1.0003	1.0000	0°
			0.9957	90°
			0.9908	180°
			(c)	

All zenith angles are 12.95°.

g = asymmetry factor

ψ = relative azimuth

↑ Radiation Propagation

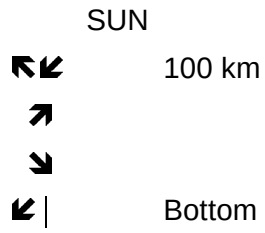

5.3.3.1 Aerosol Angular Scattering Function

The MODTRAN program offers the user three choices on handling the aerosol phase functions:

(1) They can use the standard phase functions stored in the program for the various aerosol models;

(2) They can use a Henyey-Greenstein type phase function, with a specified value for the asymmetry parameter;

(3) They can input their own phase functions for the different altitude regions.

5.3.3.2 Standard MODTRAN Phase Functions

The standard aerosol phase functions stored in the MODTRAN program correspond to the different aerosol models available within the MODTRAN program. It is therefore recommended that this option be chosen whenever the MODTRAN aerosol models are used for solar scattering. These standard phase functions were originally developed to approximate the exact phase functions, within about 20 percent, for any of the various aerosol models available in LOWTRAN as a function of wavelength, between 0.2 and 40 μm. The development of this standard set of approximate phase functions was discussed in Appendix D,(Ref.3) along with details of their implementation in the LOWTRAN program.

The number of phase functions in this set represents a compromise between accuracy and memory requirements. The nominal accuracy of 20 percent is compatible with the other uncertainties in using the aerosol models (such as determining the concentration of the aerosols). If greater accuracy is desired in specifying the phase function, the phase functions for all aerosol models, for a number of wavelengths, is available as a supplemental data file from Phillips Laboratory / Geophysics Directorate' s Simulation Branch of the Optical Environment Division. The phase functions are tabulated and discussed fully in a separate report by Shettle et al.[277]

5.3.3.3 Henyey-Greenstein Phase Function

In addition to the standard MODTRAN phase functions corresponding to the different aerosol models built into MODTRAN, the user has the option of specifying a Henyey-Greenstein scattering function be used. The Henyey-Greenstein [278] function is given by:

$$P_{HG}(\gamma) \;=\; \frac{1}{4\pi}\,\frac{(1-g^2)}{(1-2g\cos\gamma+g^2)^{3/2}} \quad , \tag{117}$$

where γ is the scattering angle and g is the asymmetry parameter,

$$g \;=\; \int_{4\pi}\int \cos\gamma\; P(\gamma)\, d\Omega \quad , \tag{118}$$

with P(γ) normalized as in EQ. (116) The asymmetry parameter gives a measure of the asymmetry of the angular scattering. It has a value of +1 for complete forward scattering, 0 for isotropic or symmetric scattering, and -1 for complete backscattering.

5.3.3.4 User-Defined Phase Functions

The MODTRAN code allows the user to input their own phase functions for the different altitude regions. These scattering functions can be defined at up to 50 different angles, as specified by the user. The same angles must be used for all four altitude regions.

When inputting their own phase functions the user should make sure they are normalized as in EQ. (116). The literature is not standard on this convention, and other conventions are used, the most common alternate form has the integral (Eq. 116) equal to 4π.

5.3.3.5 Molecular Scattering Phase Function

The angular distribution of light scattered by the air molecules is described by the Rayleigh scattering phase function

$$P(\gamma) = \frac{3}{16\pi} \bullet \frac{2}{2+\delta} \left[(1+\delta) + (1-\delta)\cos^2\gamma \right] , \quad (119)$$

where δ is the depolarization factor that gives the correction for the depolarization effect of scattering from anisotropic molecules. When δ goes to zero, that is, no depolarization, or symmetric molecules, EQ. (119) reduces to

$$P(\gamma) = \frac{3}{16\pi} \left[1 + \cos^2\gamma \right] , \quad (120)$$

which is a commonly used approximation for the Rayleigh phase function.

A value of $\delta = 0.0295$ (Kasten)[279] is used in EQ. (119). Young[280] has given a value of $\delta = 0.0279$ for dry air based on more recent measurements. With all constants evaluated, EQ. (119) becomes

$$P(\gamma) = 0.06055 + 0.05708\cos^2\gamma \quad . \quad (121)$$

Figures 58 and 59 show some representative calculations from LOWTRAN using the single scattering option. In these figures, the solid line represents the radiance emitted by the atmosphere, the dashed line the path scattered radiance and the dotted line the ground reflected radiance (if any). The atmospheric profile in all cases is the 1976 U.S.

Standard Atmosphere, and the rural aerosol model with 10-km meteorological range (VIS = 10km). The surface albedo is 0.05. independent of wavenumber corresponding to an emissivity of 0.95. The solar zenith angle is 45°; results are shown for relative path azimuth angles of both 0° and 180°. (see Appendix C of reference 3 for a discussion of the scattering geometry).

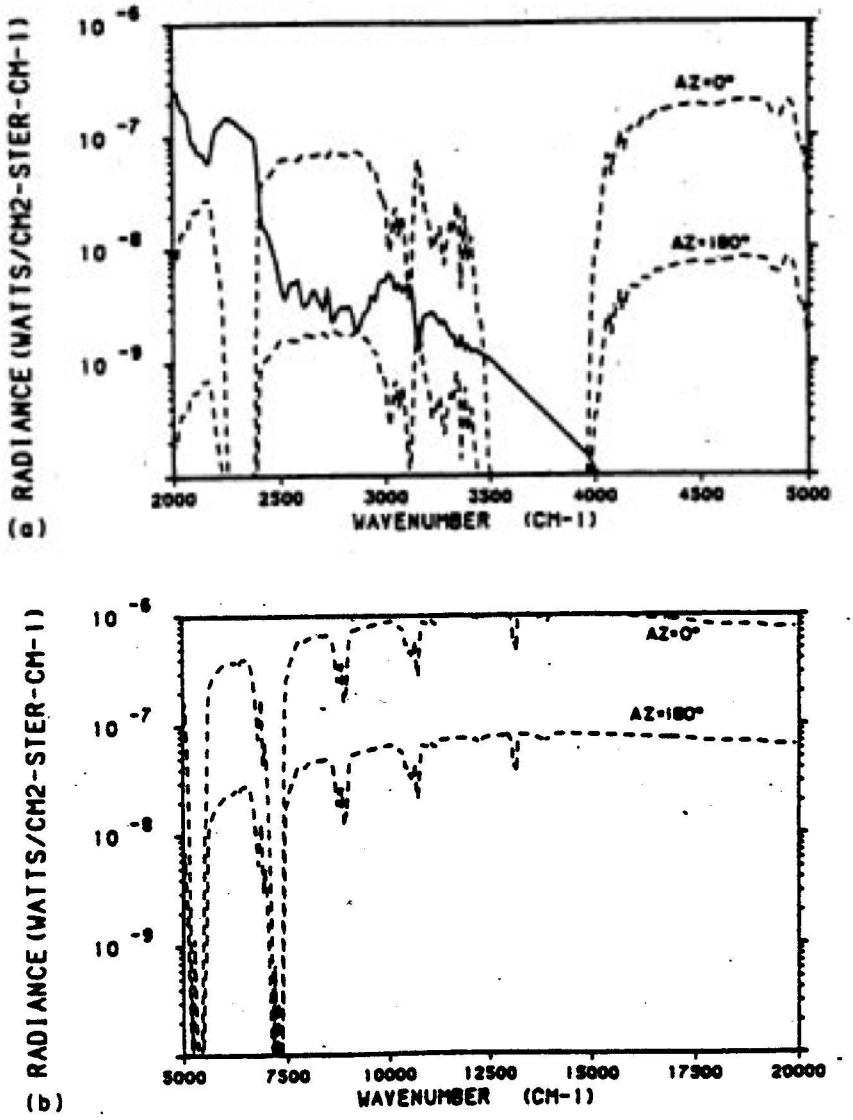

Figure 58. Calculated Radiances for the Following Conditions: Observer at the Ground Looking to Space with a Zenith Angle of 30°, Solar Zenith Angle of 45°, Relative Azimuths of 0° and 180°, U.S. Standard Atmosphere 1976, Rural Aerosol Model, VIS = 10km. Solid Line is Atmospheric Emission, Dashed Lines are Path Scattered Radiances. (a) 2000 cm^{-1} to 5000cm^{-1}, (b) 5000 cm^{-1} to 20000 cm^{-1}.

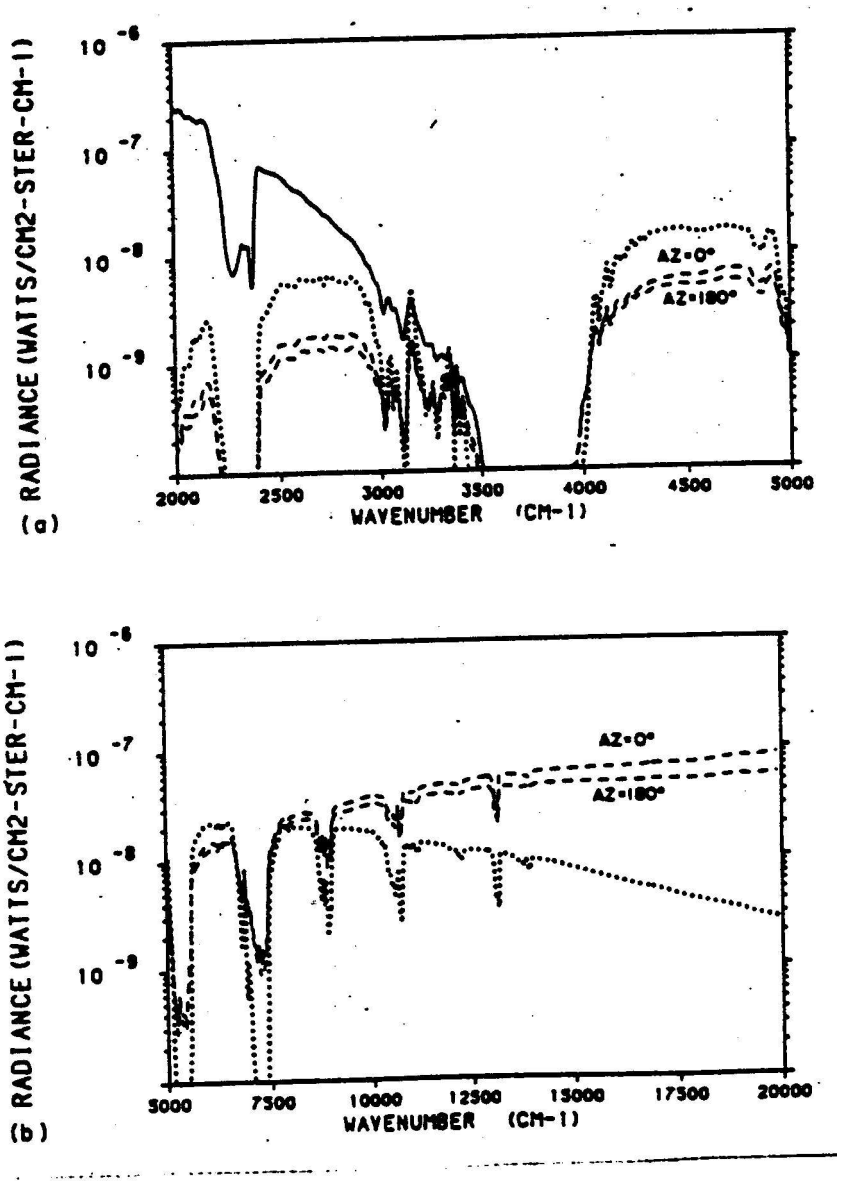

Figure 59. Calculated Radiances for the Following Conditions: Observer at 100km Looking at the Ground With a Zenith Angle at 100 km of 150°, Solar Zenith Angle is 45° , Relative Azimuths of 0° and 180°, Ground Albedo of 0.5, U.S. Standard Atmosphere 1976, Rural Aerosol Model VIS = 10 km. Solid Line is Atmospheric Emission, Dashed Lines are Path Scattered Radiances, Dotted Line is Ground Reflected Radiance. (a) 2000 cm^{-1} to 5000 cm^{-1} and (b) 5000-20000 cm^{-1}.

In Figure 58, the observer is on the ground looking out to space with a zenith angle of 30°. The upper dashed line corresponds to a relative azimuth of 0° with a scattering angle of 15°, while the lower dashed line is 180° relative azimuth with a scattering angle of 75°. The figure shows that for the relative azimuth of 0°, the scattered radiance

dominates everywhere above 2400 cm^{-1}, except around the strong CO_2 absorption band centered at 3700 cm^{-1}. For the relative azimuth of 180°, the scattered radiance is more than an order of magnitude less. This difference is due entirely to the difference in the scattering angles; the line-of-sight path and the scattering point-to-sun paths are otherwise identical. The reason for this difference is as follows: the bulk of the scattering occurs in the boundary layer where the rural aerosol model applies. The phase function for the rural aerosol model has a strong forward peak for these wavelengths. The large difference in the phase function between a scattering angle of 15° and 75° accounts for the large difference in the scattered radiance.

In Figure 59, the observer is at 100km looking down at the earth with a zenith angle of 150° (This is the reverse of the path in Figure 58). Again the upper dashed line corresponds to the relative azimuth of 0° with a 105° scattering angle and the lower one corresponds to 180° relative azimuth with a scattering angle of 165°. In this case the ground reflected solar radiance is greater than the path scattered radiance below 5000 cm^{-1} and greater than the atmospheric emission above 4000 cm^{-1}. The path scattered radiances for the two relative azimuths are now quite similar since the difference in the phase function between 105° and 165° is small. In the visible ($\sim$ 17500 cm^{-1}) the ground reflected radiance is more than an order of magnitude less than the path scattered radiance so that the ground is effectively obscured by the haze above it. Note, however, that the assumed albedo of 0.05 is low for the visible region of the spectrum.

5.3.4 Recommendations of Usage

The inclusion of single scattered solar radiance in LOWTRAN 6 is a significant improvement over previous versions that calculated the atmospheric emission only. The single scattering approximation is valid over a broad range of conditions found in the atmosphere. However, there are also conditions of interest in the atmosphere where multiple scattering and/or internal sources must be included to accurately calculate the atmospheric radiance. There is no simple indicator that predicts the conditions for which the single solar scattering approximation is acceptable: rather the range of applicability depends upon a large set of parameters including the atmospheric profile, the optical path, the solar geometry, the aerosol phase function, and the wavenumber region. The user will find some guidance in Section 4 of Ridgway et al. [268]. The following general comments, in part drawn from this source, may be useful. However, the user must be aware that they may not apply in all cases and are

indicative only. Also, these comments apply only to the validity of the single scattering approximation and not the uncertainties in the atmospheric data.

1... The single scattering approximation always underestimates the scattered radiance compared to multiple scattering.

2 The single scattering approximation becomes less valid with increasing scattering optical depth and with increasing single scattering albedo. For a scattering optical depth of less than about 0.7, the ratio of multiply scattered to singly scattered radiances should be less than 1.5. For scattering optical depths greater than about 2, the ratio may be much larger.

3 For an observer in space looking down at the ground in a window region where the total optical depth is less than 2, the ration of multiply scattered to singly scattered radiance is in most cases less than 2.0 and in many cases less than 1.5/ And contrary to intuition, the ratio decreases as the solar zenith angle increases and/or the path zenith angle decreases (note: a path zenith angle of 180° is straight down.

4...For an observer at the ground, the ratio of multiple to single scattered radiance increases with both the path and the solar zenith angle, and in general, single scattering is a poor approximation (error greater than a factor of 2) for cases where both the zenith angles are greater than 70.

5...Multiple scattering effects are dominant in clouds and thick fog.

6...Single scattering is a good approximation for early twilight cases, that is, where the sun is just below the horizon. For late twilight cases, multiple scattering becomes significant.

7...Single scattering is a good approximation when looking near the sun, since the scattering is dominated by the large forward peak.

8 In general, the aerosol scattering optical depth increases with wavenumber so that scattering in the infrared is less than that in the visible.

From a purely mechanical point-of-view, the single scattering option should not be used along with either the cirrus cloud model, or the rain model since the program does not

compute the scattered radiance from these aerosols. For an optical path looking directly at the sun, the single scattering model includes only the scattered radiance, and not the transmitted solar radiance.

5.3.5 Directly-Transmitted Solar Irradiance

An additional option has been provided to allow the user to compute the directly transmitted solar irradiance (flux), that is, the irradiance measured by an observer looking directly at the sun. This irradiance is given by:

$$\bar{I} = \bar{I}_{\nu}^{SUN} \, \bar{\tau}_{e}^{A+M} \quad . \tag{122}$$

Note that all scattered light is lost and that no scattering into the path is included.

Instructions for using this option are in Section 3.2.3.1 of Ref. 2.

An example of the directly transmitted solar irradiance is given in Figure 60. The dashed line is the solar irradiance at the top of the atmosphere. The solid line is the transmitted irradiance for a vertical path from the ground, for the U.S. Standard Atmosphere 1962 and no aerosol extinction.

As mentioned in Section 5.2, the model now includes a new solar spectrum for calculating scattered and directly transmitted solar irradiances. The recent values of VanHoosier et.al.[31] have been adopted in the UV (0.2 to 0.35 μm) with a LOWTRAN compatible resolution (20 cm^{-1}). This data was obtained from the Shuttle platform (the Solar Ultraviolet Spectral Irradiance Monitor (SUSIM) on Spacelab 2) at 0.15nm resolution and subsequently converted to frequency for smoothing. The data stored in MODTRAN actually begins at 0.174 μm recognizing that plans exist to extend the code into the UV. In the near UV to visible range (0.35 to 0.86 μm), the data of Neckel and Labs[33] have been adopted. Because these data have a resolution of 1-2 nm, they under-represent the actual variability in the solar Fraunhofer structure at the stated 20 cm^{-1} resolution. Estimated accuracy of the composite MODTRAN compilation is 5-10% for the SUSIM spectral range (including feature replication at 20 cm^{-1} resolution) and 5% for the near UV and visible range when degraded to 100 cm^{-1} resolution.
NOTE: Because of general calibration difficulties in the UV, measured solar irradiances differ by as much as 10% in absolute magnitude[258], while relative spectral detail is reproducible to much higher accuracy.

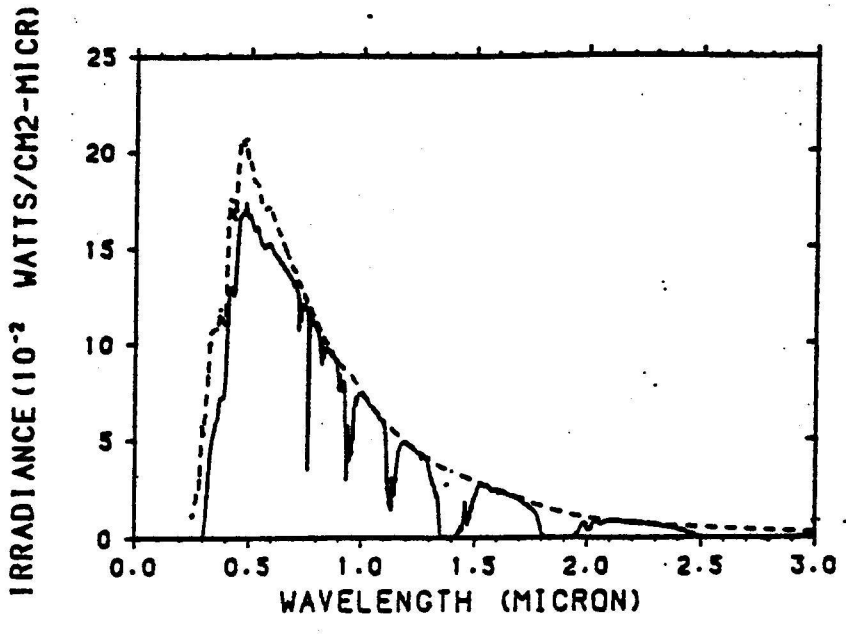

Figure 60. Solar Radiance (Dashed Line) and Directly Transmitted Solar Irradiance (Solid Line) for a Vertical Path, From the Ground, U. S. Standard Atmosphere 1976, No Aerosol Extinction.

5.4 NEW MULTIPLE SCATTERING ALGORITHM

5.4.1 Introduction

This description of the multiple scattering algorithm built into LOWTRAN 7 and MODTRAN 2 is a synopsis gleaned from the report by Isaacs et al.[36]

Optimal design and deployment of electro-optical (EO) remote sensing and communication systems requires accurate modeling and prediction of the effects of the ambient environment on atmospheric transmission. Atmospheric transmittance/ radiance models such as AFGL' s LOWTRAN (Kneizys et al.,[2]) and FASCODE (Anderson et al., [178]) have been developed within this context to provide the capability to assess potential adverse environmental impacts on EO system performance.

In order to accurately predict atmospheric effects on the propagation of visible, infrared and microwave radiation, it is necessary to treat the extinction mechanisms including molecular scattering and absorption, and particle (aerosols, clouds and precipitation) scattering and absorption, characterizing the ambient atmosphere. In the present Phillips Laboratory' s transmittance/radiance models, these processes are adequately included in the treatment of path transmission. However, simplified

treatments are employed to simulate the effects of scattering on the calculation of radiance. For thermal infrared and microwave radiation, for example, particle scattering in earlier versions of LOWTRAN had been treated as an enhancement to extinction but not as a source term. This approach leads to an underestimate of radiance for paths where multiple scattering is important (Ben-Shalom et al.,[281]). Earlier versions of LOWTRAN used the single scattering approximation for evaluating solar radiances (Ridgway et al.,[268]) While the single scattering implementation is straightforward, its application introduces errors which are functions of wavelength, sun/sensor geometry, and surface optical properties (see Isaacs and Özkaynak, [282] and Dave,[283]). These errors are primarily due to neglecting higher order scattering and surface reflection. In FASCODE, particle scattering has been treated as equivalent to absorption. All scattered radiation is thus re-emitted as if it were absorbed, i.e., the scattered radiation is conserved. This conservative scattering approach can lead to an overestimate of radiance.

In order to provide a more realistic simulation of radiation in spectral regions and along atmospheric paths where multiple scattering (MS) is a significant contribution to the source function, an efficient and accurate scattering parameterization has been incorporated into the MODTRAN and FASCODE models.

5.4.2 Stream Approximation

Selection of an appropriate treatment of multiple scattering (MS) for application to the MODTRAN and FASCODE models is severely constrained by competing requirements of desired efficiency and accuracy, and limitations imposed by the inherent code structures of these models. Additionally, it was important to provide an approach which is uniformly applicable to all spectral regions considered and equally appropriate for implementation within both MODTRAN and FASCODE. Based on these considerations, the MS parameterization selected consisted of a finite stream approach (using two streams for simplicity) to approximate the scattering source function.

This approach could be implemented directly in FASCODE since it is essentially a monochromatic calculation. It is known, however, that there exist difficulties in calculating the transmittance/radiance averaged over a finite spectral interval in a non-gray gaseous absorber with multiple scattering because the commonly-used band models are not applicable (see Stephens, [284]). This was the driving factor for implementing an MS treatment within LOWTRAN. The best approach to solve this problem is the use of the k-distribution method, which decouples the multiple scattering from the gaseous spectral integration so that the available (monochromatic) multiple

scattering algorithms can be used directly. For LOWTRAN, the stream approximation is performed through an interface routine consisting of the k-distribution method. For practical purposes, this consists of decomposing the band model determined optical properties into a set of equivalent monochromatic calculations which are then summed to give the spectrally averaged results.

As mentioned earlier, the multiple scattering parameterization had to be accommodated by the existing MODTRAN/LOWTRAN and FASCODE code structures. This constraint is particularly important for FASCODE. In the FASCODE application, gaseous absorption is evaluated directly from the line-by-line calculation. Fluxes required for the stream approximation are calculated via the parameterized adding method. The adding method is particularly consistent with the code structure of both radiance/transmittance models since they treat one layer at a time.

In the FASCODE model, for example, the evaluation of layer optical properties always commences with that level in the selected path with the highest pressure and the selected spectral sampling interval decreases with pressure. This approach insures that the layer spectral resolution is consistent with the decrease of Voight line widths at higher altitudes. From the perspective of the line-by-line calculation, this method is computationally quite efficient. However, it is inconsistent with monochromatic multiple scattering treatments. In order to accommodate the sampling requirements of both the line-by-line and multiple scattering calculations, the FASCODE implementation employs the adding formalism to aid in the merging of the scattered fluxes from successive layers.

A generic outline of the basic theory is provided here. This prescription is modified slightly for specific application to the MODTRAN/LOWTRAN and FASCODE models.

5.4.2.1 Radiance and Source Function

The desired radiance I_ν at wavenumber ν for an arbitrary path with zenith angle cosine and azimuth angle (μ,ϕ) is given by the solution to the radiative transfer equation (RTE):

$$\mu \frac{d}{d\tau} \; I_\nu \; (\tau,\mu,\phi) \; = \; I_\nu(\tau,\mu,\phi) - J_\nu \; (\tau,\mu,\phi) \; . \qquad (123)$$

Here τ_ν is the optical thickness, μ is then cosine of the path zenith angle, and ϕ is the azimuth angle relative to the sun' s azimuth. Vertical optical depth τ_ν, will depend on the relevant mechanisms determining the extinction of electromagnetic radiation for

the spectral region characterized by wavenumber ν. In general these mechanisms include: (a) molecular absorption, k_a, (b) molecular scattering, k_S, (c) particulate absorption, σ_a and (d) particulate scattering, σ_S. Optical depth is given by integrating the relevant vertical extinction coefficient profiles according to:

$$\tau_\nu(z) = \int_z^\infty \left[k_a(z) + k_S(z) + \sigma_a(z)\ \sigma_S(z)\right] dz \qquad (124)$$

The general source function, J_ν, including scattering of solar radiation and thermal emission, is given by:

$$J(\tau,\mu,\phi) = J_O(\tau,\mu,\phi) + J_{MS}(\tau,\mu,\phi) \qquad (125)$$

where

$$J_O(\tau,\mu,\phi) = \frac{\omega_O(\tau)}{4\pi}\pi F e^{-\tau/\mu_O} P(\Omega;-\Omega_O) + \left[1-\omega_O(\tau)\right] B\left[\Theta(\tau)\right] \qquad (126)$$

and

$$J_{MS}(\tau,\mu,\phi) = \frac{\omega_O(\tau)}{4\pi} \int_\Omega P(\Omega;\Omega')\ I(\tau,\Omega')\, d\Omega' \quad . \qquad (127)$$

Here, ω_O is the single scattering albedo, P is the appropriate angular scattering or phase function, and B is the Planck function at temperature Θ. The extraterrestrial solar irradiance is given by F and the path and solar directions are given by Ω and Ω_O, respectively. The first term in Equation 126 is the single scattering of solar radiation while the second is the local thermal emission.

Radiance solutions to the RTE (Eq. 123) are subject to boundary conditions at the top of the atmosphere ($\tau = 0.0$) for downward radiance and at the earth' s surface ($\tau = \tau^*$) for upward radiance. At $\tau = 0.0$, downward diffuse radiance from space is zero (the direct solar irradiance is accounted for via the primary source function) resulting in:

$$I_b(0,-\mu,\phi) = 0.0 \qquad (128)$$

(At millimeter wave frequencies a contribution due to emission at the cosmic background effective temperature of 2.7K may be included when high accuracy is required.)

Boundary conditions at the surface will depend on the nature of the surface reflectance/emittance properties. The most common assumption is that of Lambert reflectance, i.e. the upward isotropic flux given by a constant surface albedo, r, times the downward flux. Upward and downward fluxes $F^{\pm}(\tau)$ at optical depth τ, are defined respectively as:

$$F^{\pm}(\tau) = \int_0^{2\pi} \int_0^{1} \mathrm{I}(\tau, \pm\mu, \phi)\, \mu\, d\mu\, d\phi \qquad (129)$$

This results in a lower boundary condition upward radiance of:

$$\mathrm{I}_b(\tau^*, \mu, \phi) = \frac{r}{\pi}\left[\pi F \mu_0 \exp(-\tau^*/\mu_0) + \int_0^{2\pi} \int_0^{1} \mathrm{I}(\tau^*, -\mu, \phi)\, \mu\, d\mu\, d\phi\right]$$

$$+ \quad (1-r)\,\mathrm{B}[T_s] \qquad (130)$$

The three terms on the R.H.S. of Eq. 130 are respectively: (a) reflectance of attenuated solar irradiance (in UV, near IR spectral regions). (b) reflectance of downward scattered radiance field, and (c) thermal emission due to the surface at temperature, T_S. The surface emissivity is unity minus the surface albedo, i.e., (1-r). MODTRAN requires that the surface albedo be specified, while FASCODE asks for the surface emissivity.

General radiance solutions to the RTE for upward and downward radiances, respectively, are:

$$\mathrm{I}(\tau, +\mu, \phi) = \mathrm{I}_b(\tau^*, \mu, \phi)\; e^{-(\tau^* - \tau)/\mu} + \int_{\tau}^{\tau^*} J(t, \mu, \phi)\; e^{-(t-\tau)/\mu}\; \frac{dt}{\mu} \qquad (131)$$

$$\mathrm{I}(\tau, -\mu, \phi) = \mathrm{I}_b(o, -\mu, \phi)\; e^{-\tau/\mu} + \int_{o}^{\tau} J(t, \mu, \phi)\; e^{-(\tau - t)/\mu}\; \frac{dt}{\mu} \qquad (132)$$

where the I_b are given by the boundary conditions Eq.' s 130 and 128 above, respectively. Incorporating these boundary conditions, the radiance solutions become:

$$I(\tau,\mu,\phi) = \left\{\frac{r}{\pi}\left[\pi\mu_o F e^{-\tau^*/\mu_o} + \int_0^1\int_0^{2\pi} I(\tau^*,-\mu,\phi)\,\mu\,d\mu\,d\phi\right]\right.$$

$$\left. + (1-r)\,B\left[T(\tau^*)\right]\right\}\exp-(\tau^*-\tau)/\mu + \int_\tau^{\tau^*} J(t,\mu,\phi)\; e^{-(t-\tau)/\mu}\;\frac{dt}{\mu} \qquad (133)$$

$$I(\tau,-\mu,\phi) = \int_0^\tau J(t,\mu,\phi)\; e^{-(\tau-t)/\mu}\;\frac{dt}{\mu} \qquad (134)$$

In the stream approximation, the multiple scattering contribution to the source function (Eq. 127 above) is approximated by assuming constant scattered radiances I^+ and I^- over upward (Ω^+) and downward (Ω^-) hemispheres, respectively, or from Eq. (127):

$$J_{MS}(\tau,\mu,\phi) \approx \frac{\omega_o(\tau)}{4\pi}\left[I^+(\tau)\int_{\Omega^+} P(\Omega,\Omega^+)\,d\Omega^+\right.$$

$$\left. + \; I^-(\tau)\;\int_{\Omega^-} P(\Omega,\Omega^-)\,d\Omega^-\right] \quad . \qquad (135)$$

Integrating over the angular scattering functions for the resulting azimuthally averaged backscatter fractions, B(μ), as a function of zenith angle cosine and substituting the corresponding fluxes:

$$I^\pm(\tau) = F^\pm(\tau)/\pi \qquad (136)$$

results in

$$J_{MS}(\tau,\pm\mu,\phi) \approx \frac{\omega_o(\tau)}{\pi}\left\{F^\pm(\tau)\left[1-\beta(\mu)\right] + F^\mp(\tau)\,\beta(\mu)\right\} \quad . \qquad (137)$$

This simple expression for the multiple scattered contribution to the source function is added to the single scattering and thermal emission contributions for the general source function, J (Eq. (125)). The source function is then integrated along with the desired path (as in Eqs. (133) or (134)) to obtain the desired total radiance including the approximated MS contribution.

The evaluation of the approximated MS source function (Eq. 137) requires local fluxes F^+ and F^-, backscatter fractions β (u), and single sttering albedos, ω_0. The backscatter fractions are given as functions of zenith angle cosine and asymmetry factor by Wiscombe and Grams [285] (see Figure 61). A small error is introduced by assuming these backscatter fractions for the equivalent Henyey-Greenstein phase function rather than integrating the actual function. The single scattering albedo, $\omega_0(\tau)$, for a given layer with total optical thickness $\Delta\tau$ is:

$$\omega_o(\tau) \quad = \quad \Delta\tau_s/\Delta\tau \tag{138}$$

where $\Delta\tau_S$ is the total scattering optical thickness of the layer. Discretizing equation (137) for a given layer, N, the contribution of multiple scattering is approximated as:

$$J_{SA}^{N} \quad (\pm\mu) = J_o + \frac{\omega_o{}^{N}}{\pi} \left\{ F_N^{\pm} \left[1 - \beta^N(\mu, g^N) \right] \quad + \quad F_N^{\mp} \; \beta^N(\mu, g^N) \right\} \qquad . \tag{139}$$

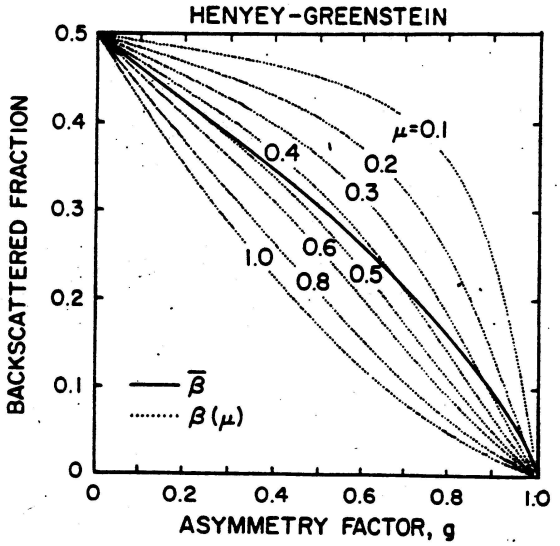

Figure 61. Backscattered Fractions $\bar{\beta}$ *and* $\beta(\mu)$ for the Henyey-Greenstein Phase Function Versus the Asymmetry Factor g for a Range of Values of μ (Wiscombe and Grams,[285])

Here the fluxes are taken as the layer mean quantities evaluated at a level halfway through the layer. The asymmetry factor, g, is a measure of the directional scattering and can be evaluated from the phase function.

Once the source function is approximated, the path radiance can be evaluated. Along a path consisting of layers (N) and the layer above (N+1) with transmissions T_N and T_{N+1}, respectively, for example, the emission, E, depends on the path integral of the total source function:

$$E^{+}_{N+1} = E^{+}_{N}\ T_{N+1} + J_{SA}^{N+1}\ (+\mu)(1-T_{N+1}) \tag{140}$$

for downward looking and:

$$E^{-}_{N+1} = E^{-}_{N} + (1-T_{N+1})\ J_{SA}^{N+1}\ (-\mu)\ T_N \tag{141}$$

for upward looking, where the intrinsic layer emission is:

$$E^{\pm}_{N} = (1-T_N)\ J_{SA}^{N}\ (\pm\mu) \tag{142}$$

5.4.2.2 Layer Fluxes

Fluxes approximate the required radiances for evaluation of the multiply scattered source function. Upward and downward fluxes (F^+ and F^- respectively) for individual isolated layers are evaluated using an appropriate flux parameterization. For example, for solar scattering, the hybrid modified delta Eddington approximation (Meador and Weaver, [286]) is used. The chosen flux parameterization also provides intrinsic layer reflection and transmission functions, R and T. These fluxes are calculated using standard two stream parameterization approaches. To accommodate the flux parameterizations, optical properties for the whole atmosphere (i.e., surface to space) are required. This approach for calculating fluxes thus consists of two steps: (1) evaluating local layer (i.e., intrinsic) fluxes for each atmospheric layer, and (2) combining these to obtain the actual flux profiles using the adding method.

Upward and downward layer fluxes for solar radiation are given by:

$$F^{+} = Ae^{k\tau} + Be^{-k\tau} + Ce^{-\tau/\mu_o} \tag{143}$$

$$F^{-} = \frac{1}{\gamma_2}\left\{A(\gamma_1-k)e^{k\tau} + B(\gamma_1+k)e^{-k\tau} + Ye^{-\tau/\mu_0}\right\} \tag{144}$$

Where the appropriate constants are given by :

$$k = \sqrt{(\gamma_1^2 - \gamma_2^2)}$$

$$A = \left[B(\gamma_1 + k) + Y\right]/(k - \gamma_1)$$

$$B = (E_1 e^{k\tau^*} + E_2 e^{-\tau^*/\mu_o})/(E_3 e^{k\tau^*} + E_4 e^{-k\tau^*}) \qquad (145)$$

$$C = \pi\omega_o \left\{\frac{\beta(\mu_o)}{\mu_o} - \gamma_1\beta(\mu_o) - \gamma_2\left[1-\beta(\mu_o)\right]\right\}\left(\frac{\mu_o^2}{1-k^2\mu_o^2}\right)$$

$$Y = C\left(\gamma_1 + \frac{1}{\mu_o}\right) - \pi F\,\omega_o\beta(\mu_o)$$

and additionally:

$$E_1 = Y\left[1/(\gamma_1 - k) - r/\gamma_2\right]$$

$$E_2 = \left[-C + \pi F\mu_o r + \frac{rY}{\gamma_2}\right]$$

$$E_3 = (\gamma_1 + k)\left[1/(k-\gamma_1) + r/\gamma_2\right]$$

$$E_4 = \left[1 - r(\gamma_1 + k)/\gamma_2\right] \qquad (146)$$

$$\gamma_1 = \frac{-\left\{1 - g^2 - \omega_o(4-3g) - \omega_o g^2(4\beta_o + 3g - 4)\right\}}{4\left[1 - g^2(1-\mu_o)\right]}$$

$$\gamma_2 = \frac{\left\{7 - 3g^2 - \omega_o(4+3g) + \omega_o g^2(4\beta_o + 3g)\right\}}{4\left[1 - g^2(1-\mu_o)\right]}$$

Here, r is the Lambert surface albedo and the solar zenith angle cosine is μ_o

The transmission and reflection functions used later in the flux adding are given by:

$$R = F^{+}/\mu_o \pi F$$

$$T = F^{-}/\mu_o \pi F + \exp^{\left(-\tau/\mu\right)} \quad (147)$$

For the thermal fluxes, a linear Planck function relation across an atmospheric layer is used. In so doing, the parameterized two-stream solutions for emission from the layer top and layer bottom, and for total transmission and reflection are:

$$F^{+} = a\left(PB_t - mQ - B_b\right)/D$$

$$F^{-} = a\left(PB_b + mQ - B_t\right)/D$$

$$T = a/D \quad (148)$$

$$R = uv\left(e^{\tau 1} - e^{\tau 1}\right)/D$$

where B_τ and B_b are the Planck intensity at the layer top and bottom and:

$$a^2 = 1 - \omega_o$$

$$m = \left(B_b - B_t\right)/\tau$$

$$P = ve^{\tau_1} + ue^{-\tau 1}$$

$$Q = ve^{\tau 1} - ue^{-\tau 1} - a \quad (149)$$

$$D = v^2 e^{\tau 1} - u^2 e^{-\tau 1}$$

$$u = \left(1-a\right)/2$$

$$v = \left(1+a\right)/2$$

$$\tau 1 = \sqrt{3}\ a\tau$$

The optical thickness τ and the single scattering albedo ω_0 are given by:

$$\tau = ku + \tau_s(1-g) + \tau_a$$

$$\omega_o = \tau_s(1-g)/\tau \qquad (150)$$

Here k is the gas absorption coefficient (for a particular wavelength and probability interval), u is the gas amount, τ_S is the scattering optical thickness, τ_a is the absorption optical thickness and g is the asymmetry factor for the particulate matter in the layer.

5.4.2.3 Flux Adding Method

To obtain the actual flux profile throughout the atmosphere, intrinsic layer fluxes are combined algebraically using the adding method. In this method, fluxes, reflections, and transmissions are used to add individual layers together. Composite upward fluxes, $1_{F^+_N}$, and reflection functions R^+_N, obtained upon adding two isolated layers, N and
(N-1) are given by:

$$1_{F^+_N} = F^+_N + T_N(1_{F^+_{N-1}} + F^-_N \; R^+_{N-1})(1-R_N R^+_{N-1})^{-1} \qquad (151)$$

$$R^+_N = R_N + R^+_{N-1} \; T^2_N \; (1-R_N R^+_{N-1})^{-1} \qquad (152)$$

Analogous equations provide composite downward fluxes and reflection functions, $1_{F^-_N}$ *and* R^-_N, respectively. The composite upward and downward fluxes provide the actual upward and downward fluxes at layer interfaces including the effects of all layers above and below. For example, the upward and downward fluxes at the boundary between layers N and (N+1) are given by:

$$2_{F^+_N} = (1_{F^+_N} + 1_{F^-_{N+1}} \; R^+_N)(1-R^+_N \; R^-_{N+1})^{-1} \qquad (153)$$

$$2_{F^-_{N+1}} = (1_{F^-_{N+1}} + 1_{F^+_N} \; R^-_{N+1})(1-R^+_N \; R^-_{N+1})^{-1} \qquad (154)$$

Once obtained, these fluxes are substituted int Eq. (139) above to provide the approximation of the MS source function.

5.4.2.4 Band Model Considerations

For LOWTRAN, it is necessary to integrate the spectral radiance values over a finite spectral interval (~ 20 cm^{-1}). The basic problem encountered in the calculation of radiative transfer in low spectral resolution in a hazy or cloudy atmosphere is the coupling between the processes of scattering and absorption and absorption due to cloud/aerosol particles and absorption by atmospheric gases. The main difficulty is that the integration over frequency cannot be properly accounted for by the usual band model technique for gaseous absorption because they do not allow for multiple-scattering. A direct line-by-line integration over frequency would be very time consuming. One alternative way of carrying out the frequency integration is to use the "k-distribution method" for homogeneous layers (Arking and Grossman, [287]) and the "correlated k-distribution approximation" for inhomogeneous atmospheres (cf. Wang and Ryan, [288]).

For gaseous absorption, the k-distribution method is comparable to line-by-line calculations (Arking and Grossman, [287]). This method is equivalent to the exponential-sum fitting method (see Wiscombe and Evans, [289]) and to the path length distribution method (see Bakan et al., [290]). However, in general, the latter two methods use scaling approximations to account for atmospheric inhomogeneity while the correlated-k approximation assumes certain relationships between k values at different pressure and temperature levels. The accuracy of the approximation is excellent for the 9.6 μm 0_3 band thermal radiation calculations (see Lacis et al., [291]).

Yamamoto et al. ([292,293]) used finite sums of exponentials to describe the non-grey nature of water vapor absorption and carried out solutions of the equation of transfer for homogeneous band layers using both Chandrasekhar' s principles of invariance as well as the discrete ordinate technique. Both techniques require extensive numerical calculations. On the other hand, two stream approximations together with the correlated-k approximation have been used to study the radiative effects of aerosols (see Hansen et al.,[294]).

As summarized recently by Stephens on efficient and accurate radiation parameterizations (pg. 862 of the paper[284]): "...Only the k-distribution approach can be readily incorporated into scattering models..."

In a homogenous gas layer, the k-distribution function is formally related to the mean transmission function $T_{\Delta\nu}(u)$,

$$T_{\Delta\nu}(u) \equiv \frac{1}{\Delta\nu}\int_{\Delta\nu} e^{-ku}\,d\nu \equiv \int_o^\infty f(k)\,e^{-ku}\,dk$$

$$\equiv \int_0^1 e^{-ku}\, dg = \sum_{i=1}^{n} e^{-k_i u}\, \Delta g_i \qquad (155)$$

where $\Delta\nu$ is the narrow repeated interval (20 cm^{-1} in LOWTRAN) and u is the gas amount. The f (k) for a given gas at a specified $\Delta\nu$ is the probability density function such that f(k)dk is the fraction of the frequency interval for which the absorption coefficient is between k and k+dk. Eq. (155) reveals that the transmission depends on the distribution of k-values within $\Delta\nu$, but not on the ordering of the values. The cumulative k-distribution function is g(k), while ($k_{i,}.\Delta g_i$) are the discreet sets of values to approximate the integral.

By expressing the band model transmission as the sum of exponentials, the multiple scattering calculation for each component can be performed independently as if it were a monochromatic problem. These are weighted and summed (as in Eq. (155)) to recover the essential band model character of the problem.

The fit of Wiscombe and Evans [289] has been used for the two LOWTRAN transmission functions of water vapor/uniformly mixed gases, and ozone. The accuracy of the fitting is in general within a few percent for T > 0.1. For inhomogeneous atmospheres, we adopt the same scaling approximation used in LOWTRAN, i.e.,

$$k_i(P,\Theta) = k_i(P_o,\Theta_o)\frac{P}{P_o}\sqrt{\frac{\Theta_o}{\Theta}} \qquad (156)$$

where Θ_o and P_o are reference temperatures and pressures, respectively.

5.4.3 Implementation in MODTRAN 2 and LOWTRAN 7

This section describes the technical details of incorporating the multiple scattering treatment into MODTRAN along with the required k-distribution method needed by LOWTRAN 7.

5.4.3.1 Modified k-Distribution Method (LOWTRAN 7 Only)

Because of the complicated molecular absorption band structure of the gases, a rigorous frequency integration would require a line-by-line integration which clearly is very time consuming and therefore unacceptable for implementation in the LOWTRAN model. Instead, the application of the absorption coefficient (k) distribution method

(Wang and Ryan[288] and Stephens[284]) has been adopted for LOWTRAN 7. In a homogenous gas layer, the k-distribution function is formally related to the mean transmission function $T_{\Delta\nu}(u)$, by:

$$T_{\Delta\nu}(u) \equiv \frac{1}{\Delta\nu}\int_{\Delta\nu} e^{-ku}\,d\nu \equiv \int_o^\infty f(k)e^{-ku}\,dk$$

$$\equiv \int_0^1 e^{-ku}\,dg = \sum_{i=1}^{n} e^{-k_i u}\,\Delta g_i \qquad (157)$$

where $\Delta\nu$ is the narrow repeated interval (20 cm^{-1} in LOWTRAN) and u is the gas amount. The f(k) for a given gas at a specified $\Delta\nu$ is the probability density function of the frequency interval for which the absorption coefficient is between k and k + dk. Equation 151 reveals that the transmittance depends on the distribution of k-values within $\Delta\nu$ but not on the ordering of the values. The cumulative k-distribution function is g(k), while (k_i, Δg_i) are the discreet set of values to approximate the integral.

For the summation in Eq. 151 to be useful with LOWTRAN, values for k and Δg must be found to fit the LOWTRAN transmission data for water vapor, the uniformly mixed gases and ozone. The transmission for water vapor/uniformly mixed gases and ozone may be expressed as:

$$T_1 = T(H_2O^+) = \sum_{i=1}^{M} e^{-k_i u_1}\,\Delta g_i \qquad (158)$$

$$T_2 = T(O_3) = \sum_{j=1}^{N} e^{-k_j u_2}\,\Delta g_j \qquad (159)$$

The problem of fitting LOWTRAN transmission data (previous versions before LOWTRAN 7) as an exponential sum had been handled successfully by Wiscombe and Evans[289], using 10 k and Δg values for H_2O^+ and six for O_3. Making use of the Wiscombe and Evans exponential sum fit of the LOWTRAN transmission data, Isaacs et al.[36] modified this method and reduced the necessary number of k' s to six.

It is important to remember that the k-distribution transmittances are only employed in the determination of the multiply scattered source function. The adding of radiances based on the source function depends on the original LOWTRAN transmittances. Thus, errors in the combined k-distribution/stream approximation approach for multiple scattering are not propagated beyond the approximate multiple scattering approach.

Coordination of the new LOWTRAN 7 band model with the k-distribution.

The development of the new band model formulation utilized in LOWTRAN 7 (explained fully in section 4.1), necessitated further refinements in the proposed k-distribution method. The Pierluissi[13] double exponential band model formulation is given by:

$$\tau_P(x,a) = e^{-(x)^a} \tag{160}$$

where x = CW and C is the band model absorption coefficient, while:

$$W = \left(\frac{P}{P_o}\right)^n \left(\frac{T_o}{T}\right)^m U \tag{161}$$

U = PL which equals the true layer amount, and W is the scaled absorber amount. The band model parameters *a, n and m* are listed in Table 32 as a function of molecule and specific spectral band for that molecule.

For multiple scattering calculations of layer fluxes, Abreu and Kneizys modified the k-distribution method, replacing the Isaacs et al[36] six k method with a three term k-distribution, capable of accommodating the Pierluissi band model. This three term k-distribution is described as:

$$\tau_k(x,a) = G_1 e^{-k_1 x} + G_2 e^{-k_2 x} + G_3 e^{-k_3 x} \tag{162}$$

The constants G_1, G_2,, G_3 and k_1, k_2, k_3 were determined from a non-linear least squares fit to τ_p as a function of a and x with a constraint of the ratio' s of the k' s.

The G' s are listed in Table 33 and the k' s are listed in Table 34, as a function of molecule and specific spectral band. When more than one molecule absorbs at the

same frequency, we neglect the cross terms in the k-distribution representation (in order to minimize computational time).

Table 32. Band Model Parameters for each Absorbing Molecule.

ABSORBER	SPECTRAL RANGE (cm^{-1})	Band Model Parameters a	n	m
Ammonia	0 - 385	0.4704	0.8023	- 0.9111
(NH_3)	390 - 2150	0.6035	0.6968	0.3377
Carbon	425 - 835	0.6176	0.6705	- 2.2560
Dioxide	840 - 1440	0.6810	0.7038	- 5.0768
(CO_2)	1805 - 2855	0.6033	0.7258	- 1.6740
	3070 - 3755	0.6146	0.6982	- 1.8107
	3760 - 4065	0.6513	0.8867	- 0.5427
	4530 - 5380	0.6050	0.7883	- 1.3244
	5905 - 7025	0.6160	0.6899	- 0.8152
	7395 - 7785	0.7070	0.6035	0.6026
	8030 - 8335	0.7070	0.6035	0.6026
	9340 - 9670	0.7070	0.6035	0.6026
Carbon	0 - 175	0.6397	0.7589	0.6911
Monoxide	1940 - 2285	0.6133	0.9267	0.1716
(CO)	4040 - 4370	0.6133	0.9267	0.1716
Methane	1065 - 1775	0.5844	0.7139	- 0.4185
(CH_4)	2345 - 3230	0.5844	0.7139	- 0.4185
	4110 - 4690	0.5844	0.7139	- 0.4185
	5865 - 6135	0.5844	0.7139	- 0.4185
Nitric	1700 - 2005	0.6613	0.5265	- 0.4702
Oxide				
(NO)				
Nitrogen	580 - 925	0.7249	0.3956	- 0.0545
Dioxide	1515 - 1695	0.7249	0.3956	- 0.0545
(NO_2)	2800 - 2970	0.7249	0.3956	- 0.0545
Nitrous	0 - 120	0.8997	0.3783	0.9399
Oxide	490 - 775	0.7201	0.7203	- 0.1836
(N_2O)	865 - 995	0.7201	0.7203	- 0.1836
	1065 - 1385	0.7201	0.7203	- 0.1836
	1545 - 2040	0.7201	0.7203	- 0.1836
	2090 - 2655	0.7201	0.7203	- 0.1836
	2705 - 2865	0.6933	0.7764	1.1931
	3245 - 3925	0.6933	0.7764	1.1931
	4260 - 4470	0.6933	0.7764	1.1931
	4540 - 4785	0.6933	0.7764	1.1931
	4910 - 5165	0.6933	0.7764	1.1931

Table 32. (continued) Band Model Parameters for each Absorbing Molecule.

ABSORBER	SPECTRAL RANGE (cm^{-1})	Band Model Parameters a	n	m
Oxygen	0 - 265	0.6011	1.1879	2.9738
(O_2)	7650 - 8080	0.5641	0.9353	0.1936
	9235 - 9490	0.5641	0.9353	0.1936
	12850 - 13220	0.5641	0.9353	0.1936
	14300 - 14600	0.5641	0.9353	0.1936
	15695 - 15955	0.5641	0.9353	0.1936
	49600 - 52710	0.4704	0.9353	0.1936
Ozone	0 - 200	0.8559	0.4200	1.3909
(O_3)	515 - 1275	0.7593	0.4221	0.7678
	1630 - 2295	0.7819	0.3739	0.1225
	2670 - 2845	0.9175	0.1770	0.9827
	2850 - 3260	0.7703	0.3921	0.1942
Sulfur	0 - 185	0.8907	0.2943	1.2316
Dioxide	400 - 650	0.8466	0.2135	0.0733
(SO_2)	950 - 1460	0.8466	0.2135	0.0733
	2415 - 2580	0.8466	0.2135	0.0733
Water	0 - 345	0.5274	0.9810	0.3324
Vapor	350 - 1000	0.5299	1.1406	- 2.6343
(H_2O)	1005 - 1640	0.5416	0.9834	- 2.5294
	1645 - 2530	0.5479	1.0443	- 2.4359
	2535 - 3420	0.5495	0.9681	- 1.9537
	3425 - 4310	0.5464	0.9555	- 1.5378
	4315 - 6150	0.5454	0.9362	- 1.6338
	6155 - 8000	0.5474	0.9233	- 0.9398
	8005 - 9615	0.5579	0.8658	- 0.1034
	9620 - 11540	0.5621	0.8874	- 0.2576
	11545 - 13070	0.5847	0.7982	0.0588
	13075 - 14860	0.6076	0.8088	0.2816
	14865 - 16045	0.6508	0.6642	0.2764
	16340 - 17860	0.6570	0.6656	0.5061

Table 33. k-Distribution Band Model Parameters for each Absorbing Molecule.

ABSORBER	SPECTRAL RANGE (cm^{-1})	Model a	k-Distribution Parameters G1	G2	G3
Ammonia	0- 385	0.4704	0.2858	0.2698	0.4444
(NH_3)	390- 2150	0.6035	0.1342	0.3539	0.5119
Carbon	425- 835	0.6176	0.1203	0.3482	0.5315
Dioxide	840- 1440	0.6810	0.0697	0.3035	0.6268
(CO_2)	1805- 2855	0.6033	0.1344	0.3540	0.5116
	3070- 3755	0.6146	0.1232	0.3496	0.5272
	3760- 4065	0.6513	0.0909	0.3272	0.5819
	4530- 5380	0.6050	0.1327	0.3534	0.5139
	5905- 7025	0.6160	0.1218	0.3489	0.5293
	7395- 7785	0.7070	0.0543	0.2807	0.6650
	8030- 8335	0.7070	0.0543	0.2807	0.6650
	9340- 9670	0.7070	0.0543	0.2807	0.6650
Carbon	0- 175	0.6397	0.1004	0.3353	0.5643
Monoxide	1940- 2285	0.6133	0.1245	0.3502	0.5253
(CO)	4040- 4370	0.6133	0.1245	0.3502	0.5253
Methane	1065- 1775	0.5844	0.1544	0.3577	0.4879
(CH_4)	2345- 3230	0.5844	0.1544	0.3577	0.4879
	4110- 4690	0.5844	0.1544	0.3577	0.4879
	5865- 6135	0.5844	0.1544	0.3577	0.4879
Nitric	1700- 2005	0.6613	0.0833	0.3196	0.5971
Oxide					
(NO)					
Nitrogen	580- 925	0.7249	0.0453	0.2642	0.6905
Dioxide	1515- 1695	0.7249	0.0453	0.2642	0.6905
(NO_2)	2800- 2970	0.7249	0.0453	0.2642	0.6905
Nitrous	0- 120	0.8997	0.0017	0.0956	0.9027
Oxide	490- 775	0.7201	0.0476	0.2687	0.6837
(N_2O)	865- 995	0.7201	0.0476	0.2687	0.6837
	1065- 1385	0.7201	0.0476	0.2687	0.6837
	1545- 2040	0.7201	0.0476	0.2687	0.6837
	2090- 2655	0.7201	0.0476	0.2687	0.6837
	2705- 2865	0.6933	0.0621	0.2929	0.6450
	3245- 3925	0.6933	0.0621	0.2929	0.6450
	4260- 4470	0.6933	0.0621	0.2929	0.6450
	4540- 4785	0.6933	0.0621	0.2929	0.6450
	4910- 5165	0.6933	0.0621	0.2929	0.6450

Table 33. (Continued) k-Distribution Band Model Parameters for each Absorbing Molecule.

ABSORBER	SPECTRAL RANGE (cm^{-1})	Model a	k-Distribution Parameters G1	G2	G3
Oxygen	0- 265	0.6011	0.1367	0.3547	0.5086
(O_2)	7650- 8080	0.5641	0.1771	0.3554	0.4675
	9235- 9490	0.5641	0.1771	0.3554	0.4675
	12850-13220	0.5641	0.1771	0.3554	0.4675
	14300-14600	0.5641	0.1771	0.3554	0.4675
	15695-15955	0.5641	0.1771	0.3554	0.4675
	49600-52710	0.4704	0.2858	0.2698	0.4444
Ozone	0- 200	0.8559	0.0067	0.1380	0.8553
(O_3)	515- 1275	0.7593	0.0309	0.2317	0.7374
	1630- 2295	0.7819	0.0233	0.2100	0.7667
	2670- 2845	0.9175	0.0005	0.0785	0.9210
	2850- 3260	0.7703	0.0270	0.2212	0.7518
Sulfur	0- 185	0.8907	0.0025	0.1043	0.8932
Dioxide	400- 650	0.8466	0.0082	0.1471	0.8447
(SO_2)	950- 1460	0.8466	0.0082	0.1471	0.8447
	2415- 2580	0.8466	0.0082	0.1471	0.8447
Water	0- 345	0.5274	0.2193	0.3349	0.4458
Vapor	350- 1000	0.5299	0.2164	0.3369	0.4467
(H_2O)	1005- 1640	0.5416	0.2063	0.3433	0.4504
	1645- 2530	0.5479	0.1962	0.3486	0.4552
	2535- 3420	0.5495	0.1945	0.3498	0.4557
	3425- 4310	0.5464	0.1985	0.3475	0.4540
	4315- 6150	0.5454	0.1985	0.3475	0.4540
	6155- 8000	0.5474	0.1962	0.3486	0.4552
	8005- 9615	0.5579	0.1841	0.3534	0.4625
	9620-11540	0.5621	0.1794	0.3549	0.4657
	11545-13070	0.5847	0.1541	0.3576	0.4883
	13075-14860	0.6076	0.1301	0.3525	0.5174
	14865-16045	0.6508	0.0913	0.3275	0.5812
	16340-17860	0.6570	0.0865	0.3229	0.5906

Table 34. k-Distribution Band Model Parameters for each Absorbing Molecule.

ABSORBER	SPECTRAL RANGE (cm^{-1})	Model a	k-Distribution Parameters K1	K2	K3
Ammonia	0- 385	0.4704	19.9507	1.7956	0.2993
(NH_3)	390- 2150	0.6035	27.8458	2.5061	0.4177
Carbon	425- 835	0.6176	29.4277	2.6485	0.4414
Dioxide	840- 1440	0.6810	37.0842	3.3376	0.5563
(CO_2)	1805- 2855	0.6033	27.8241	2.5042	0.4174
	3070- 3755	0.6146	29.0834	2.6175	0.4363
	3760- 4065	0.6513	33.4608	3.0115	0.5019
	4530- 5380	0.6050	28.0093	2.5208	0.4201
	5905- 7025	0.6160	29.2436	2.6319	0.4387
	7395- 7785	0.7070	40.1951	3.6176	0.6029
	8030- 8335	0.7070	40.1951	3.6176	0.6029
	9340- 9670	0.7070	40.1951	3.6176	0.6029
Carbon	0- 175	0.6397	32.0496	2.8845	0.4807
Monoxide	1940- 2285	0.6133	28.9354	2.6042	0.4340
(CO)	4040- 4370	0.6133	28.9354	2.6042	0.4340
Methane	1065- 1775	0.5844	25.8920	2.3303	0.3884
(CH_4)	2345- 3230	0.5844	25.8920	2.3303	0.3884
	4110- 4690	0.5844	25.8920	2.3303	0.3884
	5865- 6135	0.5844	25.8920	2.3303	0.3884
Nitric	1700- 2005	0.6613	34.6834	3.1215	0.5203
Oxide					
(NO)					
Nitrogen	580- 925	0.7249	42.2784	3.8051	0.6342
Dioxide	1515- 1695	0.7249	42.2784	3.8051	0.6342
(NO_2)	2800- 2970	0.7249	42.2784	3.8051	0.6342
Nitrous	0- 120	0.8997	59.3660	5.3429	0.8905
Oxide	490- 775	0.7201	41.7251	3.7553	0.6259
(N_2O)	865- 995	0.7201	41.7251	3.7553	0.6259
	1065- 1385	0.7201	41.7251	3.7553	0.6259
	1545- 2040	0.7201	41.7251	3.7553	0.6259
	2090- 2655	0.7201	41.7251	3.7553	0.6259
	2705- 2865	0.6933	38.5667	3.4710	0.5785
	3245- 3925	0.6933	38.5667	3.4710	0.5785
	4260- 4470	0.6933	38.5667	3.4710	0.5785
	4540- 4785	0.6933	38.5667	3.4710	0.5785
	4910- 5165	0.6933	38.5667	3.4710	0.5785

Table 34. (Continued) k-Distribution Band Model Parameters for each Absorbing Molecule.

ABSORBER	SPECTRAL RANGE (cm^{-1})	Model a	k-Distribution Parameters K1	K2	K3
Oxygen	0- 265	0.6011	27.5869	2.4828	0.4138
(O_2)	7650- 8080	0.5641	24.1314	2.1718	0.3620
	9235- 9490	0.5641	24.1314	2.1718	0.3620
	12850-13220	0.5641	24.1314	2.1718	0.3620
	14300-14600	0.5641	24.1314	2.1718	0.3620
	15695-15955	0.5641	24.1314	2.1718	0.3620
	49600-52710	0.4704	19.9507	1.7956	0.2993
Ozone	0- 200	0.8559	55.6442	5.0080	0.8347
(O_3)	515- 1275	0.7593	46.1189	4.1507	0.6918
	1630- 2295	0.7819	48.5155	4.3664	0.7277
	2670- 2845	0.9175	60.7802	5.4702	0.9117
	2850- 3260	0.7703	47.2982	4.2568	0.7095
Sulfur	0- 185	0.8907	58.6298	5.2767	0.8794
Dioxide	400- 650	0.8466	54.8078	4.9327	0.8221
(SO_2)	950- 1460	0.8466	54.8078	4.9327	0.8221
	2415- 2580	0.8466	54.8078	4.9327	0.8221
Water	0- 345	0.5274	21.8352	1.9652	0.3275
Vapor	350- 1000	0.5299	21.9588	1.9763	0.3294
(H_2O)	1005- 1640	0.5416	22.4234	2.0181	0.3364
	1645- 2530	0.5479	22.9517	2.0657	0.3443
	2535- 3420	0.5495	23.0750	2.0768	0.3461
	3425- 4310	0.5464	22.8262	2.0544	0.3424
	4315- 6150	0.5454	22.8262	2.0544	0.3424
	6155- 8000	0.5474	22.9517	2.0657	0.3443
	8005- 9615	0.5579	23.6654	2.1299	0.3550
	9620-11540	0.5621	23.9774	2.1580	0.3597
	11545-13070	0.5847	25.9207	2.3329	0.3888
	13075-14860	0.6076	28.2957	2.5466	0.4244
	14865-16045	0.6508	33.3998	3.0060	0.5010
	16340-17860	0.6570	34.1575	3.0742	0.5124

5.4.3.2 Inhomogeneous Atmosphere

For inhomogeneous atmospheres, we adopt the same scaling approximation used in LOWTRAN (see Eq. 156):

$$k_i(P,\Theta) \;=\; k_i(P_o,\Theta_o)\,\frac{P}{P_o}\sqrt{\Theta_o/\Theta}$$

The adding method (as discussed in Section 3.1.2 of the Isaacs report[36]) is used for calculating the thermal radiation flux in an inhomogeneous atmosphere. Basically, the parameters used are F^+, F^-, T,. and R, as presented in Section 3.1.2 of the Isaacs report.

5.4.3.3 Stream Approximation, Source Function, and Radiance Calculation

Again, we use the same procedures discussed in Section 3.1.3 of the Isaacs report[36] to calculate the radiance from the source function and stream approximation.

The multiple scattered contribution to the source function is approximated by (Eqs. 137, 125, 126, 133 and 134)

$$J_{MS}(\tau,\pm\mu,\phi) \approx \frac{\omega_o(\tau)}{\pi}\left\{F^{\pm}(\tau)\left[1-\beta(\mu)\right]+F^{\mp}(\tau)\,\beta(\mu)\right\}. \qquad (163)$$

The total source function is:

$$J(\tau,\mu,\phi) \;=\; J_O(\tau,\mu,\phi) \;+\; J_{MS}(\tau,\mu,\phi) \qquad (164)$$

where:

$$J_O(\tau,\mu,\phi) \;=\; \frac{\omega_O(\tau)}{4\pi}\,\pi F e^{-\tau/\mu_O}\,P(\Omega;-\Omega_O)+\left[1-\omega_O(\tau)\right]\mathrm{B}\left[\Theta(\tau)\right] \qquad (165)$$

The single scattered contribution to J_O above is taken directly from the single scattering algorithm used in earlier versions of LOWTRAN. (Actually the summed multiply scattered radiance is added to the summed singly scattered radiance).

One essential difference between the multiple scattering radiance implementation and the previous single scattering version is the treatment of surface reflection. Through the surface boundary condition, surface reflection affects the flux profile and hence the source function throughout the atmosphere. From the radiance solutions:

$$\mathrm{I}(\tau,\mu,\phi) = \left\{\frac{r}{\pi}\left[\pi\mu_o F e^{-\tau^*/\mu_o} + \int_0^1\int_0^{2\pi} \mathrm{I}(\tau^*,-\mu,\phi)\,\mu\,d\mu\,d\phi\right]\right.$$

$$\left. + (1-r)\,B\left[T(\tau^*)\right]\right\} \exp-(\tau^*-\tau)/\mu + \int_\tau^{\tau^*} J(t,\mu,\phi)\; e^{-(t-\tau)/\mu}\;\frac{dt}{\mu} \qquad (166)$$

$$\mathrm{I}(\tau,-\mu,\phi) = \int_0^{\tau} J(t,\mu,\phi)\;\; e^{-(\tau-t)/\mu}\;\;\frac{dt}{\mu} \qquad (167)$$

It can be seen that surface reflection can increase both upward and downward radiances through the source function. For upward radiances, there is a more drastic difference between the single scattering treatment and the implemented multiple scattering version. This concerns reflection of downward scattered radiance from the surface and back to a downward looking observer (the second term in the brackets in Eq. (166)). This contribution is not included in standard single scattering calculations, although the reflected attenuated direct solar term is (i.e., the first term in Equation 166).

The addition of multiple scattering to MODTRAN was made with a minimum of changes to the source code and input deck. Only one new input parameter, IMULT, was added. IMULT, read as the fourth variable on card 1, is set to one for multiple scattering calculations. If aerosols are not included (clear sky case), calculations are performed independent of the value of IMULT.

The main program has been altered to allow the path geometry calculations (called from subroutine GEO) to be accessed twice, once for the original single scatter path and once for the entire atmosphere, required for computation of the multiply scattered radiance. The reason for the second path geometry call is that the thermal and solar source functions used to determine the multiply scattered radiance contribution are functions of the upward and downward flux at each layer. The Multiply scattered flux at a given layer will, in part, be determined by radiation from all atmospheric layers, even those above or below the layers between the observer and target. To calculate the fluxes at each layer, it is therefore necessary to add the flux contributions from the surface up to space, and back down to the surface again. This adding procedure, executed in the new subroutine FLXADD, is discussed in detail in Section 3.1.2.1 and 3.1.2.2 of the Isaacs report[36].

A flag (variable ITEST) has been incorporated into RFPATH for the purpose of isolating the refracted viewing path zenith angle for each layer, as opposed to the solar zenith angle, calculated for the solar cases in a later pass through RFPATH.

A number of changes were incorporated into subroutine TRANS. After calculating the cumulative path parameters used in the original scattering routines, it calls MSRAD, where the aerosol scattering and extinction, H_20 continuum and Rayleigh scattering optical thickness for each layer are calculated, The asymmetry factor for each layer is also calculated based on model extinction and absorption data added to EXABIN, AEREXT, and EXTDTA, and aerosol effective absorber amounts for the four vertically spaced aerosol regions. MSRAD calls subroutine FLXADD.

Subroutine FLXADD calculates the six degraded k components of the H_20/uniformly mixed gas transmission for each layer, as well as the molecular absorption optical thickness (see section 5.4.3 for a detailed description of the necessary modifications needed to accommodate the Pierluissi[13] double exponential formulation). It is then added to the continuum, aerosol extinction, and molecular scattering optical thickness from MSRAD to provide the total optical thickness for each layer and k-value, as well as the corresponding single scatter albedo. The diffuse flux contribution for each isolated layer and k-value is computed from the applicable two-stream approximation, either solar or thermal, and combined in the flux adding routine to determine the total upward and downward flux for each layer for each k value. The diffuse solar downward flux is summed over k value and returned to evaluate the surface reflected downward diffuse solar flux. Function PLANCK returns the black body radiance for a particular wavenumber and temperature in units of Wcm^{-2} $strad^{-1}/cm^{-1}$, while subroutine ALEVEL returns the layer number corresponding to a particular height, the top layer of the atmosphere is layer 1. Knowing the upward and downward fluxes as well as the backscatter parameter β returned from function BETABS, the multiple scattered source function can be determined.

Returning to MSRAD, the radiance is summed over the viewing path (between H1 and H2) and k-values to provide the multiply scattered diffuse radiance contribution. For a downward looking (upward radiance) calculation, the multiply scattered radiance at the upper boundary may be expressed by

$$\mathrm{I}^{+}(n_t) = \sum_{k=1}^{6}\left\{(1-T'_{n_t})\,S(k,n_t) + \sum_{i=n_t}^{n_b-1}(T'_{i+1}-T_i)\;\; S(k,i+1)\right\}\Delta g_k + \mathrm{I}_s \quad (168)$$

where n_b is the bottom layer, n_t the top layer, S(k,i) the source function for a particular k value and layer i. T_i' is the transmission from the upper boundary (H2) through layer i along the viewing path. The total upward radiance also includes I_S, a direct solar reflection surface contribution or surface thermal emission term, which includes the contribution due to the reflection of the single and multiple scattered solar radiance.

For a thermal case,

$$I_s = B_s T_t \varepsilon \quad (169)$$

where B_S is the black body function for a given surface temperature and frequency, T_t is the total atmospheric transmissivity, and ε is the surface emissivity. For the single scatter solar case,

$$I_s = a_s \mu_o T_t S/\pi \quad , \quad (170)$$

where a_S is the surface albedo, μ_0 the cosine of solar zenith angle at the surface, and S the direct solar intensity at the surface. With multiple scattering (IMULT=1), the single and multiple scatter reflection terms are added, so that:

$$I_s = a_s \mu_o T_t S/\pi + a_s F_s^- T_t/\pi \quad , \quad (171)$$

where F_s^- is the downward diffuse flux at the surface.

`For an upward looking (downward radiance) case, the multiply scattered radiance is expressed by:

$$I^-(n_b) = \sum_{k=1}^{3} \left\{ (1-T_{n_b}) S(k,n_b) + \sum_{i=n_b}^{n_t+1} (T_i - T_{i-1}) S(k,i-1) \right\} \Delta g_k \quad (172)$$

where T_i is the transmission from the lower boundary (H1) through layer i along the viewing path. At this point, the path parameters are reloaded, and TRANS is executed once more for the single scattering case. The single scatter diffuse radiance is added to the multiple scatter term and the boundary radiance contributions (if any) to yield the total thermal radiance, while the solar/lunar radiance is the sum of the single and multiple scatter terms plus a surface reflection term where applicable. MSRAD and FLXADD are not called for the MODTRAN single scatter case.

5.4.3.4 Notes on the Operation of Codes with Multiple Scattering

Unlike the earlier LOWTRAN models, the new MODTRAN/LOWTRAN 7 requires a complete atmospheric profile (surface to surface) to properly calculate the multiple scattering contribution to the radiance. For a calculation involving a path from 0-1 km, for example, it is still necessary to choose the desired stratospheric as well as higher level aerosol distribution set by IVULCN on card 2. For a 3-20 km path, the boundary layer aerosols, set using IHAZE, on card 2 or user-defined via card 2D, will now affect the calculated radiance. The earlier versions of LOWTRAN, performing single scattering calculations, required aerosol information only along the path between the observer and target.

When the models are run for solar single scattering only, (IMULT = 0), the output for a solar case includes the reflected attenuated direct solar radiance under the heading GROUND REFLECTED. However, in many cases, the ground reflected diffuse

radiance due to single and multiple scattering is of the same order of magnitude as the direct reflected radiance. The output with multiple scattering activated (IMULT =1) has therefore been altered to include both the total (diffuse single and multiple scattered and direct) and direct reflection terms.

Running MODTRAN with multiple scattering results in a several-fold increase in CPU time. The atmospheric profile and path being used may not produce a significant multiple scattering contribution, possibly resulting in wasted computer time. Both the total (single and multiple) and single scattered radiance are included under the heading PATH SCATTERED RADIANCE. If in doubt, the user can run a multiple scattering calculation to determine the relative size (s) of the single and multiple scatter contributions. If multiple scattering is negligible, future calculations may be made with the more economical single scatter (IMULT = 0) option.

5.4.4 Comparison to Exact Calculations

5.4.4.1 Solar Multiple Scattering

In order to verify the correct operation of the implemented multiple scattering treatment for both solar and thermal regimes, comparisons were made to exact results.

In the case of solar multiple scattering, exact results were obtained for a variety of cases during the trade-off analysis summarized in Appendix A of the Isaacs report[36]. Exact solutions to the radiative transfer equation for solar multiple scattering were obtained using the Gauss-Seidel iterative method based on a code by Dave[283]. This algorithm evaluates the fluxes and radiances for inhomogeneous atmospheres with arbitrary vertical distributions of anisotropically scattering aerosol overlying a Lambertian reflecting surface.

A number of special modifications of LOWTRAN were necessary to accommodate the comparison. These included reading in the same aerosol extinction and absorption coefficients, asymmetry factor, and phase function as were used for the Dave model runs, and forcing LOWTRAN to use the quantities with the same vertical distribution as the Dave code. (Ordinarily, user supplied aerosol data read into LOWTRAN will only be used in the lowest 2 km of the atmosphere). These changes made the comparison as close as possible to a direct one. The LOWTRAN code was run at 0.55 μm with the sun at a zenith angle of 60°.

The first test of the LOWTRAN implementation is whether the adding method is calculating the correct fluxes for use in the stream approximation of the multiply scattered source function. Table 35 compares the emergent fluxes calculated by the

exact code and LOWTRAN. For simplicity, all fluxes and radiances plotted in the Isaacs report[36] (pages 81-85) have been normalized to correspond to π units of incident solar irradiance. To obtain the appropriate engineering units (watts/cm^2 cm-^{1}, and watts/cm^2 str cm-^{1}, for flux and radiance, respectively), the normalized values can be multiplied by 1.719 x 10-^{6}. As can be seen from the results, the solar two stream approximation and flux adding procedure in LOWTRAN is reproducing the exact values quite well throughout the range of optical thichnesses and surface albedos examined. The errors, on the order of a few percent, are to be expected from the two stream approximation.

Table 35. Comparison of Solar Multiply Scattered Emergent Fluxes
(Normalized to π Units of Incident Irradiance) from
FLXADD Subroutine (L) and Exact calculation (E).

	Upward Flux $F^+(\pi = 0)$		Downward Flux $F^-(\pi = \pi^*)$	
π^*	r = 0.0 L / E	r = 0.4 L / E	r = 0.0 L / E	r = 0.4 L / E
0.25	.188 / .191	.611 / .634	.323 / .316	.367 / .371
0.50	.244 / .256	.562 / .584	.503 / .489	.536 / .544
1.00	.316 / .324	.492 / .515	.599 / .567	.605 / .615

A good comparison between the exact radiance calculation as a function of path zenith angle (theta) and those obtained from using either the solar single scattering option or the multiple scattering option can be seen in the Isaacs[36] report (Figures 4-9 to 4-12, pgs. 81-84). Plotted are the normalized emergent upward and downward radiances for an optical depth of 0.5 and surface albedos of 0.0 and 0.4. The plots extend to a maximum zenith angle of 60° since at larger angles the effects of refraction in the MODTRAN code make it difficult to compare to the plane parallel exact results. In all cases it can be seen that the addition of the multiply scattered contribution to path radiance in MODTRAN has considerably improved the simulation as compared to that obtained from the exact code. The improvement is considerable, especially for upward radiance when there is surface reflection (see Figure 4-11). This is because although the single scatter version of LOWTRAN included the surface reflection of the attenuated direct solar beam, it contained no provision to treat the reflected downward scattered radiance. This contribution (which is the second term in the brackets in Equation (166)) may be considerable when multiple scattering is a factor and the MS

option is included in the calculation, since the downward scattered flux is calculated as a result of the adding method.

The relative accuracies as a function of path zenith angle expressed as percent errors obtained in the comparison between MS calculations and the exact calculations for all optical depths evaluated are summarized in (Figures 4-13 and 4-14, Pg. 85-86 of the Isaacs report[36]) for surface albedos of 0.0 and 0.4, respectively. In general, the solar multiple scattering approach implemented within the models underestimates radiance by 10 or 20 percent. These accuracies are consistent with those obtained off line in the trade-off analysis.

5.4.4.2 Thermal Multiple Scattering

The MODTRAN/LOWTRAN thermal multiple scattering method was compared to the thermal multiple scattering routine in FASCODE. The FASCODE MS had been compared to exact multiple scattering using the discrete ordinate method. In general, the degraded FASCODE calculations are within 10% of the answers obtained when using MODTRAN.

A significant problem with the previous treatment of thermal scattering within earlier versions of LOWTRAN, was the failure to provide a source function to introduce multiply scattered radiance contributions along the observed path. As a consequence, LOWTRAN seriously underestimated path radiance for long paths near the horizon where multiple scattering contributes significantly (Ben-Shalom et al.,[281]). For a good comparison of this effect see the Isaacs report[36] (pgs. 79-92, Figures 4-17 to 4-20).

6. Validation and Applications

Throughout the development of the MODTRAN model it has been meticulously compared to FASCODE calculations. It is of course extremely important to compare any model to actual measurements. An interferometric measurement by a Bomem FTS taken on 2 July 1992 at Sudbury, Ma; is compared with a MODTRAN 2 calculation in Figure 62. Possible differences may arise from several factors; errors in the forward calculations, the input profiles of temperature and water vapor supplied by supporting radiosonde data, and the instrumental calibration. The actual agreement, except for the 10 micron ozone, is within a few % RMS. This instrument, a Double Beam Interferometer Sounder (DBIS), was designed and operated by the Defense Research Establishment Valcartier (DREV), Canada. The instrument and the calibration are described fully in a paper by Theriault et al.[295].

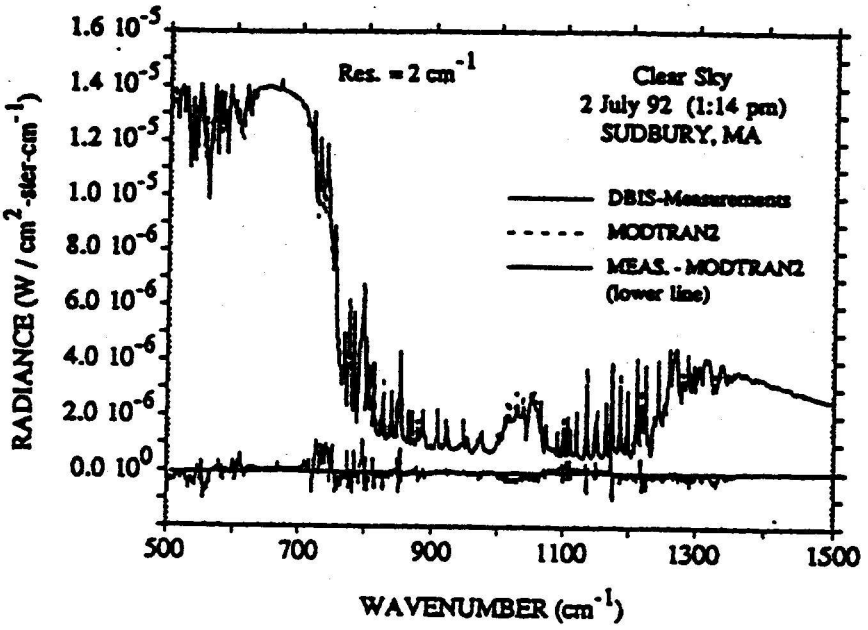

Figure 62. Atmospheric Up-looking Emission Spectra as Measured and Calculated by the DBIS Interferometer and MODTRAN 2 Calculations. Input Specifications for MODTRAN were Provided by Supporting Radiosonde Profiles of Temperature and Water Vapor.

The Theriault paper describes the development of a successful simultaneous (temperature and water vapor profile) retrieval algorithm, based primarily on FASCOD3 forward calculations, with accompanying derivative matrices. Traditionally the derivative matrices required for the least square residual technique embody time-consuming forward runs of full-path FASCODE radiance predictions, each run differing

from the preceding run by a single small perturbation, $x = x_o + x'$, where x = T(K) or $H_2O(g/m^3)$, for each layer, l. The Jacobian matrix is then defined as the set of differences in total radiance:

$$\frac{dR(x,1)}{dx} = \frac{R(x,1) - R_o}{x'} \qquad (173)$$

where: R_o is the unperturbed total radiance and

R(x,1) is the total radiance with a single perturbation ($x = x_o + x'$ and $x' = T'$ or H_2O) at layer 1

The size of the original matrix is j by k, where j is the number of spectral channels, dependent on spectral resolution, and k is (at minimum) the number of atmospheric layers or boundaries times the number of constituents undergoing perturbation in the simultaneous retrieval.

Moncet and colleagues[296] have recently devised a method which greatly optimizes calculations of the Jacobian elements, principally based on FASCODE. However, even with these modifications, this task will still consume a formidable amount of computer time. This has prompted an investigation into the feasibility of employing MODTRAN 2 for the Jacobian calculations. The task did not require a modification of MODTRAN, instead the outline above was followed: each full path radiance calculation was carried out with and without the perturbation at each layer over the spectral range of the DBIS instrument. The subsequent derivative matrix elements were then compared to the equivalent FASCODE elements. The agreement, as seen in Figures 63,64 and 65 (all typical), is remarkably good for both temperature and water vapor perturbations. The RMS differences in the Jacobian radiances (Eq. 173 with the denominator set to unity) are of the order of 1.0E-08 to 1.0E-10 compared to an average radiance of 3.0E-06 $W/(cm^2\text{-ster-}cm^{-1})$, smaller than 3 parts in 1000.

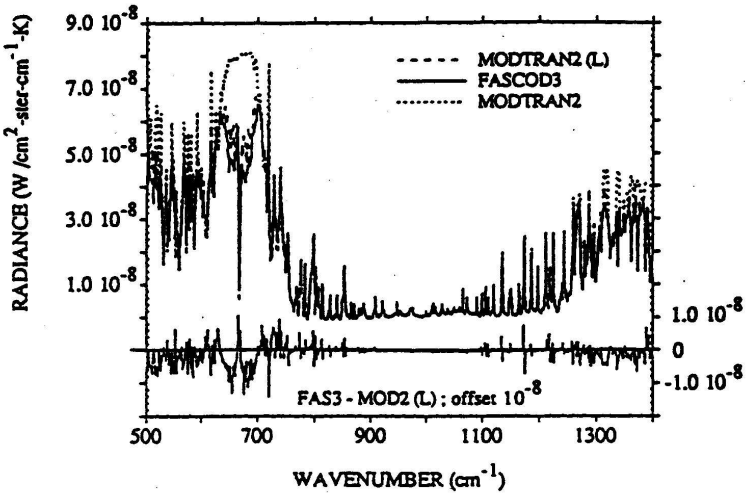

Figure 63. Temperature Jacobians for a 2 K Temperature Perturbation Centered at 0.2 km, where the Original Temperature and Water Vapor Profiles Correspond to the Supporting Radiosonde Data for Figure 62. Note that MODTRAN 2, without the "linear in Tau" Approximation Cannot Follow the Sensitivity of FASCOD3 and MODTRAN 2(L) when the Transmittance is Optically Thick Due to CO_2 and H_2O.

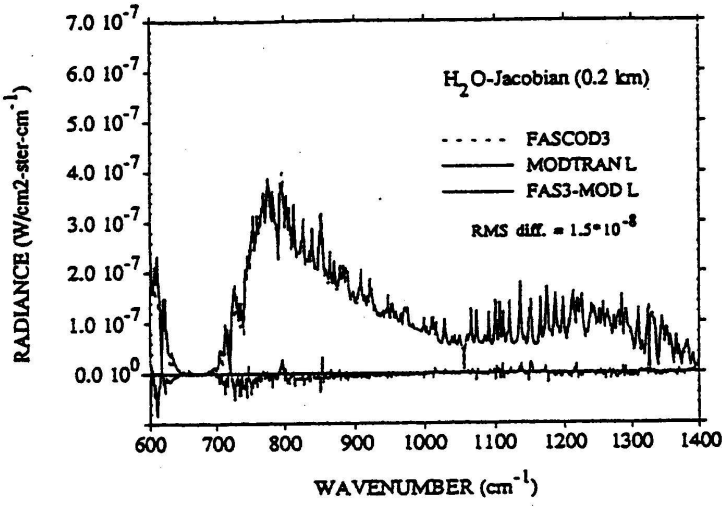

Figure 64. Water Vapor Jacobians for a 0.1 g/m^3 Perturbation at 0.2 km for the same Conditions as in Figure 63. Note the Magnitude of the RMS Deviations Relative to the Maximum in the Jacobian and the Corresponding Total Radiance in Figure 62.

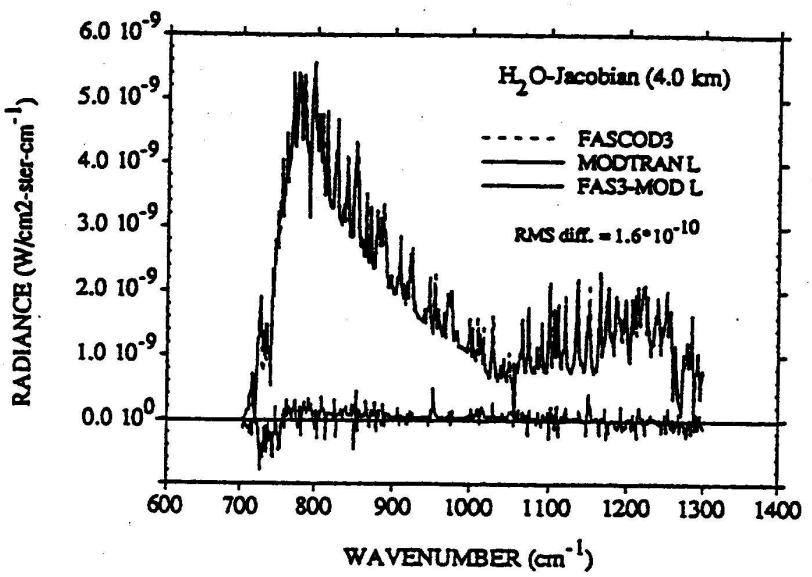

Figure 65. Same Calculations as in Figure 64 Except that the Perturbation Occurs at 4 km. While the Maximum Magnitude of the Jacobian has Fallen by two Orders of Magnitude, the Relative RMS Differences with FASCODE Remain Unchanged.

Another way of looking at the "second order" noise imposed by substituting MODTRAN-derived Jacobian elements for FASCODE' s Jacobian' s is that the RMS noise in the system is potentially increased by a factor of 1.05 over that previously calculated for the line-by-line Jacobian noise. This number is approximated by:

$$\left[(RMS\ noise)/R(v')\right] / \left[J(v')/R(v')\right] \quad \approx \quad 1/20 \qquad (174)$$

where v' denotes the frequency of the Jacobian (J) maximum. That is, the inherent signal/noise ratio of MODTRAN Jacobians is approximately 20 for these three typical cases. It should be noted that the magnitude of any particular Jacobian element represents (in these cases) that layer' s contribution to the total radiance. Therefore, the H_2O Jacobian at 4km, with a maximum value of 5.0E--09 (at 800 cm^{-1}) compared to a total radiance of 2.5E-06, contributes less than 0.2% to the total signal, while the Jacobian at 0.2km contributes approximately 12% to the signal. However, the additional RMS MODTRAN induced noise in the Jacobians is approximately the same fraction for each; for instance, the S/N is 26 at 4km and 20 at 0.2km. Therefore, there appears to be no systematic altitude-dependent impact when substituting MODTRAN for FASCODE Jacobians.

A pair of inversions for the above mentioned DBIS measurement (2 July 1992) have been performed using the Theriault-Moncet algorithm with similar channel; selection and damping factors, as described by Theriault, et al.[295]. Figure 66 displays the first guess inputs, the radiosonde profiles, and the inverted profiles, using both the FASCODE and MODTRAN-derived Jacobian matrices. The differences in the inverted profiles are typically small but not insignificant. The MODTRAN Jacobians introduce an additional oscillation, particularly in the H_2O profile. A preliminary attempt to account for a 5% increase in system noise introduced by MODTRAN (by adopting a slightly larger damping) reduced the oscillation appropriately, but not without a parallel loss in information content. This accounting of noise sources can, of course, be documented according to the definitions of Rodgers[297]. However, the initial success in reproducing accurate Jacobians, substituting them directly into an existing inversion algorithm, and retrieving realistic profiles is very promising.

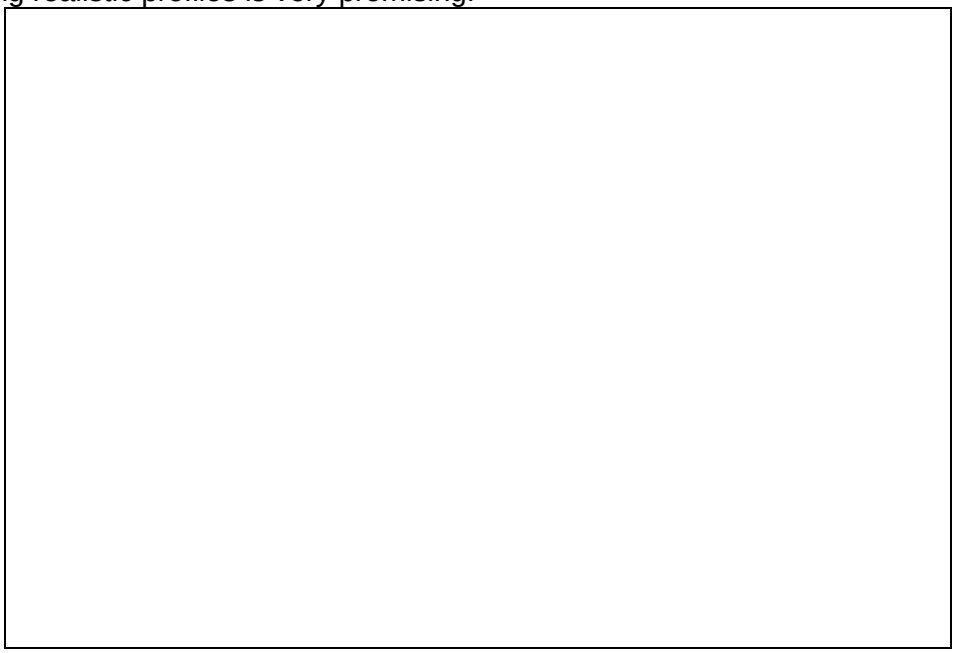

Figure 66. Simultaneous Retrieval of Temperature and Water Vapor Profiles for Conditions Appropriate to Figure 62., Using Both FASCOD3- and MODTRAN-Derived Jacobians. In each Instance, FASCOD3, with the Exact Profiles, was used for the Forward Radiance Simulation, while the Inversion was Initialized with the "Guess" Profiles.

7. Discussion of Future Modifications

The capabilities of the MODTRAN 2 model have yet to be fully exploited. The increased accuracy of the newly developed band model parameters (HITRAN92 compatible), coupled with the LOWTRAN 7 and FASCOD3 common elements (see Chapter 2) for e.g.; coarse continua CO_2, H_2O, N_2, O_2, etc.), spherical refractive geometry, default constituent profiles for gases, clouds, aerosols, fogs, rain models and thermal multiple scattering, combined with "ease of use", suggest that MODTRAN 2 may be an effective tool throughout the fields of atmospheric remote sensing and radiative transfer. For most observational conditions and spectral domains, the accuracy of MODTRAN 2 transmittance calculations fall within a few percent of FASCOD3 predictions, both statistically and in spectral detail. The agreement is sufficiently good that, for simulations at 2 cm^{-1} and greater resolution, MODTRAN 2 may be substituted for FASCODE for most applications. In addition, layer-specific radiance contributions, represented by the detailed agreement in the Jacobian comparisons (see Chapter 6), suggest that MODTRAN 2 may also be appropriate for broader applications. Further studies that continue to explore these layer-specific attributes, based on flux-divergence quantities (leading to rapid estimates of up- and down-welling fluxes, heating/cooling rates, and photodissociation rates) will be conducted in the future.

The speed, accuracy and user-friendliness of MODTRAN make it extremely attractive for enhancements and vectorization. Near term plans include the addition of new molecular cross sections, including IR chloro-fluorocarbons (CFC' s) and additions to the UV (specifically, SO_2 and NO_2). These additions will allow MODTRAN to effectively calculate heating and cooling rates, as well as photochemical photo-dissociation rate calculations, both are required inputs for pollution and climate change studies. Longer term plans call for the evolution of several new models based on or appended to MODTRAN; e.g. AURIC E[298,299] (a MODTRAN extension to 0.1 microns), an expanded model MOSART[300] (combining MODTRAN with improved surface reflectance and enhanced cloud models from the APART 7 model[301]).

In the upper atmosphere (above 120 km) a chemical treatment for the effects of non-local thermodynamic equilibrium conditions (NLTE) is a necessity. A new model combining MODTRAN 2 and the SHARC-3 model[302] is currently being developed into a model called SAMM[303]. MODTRAN, FASCODE and LOWTRAN are also included in the new all-inclusive radiative transfer model, PLEXUS[304].

REFERENCES

1. Berk, A., Bernstein, L.S., Robertson, D.C., "MODTRAN: A Moderate Resolution Model for LOWTRAN 7", GL-TR-89-0122, 1989.

2. Kneizys, F.X., Shettle, E.P., Abreu, L.W., Chetwynd, J.H., Anderson, G.P., Gallery, W.O., Selby, J.E.A. and Clough, S.A. (1988), Users Guide to LOWTRAN 7, AFGL-TR-88-0177, (NTIS AD A206773).

3. Kneizys, F.X., Shettle, E.P., Gallery, W.O., Chetwynd, J.H., Abreu, L.W. Selby, J.E.A., Clough, S.A. and Fenn, R.W, (1983), Atmospheric Transmittance/Radiance: Computer Code LOWTRAN 6, AFGL-TR-83-0187, (NTIS AD A137796).

4. Kneizys, F.X., Shettle, E.P., Gallery, W.O., Chetwynd, J.H., Abreu, L.W., Selby, J.E.A., Fenn, R.W., and McClatchey, R.A. (1980), Atmospheric Transmittance/ Radiance: Computer Code LOWTRAN 5, AFGL-TR-80-0067, (NTIS AD A 088215) .

5. Robertson, D.C., Bernstein, L.S., Haimes, R., Wunderlich, J. and Vega, L., 5 cm^{-1} Band Model Option to LOWTRAN 5, Appl. Opt., 20: 3218 (1981)

6. Selby, J.E.A., Kneizys, F.X., Chetwynd, Jr., J.H., and McClatchey, R.A. (1978) Atmospheric Transmittance/Radiance: Computer Code LOWTRAN 4, AFGL-TR-78-0053, AD A058643.

7. Selby, J.E.A., Shettle, E.P., and McClatchey, R.A. (1976) Atmospheric Transmittance from 0.25 to 28.5 μm: Supplement LOWTRAN 3B, AFGL-TR-76-0258, AD A040701.

8. Selby, J.E.A. and McClatchey, R.A. (1975) Atmospheric Transmittance from 0.25 to 28.5 μm: Computer Code LOWTRAN 3, AFCRL-TR-75-0255, AD A017734.

9. Selby, J.E.A, and McClatchey, R.A. (1972) Atmospheric Transmittance from 0.25 to 28.5 μm: Computer Code LOWTRAN 2, AFCRL-TR-72-0745, AD A763721

10. Anderson, G.P., Clough, S.A., Kneizys, F.X., Chetwynd, J.H., and Shettle, E.P. (1986) AFGL Atmospheric Constituent Profiles (0-120 km), AFGL-TR-86-0110,

AD A175173.

11. NASA (1966), U.S. Standard Atmosphere Supplements, 1966, U.S. Government Printing Office, Washington, D.C .

12. NASA (1976), U.S. Standard Atmosphere Supplements, 1976, U.S. Government Printing Office, Washington, D.C .

13. Pierluissi, J.H. and Maragoudakis, C.E. (1986) Molecular Transmission Band Models for LOWTRAN, AFGL-TR-86-0272, AD A180655

14. Clough, S.A., Kneizys, F.X., Rothman, L.S. and Gallery, W.O., (1981) Atmospheric Spectral Transmittance and Radiance: FASCOD1B, SPIE vol 277/Atmospheric Transmission.

15. Burch, D.E. and Alt. R.L. (1984) Continuum Absorption by H_2O in the 700-1200 cm^{-1} and 2400-2800 cm^{-1} Windows, AFGL-TR-84-0128 AD A147391

16. Burch, D.E. (1985) Absorption by H_2O in Narrow Windows between 3000 and 4200 cm^{-1}, AFGL-TR-85-0036, AD A166648.

17. Devir, A.D., Ben-Shalom, A., Lipson, S.G., Oppenheim, U.P., and Ribak, E. (1985) Atmospheric Transmittance Measurements: Comparison with LOWTRAN 6 Report RAA/99-85, Technion-Israel Institute of Technology, Haifa 32000, Israel.

18. Jacor, ?? H2O cont WL/LL report ???

19. Anderson, G.P., Chetwynd, J.H., Theriault, J.-M., Acharya, P.K., Berk, A., Robertson, D.C., Kneizys, F.X., Hoke, M.L., Abreu, L.W., and Shettle, E.P. (1992) MODTRAN 2: Suitability for Remote Sensing, SPIE, Vol xxxxx

20. Rothman, L.S., Gamache, R.R., Tipping, R.H., Rinsland, C.P., Smith, M.A.H., Benner, D.C., Malathy Devi, V., Flaud, J.-M., Camy-Peyret, C., Perrin, A., Goldman, A., Massie, S.T., Brown, L.R., and Toth, R.A. (1992) The HITRAN Molecular Database: Editions of 1991 and 1992, J. Quant. Spectrosc. Radiat. Transfer, vol 48 no. 5/6, pp. 469-507

21. Acharya, P.K., Robertson, D.C., and Berk. A. (1993), Upgraded Line-of-Sight Geometry Package and Band Model Parameters for MODTRAN, PL-TR-93-212722. Yoshino, K., Cheung, A.S-C, Esmond, J.R., Parkinson, W.H., Freeman, D.E., Guberman, S.L., Jenouvrier, A., Coquart, B., and Merienne, M.F. (1988) Improved Absorption Cross Sections of Oxygen in the Wavelength Region 205-240 nm of the Herzberg Continuum, Planet, Space Sci .36: 1469-1475.

23. Johnston, H.S., Paige, M., and Yao, F. (1984) Oxygen Absorption Cross Sections in the Herzberg Continuum and between 206 and 327K, J. Geophys Res. 89: 11661-11665.

24. Shardanand (1977) Nitrogen-Induced Absorption of Oxygen in the Herzberg Continuum, J. Quant. Spectrosc. Radiat. Transfer 18:525-530.25. Frederick, J..E. and Hudson, R.D. (1979) Predissociation Linewidths and Oscillator Strengths for the (2-0) to (13-0) Schumann-Runge Bands of O_2, J. Molec. Spectrosc, 74:247-258.

26. Yoshino, K., Freeman, D.E., and Parkinson, W.H. (1984) Atlas of the Schumann-Runge Absorption bands of O_2 in the Wavelength Region 175-205 nm., J. Phys. Chem. 13:207.

27. Bass, A.M. and Paur, R.J. (1985) The Ultraviolet Cross-Sections of Ozone. Measurements in Atmospheric Ozone, Proceedings of the Quadrennial Ozone Symmposium in Halkidiki, Greece, edited by C. Zeferos and A. Ghaz, pp. 606-616 D. Reidel, Inc.

28. Molina, L.T. and Molina, M.J. (1986) Absolute Absorption Cross Sections of Ozone in the 185-350 nm Wavelength Range, J. Geophys. Res 91:14501-14509.29. Yoshino K., Freeman, D.E., Esmond, J.R., and Parkinson, W.H. (1988) Absolute Absorption Cross Section Measurements of Ozone in the Wavelength Region 238-335 nm and the Temperature Dependence, Planet. Space Sci. 36:395-398.30. Cacciani, M., diSarra, A., and Fiocco, G. (1987) Laboratory Measurements of the Ozone Absorption Coefficients in the Wavelength Region 339-362 nm at Different Temperatures, Dept. of Physics, University of Roma - La Sapienza, Italy, Internal Note No. 882.

31 VanHoosier, M.E., Bartoe, J.D., Brueckner, G.E., and Prinz, D.K. (1988) Absolute Solar Spectral Irradiance 120 nm-400 nm : Results from the Solar Ultraviolet Spectral Irradiance Monitor (SUSIM) Experiment on Board Spacelab 2, Astro, Lett. and Communications 27:163-168.

32. VanHoosier, M.E. and Brueckner, G.E. (1987) Solar Ultraviolet Spectral Irradiance Monitor (SUSIM): Calibration Results from Spacelab 2, Proceedings of the 8th Workshop on Vacuum Ultraviolet Radiometric Calibration of Space Experiments,19 March 1987.

33. Neckel, H. and Labs, D. (1984) The solar radiation between 3300 and 12500 A, Solar Phys. 90:205-258.34. Wehrli, Ch. (1985) Extra-Terrestrial Solar Spectrum, Publication No. 615, July 1985, Physikalisch-Meteorologisches Observatorium and World Radiation Center, CH-7260 Davos-Dorf, Switzerland.

35. Thekeakera, M.P. (1974) Extra-Terrestrial Solar Spectrum, 3000-6100 A° at 1 A° Intervals, Appl. Opt. 13:518-522.

36. Isaacs, R.G., Wang, W-C., Worsham, R.D. and Goldenberg, S. (1986) Multiple Scattering Treatment for use in the LOWTRAN and FASCODE Models, AFGL-TR-86-0073, AD A173990.

37. Isaacs, R.G., Wang, W-C., Worsham, R.D. and Goldenberg, S. (1987) Multiple Scattering LOWTRAN and FASCODE Models, Appl. Opt 26:1272-1281.38. Gathman, S.G., de Leeuw, G., Davidson, K.L., and Jensen, D.R. (1989) The Naval Oceanic Vertical Aerosol Model: Progress Report, AGARD Conference Proceedings No. 454, Atmospheric Propagation in the UV, Visible, IR, and mm-Wave Region and Related Systems Aspects, Copenhagen, Denmark.

39. Falcone, V.J., Abreu, L.W. and Shettle, E.P. (1979) Atmospheric Attenuation of Millimeter and Submillimeter Waves: Models and Computer Code, AFGL-TR-79-0253, (NTIS AD A)

40. Clough, S.A., Kneizys, F.X., Shettle, E.P., and Anderson, G.P. (1986) Atmospheric Radiance and Transmittance: FASCOD2, Proc. of the Sixth Conference on

Atmospheric Radiation, Williamsburg, VA. American Meteorological Society, Boston, MA. 141-144.

41. Longtin, D.R., Shettle, E.P., Hummel, J.R., and Pryce, J.D. (1988) A Desert Aerosol Model for Radiative Transfer Studies, pg. 261-269 in Aerosols and Climate, ed. by P.V. Hobbs and M.P. McCormick, A. Deepak Publishing, Hampton, VA.

42. Longtin, D.R., Shettle, E.P., Hummel, J.R., and Pryce, J.D. (1988) A. Wind Dependent Desert Aerosol Model: Radiative Properties, AFGL-TR-88-0112.

43. Hummel J.R., Shettle, E.P. and Longtin, D.R. (1988) A New Background Stratospheric Aerosol Model for Use in Atmospheric Radiation Models, AFGL-TR-88-0166, (NTIS AD A)

44. Gallery, W.O., Kneizys, F.X., and Clough, S.A., (1983) Air Mass Computer Program for Atmospheric Transmittance/Radiance Calculations: FSCATM, AFGL-TR-83-0065. (NTIS AD A132108) 45. Edlen, K. (1966) The Refractive Index of Air, Metrologia 2: 12.46. Burch, D.E., and Gryvnak, D.A. (1979) Method of Calculating H_2O Transmission
Between 333 and 633 cm^{-1}, AFGL-TR-79-0054, (NTIS AD A072850) 47. Burch, D.E., and Gryvnak, D.A. (1978) Infrared Absorption by CO_2 and H_2O, AFGL-TR-78-0154, (NTIS AD A060079)

48. Burch, D.E., Gryvnak, D.A., and Pembroke, J.D. (1971) Investigation of Absorption by Atmospheric Gases, AFCRL-71-0124, (NTIS AD A882876) 49. Burch, D.E. (January 1970) Semi-Annual Technical Report, Aeronutronic Report No. U-4784.

50. Smith, M.A.H. (1982) Compilation of Atmospheric Gas Concentration Profiles from 0-50 km, NASA Tech Mem 83289, 70 pp.51. W.M.O. (1982) The Stratosphere 1981: Theory and Measurements, Report No. 11, NASA, Greenbelt, MD.

52. W.M.O. (1986) Atmospheric Ozone 1985: Assessment of Our Understanding of the Processes Controlling its Present Distribution and Change, WMO Report No. 16, W.M.O.. Geneva. Switzerland.53. Brasseur, G. and Solomon, S. (1984) Aeronomy of the Middle Atmosphere D. Reidel Publishing Co, Dordrecht, Holland, Chapter 5: Composition & Chemistry, 440 pp.

54. Russell III, J.M., Gille, J.C., Remsberg, E.E., Gordley, L.L., Bailey, P.L., Fischer, H., Girard, A., Drayon, S.R., Evans, W.F.J. and Harries, J.E. (1984b) Validation of Water Vapor Results Measured by the LIMS Experiment on Nimbus 7, J. Geophys Res; 89:, 5115-5120.

55. Keating, G.M. and Young D.F. (1985) Interim Reference Ozone Models for the Middle Atmosphere, Interim COSPAR Reference Atmosphere for Altitudes 20 -120 km,

56. Jones, R.L. and Pyle, J.A. (1984) Observations of CH4 and N2O by the Nimbus 7 SAMS: A Comparison with In Situ Data and Two-Dimensional Numerical Model Calculations, J. Geophys. Res; 89:, 5263-5379.

57. Solomon, S., Garcia, R.R., Olivero, J.J., Bevilacqua, R.M., Schwartz, P.R., Clancy, R.T. and Mahleman, D.O. (1985) Photochemistry and Transport of CO in the Middle Atmosphere, J. Atmos. Sci., 42: 1072-1083.

58 WMO and COSPAR

59. CIRA 1972, (1972) Ed, A.C. Strickland, Akademie-Verlag, Berlin, 450 pp.

60. Shettle, E.P. and Fenn, R.W., (1979) Models of the Aerosols of the Lower Atmosphere and the Effects of Humidity Variations on Their Optical Properties, AFGL-TR-79-0214, 17 September 1979.

61. Johnson, R.W., Hering, W.S., Gordon, J.I., and Fitch, B.W. (1979) Preliminary Analysis and Modeling Based upon Project OPAQUE Profile and Surface Data, AFGL-TR-79-0285.

62. Huschke, R.E. (editor) (1959) Glossary of Meteorology, American Meteorological Society, Boston, MA, 638 pp.63. Middleton, W.E.K. (1952) Vision Through the Atmosphere, University of Toronto Press, 250 pp.64. Blifford, I.H., and Ringer, L.D. (1969) The Size and Number Distribution of Aerosols in the Continental Troposphere, J. Atmos. Sci. 26: 716-726.

65. Hoffman, R.J., Rosen, J.M., Pepin, T.J., and Pinnick, R.G. (1975) Stratospheric Aerosol Measurements I: Time Variations at Northern Latitudes, J. Atmos. Sci. 32: 1446-1456.

66. Elterman, L., Wexler, R., and Chang, D.T. (1969) Features of Tropospheric and Stratospheric Dust, Appl. Opt. 8: 893-903.67. Jursa, A.S., Scientific Editor, Handbook of Geophysics and the Space Environment (1985) AFGL Publication.

68. Hãnel, G. (1976) The Properties of Atmospheric Aerosol Particles as Functions of the Relative Humidity at Thermodynamic Equilibrium with the Surrounding Air, in Advances in Geophysics, Vol 19 pp. 73-188, Edited by H.E. Landsberg, J. Mieghem , Academic Press, New York.

69. Hãnel, G. (1972) Computation of the Extinction of Visible Radiation by Atmospheric Aerosol Particles as a Function of the Relative Humidity, Based upon Measured Properties, Aerosol Sci. 3: 377-386.

70. Hale, G.M., and Querry, M.R. (1973) Optical Constants of Water in the 200-nm to 200-μm Wavelength Region, Appl. Opt. 12: 555-563.71. Volz, Frederic E. (1972) Infrared Absorption by Atmospheric Aerosol Substances, J. Geophys. Res. 77: 1017-1031.

72. Volz, Frederic E. (1973) Infrared Optical Constants of Ammonium Sulfate, Sahara Dust, Volcanic Pumice, and Flyash, Appl. Opt. 12: 564-568.

73. Whitby, K.T., and Cantrell, B. (1975) Atmospheric Aerosols-Characteristics and Measurement, International Conf. on Environmental Sensing and Assessment, Vol. 2, Las Vegas, Nev., 14-19 sep 1975.

74. Twitty, J.T., and Weinman, J.A. (1971) Radiative Properties of Carbonaceous Aerosols, J. Appl. Meteor. 10: 725-731.

75. Junge, Christian E. (1963) Air Chemistry and Radioactivity, 382 pp. Academic Press, New York.

76. Junge, C. E. (1972) Our Knowledge of the Physico-Chemistry of Aerosols in the Undisturbed Marine Environment, J. Geophys. Res. 77: 5183-5200.

77. Volz, Frederic E. (1972) Infrared Refractive Index of Atmospheric Aerosol Substance, Appl. Opt. 11: 755-759.

78. Byers, H.R. (1959) General Meteorology, 540 pp., McGraw Hill, New York 79. Silverman, B.A., and Sprague, E.D. (1970) Airborne Measurement of In-Cloud Visibility, 271-276, Second National Conference on Weather Modification, Santa Barbara, CA, 6-9 April 1970, American Meteorological Society.

80. Dyanchenko, P.V. (1962) Experimental Application of the Method of Mathematical Statistics to Microstructural Fog and Cloud Research, Translated by A.I. Voyekova, Main Geophysical Observatory.

81. Longtin, D.R., Shettle, E.P., Hummel, J.R. and Pryce, J.D., (1988), A Wind Dependent Desert Aerosol Model: Radiative Properties, AFGL-TR-88-0112, (NTIS AD A)

82. Shettle, E. P. (1984) Optical and Radiative Properties of a Desert Aerosol Model, IRS ' 84: Current Problems in Atmospheric Radiation, G. Fiocco, Ed., A. Deepak Publishing, Hampton, VA, 74-77.

83. World Climate Research Programme (1983) Report of the Experts Meeting on Aerosols and Their Climatic Effects, A. Deepak and H. E. Gerber, eds. World Climate Programme Publication WCP-55, December 1983.

84. d' Almeida, G. and Schutz, L. (1983) Number, Mass and Volume Distributions of Mineral Aerosol and Soils of the Sahara, Climate and Appl. Meteor., 22: 233-243.

85 Patterson, E.M., and Gillette, D. A. (1977) Commonalities in Measured Size Distributions for Aerosols Having a Soil-Derived Component, J. GeophYs. Res., 82: 2074-2082

86. Schutz, L. and Jaenicke, R. (1974) Particle Number and Mass Distributions Above 10 cm Radius in Sand and Aerosols of the Sahara Desert, J. Appl. Meteor., 13: 863-870.

87. Levin, Z., and Lindberg, J. A. (1979) Size Distribution, Chemical Composition, and Optical Properties of Urban and Desert Aerosols in Israel, J. Geophys. Res.,84: 6941-6950.

88. Kushelevsky, A., Shani G., and Haccoun A. (1983) Effect of Meteorologic Conditions on Total Suspended Particulate (TSP) Levels and Elemental Concentration of Aerosols in a Semi-Arid Zone, Beer-Sheva, Israel), Tellus, 35B: 55-64.

89 Cahill, T. A., Kusko, B. H., Ashbaugh, L. L., Barone, J. B, Eldred, R. A. and Walther, F. G. (1981) Regional and Local Determinations of Particulate Matter and Visibility in the Southwestern United States During June and July, 1979, Atmospheric Environment, 15: 2011-2016.

90. Annegarn, H. J., Van Greiken, R. E., Bibby, D. M. and Von Blottnitz., F. (1983) Background Aerosol Compostion in the Namib Desert, Southwest Africa, Namibia, Atmospheric Environment, 17: 2045-2053.

91. Pinnick, R. G., Jennings, S. G., and Fernandez, G. (1987) Volatility of Aerosols in the Arid Southwestern United States, J. Atmos. Sci., 44: 562-576.92. Levin, Z., Joseph, J. H. and Mekler, Y. (1980) Properties of Sharav (Khamsin) Dust: Comparison of Optical and Direct Sampling Data, J. Atmos. Sci., 37: 882-891.

93. Malm, W. C. and Johnson, C. E. (1984) Optical Characteristics of Fine and Coarse Particulates at Grand Canyon, Arizona, Atmospheric Environment, 18: 1231-1237.94. Otterman, J., Fraser, R. S., and Bahethi, O. P. (1982) Characterization of Tropospheric Desert Aerosols at Solar Wavelengths by Multispectral Radiometry from Landsat, J. Geophys. Res., 87: 1270-1278.

95. Junge, C. and Jaenicke, R. (1971) New Results in Background Aerosols, Studies from the Atlantic Expedition of the R. V. Meteor, Spring 1969, Aerosol Science, 2: 305-314.

96. Savoie, D. L. and Prospero, J. M. (1977) Aerosol Concentration Statistics for the Northern Tropical Atlantic, J. Geophys. Res., 82: 5954-5964.97. Schmidt, M., Specht,

H. and Fabian, P. (1978) Aerosol Measurements at the Algarve Coast of Portugal, Tellus, 30: 449-457.

98. Ganor, E. and Mamane, Y. (1982) Transport of Saharan Dust Across the Eastern Mediterranean, Atmospheric Environment, 16: 581-587.99. Chester, R., Sharples, E. J., Sanders, G. S. and Saydam, A. C. (1984) Saharan Dust Incursion Over the Tyrrhenian Sea, Atmospheric Environment, 18: 929-935.

100. Shaw, G. E. (1980) Transport of Asian Desert Aerosol to the Hawaiian Islands, J. Appl. Meteor., 19: 1254-1259.

101. Jaenicke, R., and Schutz, L. (1978) A Comprehensive Study of Physical andChemical Properties of the Surface Aerosols in the Cape Verde Islands Region, J. Geophys. Res., 83: 3583-3598.

102. d' Almeida, G. A. and Jaenicke, R. (1981) The Size Distribution of Mineral DustJ. Aerosol Sci., 12: 160-162.103. Gillette, D. A., Blifford, Jr., I. H. and Fryrear, D. W. (1974) The influence of wind Velocity on the Size Distributions of Aerosols Generated by the Wind Erosion of Soils, J. Geophys. Res., 79: 4068-4075.

104. Gillette, D. A. (1978) Tests with a Portable Wind Tunnel for Determining Wind Erosion Threshold Velocities, Atmospheric Environment, 12: 2309-2313.

105. Gillette, D. A., Blifford, Jr., I. H. and Fenster, C. R. (1972) Measurements of Aerosol Size Distributions and Vertical Fluxes of Aerosols on Land Subject to Wind Erosion, J. Appl. Meteor., 11: 977-987. 106. Gillette, D. A. (1978) A Wind Tunnel Simulation of the Erosion of Soil: Effect of Soil Texture, Sandblasting, Wind Speed, and Soil Consolidation on Dust Production,I, Atmospheric Environment, 12: 1735-1743.

107. Reiter, E. R. (1971) Atmospheric Transport Processes Part 2: Chemical Tracers, U. S. Atomic 382 pp. 108. Volz, F. E. (1975) Distribution of Turbidity after the 1912 Katmei Eruption in Alaska, J. Geophys. Res. 80: 2643-2648.

109. Volz, F. E. (1975) Burden of Volcanic Dust and Nuclear Debris after Injection into the Stratosphere at 40° -58° N., J. Geophys. Res. 80: 2649-2652. 110. Rosen, J.M.,

Hofmann, D.J., and Laby, J. (1975) Stratospheric Measurements II: the Worldwide Distribution,J. Atmos. Sci. 32: 1457-1462.

111. Cunnold, D.M., Gray, C.R., and Merritt, D.C. (1973) Stratospheric Aerosol Layer Detection, J. Geophys. Res. 78: 920-931.

112. Pepin, T.J., (1977) Inversion of Solar Extinction Data from the Apollo-Soyuz Test Project Stratospheric Aerosol Measurement (ASTP/SAM) Experiment, pp. 529-554 in Inversion Methods in Atospheric Remote Sounding. A workshop sponsored by Old Dominion University and the NASA Langley Research Center, Hampton, VI, 15-17 December 1976, NASA-CP-004.

113. Ivlev, L.S. (1967) Aerosol Model of the Atmosphere, Prob. Fiz. Atmos., No. 7, Leningrad, pp. 125-160, translated by Foreign Science and Technology Ctr., Dept of the Army, available from U.S. NTIS (AD 760-393).

114. Ivlev, L.S. (1969) Atmospheric Aerosol, pp. 28-42 in Radiation Characteristics of the Atmosphere and the Earth' s Surface, Ed. K. Ya Kondratev, Amerind Publishing Co., New Delhi, available from U.S. NTIS (no. TT-71-58003). 115. Rozenberg, G.V. (1966) Twilight: A Study in Atmospheric Optics, Plenum Press, New York, NY, 358 pp.

116. Clemesha, B.R., and Nakamura, Y. (1972) Dust in the Upper Atmosphere, Nature 237: 328-329.

117. Poultney, S.K. (1972) Laser Radar Studies of Upper Atmosphere Dust Layers and the Relation of Temporary Increases in Dust to Cometary Micrometeoroid Streams, Space Research 12: 403-421.

118. Rossler, F. (1968) The Aerosol Layer in the Stratosphere, Space Research 8: 633-636.

119. Rossler, F. (1972) Aerosol Layers in the Atmosphere, Space Research 12: 423-431.

120. Fogle, G., and Haurwitz, B. (1972) Noctilucent Clouds, Space Sci. Rev. 6, 279-340.

121. WCP (1986) A preliminary Cloudless Standard Armosphere for Radiation Computation, WCP-112, WMO/TD-NO 24, World Climate Research Programme, International Association of Meteorology and Atmospheric Physics/Radiation Commission.

122. Remsberg, E. E. (1971) Radiative Properties of Several Probable Constituents of Atmospheric Aerosols, PhD. Thesis, Department of Meteorology, University of Wisconsin, Madison.

123. Remsberg, E. E. (1973) Stratospheric Aerosol Properties and their Effects on Infrared Radiation, J. Geophys. Res., 78: 1401-1407.

124 Palmer, K. F. and D. Williams (1975) Optical Constants of Sulfuric Acid; Application to the Clouds of Venus?, Applied Optics, 14: 208-219. 125. Volz, F. E. (1973) Infrared Optical Constants of Ammonium Sulfate, Sahara Dust, Volcanic Pumice and Flyash, Appl. Opt., 12: 564-568.

126. Pinkley, L. W. and Williams, D. (1976) The Infrared Optical Constants of Sulfuric Acid at 250 K, J. Opt. Soc. Am., 66: 122-124. 127. Reiter, R., Jager, H., Carmuth, W., and Funk, W. (1979) The Stratospheric Aerosol Layer Observed by Lidar since October 1976. A Contribution to the Problem of Hemispheric Climate, Arch. Met. Geoph. Biokl., Ser. B, 27: 121-149.

128. D' Altorio, A., Viconti, G., and Fiocco, G. (1981) Lidar Detection of Volcanic Aerosols in the Atmosphere following the Mount St. Helen Eruption, Geophys. Res. Let., 8: 63-65.

129. Clemesha, B. R. and Simmonich, D. M. (1978) Stratospheric Dust Measurements, 1970-1977, J. Geophys. Res., 83: 2403-2408.

130. Iwasaka, Y., Hayashida, S., and Ono, A. (1983) Increasing Backscattered Lightfrom the Stratospheric Aerosol Layer Radar after Mt. El Chichon Eruption, Laser Radar Measurement at Nagoya (35° N, 137° E), Geophys. Res. Let., 6: 440-442.

131. Hirono, M., Fujiwara, M., Shibata, T., and Kugumiya, N. (1981) Lidar Observations of Mt. St. Helens in May 1980, Geophys. Res. Let., 9: 1019-1022.

132. McCormick, M. P., Swissler, T. J. (1983) Stratospheric Aerosol Mass and Latitudinal Distribution of the El Chicon Eruption Cloud for October 1982, Geophys. Res. Let., 9: 877-880.

133. Clemesha, B. R. and Simmonich, D. M. (1983) Lidar Observations of the El Chicon Dust Cloud at 23° S, Geophys. Res. Let., 10: 321-324. 134. Hirono, M., Fujiwara, M., and Shibata, T. (1981) Lidar Observation of Sudden Increases of Aerosols in the Stratosphere Caused by Volcanic Injections: I. Soufriere 1979 event, J. Atmos. Terr. Phy, 43: 1127-1131.

135. Hirono, M., Fujiwara, M.,and Shibata, T. (1982) Lidar Observation of Sudden Increases of Aerosols in the Stratosphere Caused by Volcanic Injections: II. Sierra Negra Event, J. Atmos. Terr. Phy, 44: 811-818.

136. Hirono, M. and Shibata, T. (1983) Enormous Increase of Stratospheric Aerosols over Fukuoro due to Volcanic Eruption of El Chicon in 1982, Geophys. Res. Let. 10: 152-154.

137. D' Altorio, A. and Visconti, G. (1983) Lidar Observations of Dust Layers' Transience in the Stratosphere Following the El Chichon Volcanic Eruption,Geophys. Res. Let., 10:27-30.

138. Rosen, J. M., Hofmann, D. J., and Laby, J., (1975) Stratospheric Aerosol Measurements, II, Worldwide Distribution, J. Atmos. Sci., 32:1457-1462.

139. Hofmann, D. J., and Rosen, J. M., (1982) Balloon-borne Observations of Stratospheric Aerosol and Condensation Nuclei During the Year Following the Mt. St. Helens Eruption, J. Geophys. Res., 87: 11039-11061.

140. Hofmann, D. J., and Rosen, J. M., (1983) Stratospheric Sulfuric Acid Fraction and Mass Estimate for the 1982 Volcanic Eruption at El Chichon, GeophYs. Res. Let, 10: 313-316.

141. Hofmann, D. J., and Rosen, J. M., (1984) On the Temporal Variation of Stratospheric Aerosol Size and Mass During the First 18 Months Following the 1982 Eruption of El Chichon, J. Geophys. Res., 89: 4883-4890.

142. Pinnick, R. G., Rosen, J. M., and Hofmann, D. J., (1976) Stratospheric Aerosol Measurements, III, Optical Model Measurements, J. Atmos. Sci., 33: 304-314.

143. Oberbeck, V. R., Farlow. N. H., Fong, W., Snetsinger, K. G., Ferry, G. V. Ferry and Hayes, D. M., (1982) Mount St. Helens Aerosol Evolution, Geophys. Res,Let.,9 :1089-1092.

144. Knollenberg, R. G., and Huffmann, D., (1983) Measurements of the Aerosol SizeDistributions in the El Chichon Cloud, Geophys. Res. Let., 10: 1025-1028.

145. Oberbeck, V. R., Danielsen, E. F., Snetsinger, K. G., Ferry, G. V., Fong, W.,Hayes, D. M., (1983) Effect of the Eruption of El Chichon on Stratospheric Aerosol Size and Composition, Geophys. Res. Let., 10: 1021-1024.

146. Wilson, J. C., Blackshear, E. D., and Hyun, J. H., (1983) Changes in the sub-2.5 micron Diameter Aerosol Observed at 20 km Altitude after the Eruption of El Chichon, Geophys. Res. Let., 10: 1029-1032.

147. Witteborn, F. C., O' Brien, K., Crean, H. W., Pollack, J. B., and Bilski, K. H., (1983) Spectroscopic Measurements of the 8- to 13- Micrometer Transmission of the Upper Atmosphere Following the El Chichon Eruptions, Geophys. Res. Let.,10: 1009-1012.

148. Dutton, E., and DeLuisi, J., (1983) Extinction of Solar Radiation by the El Chichon Dust Cloud, Geophys. Res. Let., 10: 1013-1016.

149. Woods, D. C., and Chuan, R. L., (1983) Size-Specific Compositions of Aerosols in the El Chichon Volcanic Cloud, Geophys. Res. Let., 10: 1041-1044.

150. Patterson, E. M. (1981) Measurements of the Imaginary Part of the Refractive index Between 300 and 700 nanometers for Mount St. Helens Ash, Science, 211: 36-838.

151. Patterson, E. M., Pollard, C. O., and Galindo, I., (1983) Optical Properties of the Ash from El Chichon, Geophys. Res. Let., 10: 317-320.

152. Mossop, S.C., (1964) Volcanic Dust Collected at an Altitude of 20 km, Nature 203: 824-827.

153. Newkirk, G. Jr., and Eddy, J.A. (1964) Light Scattering by Particles in the Upper Atmosphere, J. Atmos. Sci. 21: 35-60.

154. Rosen, J.M. (1969) Stratospheric Dust and its Relationship to the Meteoric Influx Space Sci. Rev. 9: 58-89.

155. Poultney, S. K. (1974) Times, Locations and Significance of Cometary Micro Meteoroid Influxes in the Earth' s AtmosphereSpace Res. 14: 707-708.

156. Divari, N.B., Zaginalio, Yu. I., and Koval' chuk, L.V. (1973) Meteoric Dust in the Upper Atmosphere, Solar System Res. 7: 191-196. (Translated from Astronomicheskii Vestnik 7: 223-230).

157. Shettle, E. P., and Volz, F. E. (1976) Optical Constants for a Meteoric Dust Aerosol Model, in Atmospheric Aerosols: Their Optical Properties and Effects, a Topical Meeting on Atmospheric Aerosols Sponsored by Optical Society of America and NASA Langley Research Center, Williamsburg, Virginia, 13-15 December 1976, NASA CP-2004.

158. Gaffey, M.J. (1974) A Systematic Study of the Spectral Reflectivity Characteristics of the Meteorite Classes with Applications to the Interpretation of Asteroid Spectra for Mineralogical and Petrological Information, Ph. D Thesis, M.I.T.

159. Farlow, N.H. and Ferry, G.V. (1972) Cosmic Dust in the Mesophere Space Res. ;2: 369-380.

160. Kornblum, J.J. (1969) Micro-meteoroid Interaction with the Atmosphere J. Geophys. Res. 74: 1893-1907.

161. Kornblurn, J.J. (1969) Concentration and Collection of Meteoric Dust in the Atmosphere, J. Geophys. Res. 74: 1908-1919.

162. National Aeronautics and Space Administration (1969) Meteoroid Environment Model, 1969 (Near Earth to Lunar Surface), NASA SP-8013 (March 1969).

163. Soberman, R. K., and Hemenway C. L. (1965) Meteoric Dust in the Upper Atmosphere, J. Geophys. Res 70: 4943-4949.

164. Lindblad, B.A., Arinder, G., and Wiesel, T. (1973) Continued Rocket Observations of Micro-Meteorites, Space Res. 13: 1113-1120.

165. Filippov, V. L., and Mirumyants, S. O. (1972) Aerosol Extinction of Visible and Infrared Radiation as a Function of Air Humidity, Izv, Atmos. Oceanic Phvs. 8: 571-574.

166. Kasten, F. (1968) Falling Speed of Aerosol Particles, J. Appl. Meteor. 7: 944-947.

167. Diermendjian, D. (1973) On Volcanic and Other Turbidity Anomalies, Advances in Geophys. 16: 267-296.

168. Fitzgerald, J. W. (1978) On the Growth of Aerosol Particles With Relative Humidity, NRL Memo Rpt. 3847.

169. Hãnel, G. (1971) New Results Concerning the Dependence of Visibility on Relative Humidity and their Significance in a Model for Visibility Forecasts, Contrib. Atmos. Phys. 44: 137-167.

170. Larson, R,E., and Bressan, D.J. (1980) Air Mass Characteristics over Coastal Areas as Determined by Radon Measurements, Preprint of Second Conference on Coastal Meteorology, 30 January - 1 February 1980, Los Angeles, CA.; published by A. M, S., Boston, Mass.

171. Heaps, M. G. (1982) A Vertical Structure Algorithm for Low Visibility/Low Stratus Conditions, ASL-TR-0111, US Army Atmospheric Sciences Laboratory, White Sands Missile Range, N.M.

172. Heaps, M. G. , and Johnson, R. D. (1983) An Empirical Algorithm for the Vertical Structure of Atmospheric Extinction, ASL-TR-0142, US Army Atmospheric Sciences Laboratory, White Sands Missile Range, N.M.

173. Lindberg, J.D. (1982) Early Wintertime Fog and Haze. Report on Project Meppen 80, ASL-TR-0108, US Army Atmospheric Sciences Laboratory, White Sands Missile Range, N.M.

174. Hoihjelle, D. L., Pinnick, R. G., Lindberg, J. D., Loveland, J R. B., Stenmark, E. B.,and Petracca, C. J. (1976) Balloon-borne Aerosol Particle Counter Measurement Made in Wintertime at Grafenwohr, West Germany ECOM-DR-76-3, US Army Atmospheric Sciences Laboratory, White Sands Missile Range, N.M.

175. Pinnick, R. G., Hoihjelle, D. L., Fernandez, G., Stenmark, E. B., Lindberg, J. D., Jennings, S. G., and Hoidale, G. B. (1978) Vertical Structure in Atmospheric Fog and Haze and Its Effect on IR Extinction, ASL-TR-0010, US Army Atmospheric Sciences Laboratory, White Sands Missile Range, N.M.

176 Duncan, L D, Lindberg, J. D., and Loveland, R. B. (1980) An Empirical Model of the Vertical Structure of German Fogs, ASL-TR-0071, US Army Atmospheric Sciences Laboratory, White Sands Missile Range, N.M. 177. Marshall, J.S., and Palmer, W.M.K. (1948) The Distribution of Raindrops with Size, J. Meteorlol. 5: 165-166.

178. Anderson, G.P.,Clough, S.A., Kneizys, F.X., Shettle, E.P., Abreu, L.W. Chetwynd, J.H. and Hall, L.A. (1988) FASCOD3: Spectral Simulation, I.R.S. 1988 International Symposium, Lille, France, pg. 372-375.

179. Shettle, E. P., Fenn, R. W., and Mill, J. D. (1983) The Optical and Infrared Properties of Atmospheric

180. Joss, J., and Waldvogel, A. (1969) Raindrop Size Distributions and Sampling Size Errors, J. Atmos.

181. Sekhon, R. S., and Srivastava, R. C. (1971) Doppler Radar Observations of Drop-Size Distributions i

182. Berry, F.A., Bollary, E., and Beers, N.R. (1945) Handbook of Meteorology,Chapter 11, McGraw Hill.

183. Mason, B.J. (1971) The Physics of Clouds, Clarendon Press, Oxford.184. Borovikov, A.M., Khrgian, A.K.H., and others (1963) Cloud Physics, US Dept of Commerce, Office of Tech. Svcs. 185. Carrier, L.W., Cato, G.A., and von Essen, K.J. (1967) The Backscatter and Extinction of Visible and Infrared Radiation by Selected Major Cloud Models, App. Optics 6: 1209-1216. 186 Luke, J.D. (1968) Penetrability of Haze, Fogs, Clouds and Precipitation by Radiant Energy over the Spectral Range 0.1 micron to 10 centimeters, NAVWAG Study 61, AD A847658.

187. Diem, M. (1948) Messurngen der Grosser von Wolkenelementen II, Meteorologiscte Rundeschen 9/10: 261-273.

188. Weickman, H.K. and Aufra Kampe, H.J. (1953) Physical Properties of Cumulus Clouds, J. Meteor. 16: 204-211.

189. Durbin, W. (1959) Droplet Sampling in Cumulus Clouds, Tellus 7: 202-215.

190. Gates, D., and Shaw, C. (1960) Infrared Transmission of Clouds, J. Opt. Sci. Am. 50: 876-882.

191. Squires, P. and Twomey, S. (1960) The Relation Between Cloud Droplet Spectral and the Spectrum of Cloud Nuclei, Amer. Geophys. Uni. 15: 211-219.

192. Silverman, B.A. and Sprague, E.D. (1970) Airborne Measurements of In-Cloud Visibility, Natl. Conf. on Weather Modification of the A.M.S., April 6-9, Santa Barbara, CA.

193. Blau, H.H., Fowler, M.G., Chang, D.T., and Ryan, R.T. (1972) Cloud Microstructure Studies, ERT P-375 Final Report NASA Contract NAS 5-21696.

194. Mie, G. (1908) Beitrage zur Optik Truber Median, Speziell Kollodaler Metallosungen, Ann der Ohys. 25: 377-445.

195. Ray, P.S. (1972) Broadband Complex Refractive Indices of Ice and Water, App. Opt. 11: 1836-1844.

196. World Meteorological Organization (1956) International Cloud Atlas, vol. 1, Geneva, Switzerland.

220. Ludwig, C.B., Malkmus, W., Reardon, J.E., and Thomson, J.A.L., Handbook of Infrared Radiation from Combustion Gases, NASA Report SP-3080 (1980). 221. Curtis, A.R., Q. J. R. Meteorol. Soc., 78: 165 (1952) 222 Godson, W.L., J. Meteorol., 12: 123 (1955)

223. Anding, D. Band Model Methods for Computing Atmospheric Slant-Path Molecular Absorption, Rpt. No. 7142-12-T, Willow Run Laboratories, Institute of Science and Technology, University of Michigan, Ann Arbor, MI (1967) 224. LaRocca, A.J., and Turner, R.E., Atmospheric Transmittance and Radiance: Methods of Calculation, Rpt. No. 107600-10-T, Environmental Research Institute of Michigan, Ann Arbor, MI (June 1975)

225. Penner, S.S., Quantitative Molecular Spectroscopy and Gas Emissivities, (Addison Wesley, London, 1959).

226. Sharma, R.D., Sundberg, R.L., Bernstein, L.S., Duff, J.W., Gruninger, J.H., Robertson, D.C. and Healey, R.J. (1991) Description of SHARC-2, The Strategic High Altitude Atmospheric Radiance Code, PL-TR-91-2071 (NTIS AD A).

227. Pierluissi, J.H., Tomiyama, K., and Gomex, R.B., (1979) Analysis of the LOWTRAN Transmission Functions, Appl. Opt. 18: 1607.

228. Gruenzel, R.R., (1978) Mathematical Expressions for Molecular Absorption in LOWTRAN 3B, Appl. Opt. 17: 2591.

229. Pierluissi, J.H., and Gomez, R.B., (1984) Study of Transmittance Models for the 15 micron-CO_2 Band, Proceedings of the Sixth Conference on Aerospace and Aeronautical Meteorology (American Meteorological Society, Boston, Ma.

230. Elsasser, W.M., (1942) Heat Transfer by Infrared Radiation in the Atmosphere Harvard Meteorological Studies 6 (Howard U.P., Cambridge, Ma.).

231. Goody, R.M., (1952) A Statistical Model for Water Vapor Absorption, Q.J.R. Meteorological Society, 78: 165.

232. Smith, W.L., (1969) Polynomial Representation of Carbon Dioxide and Water Vapor Transmission, NESC-47 (Natl. Environ. Sat. Center, Washington, D.C.

233. Valley, S.L., (1965) Handbook of Geophysics and Space Environments, (McGraw-Hill, New York, NY).

234. Rothman, L.S. (1981) AFGL Atmospheric Line Parameters Compilation: 1980 Version, Appl. Opt. 20: 791.

235. Rothman, L.S., Goldman, A., Gillis, J.R., Gamache, R.R., Pickett, H.M., Poynter, R.L., Husson, N., and Chedin, A. (1983b), AFGL Trace Gas Compilation: 1982 Version, Appl. Opt., 22: 1616-1627.

236. Burch, et al., (1962) Infrared Absorption by Carbon Dioxide, Water Vapor and Minor Atmospheric Constituents, AFCRL-TR-62-698.

237. Burch, D.E., et al., (1975) Infrared Absorption by H_2O, NO_2 and N_2O_4, AFCRL-TR-75-0420, (Ad A019686).

238. France, W.L., Williams, D., (1966) Total Absorptance of Ammonia in the Infrared, J. Opt. Soc. Am. 56: 70.

239. Ford, D.L., and Shaw, J.H., (1965)Total Absorptance of the NO Fundamental Band, Appl. Opt. 4: 1114.

240. Burch, D.E., and Gryvnak, D.A., (1976) Strengths, Widths and Shapes of the Oxygen Lines Near 7600 Angstroms, U-4076, Philco-Ford Corp.,Newport Beach, CA.

241. Burch, D.E., Gryvnak, D.A., and Williams, D., (1962) Total Absorptance of Carbon Dioxide in the Infrared, Appl. Opt. 1: 759.

242. Burch, D.E., Gryvnak, D.A., and Petty, R.R., (1968) Absorption of Infrared Radiation by CO_2 and H_2O, II. Absorption by CO Between 8000 and 10000 cm^{-1} (1-1.25 microns), J. Opt. Soc. of Am. 158: 335.

243. Burch, D.E. et al., (1969) Absorption of Infrared Radiant Energy by CO_2 and H_2O, IV. Shapes of Collisioned-Broadened CO_2 Lines, J. Opt. Soc. of Am. 59: 267.

244. Burch, D.E., Pembrook, J.D., and Gryvnak, D.A., (1971) Absorption and Emission by SO Between 1050 and 1800 cm^{-1} (9.5-7 m), U-4947, Philco-Ford Corp., Newport Beach, Ca.

245. Pierluissi, J.H., and Maragoudakis, C.E., (1984) Molecular Transmission Band Models for the Uniformly Mixed and the Trace Gases, AFGL-TR-84-0320, (NTIS AD A160442).

246. Goldman A., Kyle, T.G., and Bonomo, F.W. (1971) Statistical Band Model Parameters and Integrated Intensities for the 5.9-μ, 7.5-μ, and 11.3-μ bands of HNO_3 Vapor, Appl. Opt. 1: 65.

247. Reddy, S.R., and Cho, C.W. (1965) Canada J. Physics 43: 2331.

248. Shapiro, M.M., and Gush, H.P. (1966) Canada J. Physics 44: 949.

249. McClatchey, R.A., Fenn, R.W., Selby, J.E.A., Volz, F.E., and Garing, J.S. (1972) Optical Properties of the Atmosphere (Third Edition), AFCRL-72-0497 (NTIS AD A753075).

255. Watanabe, K., (1958) Ultraviolet Absorption Processes in the Upper Atmosphere, Advances in Geophysics 5, 153-221.

256. Frederick, J.E., (1982) Solar Irradiance in the Stratosphere: Implications for the Herzberg Continuum Absorption of O2, Geophys. Res. Lett. 9, 461-464.

257. Anderson, G.P. and Hall, L.A. (1983) Attenuation of Solar Irradiance in the Stratosphere: Spectrometer Measurements Between 191 and 207 nm, J. Geophys. Res.,88, 6801-6806.

258. Anderson, G.P. and Hall, L.A. (1989) Solar Irradiance Between 2000 and 3100A With Spectral Band Pass of 1A, J. Geophys. Res. 94, 6435-6441.

259. Cann, M.W.P., Shin, J.B., and Nicholls, R.W. (1984) Oxygen Absorption in the Spectral Range 180-300nm for Temperatures to 3000K and Pressures to 50 Atmospheres, Can. J. Phys., 62, 1738-1751.

260. Trakhovsky, E.A., Ben-Shalom, A., Oppenheim, U.P., Devir, A.D., Balfour, L.S., and Engel, M. (1989) Contribution of Oxygen to Attenuation in the Solar Blind UV Spectral Region, Appl. Opt. 28, 1588-1591.

261. Yoshino, K., Freeman, D.E., and Parkinson, W.H., (1983) High Resolution Absorption Cross Section Measurements and Band Oscillator Strengths of the (1-0)-(12-0) Schumann-Runge Bands of O2, Planet. Space Sci., 31, 339-353. 262. Anderson, G.P. and Hall, L.A. (1986) Stratospheric Determination of O2 Cross Sections and Photodissociation Rate Coefficients: 191-215nm, J. Geophys. Res. 91, 14509-14514.

263. Steinfeld, J.I., Adler-Golden, S.M., and Gallagher, J.W., (1987) Critical Survey of Data on the Spectroscopy and Kinetics of Ozone in the Mesosphere and Thermosphere, J. Phys. Chem. Ref. Data, 16, 911-942.

264. Katayama, D.H. (1979) New Vibrational Quantum Number Assignments for the UV Absorption Bands of Ozone Based on the Isotope Effect, J. Chem. Phys. 71, 815-820.

265. Cacciani, M., diSarra, A., Fiocco, G., and Amoruso, A. (1989) Absolute Determination of the Cross Sections of Ozone in the Wavelength Region 339-355nm at Temperatures 220-293K, J. Geophys. Res. 94, 8485-8490.

266. Cornette, W.M. (1992) Robust Algorithm for Correcting the Layer Problem in LOWTRAN, Appl. Opt. 31, 5767.

267. Wiscombe, W.J. (1976) Extension of the Doubling Method to Inhomogenous Sources, J. Quant. Spectrosc. Radiat. Transfer 16, 477.

268. Ridgway, W.L., Harshvardan, and Arking, A. (1991) Computation of Atmospheric Cooling Rates by Exact and Approximate Methods, J. Geophys. Res. 96, 8969.

269. Clough, S.A., Iacono, M.J., and Moncet, J.-L. (1992) Line-by-Line Calculations of Atmospheric Fluxes and Cooling Rates: Application to Water Vapor, J. Geophys. Res. 97, 15761.

270. Frhlich, C. (1983) Data on Total and Spectral Solar Irradiance: Comments, Appl. Opt. 22: 3928.

271. Ridgeway, W.L., Moose, R.A., and Cogley, A.C. (1982) Single and Multiple Scattered Radiation, AFGL-TR-82-0299, (NTIS AD A126323).

272. Turner, R.E., et al (1975) Natural and Artificial Illumination in Optically Thick Atmospheres, Environmental Research Institute of Michigan, Report No. 108300-4-F

273. Condron, T.P., Lovett, J.J., Barnes, W.H., Marcotte, L., and Nadile, R. (1968) Gemini 7 Lunar Measurements, AFCRL-68--0438, AD A678099.

274. Lane, A.P., and Irvine, W.M. (1973) Astron. J. 78.

275. Bullrich, K. (1948) Ber. Deutsch. Wettered, U.S. Zone No. 4.

276. Sharma, S. (1980) An Accurate and Computationally Fast Formulation for Radiative Fields and Heat Transfer in General, Plane-Parallel, Non-Grey Media With Anisotropic Scattering, PhD Thesis, University of Illinois at Chicago 277. Shettle, E.P.,Turner, V.D., and Abreu, L.W., (1983) Angular Scattering Properties of the Atmospheric Aerosols, Fifth Conference on Atmospheric Radiation, October 31-November 4, Baltimore, MD, A.M.S.

278. Henyey, L.G., and Greenstein, J.L. (1941) Diffuse Radiation in the Galaxy, Astrophys. J. 93:70-83

279. Kasten, F. (1968) Rayleigh-Cabannes Streuung in Trockener Luft Unter Berucksichtigung Neuerer Depolarisations-Messungen, Optik, 27: 155-166. 280. Young, A.T. (1980) Revised Depolarization Corrections for Atmospheric Extinction, Appl. Opt. 19: 3427-3428.

281. Ben-Shalom, A., Barzilia, B., Cabib, D., Devir, A.D., Lipson, S.G. and Oppenheim U.P. (1980) Appl. Opt. 19: 6, 838.

282. Isaacs, R.G. and Özkaynak (1980) Uncertainties Associated with the Implementation of Radiative Transfer Theory within Visibility Models, Second Joint Conference on Applications of Air Polution Meteorology, New Orleans, LA, 24-27 March 1980, 362-369. A.M.S., Boston, MA.

283. Dave, J.V. (1981) Transfer of Visible Radiation in the Atmosphere, Atmos. Env., 15: 10/11, 1805-1820.

284. Stephens, G. (1984) The Parameterization of Radiation for Numerical Weather Prediction and Climate Models, Mon. Weather Rev. 112: 826-867.

285. Wiscombe, W.J. and Grams, G.W. (1976) The Backscattered Fraction in Two-Stream Approximations, J. Atmos. Sci. 33: 2440-2451.

286. Meador, W.E. and Weaver, W.R. (1980) Two-Stream Approximations to Radiative Transfer in Planetary Atmospheres: A Unified Description of Existing Methods and a New Improvement, J. Atmos. Sci. 37: 630-643.

287. Arking, A. and Grossman K. (1972) The Influence of Line shape and Band Structure on Temperatures in Planetary Atmospheres, J. Atmos. Sci. 29: 937.

288. Wang, W.-C. and Ryan, P.B. (1983) Overlapping Effect of Atmospheric H_2O, CO_2 and O_3 on the CO_2 Radiative Effect, Tellus, 35B: 81-91.

289. Wiscombe, W.J. and Evans, J.W. (1977) Exponential-Sum Fitting of Radiative Transmission Functions, J. Comput. Phys. 24: 416-444.

290. Bakan, S., Koepke, P. and Quenzel, H. (1978) Radiation Calculations in Absorption Bands: Comparison of Exponential Series and Path Length Distribution Method, Beit. Physics der. Atmos. 51: 28-30.

291. Lacis, A.A., Wang, W.-C. and Hansen, J.E. (1979) Correlated k-Distribution Method for Raditive Transfer in Climate Models: Application to Effect of Cirrus Cloud on Climate, NASA Publ. 2076, E.R. Kreins, Ed., 416 pp.

292. Yamamoto, G., Tanaka, M. and Asano, S. (1970) Radiative Transfer in Water Clouds in the Infrared Region, J. Atmos. Sci. 27: 282-292.

293. Yamamoto, G., Tanaka, M. and Asano, S. (1971) Radiative Heat Transfer in Water Clouds in the Infrared Radiative, J. Quant. Spectrosc. Radiat. Trans, 11: 697-708.

294. Hansen, J.E., Lacis, A.A., Lee, P. and Wang, W.-C., (1980) Climatic Effects of Atmospheric Aerosol, Aerosols: Anthropogenic and Natural Sources and Transport, Ann. N.Y. Acad. Sci. 338: 575-587.

295. Theriault, J.-M., Anderson, G.P., Chetwynd, J.H., Qu, Y., Murphy, E., Turner, V., Cloutier, M., and Smith, A. (1993) Retrieval of Tropospheric Profiles from IR Emission Spectra: Investigations with the Double Beam Interferometer Sounder (DBIS), Optical Remote Sensing of the Atmos, Tech. Digest 5, 78.

296. Moncet, J.-L. (1993) Atmospheric and Environmental Research Inc., Private Communication.

297. Rodgers, C.D. (1987) A General Error Analysis for Profile Retrieval, Advances in Remote Sensing Retrieval Methods, pg. 285. 298. Anderson, G.P., Hall, L.A., Minschwaner, K., Yoshino, K., Betchley, C., and Conant, J.A. (1992) Ultraviolet O_2 Transmittance: AURIC Implementation, Proc. of the Soc. Photo. Opt. Instrum. Eng., 1764, 108.

299. Link, R., Strickland, D.J. and Daniell, R.E., (1992) AURIC Airglow Modules: Phase 1 Development and Application, Proc. of the Soc. Photo. Opt. Instrum. Eng., 1764, 132.

300. Anderson, G.P. (1994) MOSART (Moderate Spectral Atmospheric Radiance Transmittance Code), combining MODTRAN 2 and APART 7, under development by PL/GPOS.

301. Cornette, W.M., (1990) Atmospheric Propagation and Radiative Transfer (APART) Computer Code (Version 7.0), R-075-90, Photon Research Assoc., San Diego, CA.

302. Sharma, R.D., Sundberg, R.L., Bernstein, L.S., Healey, R.J., Gruninger, J.H., Duff, J.W. and Robertson, D.C. (1991) Description of SHARC-2, The Strategic High-Altitude Atmospheric Radiance Code, PL-TR-91-2071.

303. SAMM (SHARC and MODTRAN Merged), (1994), Under Development by PL/GPOS; POC: R.D. Sharma.

304. PLEXUS, an Umbrella Architecture for PL/GP Radiance and Background Codes,(1994) Under Development by PL/GPOC; POC: F.O. Clark.